STATE OF CALIFORNIA • DEPARTMENT OF TRANSPORTATION

TECHNICAL REPORT DOCUMENTATION PAGE

TR-0003 (REV 04/2024)

Lock Form

1. REPORT NUMBER	2. GOVERNMENT ASSOCIATION NUMBER	3. RECIPIENT'S CATALOG NUMBER
CA25-3668		

4. TITLE AND SUBTITLE	5. REPORT DATE
Refined Bridge Deck Design and Analysis	October 10, 2025
	6. PERFORMING ORGANIZATION CODE University of California, Davis
7. AUTHOR	8. PERFORMING ORGANIZATION REPORT NO.
Xun Wang, Rahim Ghoroubi, Brendan Grayson-Wallace, Lijuan Cheng	UCD-SESM-25-01
9. PERFORMING ORGANIZATION NAME AND ADDRESS	10. WORK UNIT NUMBER
Department of Civil and Environmental Engineering University of California, Davis 3161 Ghausi Hall, One Shields Ave. Davis, California 95616	11. CONTRACT OR GRANT NUMBER 65A0774 TO002
12. SPONSORING AGENCY AND ADDRESS	13. TYPE OF REPORT AND PERIOD COVERED Final Report 11/1/2020 – 10/31/2024
California Department of Transportation, Engineering Service Center 1801 30th Street, MS 9-2/5i Sacramento, California 95816 California Department of Transportation, Division of Research and Innovation, MS - 83 1227 O Street Sacramento, California 95814	14. SPONSORING AGENCY CODE

15. SUPPLEMENTARY NOTES

Prepared in cooperation with the State of California Department of Transportation.

16. ABSTRACT

Since the 1960's, bridge live loads (design axle loads) and truck volume have been continuously increasing. Truck loads and wheel configurations that bridge decks are designed for according to the AASHTO LRFD Bridge Design Specifications no longer reflect the modern trucks, not mentioning the larger permit vehicles (e.g., P-15) and new vehicle configurations mandated or allowed by federal or state programs such as special hauling vehicles (SHV) and emergency vehicles (EV) in the design. The approximate analysis method in the AASHTO LRFD specification that the current bridge deck design procedure is based on lacks sufficient accuracy and is not permitted by the California Amendments to AASHTO for the design of reinforced concrete decks and overhangs. In this research, an updated LRFD-based bridge deck design procedure was developed based on refined analysis methods that consider modern vehicle configurations, dynamic loads, flexural and shear demands. Fatigue-related issues were comprehensively reviewed for reinforced concrete bridge decks in the existing literature with a proposed framework for future study. A large series of finite element analyses of refined reinforced concrete bridge deck models using simplified Rigid Support Model (RSM) concept was conducted under various loading conditions and different girder spacings. The accuracy of the model was satisfactorily validated by a set of detailed 3D bridge models. These comprehensive refined analysis results were then used to develop streamlined charts and an updated deck design table (so called CA-A4, California Amendments to A4) following the same format as the existing AASHTO A4 design table. The updated design values for the negative moment in the CA-A4 cover the negative moment demands generated by the HL-93, SHV, and P-15 vehicles for girder spacings less than 13 ft. Special consideration is recommended for EV3 vehicle load and for the other special vehicle types for girder spacings greater than 13 ft. The proposed bridge deck design procedure is expected to facilitate Caltrans ensuring the safety and adequate load-carrying capacity of reinforced concrete bridge decks to meet the growing traffic demand.

17. KEY WORDS	18. DISTRIBUTION STATEMENT	
Bridge deck, analysis, design, Rigid Support Model (RSM)	No restrictions. This document is available to the public through the National Technical Information Service, Springfield, VA 22161.	
19. SECURITY CLASSIFICATION *(of this report)*	20. NUMBER OF PAGES	21. COST OF REPORT CHARGED
Unclassified	209	

DISCLAIMER STATEMENT

This document is disseminated in the interest of information exchange. The contents of this report reflect the views of the authors who are responsible for the facts and accuracy of the data presented herein. The contents do not necessarily reflect the official views or policies of the State of California or the Federal Highway Administration. This publication does not constitute a standard, specification or regulation. This report does not constitute an endorsement by the Department of any product described herein.

For individuals with sensory disabilities, this document is available in alternate formats. For information, call (916) 654-8899, TTY 711, or write to California Department of Transportation, Division of Research, Innovation and System Information, MS-83, P.O. Box 942873, Sacramento, CA 94273-0001.

Approximate Conversions to SI* Units (from FHWA)

Symbol	When You Know	Multiply By	To Find	Symbol
Length				
in	inches	25.4	millimeters	mm
ft	feet	0.305	meters	m
yd	yards	0.914	meters	m
mi	miles	1.61	kilometers	km
Area				
in^2	square inches	645.2	square millimeters	mm^2
ft^2	square feet	0.093	square meters	m^2
yd^2	square yard	0.836	square meters	m^2
ac	acres	0.405	hectares	ha
mi^2	square miles	2.59	square kilometers	km^2
Volume				
fl oz	fluid ounces	29.57	milliliters	mL
gal	gallons	3.785	liters	L
ft^3	cubic feet	0.028	cubic meters	m^3
yd^3	cubic yards	0.765	cubic meters	m^3
NOTE: volumes greater than 1000 L shall be shown in m^3				
Mass				
oz	ounces	28.35	grams	g
lb	pounds	0.454	kilograms	kg
T	short tons (2000 lb)	0.907	megagrams (or "metric ton")	Mg (or "t")
Temperature (exact degrees)				
°F	Fahrenheit	5 (F-32)/9 or (F-32)/1.8	Celsius	°C
Illumination				
fc	foot-candles	10.76	lux	lx
fl	foot-Lamberts	3.426	$candela/m^2$	cd/m^2
Force and Pressure or Stress				
lbf	pound force	4.45	newtons	N
lbf/in^2	pound force per square inch	6.89	kilopascals	kPa

*SI is the symbol for the International System of Units. Appropriate rounding should be made to comply with Section 4 of ASTM E380.

Department of Civil and Environmental Engineering
University of California at Davis
Davis, California 95616

Final Report No. CA25-3668

Refined Bridge Deck Design and Analysis

Xun Wang, PhD
Former Graduate Researcher

Rahim Ghoroubi, PhD
Former Postdoctoral Researcher

Brendan Grayson-Wallace, PhD
Former Graduate Researcher

and

Lijuan (Dawn) Cheng, PhD
Professor

October 2025

Final Report submitted to the California Department of Transportation (Caltrans) under Contract No. 65A0774 TO002

Executive Summary

Since the 1960's, bridge live loads (design axle loads) and truck volume have been continuously increasing. The truck loads and wheel configurations that the bridge decks are designed for according to the AASHTO LRFD Bridge Design Specifications no longer reflect the modern trucks, not mentioning the use of larger permit vehicles (e.g., P-15) and new vehicle configurations mandated or allowed by federal or state programs such as special hauling vehicles (SHV) and emergency vehicles (EV) in the design. The approximate analysis method in the AASHTO LRFD specification that the current bridge deck design procedure is based on was initially developed in the 1930's, and its accuracy is of concern due to simplified assumptions and approximations in the procedure. In addition, the California Amendments to AASHTO do not permit the empirical design of reinforced concrete decks and overhangs due to concerns associated with durability of such members under high average daily truck traffic applications. Laboratory and in-situ testing of concrete bridge decks designed by the empirical method have also demonstrated concrete cracking and potential reinforcement corrosion in such members, as well as insufficiency in the empirical reinforcement to resist shrinkage stresses. Therefore, a more accurate, safe and reliable bridge deck design procedure needs to be developed that considers these impacts to ensure the safety and adequate load-carrying capacity of bridges to meet the growing traffic demands in the State.

Advanced methods of analysis have gained much interest and popularity. For instance, refined analysis methods using 2-D finite element (FE) method have been in practice for almost 50 years in some European countries, where approximate analysis methods are no longer included in the current Eurocodes. However, application of refined analysis methods in the US has been limited to unique or complex bridges, bridges deemed substandard using approximate analysis, analysis of nonstandard permit loads and other special cases. Nevertheless, the current AASHTO LRFD Bridge Design Specifications require the refined analysis for allowable cases without providing much guidance as to how it should be carried out. Neither does it recommend any specific refined analysis method for bridge decks despite of the list of general methods (e.g., finite difference/element/strip method, grid analogy method, yield line method, etc.). The ACI 343R-95 provides a similar list with a statement that "a deck slab may be designed by any procedure satisfying the conditions of equilibrium and geometrical compatibility, provided it is shown that the strength and serviceability criteria are met". The ACI 343R-95 also recognizes the "arching action" in cases of beam-supported thin deck slabs, which, however, does not provide any specific method to account for the effect of such arching action in the design.

In this research, an updated LRFD-based bridge deck design procedure was developed based on refined analysis methods that consider modern vehicle configurations, dynamic loads, flexural and shear demands, and various design parameters. Fatigue-related issues were comprehensively reviewed for reinforced concrete bridge decks in the existing literature with a proposed framework for future study. A large series of finite element analyses of refined reinforced concrete bridge deck models using the simplified Rigid Support Model (RSM) concept was conducted under various loading conditions and different girder spacings. The accuracy of the model was satisfactorily validated by a set of detailed 3D bridge models. These comprehensive refined analysis results were then used to develop streamlined charts and an updated deck design table (so called CA-A4, California Amendments to A4) following the same format as the existing AASHTO A4 design table. The updated design values for the negative moment in the CA-A4 cover the negative moment demands generated by the HL-93, SHV and P-15 vehicles for girder spacings

less than 13 ft. Special consideration is recommended for EV3 vehicle load and for the other special vehicle types for girder spacings greater than 13 ft. The proposed updated design procedure will provide increased cost savings by going beyond use of approximate, simplistic and conservative design methods in the existing specifications. It will also enhance the structural safety by more rigorous assessment of required modern loads and accurate modeling of system/local structural behavior.

Scope of Work

This research project has two phases, the first phase of research was conducted by the former student researcher Dr. Xun Wang with the primary intent of investigating a feasible finite element modeling strategy to obtain the load demands of reinforced concrete bridge decks subjected to various vehicle loads, by means of a refined analysis approach. A serious of parametric studies were performed to explore the influences due to various factors from FE model setting, structural layout and geometry, and load configuration, etc. A comprehensive literature review was conducted focusing on the fatigue topics of reinforced concrete bridge decks, including fatigue performance, existing models, and design recommendations for both the material and structural levels.

The second phase of research was conducted by Dr. Rahim Ghoroubi (former postdoc researcher) and Dr. Brendan Grayson-Wallace (former graduate student). Dr. Rahim Ghoroubi conducted a comprehensive analysis of bridge modeling under various load combinations for HL-93 and EV3 trucks. The study was carried out using ATENA software with a rigid support model. Girder spacings of 4, 6, 9, 12, and 15 ft were selected, with 4 cells modeled for most span scenarios and 2 cells for the 9-ft and 15-ft span scenarios. The analysis aimed at identifying all critical loading scenarios to determine the maximum moments and shear forces and their locations on the bridge deck. Results were compared against the existing AASHTO Table A4 using percentage ratios with applied load factors to evaluate code compliance. The findings provided key design insights, indicating that the negative moment capacity should be increased based on the calculated values. The series of analyses was finally completed with Dr. Brendan Grayson-Wallace's effort where load combinations for SHV truck and P-15 permit vehicle were included. Based on all these results, updated design values were proposed for the negative bending moment (California amendment table named as CA-A4).

Table of Contents

List of Figures

List of Tables

1 INTRODUCTION

1.1 Background and Motivation

Over the past several decades, a significant transformation in vehicle dynamics, particularly with trucks, has imposed new challenges on bridge infrastructure. The increase in both the physical size and operational frequency of these vehicles necessitates a critical reevaluation of bridge design standards. The guidelines set forth by the AASHTO LRFD Bridge Design Specifications, which were once considered adequate, now fall short in addressing the realities faced by today's bridge structures. These include not only the advent of larger, legally permitted trucks, but also the introduction of specialized vehicles (e.g., special hauling vehicles) and emergency vehicles (EV) through various legislative actions. Additionally, concrete shear has been reported to control the load rating of concrete bridges in much of the current state of practice (Holt et al. 2018), which includes the deck. Existing and new bridges are also among the structures that are prone to loss of performance, cracking and failure under high-cycle fatigue loading caused by daily traffic during their service lives (Schijve 2009). With bridges enduring constant use and facing escalating traffic volumes, the incidence of wear, cracking, and potential failure has become a pressing issue. This situation underscores an urgent need for a revamped and robust bridge deck design methodology that accurately reflects the spectrum of modern vehicular loads and ensures the longevity and safety of bridge infrastructure.

In the current AASHTO LRFD Bridge Design Specifications (AASHTO 2017), the bridge deck design, specifically in Appendix A4, uses the approximate elastic method that simplifies the deck design by treating it as a series of transverse strips supported by rigid girders. It focuses on flexural resistance and control of cracking, while shear and fatigue designs are not required for typical deck slabs. In general, bridge deck analysis methods in AASHTO are categorized as either approximate or refined, while an empirical method for monolithic concrete bridge decks satisfying specific conditions is allowed. For the approximate methods, the accuracy is of concern due to simplifying assumptions and they do not account for the modern and more complicated loading configurations.

For the empirical design method, the California Amendments to AASHTO (Caltrans 2019) does not permit such an empirical design of reinforced concrete (RC) decks and overhangs due to concerns associated with durability of such members under high average daily truck traffic applications. Laboratory and in-situ testing of concrete bridge decks designed by the empirical method have also demonstrated concrete cracking and potential reinforcement corrosion in such members (Cuelho et al. 2006; Meadway 2008), as well as insufficiency in the empirical reinforcement to resist shrinkage stresses (Nowak et al. 2003). Therefore, more advanced methods of analysis (i.e., refined methods of analysis) have gained much interest and popularity. In fact, refined analysis methods such as 2-D finite element (FE) method have been in practice for almost 50 years in some European countries (Hida et al. 2010), where approximate analysis methods are no longer included in the current Eurocodes (Eurocode 2002).

However, application of refined analysis methods in the US has been limited to unique or complex bridges, bridges deemed substandard using approximate analysis, analysis of nonstandard permit loads and other special cases (Hida et al. 2010). Nevertheless, the current AASHTO LRFD Bridge Design Specifications require the refined analysis for the aforementioned cases without providing much guidance as to how it should be carried out (Adams et al. 2019). Furthermore, the current AASHTO LRFD Specifications do not recommend any specific refined analysis method

for bridge decks although a list of general methods is suggested such as finite difference method, finite element method (FEM), finite strip method, grid analogy method, and yield line method. The ACI 343R-95 (ACI 1995) provides a similar list with a statement that "a deck slab may be designed by any procedure satisfying the conditions of equilibrium and geometrical compatibility, provided it is shown that the strength and serviceability criteria are met". In addition, the ACI 343R-95 recognizes the "arching action" in cases of beam-supported thin deck slabs (Csagoly and Lybas 1989; Batchelor et al. 1978), which, however, does not provide any specific method to account for the effect of such arching action in the design.

1.2 Existing AASHTO LRFD Deck Slab Design

The AASHTO Appendix A4 provides a practical way to design concrete bridge deck slabs by utilizing the approximate elastic method. The live load moments for bridge deck slab design, calculated per unit length (e.g., kip-ft/ft), are determined for both positive and negative bending in interior bays using the AASHTO LRFD Table A4-1 (see Appendix A at the end of this report), which include the dynamic load allowance factors. For overhangs, the live load moments are determined by placing a single axle on the effective strip width. These deck slab design moments are hereinafter referred to as "AASHTO A4 design table values". As this design procedure was established in AASHTO back in 1930's, the impact of the approximate analysis methods on the accuracy and reliability of the existing AASHTO LRFD bridge deck slab design specifications is not clear.

In addition, according to the current AASHTO LRFD Bridge Design Specifications, fatigue needs not be investigated for concrete deck slabs in multi-girder applications or reinforced concrete box culverts. This recommendation is based on the measured stresses in concrete deck slabs of bridges in service that are observed to "be far below the infinite fatigue life, most probably due to internal arching action". Besides, the AASHTO only requires a fatigue check for RC components only if the compressive stress due to unfactored loads and prestress in RC components is less than a certain limit, or the tensile stress in the concrete exceeds the Service III limit. In such a case, simplified equations are provided to determine the constant amplitude fatigue threshold of steel reinforcements $(\Delta F)_{TH}$ to be checked with the factored stress range in the reinforcement due to the live loads ($\gamma\Delta f$). According to AASHTO, the only stress limitation on concrete is for prestressed components in other than segmentally constructed bridges, where the compressive stress due to Fatigue I load combination and one-half the sum of the unfactored effective prestress and permanent loads shall not exceed $0.4f'_c$ after losses. Similar limitation is stated in ACI 215, recommending the stress range in concrete shall not exceed 40% of its compressive strength when the minimum stress is zero, or a linearly reduced stress range as the minimum stress is increased so that the permitted stress range is zero when the minimum stress is $0.75f'_c$. This recommendation is basically a modified Goodman model that takes into account the effect of loading ratio (R), while this important effect is neglected in AASHTO.

1.3 California Amendments to AASHTO LRFD Deck Design

Over the years, Caltrans has developed amendments to the AASHTO LRFD Bridge Design Specifications to align them with California's bridge design practices. These amendments, first introduced in 1999, were formalized with a transition date of April 2006 for state-designed bridges and October 2006 for those by local agencies. For concrete deck slab design, the current CA Amendments contain key aspects related to the minimum deck thickness, deck reinforcement,

minimum cover, empirical design, deck and soffit slab details, deck service life, and prestressed concrete. In essence, Caltrans has integrated its own design standards and practices into the AASHTO LRFD framework, ensuring that bridges designed in California meet specific performance and longevity requirements. However, the AASHTO LRFD Table A4-1 still forms the base in the CA Amendments for the design moments of reinforced concrete deck slabs.

In terms of fatigue, the California Amendments to AASHTO states the same for approach slabs and slab bridges as the existing AASHTO design.

1.4 Objective and Scope

The objective of this research is to develop an updated LRFD-based bridge deck design procedure based on rigorous and refined analysis methods that consider modern vehicle configurations (including HL-93, permit, special hauling and emergency vehicles), dynamic loads, flexural and shear demands, and fatigue. The developed procedure will provide updated streamlined design table and charts suitable for production design. Below is a summary of the executed scope of this completed study:

Task 1: Develop updated deck design method using finite element models in computer-based analysis

- *1A*: establish appropriate finite element models on the three major bridge types (*Deliverable*: a structural model for each bridge type, i.e., CIP box, CIP/PS box, and PC/PS "I" girder bridge)
- *1B*: update truck loading demands and vehicle loading configurations for the design of bridge deck (*Deliverable*: develop structural models with updated truck loading and vehicle configurations)
- *1C*: update deck load demand procedures (*Deliverable*: design procedures for estimating deck loading)

Task 2: Conduct literature survey and develop design framework with appropriate concrete fatigue model (*Deliverable*: a report on practical strategy or design framework to incorporate fatigue models into the design of bridge deck)

Task 3: Conduct parametric studies on various deck to girder systems (*Deliverable*: a spreadsheet that identifies the bridge attributes identified above and the corresponding moment, shear, and torsion demands)

Task 4: Quantitatively assess AASHTO LRFD approximate analysis method on deck design (*Deliverable*: a report documenting in detail the specifications and assumptions employed in each of the two methods, each method's associated analysis procedures, and the final assessment of the results)

Task 5: Generate simplified design procedure for production design (*Deliverable*: a bridge deck design procedure to be used for production design)

Task 6: Recommendations on changes to AASHTO design specification and California Amendments (*Deliverable*: recommendation on changes to the AASHTO LRFD with CA Amendments based on analysis results)

Task 7: Prepare final report on research findings and technology transfer (*Deliverable*: a final report of research findings)

In addition to the Caltrans Technical Advisory Committee (TAC) team, the consulting team from Modjeski and Masters (M&M), Inc. was consulted on Task 4. M&M has a long history of research and support activities associated with specification development and implementation. This includes leading numerous NCHRP projects that resulted in the development of new

specifications and guidelines, e.g., the Guide Specification for Service Life Design of Highway Bridges (Murphy et al. 2019) and working directly with FHWA to develop manuals and guides (e.g., Adams et al. 2019).

The completed work in this project is expected to have potential broad impacts in the engineering design and evaluation of our State's bridge infrastructure, including: (1) Potential cost savings by going beyond use of approximate, simplistic and conservative design methods in the existing specs; (2) Improved structural safety by more rigorous assessment of required modern loads and accurate modeling of system/local behavior; (3) Enhanced safety evaluation by full consideration of deck flexural, shear, torsion and fatigue; and (4) Accomplishing sustainability by more frequent salvaging of existing infrastructures. Therefore, the final product of this work is of particular interest to industry, Caltrans and other State DOT design engineers, bridge maintenance personnel, contractors, and specialty subcontractors such as inspection and repair crews.

1.5 Report Outline

The current report is organized in 11 chapters including the current one, which serves as an introduction on the topic and highlights the significance, scope, objective, and significance of the work. Chapter 2 comprehensively presents the finite element modeling in computer-based analysis with the adoption of the validated RSM in Chapter 3. Chapter 4 is dedicated to a thorough literature review of the fatigue of reinforced concrete bridge decks with a proposed framework to tackle the fatigue-related design issue. Case studies of load demand under various design parameters of bridges are presented in Chapter 5 based on a comprehensive concrete bridge databased in California. Chapter 6 focuses on the production run of numerous bridge cases under the HL-93, P-15, SHV, and EV loading configurations, where the results are used to develop the proposed CA A4 Amendments, the updated deck design procedure in Chapter 8. The assessment of the existing AASHTO A4 design is presented in Chapter 7. Chapter 9 highlights the conclusions, limitations, and future research propositions. Chapter 10 serves as the bibliography of this report. In addition to these main 10 chapters, this report includes three appendices organized in Chapter 11.

2 FINITE ELEMENT (FE) MODELING

2.1 Background

This section is dedicated to the creation of finite element (FE) modeling strategies of bridge deck slabs in a computer-based analysis, laying the important foundation for the development of an updated deck design methodology in the subsequent sections.

The current AASHTO LRFD deck design procedure is based on a transverse strip approximation using the flexural beam analogy. Regardless of simplicity, several assumptions and approximations in this procedure are no longer valid in the practice (Abughneam 2019), e.g., the simple beam approximation instead of the more realistic two- or four-sided plate theory. Among the refined analysis methods, the grillage analogy involves 2-D models built of line elements interconnected in a manner to be relatively faithful to the structure geometry (Hambly 1991). It is widely used in girder bridge analysis because it is relatively easy to use and understand (Nowak et al. 2000). These benefits traditionally favored the method over 2-D FEM. However, in today's environment of inexpensive, high-powered computers, coupled with elaborate analysis programs and user-friendly graphical interfaces, the FEM is replacing the grillage method even for more straightforward bridge decks. The grillage method is also reported to show inherent inaccuracies that result in less reliable shear force determination, especially when modeling bridges with high skew (O'Brien et al. 2014). Therefore, among various refined analysis methods, the FEM has become the method of choice for most refined analyses of bridge structures. The reason is attributed to the flexibility of application, ease of use, and continuing increase in the computing power available to bridge designers (Adams et al. 2019). Furthermore, it is believed that the use of FEM can save clients' money on initial design, because future changes in design of the structure are more easily addressed. Even more money is saved on assessment and load rating of the structure because the model for this analysis is already available for future use by the assessment engineers (Hida et al. 2010; Nowak et al. 2000).

The recently published *Manual for Refined Analysis in Bridge Design and Evaluation* (Adams et al. 2019) states that currently, for most cases of design of concrete deck slab on girder highway bridges, a 2-D plate on eccentric beam (PEB) would be the recommended refined analysis procedure. This model combines a line element girder and cross-frame/diaphragm grid with a plate or shell element deck including the geometric offset of the deck from the girder centroids. One big advantage of PEB models is that they can explicitly model the behavior of bridges with a large skew or curvature. A PEB analysis requires less compromise and fewer assumptions in defining the elements of the mesh and is capable of modeling the membrane stiffness of the deck. Although increasing the level of refinement from a 2-D PEB to a 3D solid FEM leads to an increased analysis accuracy, little benefit is found in the application of 3D models beyond simpler 2-D ones (Abughneam 2019; Zokaie et al. 1991). Furthermore, the output of FE analyses is not always in a form that can be directly utilized for AASHTO LRFD design; and hence, post-processing would be essential to derive forces and moments (Adams et al. 2019; O'Brien et al. 2014). Consequently, the accuracy of 3D models can be compromised by the additional effort required for the entire design procedure. In addition, the AASHTO LRFD Bridge Design Specifications permit the use of the spine beam model to analyze box girder superstructures, provided they meet the requirements of Article 4.6.1.1, which limits the central angle of the bridge, in case of a horizontally curved one. Application of the spine beam model is quite common for analyzing such bridges (e.g., CT-Bridge) owing to the overall accuracy of the method compared to a 3D FEM (Adams et al. 2019). However, the method is not permitted for highly curved bridges,

while the local effects, especially in transverse direction, cannot be captured due to the nature of the spine model. The upstand FE model consists of a number of planes of shell FEs connected together by rigid vertical members. This model has the advantage of automatically allowing for transverse cell distortion while transverse diaphragms could also be easily incorporated into this model (O'Brien et al. 2014). In addition, an upstand FE analogy can be exploited to analyze any other bridge deck types and configurations, and is deemed a good compromise for a solid 3D FEM. Nevertheless, it is worth mentioning that a comprehensive solid 3D FE sub-modeling will be used for advanced design and assessment of hot-spot metallic connections or orthotropic decks subjected to multiaxial fatigue loading.

2.2 As-Built Bridge Prototype

To investigate the standard FE modeling strategy in the adopted commercial software package ATENA (2020), i.e., GiD and ATENA Studio V5, a representative prototype bridge #49-0165L was selected from the bridge database provided by Caltrans. It is a three-span cast-in-place prestressed (CIP/PS) concrete box girder bridge with span configurations of 38 ft, 98 ft, 38 ft, as shown in **Figure 2.1**(a). It is a rigid frame bridge supported on pier at the bents and seat-type abutments. The total width of the bridge is 42'-6", composed of two design lanes and four box cells, as present in **Figure 2.1**(b). The top bridge deck thickness is 8", while the soffit thickness is 6", with the web thickness equals to 12". The layout of the prestressed tendons is given in **Figure 2.2**, with a total jacking force of 4230 kips applied to the total cross-sectional area of the prestressed tendons of 20.89 in^2. The prestressed tendons are 270 ksi low relaxation strands, and the 28-day design compressive strength of the concrete is 4000 psi.

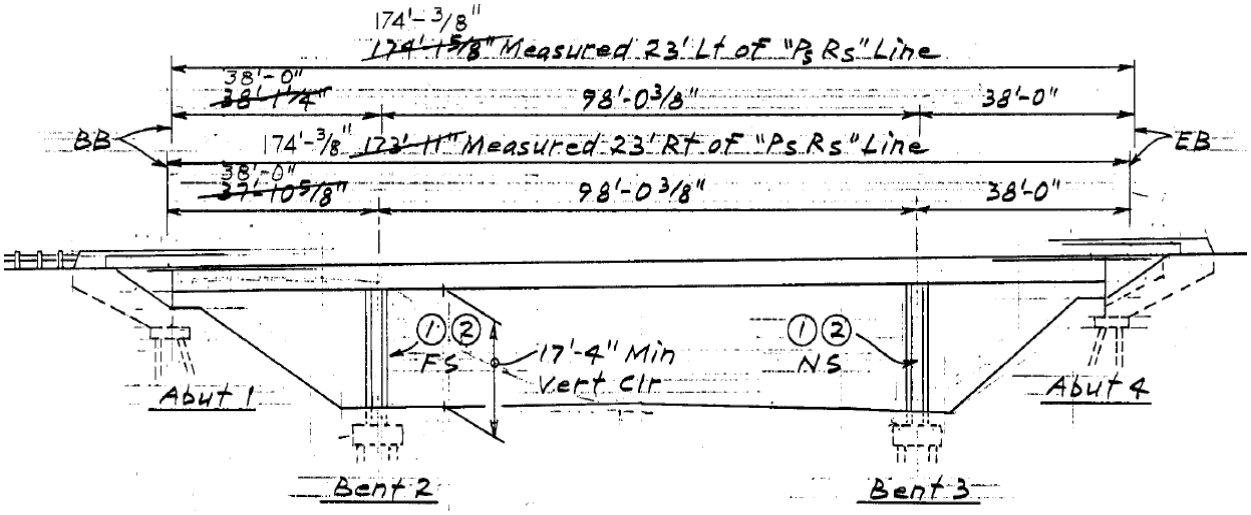

(a) Elevation

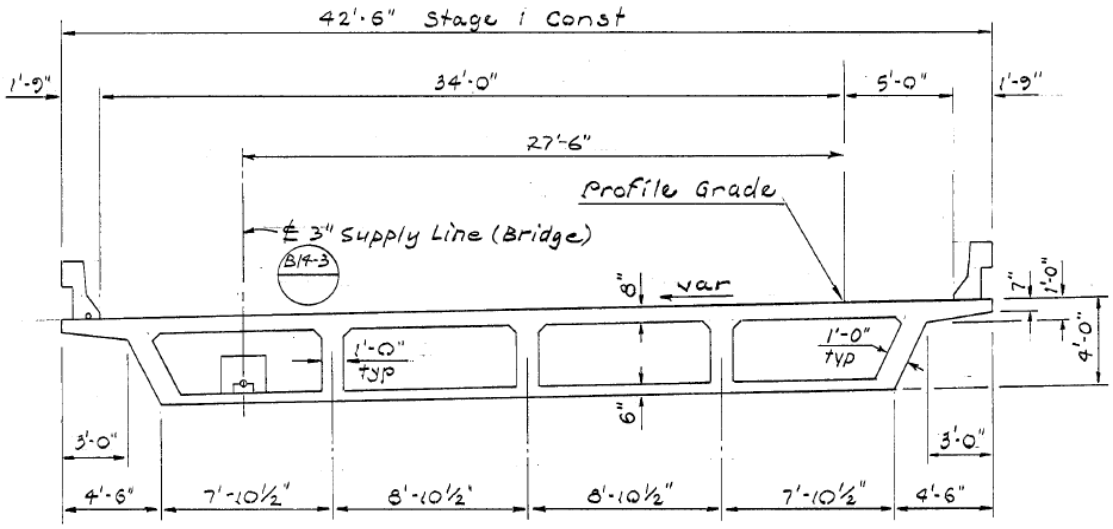

(b) Cross-section

Figure 2.1. General plan of the prototype bridge (#49-0165L)

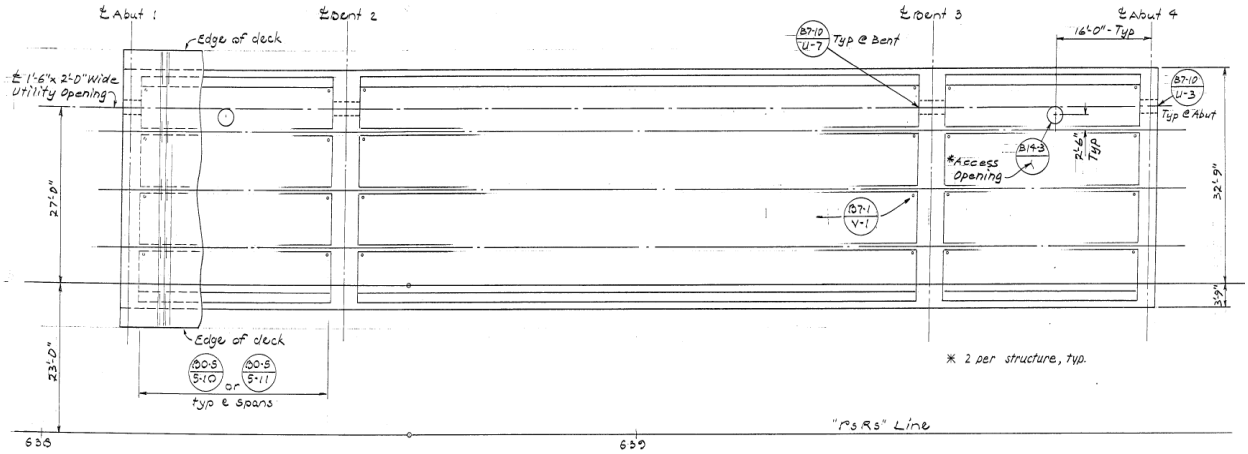

(b) Longitudinal

Figure 2.2. Layout of prestressed tendons

2.3 Pre-process in GiD

2.3.1 Geometry modeling

The ATENA Studio V5 uses GiD as the pre-process GUI software to build the analytical model. In GiD, the modeling of 3D volumes follows a sequential order of: (1) definition of key points by coordinates; (2) connection of points to create lines; (3) creation of a surface from enclosed lines; and (4) creation of a volume extruded from a surface. In this prototype bridge

model, the CAD drawing of the cross-section was imported into GiD to ease the creation of the key points and lines. However, because the concrete box girder is basically composed by multiple thin plates, e.g., top deck slab, soffit, girder web, and overhang, these structural components are built separately and combined by defining fixed surface contacts (master/slave), as presented in **Figure 2.3**. Two reasons are provided by performing this essential step: (a) the mesh setting is more flexible and maneuverable for each independent thin plate component instead of the integrated cross-section; and (b) the definition of 3D shell elements requires to assign the different local coordinate system and normal vector to each element.

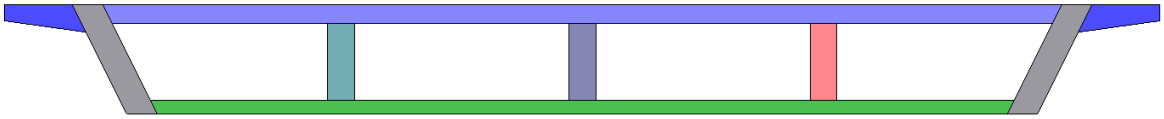

Figure 2.3. Cross-section of the prototype bridge and the master/slave contact between components

On the other hand, at the position of support, a thin rigid plate resembling the bearing in the as-built drawings was modeled and attached to the bottom of the box girder through the master/slave contact, as presented in **Figure 2.4**. It is recommended by the GiD tutorial (ATENA 2020) to create this rigid plate to indirectly apply the model restrictions. The benefits of using the rigid plate include: (a) the boundary conditions need not to be redefined when the mesh setting of the upper structural changes; (b) the local stress intensity closer to the supports can be alleviated; and (c) the physical existence of the rigid plate is more representative of the real-world boundary condition as it resembles the size of the bearing support.

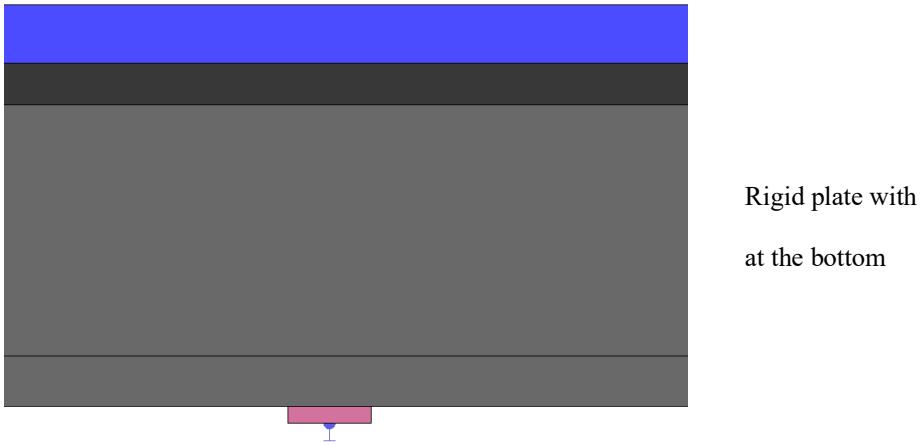

Figure 2.4. Rigid plate at the girder support with the applied boundary conditions

2.3.2 Definition of materials and elements

The GiD provides a sophisticated built-in material definition module, which enables the accurate modeling of the nonlinear behavior of materials for concrete, steel, and cohesive element, etc. However, due to the large number of interested parameters in the design of bridge deck, it is impractical to conduct the nonlinear analysis of the bridge model. In addition, the current bridge deck design is still mostly within the scope of elastic theories, with no deep consideration into the nonlinear performance of materials for both simplicity and conservatism. Moreover, the nonlinear analysis usually requires a much longer computational time, along with a frequent convergency issue. Thus, this analytical study only focuses on the linear elastic analysis of bridge decks to obtain the load demand under vehicle load for bridge deck design.

To this end, the steel reinforcements and prestress tendons are not included in the current model, assuming they only produce negligible effects on the load demands of bridge decks under vehicle load. The concrete material was defined as a linear elastic material with a modulus of elasticity of 3605 ksi and a Poisson's ratio of 0.2. The modulus of elasticity was derived from the AASHTO equation of $E_c = 33w^{1.5}\sqrt{f_c'}\ (ksi)$ where w is the weight density of concrete, and f_c' is the compressive strength of concrete which equals to 4 ksi in this study (AASHTO 2017). The material of the rigid steel plate was also defined as linear elastic material with a modulus of elasticity of 29000 ksi and a Poisson's ratio of 0.3. In addition, both the 3D solid element and the 3D shell element were investigated to compare their overall accuracy and efficiency in the numerical simulation, as shown in **Figure 2.5**. It should be noted that for the definition of shell element, it is important to correctly define the local normal vector (axis Z) which indicates the out-of-plane direction of the shell element, as presented in **Figure 2.6**. And this local normal vector depends on the orientation of the geometric volume, and it indicates the direction of the thickness of the shell element. A default four internal layers was selected for the shell element to compute the integrated moment and force within the element, and the reference thickness of the shell was consistent with the bridge details described in the as-built drawings.

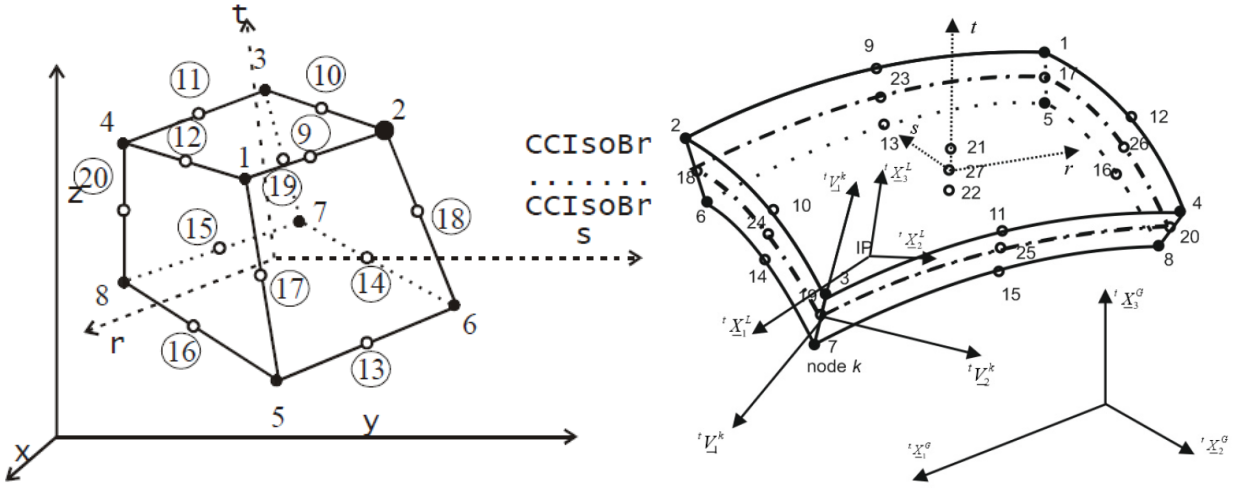

(a) 3D solid element (b) 3D shell element

Figure 2.5. 3D Concrete element types defined in GiD

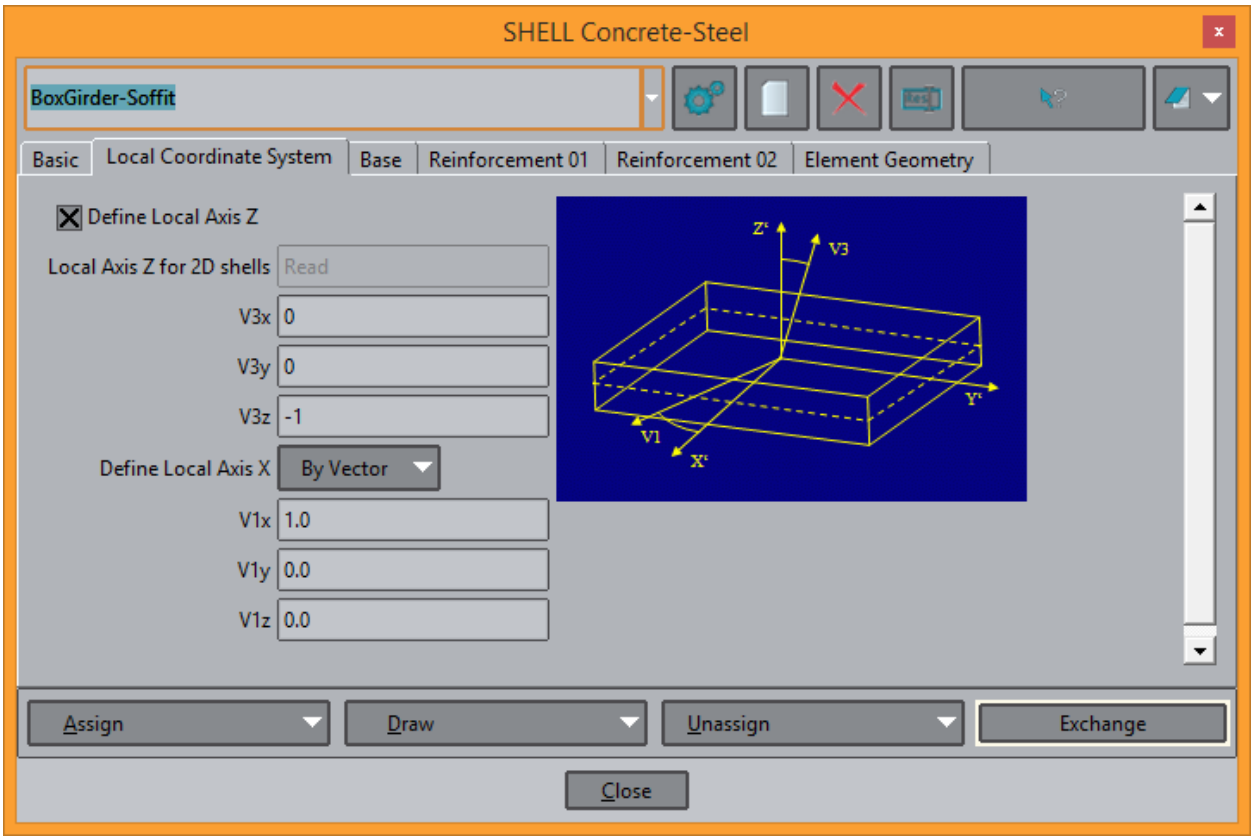

Figure 2.6. Definition of the local normal vector (axis Z) for shell element

2.3.3 Load and boundary conditions

The current study aims to obtain the updated load demand under the design trucks in CA, as a result, the HL-93 truck axle (**Figure 2.7**) was used to conduct case studies before the production run for deck slabs with various parameters. The HL-93 truck axle was applied through the tire footprint, with an equivalent tire pressure equals to 80 psi on an area of 20 in by 10 in, which corresponds to the AASHTO specified 32-kip rear axle weight. The axle load was applied to a dummy surface in the size of the tire footprint, which was connected to the top of the bridge deck by a master/slave contact. And the tire pressure was assigned by means of the "load universally for surface" condition to the dummy surfaces, as presented in **Figure 2.8**. This dummy surface will not be considered as an effective element in the numerical analysis of ATENA, but rather it serves as an intermediate to distribute the load evenly within the area and provides the flexibility of changing patch load positions without redefining the mesh setting.

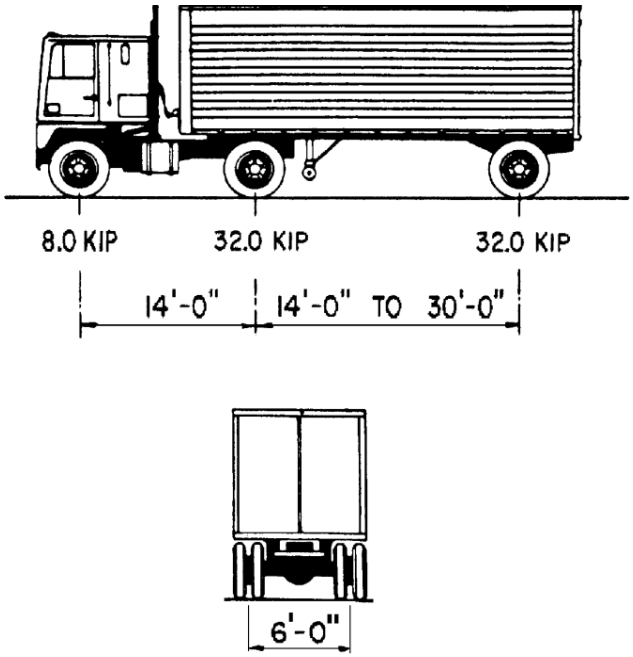

Figure 2.7. Illustration of the HL-93 design truck

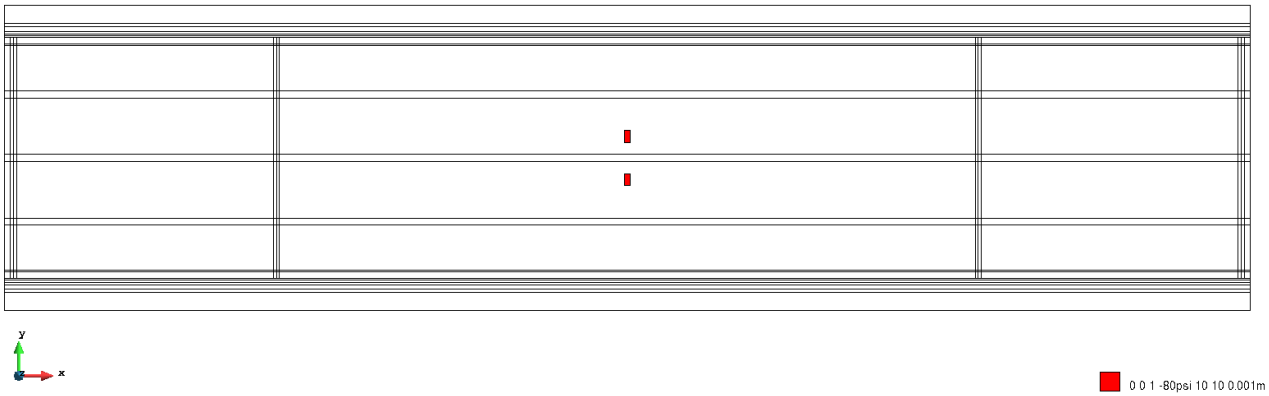

Figure 2.8. Tire footprint with the applied patch load

To determine the appropriate mesh size of the bridge model, the self-weight of the bridge model was applied as an independent load case, with the concrete weight density equals to 150 lb/ft^3. Although the prototype bridge is a rigid frame structure with two piers connected to the superstructure, the FE bridge model was simply supported at the positions of the piers and abutments for simplicity and conservatism. In **Figure 2.9**, the left end of the box girder was restrained in both horizontal and vertical directions, while all the rest supports were restrained only in the vertical direction. The close-up of the boundary condition is shown in **Figure 2.4**.

Figure 2.9. Boundary conditions of the bridge model

2.3.4 Mesh setting

The element size of the bridge model needs to be carefully adjusted to reach a balance between accuracy and computational efficiency. To address this issue, a few different mesh cases were performed, and the results of the longitudinal moment distribution were compared to the theoretical values, which will be discussed in the next section. The labeling scheme for different mesh cases is as follows: "L" represents the number of elements in the longitudinal direction of the box girder; "W" represents the number of elements in the transverse direction within each box cell; and "H" represents the number of elements in the vertical direction for each web, as shown in **Figure 2.10** where the mesh setting for the case of L60W6H3 is presented. It should be noted that the number of elements in the transverse direction of a single overhang was always set as two for consistency. The hexahedra element type was assigned to the model, as well as a linear mesh for the 3D solid element case and a quadratic mesh for the 3D shell element case. The studied mesh cases include L40W4H2, L80W4H2, L120W4H2, L120W6H3, and L120W8H4 for the 3D linear solid element case, and L60W6H3, L80W6H3 and L120W6H3 for the 3D quadratic shell element case.

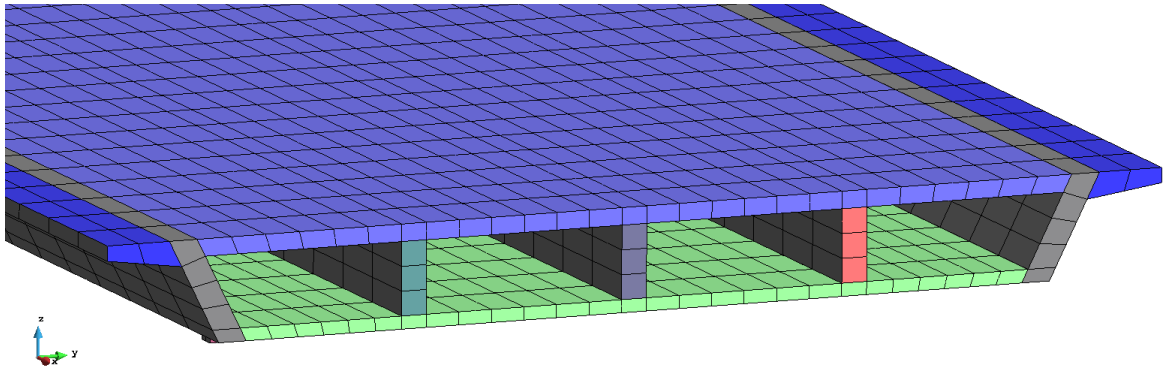

Figure 2.10. Typical mesh setting of the bridge model (L60W6H3)

2.4 Post-process in ATENA

Upon completion of the model built in GiD, the geometric information of the bridge, as well as the load, boundary condition, and mesh setting were submitted to the ATENA simulator for numerical analysis, with a default 10 load steps and iteration limit of 30 for each step. For the linear elastic analysis adopted in the current research, it does not require too many load steps to reach convergency. However, if the prestressing and nonlinear behavior of the materials need to be considered, a big number of iteration limit such as 1,000 – 2,000 is always necessary with over 100 load steps, which requires a much longer computational time.

In **Figure 2.11**, the normal stress distributions on the selected plane cuts are visualized and quantified by the color scale along the longitudinal direction. Likewise, the longitudinal moment distribution can be obtained by integrating the normal stress of each plane cut with respect to its centroid. Hence, the comparison of the FE results based on the different mesh cases is plotted in **Figure 2.12**, where **Figure 2.12**(a) represents the mesh cases for 3D linear solid element, and **Figure 2.12**(b) represents the mesh cases for 3D quadratic shell element. A tendency of convergency can be reached with a finer mesh in both plots, which infers that the FE modeling strategy is reliable. Meanwhile, the difference in moment at the mid main span of various mesh cases are calculated and summarize in **Table 2.1**. It can be seen from the table that increase the

number of elements, or equivalently decrease the element size, a more accurate moment demand will be reached compared to the theoretical value. However, the results of mesh cases adopting the 3D linear solid elements always deviate more from the theoretical value compared the 3D quadratic shell element case with a similar mesh setting. The lesser accuracy of using the solid element might be caused by the one element defined in the thickness direction, while the shell element has four default layers within its thickness. In addition, the shell element is usually more appropriate for thin plate, such like deck slabs, while the solid element is more suitable for thick geometry. It is also generally believed that a difference within 5% of the FE results is deemed sufficient for numerical approximation (Adam et al. 2019). As a result, the L60W6H3 of the 3D quadratic shell case is adopted for the prototype bridge model to investigate the load demand under vehicle load.

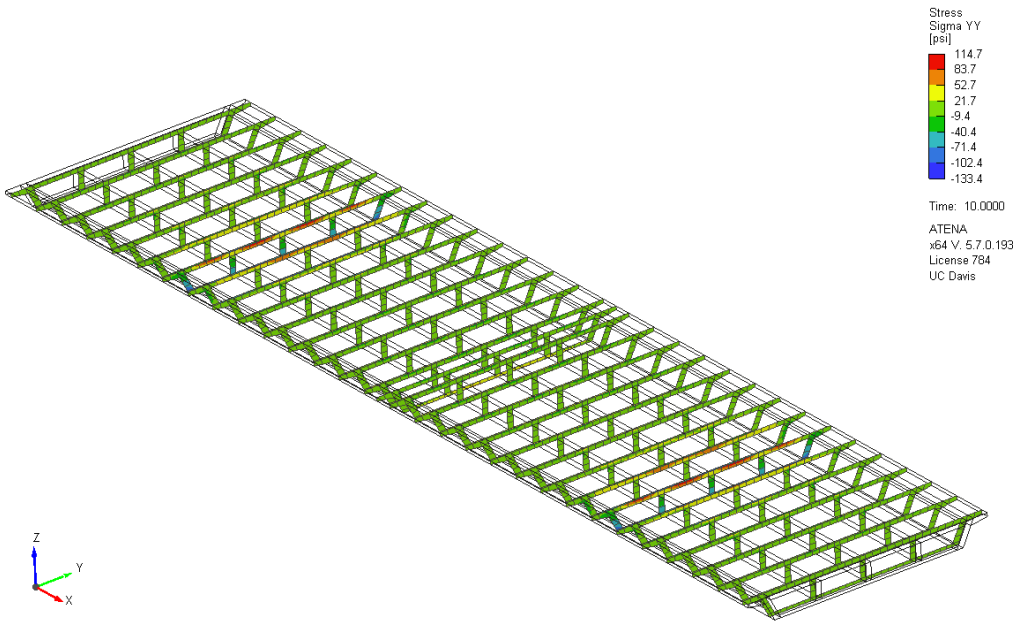

Figure 2.11. Plane cuts of the bridge model in ATENA (self-weight)

Table 2.1. Moment comparison at the mid main span of the bridge model

3D linear solid element			3D quadratic shell element		
Mesh case	Moment (kip-ft)	Difference (%)	Mesh case	Moment (kip-ft)	Difference (%)
L40W4H2	-3212.50	31.6	L60W6H3	-4607.50	1.9
L80W4H2	-3980.83	15.2	L80W6H3	-4585.00	2.3
L120W4H2	-4168.33	11.2	L120W6H3	-4583.33	2.4
L120W6H3	-4249.17	9.5	Theoretical value	-4695.00	0
L120W8H4	-4280.83	8.8	-	-	-
Theoretical value	-4695.00	0	-	-	-

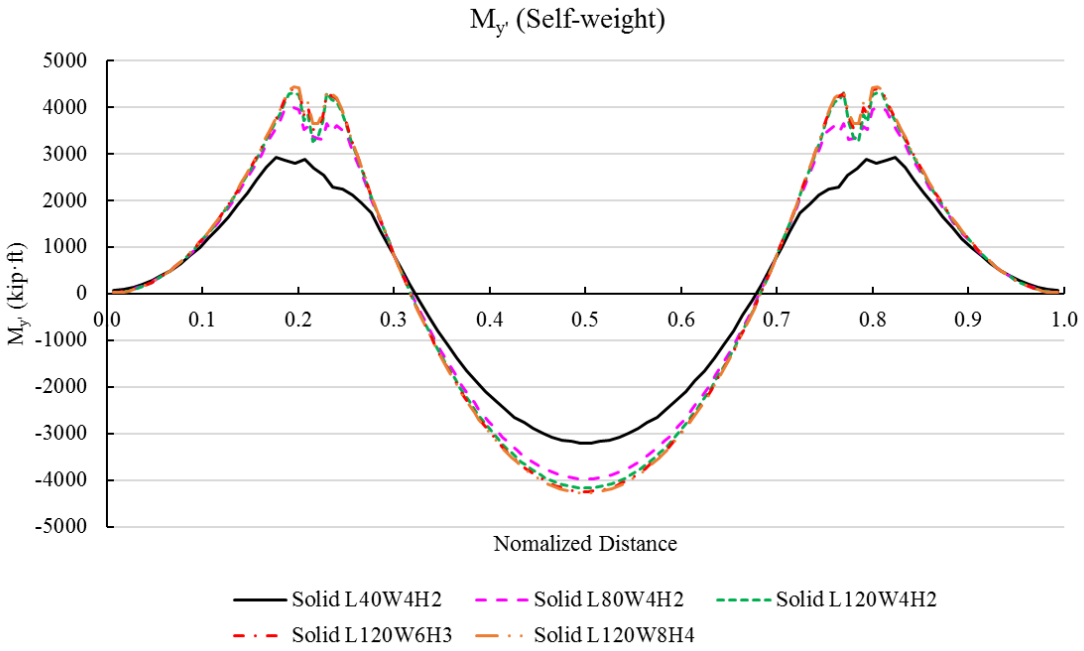

(a) 3D linear solid element

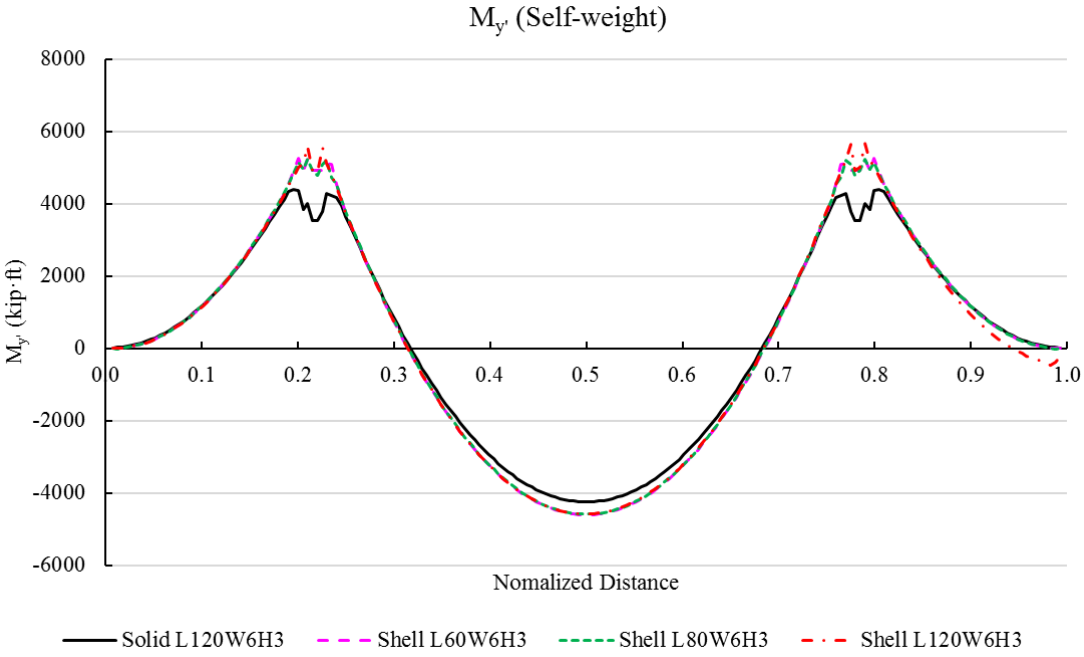

(b) 3D quadratic shell element

Figure 2.12 Comparison of longitudinal moment distribution for different mesh cases

2.5 Deck Responses Case Studies

2.5.1 Single axle load case

To investigate the influence on the load demands of bridge decks due to the longitudinal positions of the single pair of axle load, five representative bridge longitudinal positions were

studied at the 0.25*L* end span, 0.5*L* end span, 0.75*L* end span, 0.25*L* main span, 0.5*L* main span for the symmetric prototype bridge model. At each longitudinal position, four representative transverse positions of axle load cases were analyzed, which included: (1) center line (CL) exterior cell; (2) CL 2nd web; (3) CL 2nd cell; and (4) CL 3rd web (CL bridge), as presented in **Figure 2.13**. The red cross in the figure is in line with the CL axle load pair for each transverse case. In addition, to investigate the influence on the bridge deck due to different tire pressures, three representative tire pressures, i.e., 80, 100 and 133 psi, were adopted in this case study. And the corresponding tire footprint of these three different tire pressures should be 20×10", 16×10", 12×10", respectively. A typical visualized load demand is shown in **Figure 2.14**, where the left plot is the transverse moment (M_x, lbf·in/in) intensity of the deck under the axle load, and the right plot is the shear (Q_{yz}, lbf/in) intensity in y-z plane. The visualized portion of the deck slab is approximately 46'-5" long (*x* direction, or bridge longitudinal direction), and each element is 34.8" in *x* direction, and 15–16" in *y* direction (bridge transverse direction).

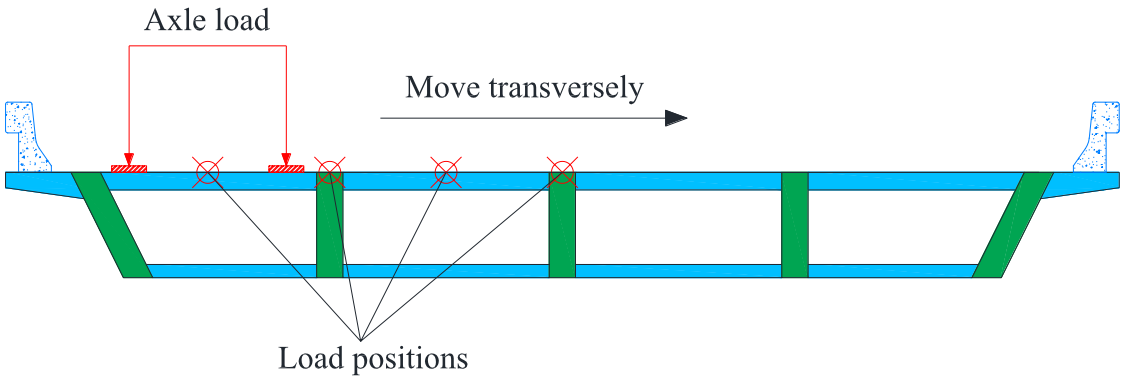

Figure 2.13. Transverse positions of axle load

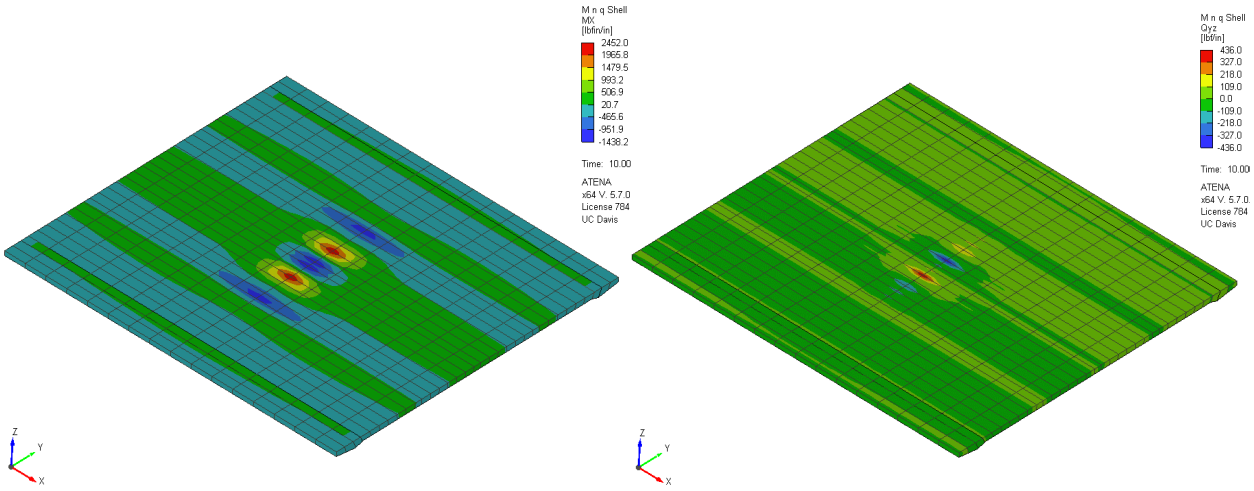

(a) Moment intensity (b) Shear intensity

Figure 2.14. Load demand intensity of bridge deck under the axle load (CL bridge, 0.5L main span, tire pressure = 80 psi)

A total of 60 different cases, i.e., five longitudinal positions × four transverse positions × three tire pressures, were analyzed to compare the peak load demands of the deck at each longitudinal

position under different patch tire pressures. The peak shear intensity was further manipulated by dividing the thickness of the deck and yielded the average peak shear stress, e.g., divide peak Q_{yz} (436 lbf/in) in **Figure 2.14**(b) by the deck thickness of 8". A series of plots are presented in **Figure 2.15**, representing the quantified difference in the load demands of both top deck and soffit due to the longitudinal positions of the axle load, as well as the influence of different patch tire pressure. It should be noted that the given nominal peak load demands at each longitudinal positions are simply based on the four transverse load cases, they do not represent the most critical cases of the deck slab under incremental vehicle loads in the transverse direction of the deck. These are raw load demands with no factors applied. In addition, the effect of tire pressure on both the peak positive moment M_x and the average peak shear Q_{yz} in the top deck are summarized in **Table 2.2** and **Table 2.3**, respectively. The effect of tire pressure on the peak negative moment M_x is negligible and thus it is not included in the table.

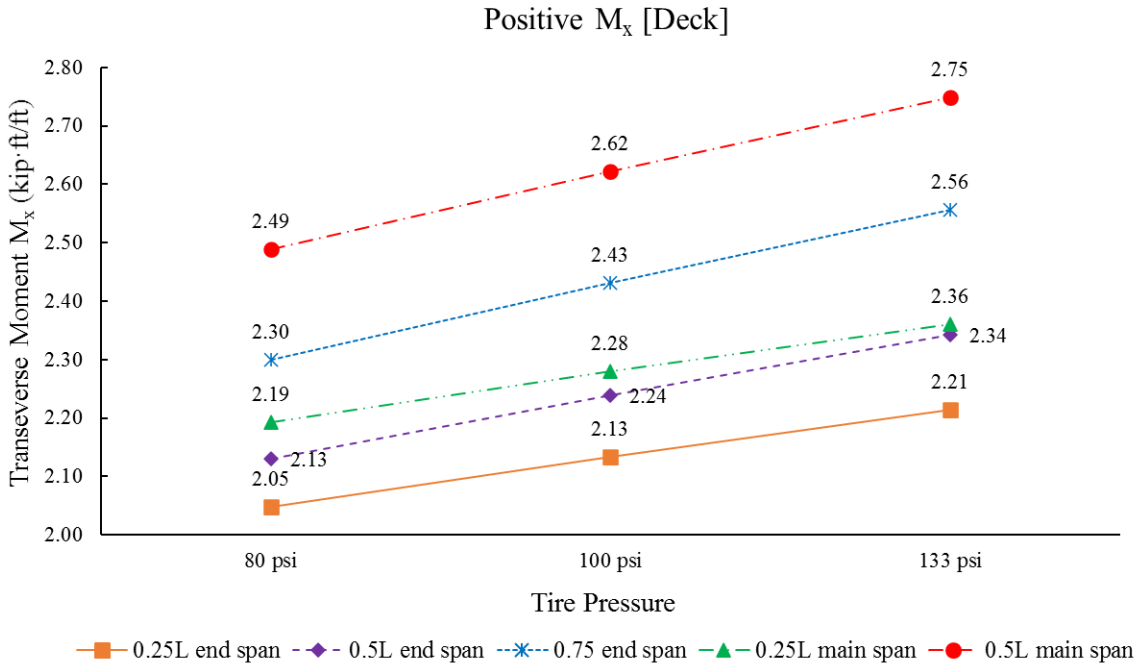

(a) Positive M_x in the top deck

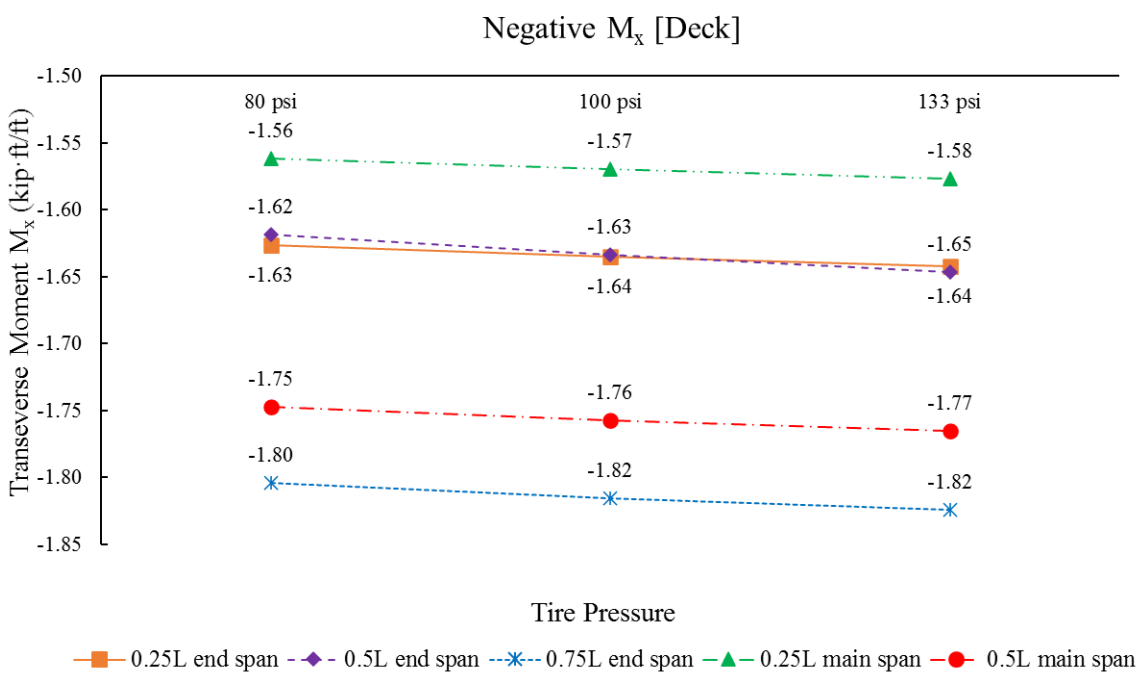

(b) Negative M_x in the top deck

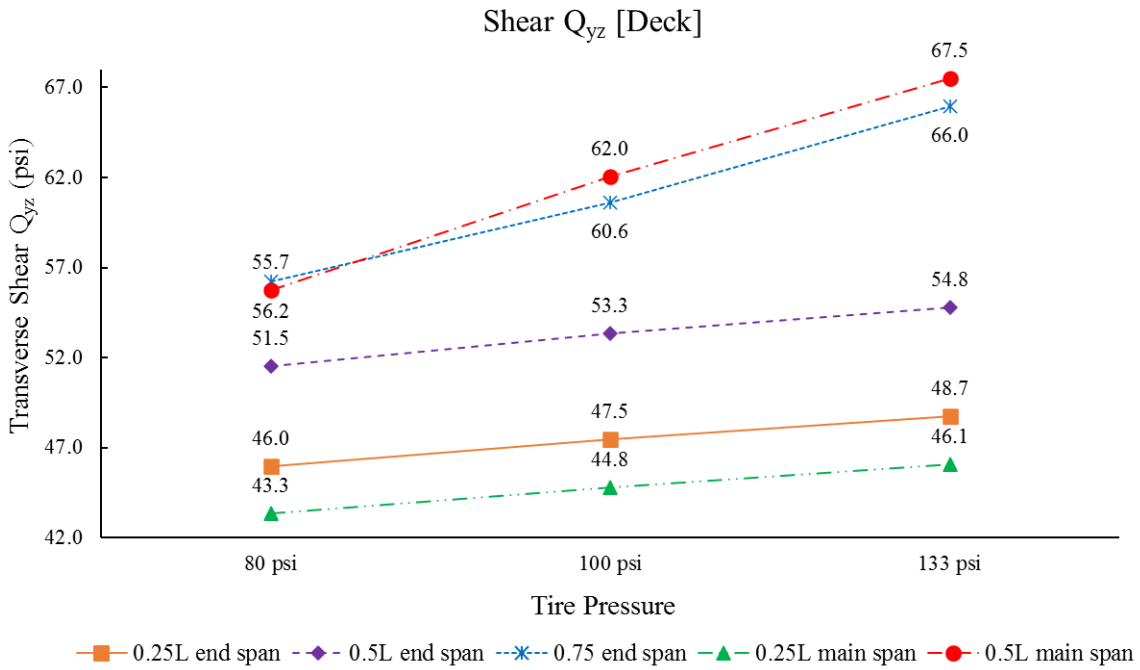

(c) Shear stress in the top deck

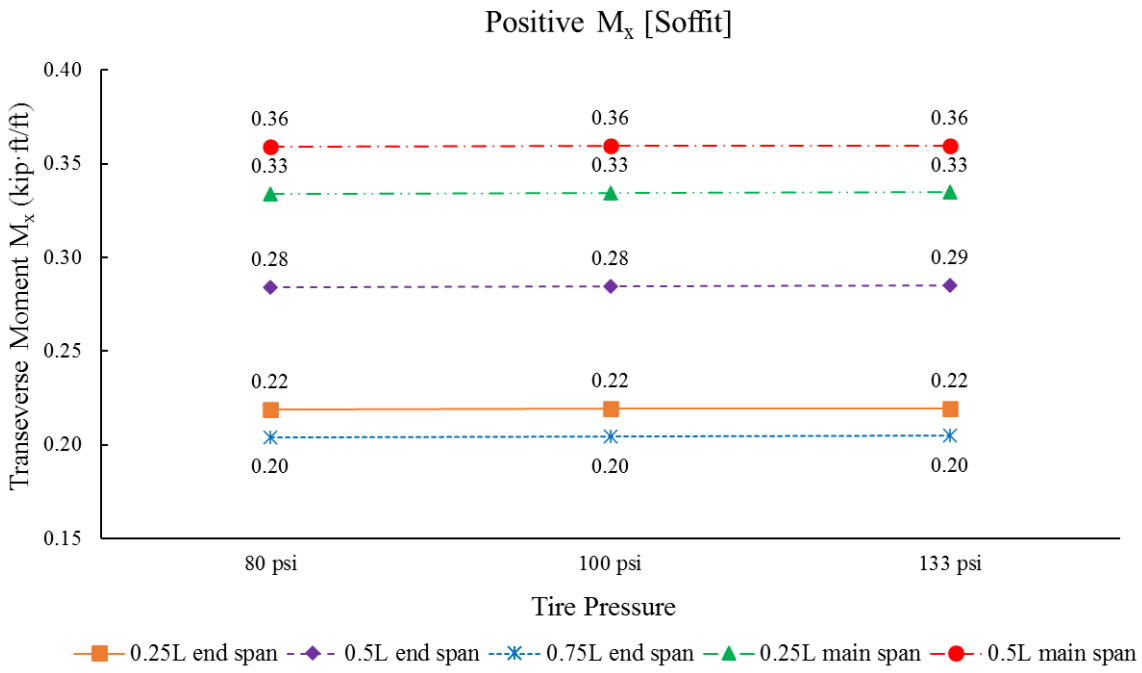

(d) Positive M_x in the soffit

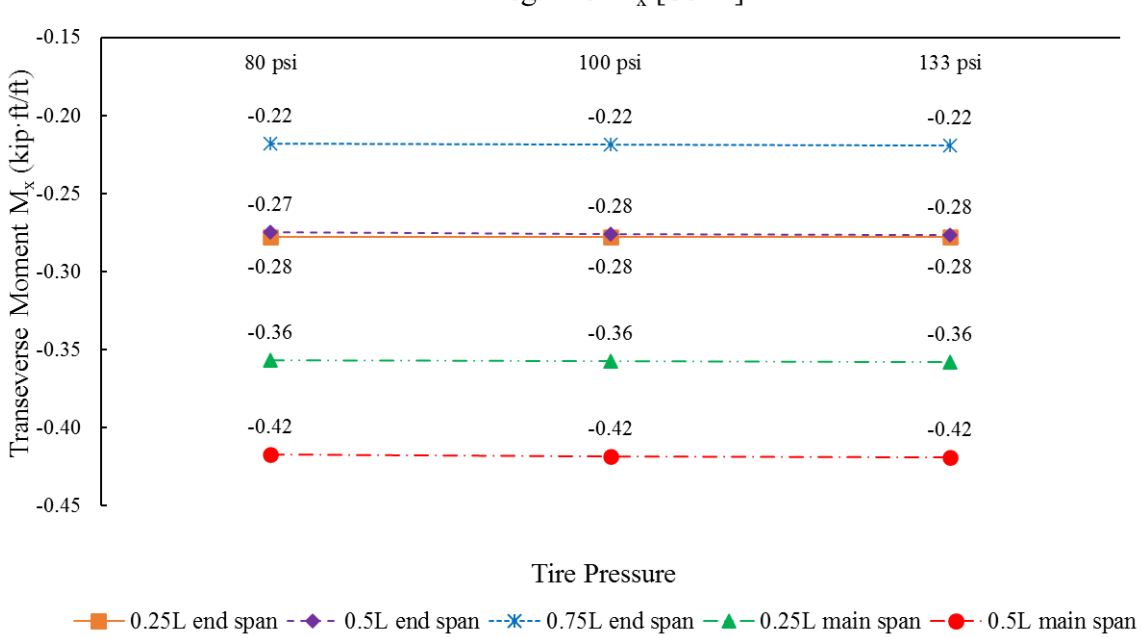

(e) Negative M_x in the soffit

Figure 2.15. Nominal peak load demands of the deck at different longitudinal positions under different patch tire pressures

Table 2.2. Effect of tire pressure on the peak positive moment M_x in the top deck

Pressure (psi)	0.25*L* end span		0.5*L* end span		0.75*L* end span		0.25*L* main span		0.5*L* main span	
	M_x (kip·ft/ft)	Diff.[a] (%)	M_x (kip·ft/ft)	Diff. (%)	M_x (kip·ft/ft)	Diff. (%)	M_x (kip·ft/ft)	Diff. (%)	M_x (kip·ft/ft)	Diff. (%)
80	2.05	-4.0	2.13	-4.9	2.30	-5.4	2.19	-3.8	2.49	-5.1
100	2.13	0	2.24	0	2.43	0	2.28	0	2.62	0
133	2.21	3.8	2.34	4.6	2.56	5.1	2.36	3.6	2.75	4.9

[a]Difference compared with the result under 100 psi tire pressure.

Table 2.3. Effect of tire pressure on the average peak shear Q_{yz} in the top deck

Pressure (psi)	0.25*L* end span		0.5*L* end span		0.75*L* end span		0.25*L* main span		0.5*L* main span	
	Q_{yz} (psi)	Diff.[a] (%)	Q_{yz} (psi)	Diff. (%)	Q_{yz} (psi)	Diff. (%)	Q_{yz} (psi)	Diff. (%)	Q_{yz} (psi)	Diff. (%)
80	45.95	-3.2	51.54	-3.4	56.24	-7.2	43.34	-3.2	55.73	-10.2
100	47.49	0	53.34	0	60.63	0	44.78	0	62.04	0
133	48.73	2.6	54.78	2.7	65.98	8.8	46.06	2.9	67.53	8.8

[a]Difference compared with the result under 100 psi tire pressure.

From the axle load case study, some conclusions are drawn as follows:

- 0.5*L* main span is the critical position for positive transverse moment in both top deck and soffit, and is the critical position for negative transverse moment in soffit;
- 0.75*L* end span is the critical position for negative transverse moment in top deck (approximately 3% larger than that at the mid-main span);
- Both 0.5*L* main span and 0.75*L* end span (difference in 2%) are the critical positions for shear in the top deck;
- For positive moment in the top deck, 2nd web is the critical position;
- For negative moment in the top deck, CL exterior cell is the critical position;
- For positive moment in the soffit, CL 2nd cell is the critical position;
- For negative moment in the soffit, CL exterior cell is the critical position for most longitudinal locations but not for the 0.5L end span in which CL 2nd cell controls the design;
- For shear in the top deck, CL exterior cell and 2nd web are the two critical positions;
- Tire pressure has an impact on the peak positive M_x in the top deck. A change from 100 psi to 80 psi, or 133 psi leads to a decrease of 3.8-5.4%, or an increase of 3.6-5.1%, respectively (**Table 2.2**);
- Tire pressure has an impact on the peak shear Q_{yz} in the top deck. A change from 100 psi to 80 psi, or 133 psi leads to a decrease of 3.2-10.2%, or an increase of 2.6-8.8%, respectively (**Table 2.3**);
- Tire pressure has a negligible influence on all the other demands (peak negative moment in the top deck, peak positive and negative moment in the soffit); and
- M_x in the soffit is much smaller than that in the top deck and it is less sensitive to the transverse position of the axle load, but it is still influenced by the longitudinal position of the axle load.

2.5.2 Case study on the distance between axles

In the previous single HL-93 axle load case study, the effect of the 2nd rear axle of the HL-93 truck was not considered. To ensure the reliability of the conclusions from the single HL-93 axle

load case study, a series of double pair axles load cases with a longitudinal spacing varying from 14' to 30' as specified in AASHTO (**Figure 2.7**) were conducted. To ease the modeling efforts, the double axles load was applied by placing the center of mass (longitudinal mid-point of the double axles) at the 0.5*L* main span or the CL bent (boundary between the main and the side span), using the same transverse position at the CL 2nd web and 80 psi tire pressure. An increment of 2' in the spacing between two pair of axles was adopted, and the typical results in the moment intensity are presented in **Figure 2.16**. It seems from these two extreme cases no significant difference was observed in either the pattern of moment distribution or the peak moment intensity of the bridge deck subjected to patch loads.

To better compare the results between different cases, the peak load demands in the top deck was also plotted in **Figure 2.17**. Although fluctuations were observed for all the three load demands, the magnitudes were relatively stable. This fluctuation was primarily caused by the relative position between the centroid of patch load and the element nodes, and it is the nature of the adopted quadratic shell element. In general, the magnitudes of FE results were higher when the centroid of patch load was applied closer to the nodes, and smaller when it was between two consecutive nodes. The fluctuation can be mitigated by using a finer mesh setting but with a higher computational cost. Thus, it can be concluded that with the minimum rear axle spacing of 14 ft, both the critical transverse moment M_x and the critical shear Q_{yz} are not influenced by the number of axle pairs. And the FE results obtained by using the single axle load case shall be sufficient to produce the most critical load demands of bridge decks subjected to vehicle load.

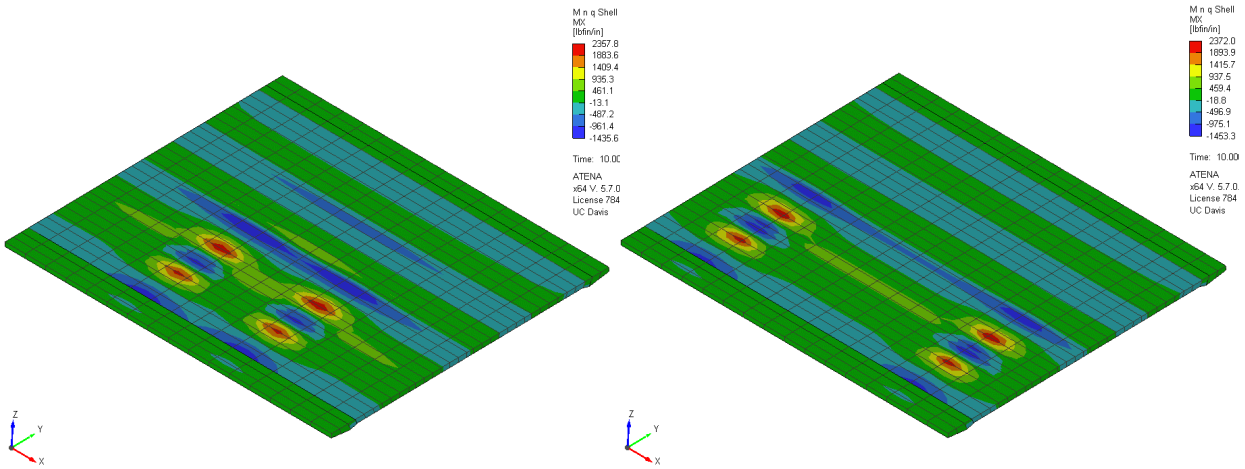

(a) Spacing of 14 ft (b) Spacing of 30 ft

Figure 2.16. Transverse moment intensity of bridge deck under the double axles load (0.5L main span)

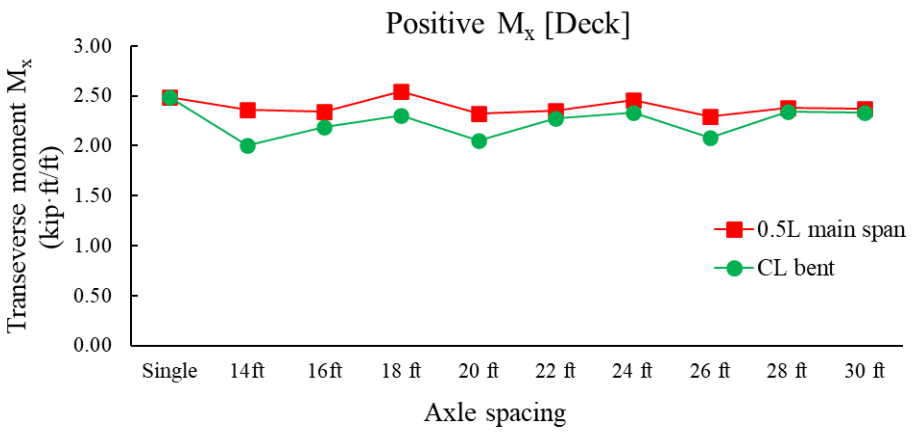

(a) Positive M_x in the top deck

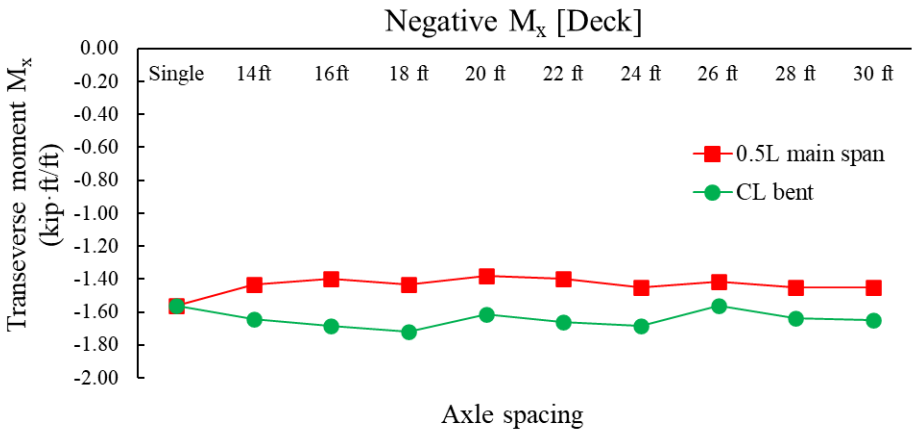

(b) Negative M_x in the top deck

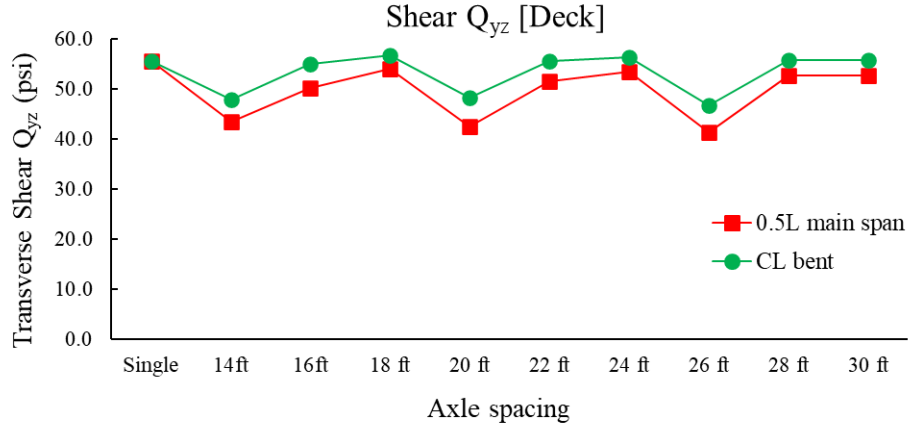

(c) Shear stress in the top deck

Figure 2.17. Nominal peak load demands of the deck under double axles load with different spacings

2.6 Summary

This chapter aims to explore the standard FE modeling methodology using the GiD and ATENA software packages, by following the concept of refined analysis on bridge decks. The first prototype box girder bridge model was constructed, and a step-by-step modeling workflow containing geometries, material definitions, selection of element type, load and boundary conditions, and mesh setting is presented in detail. In the post-process in ATENA, the longitudinal load demands of the box girder bridge were extracted and compared for different element types and mesh cases to determine the appropriate mesh setting for the refined deck analysis. Upon completion of the refined bridge model, cases studies were conducted to investigate the influence on the load demands of bridge decks due to the longitudinal position of axle load, tire pressure, and the spacing between axles. It indicates that the mid-main span and $0.75L$ end span are the two most critical longitudinal positions to yield the maximum load demands. Load demands of the soffit are much smaller than that of the top deck and the tire pressure has a nonnegligible positive effect on the load demands of bridge decks. Furthermore, the 14' minimum required spacing between HL-93 axles is sufficient to prevent the influence caused by the second pair of axle loads. Thus, a single axle load case has been verified as reliable to obtain the critical load demands of bridge decks.

3 RIGID SUPPORT MODEL

3.1 Background and Objective

Through the first phase study of refined FE modeling based on the prototype bridge, it is determined that the original scope of this study is not feasible to be completed within the proposed project period. The workload of the refined FE modeling is enormous and impractical with all the required design parameters considered, which include but not limited to, span length, span configuration, girder spacing, girder dimension, deck thickness, number of cells/girders, number of design lanes, type of truck/axle load configuration, tire pressure, transverse deck slope, etc. In addition, difficulty always exists in determining the most critical positions of multi-lane vehicles both transversely and longitudinally. Although the concept of either influence line/area, or the Pucher and Homberg Charts (Pucher et al. 1973; Homberg and Ropers 1965) can help to roughly determine the critical location of the applied concentrated load for the selected point of interest, a more precise calculation of the critical load demands, i.e., moment and shear, under different vehicle load combinations is complex and requires iteration of analysis. To address these issues, as well as to simplify the sophisticated modeling procedure for different deck configurations, a rigid support modeling strategy is proposed by the Caltrans Technical Advisory Committee (TAC) team and targeted to conservatively envelope the results of the true refined FE model as introduced in Chapter 2. This Rigid Support Model (RSM) minimizes the number of design variables and focuses only on the girder spacing, tire pressure, and critical vehicle load combination, etc. It helps to reach a balance between the modeling accuracy and availability, as a promising alternative to the true refined model.

The idea of the RSM is to restrain the vertical movement of all the girder but allow them to rotate freely, in other words, the entire superstructure is pin supported along the longitudinal direction, as illustrated in **Figure 3.1**. To alleviate the effect caused by the longitudinal restrictions and span arrangement, one sufficiently long span is assumed, with a length equals to 5×longest HL-93 truck (44'). The HL-93 axle load with a 100 psi tire pressure, equivalently 16×10" of the contact area, is used as an example load type to yield the load demands of bridge decks. This axle load will be placed at mid-span longitudinally and moves from the face of barrier to the CL bridge by an increment of approximately 10% of the girder spacing transversely (0.1*S*). The peak positive moment, negative moment, and shear stress of the top deck obtained from each load case will be documented and compared to the results from the refined FE model. This chapter aims to run two example bridge cases with different span configurations, by using both the RSM and the true refined FE model, to check if the RSM can reach the expectation of conservatively enveloping the results obtained from the true refined FE model.

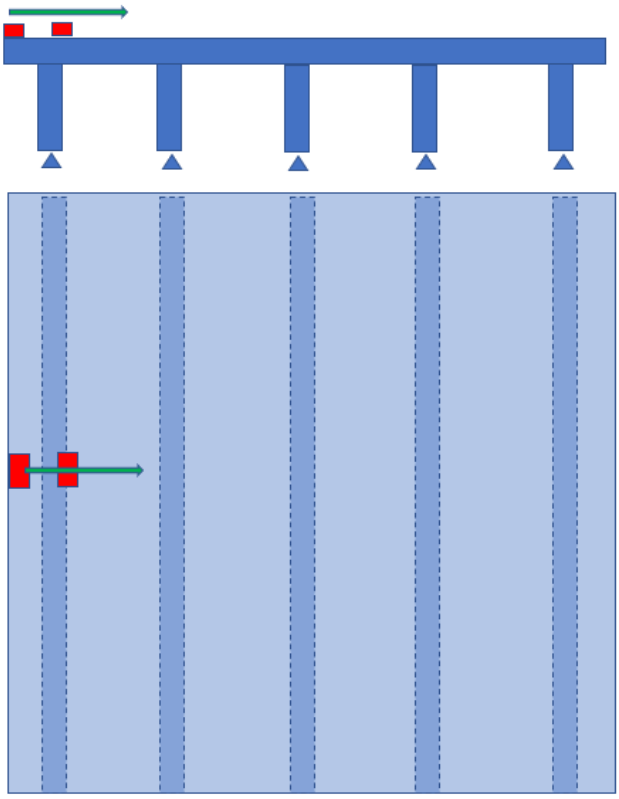

Figure 3.1. Illustration of the rigid support concept

3.2 FE Modeling and Load cases

3.2.1 Large box girder prototype bridge

To cover the bridge decks with various spacings, another prototype bridge #53-2790L with a larger box girder was also built in GiD, with the girder spacing equals to 15', representing an upper limit case as specified in the AASHTO Appendix Table A4-1 (AASHTO 2017). It is also a three-span prestressed concrete box girder bridge with a span configuration of 245 ft; 290 ft; 230 ft, as shown in **Figure 3.2**. The total width of the bridge is 69'-6", composed of four design lanes and four box cells, as present in **Figure 3.2**(b). Both the top bridge deck and soffit have a thickness of 10", with the web thickness equals to 15". The refined modeling procedure of the large box girder bridge in GiD followed the same protocols as described in Chapter 2.2 for the small box girder bridge, such that details need not be repeated here. A mesh case of L210W10H8 was determined from the mesh study for the large box girder bridge, using the same 3D quadratic shell elements (**Figure 3.3**). However, to save computational effort because of the large dimension of this prototype bridge, only the main span of the refined model adopted the finer elements where axle load was applied, while the other spans used a coarser mesh in the longitudinal direction but remained the same mesh in other directions.

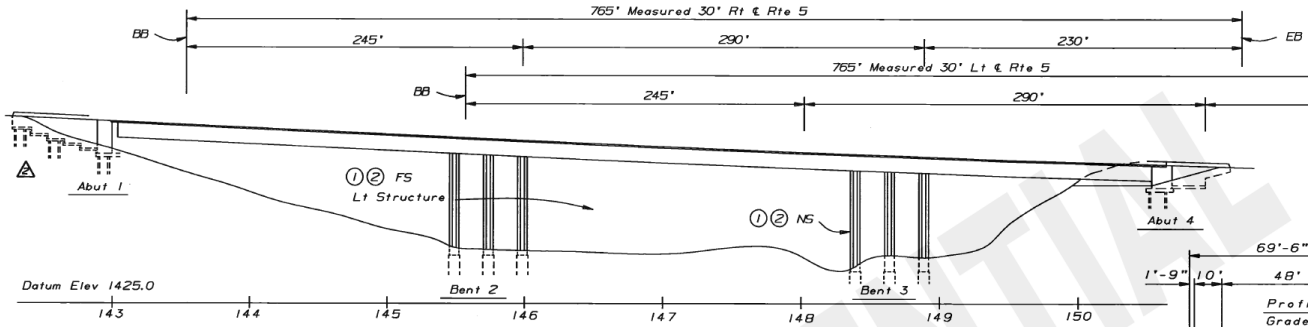

(a) Elevation

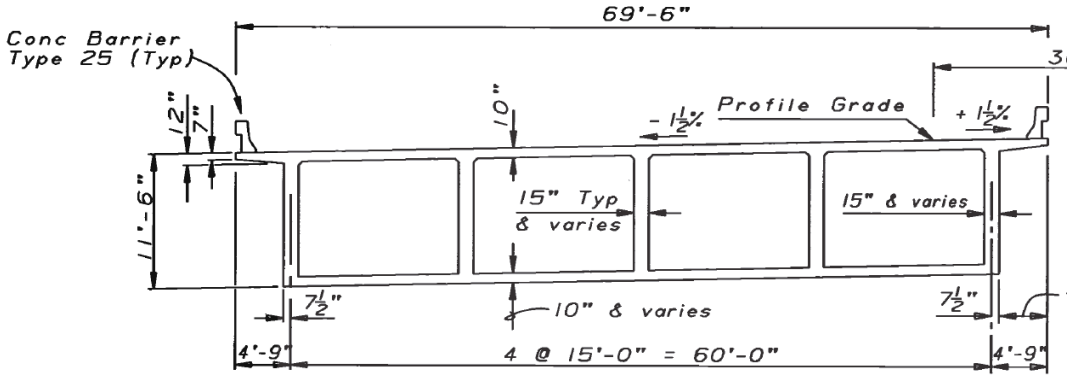

(b) Cross-section

Figure 3.2. General plan of the prototype bridge (#53-2790L)

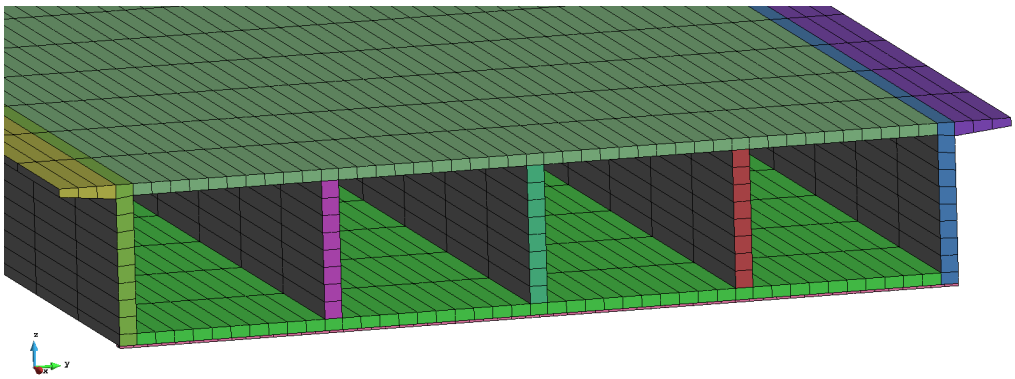

Figure 3.3. Mesh setting of the large box girder bridge (L210W10H8)

3.2.2 FE modeling of RSM

For the FE modeling of the RSM, the same longitudinal span length of 220' was used for both the small and large box girder prototype bridges. Two support types were studied in the small box girder case to restrain the vertical displacement, including: (a) distributed pin support at a constant interval (16", smaller than 0.2×girder spacing); (b) line pin support (line restriction) with spacing matches the element size, as illustrated in **Figure 3.4**. A case study with the axle load applied at the CL 2nd web was performed to compare the numerical results of the models using these two support types, and no significant difference was observed for the load demands of bridge decks, as presented in **Table 3.1**. Thus, the line pin support was selected for the two RSMs to save the computational time.

(a) Distributed pin support

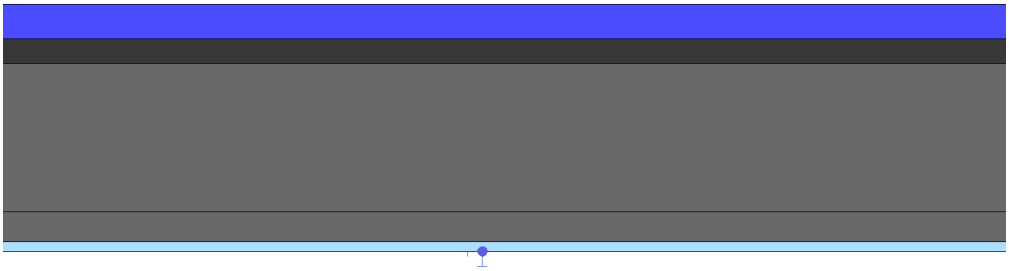

(b) Line pin support

Figure 3.4. Two support types of the RSM (small box girder bridge)

Table 3.1. Comparison of FE results for different support types (small box girder bridge)

Support Type	Max. $+M_x$ (lbf-in/in)	Max. $-M_x$ (lbf-in/in)	Max. Shear Q_{yz} (lbf/in)
Distributed pin support	2518.7	-2048	498.9
Line pin support	2517.9	-2055.1	499.5

Performing a mesh study is always inevitable in the FE modeling to ensure the reliability of the results. Similar to the strategies described in the previous chapter, mesh studies were performed for the two RSMs. Both of the models used the same mesh setting in the transverse and longitudinal directions as that of their refined counterparts, however, the number of elements in the longitudinal direction changed to 160 due to the different span length. To sum up, for the small box RSM, the size of element is 16.5" in *x* direction (bridge longitudinal direction), 15–16" in *y* direction (bridge transverse direction) for the top deck, 13–16" in *y* direction for the soffit and 11.3" in *z* direction (bridge vertical direction) for the web. For the large box RSM, the size of element is 16.5" in *x* direction, 15–16.5" in *y* direction for both the top deck and the soffit, and 14.8" in *z* direction for the web.

3.2.3 Transverse load case

For both the small box girder and the large box girder case, the HL-93 truck axle load was applied transversely at the mid-span of the RSM and moved by a roughly 0.1×girder spacing. These minor transverse cases are summarized in **Table 3.2** and **Table 3.3** for the small box and the large box case, respectively. In **Figure 3.5** or **Figure 3.6**, an example is presented to show the distance measured from the end of deck to the left face of the left tire. It indicates the relative position of the axle patch load on the bridge deck of the selected minor case. However, for the

refined models, the longitudinal positions of the axle load affect the load demands of bridge decks. According to the conclusions from the previous chapter based on the small box girder case, an axle load applied at the mid-main span and the 0.75L end span yielded the most critical load demands. Thus, the comprehensive transverse axle load cases were only applied to the mid-main span and the 0.75L end span of the true refined models.

Table 3.2.Transverse axle load cases of the small box girder case

Case	Distance between EOD and Face of Tire (in)	Case	Distance between EOD and Face of Tire (in)
Face of Barrier	21 (0.79L_0)	i	116 (0.78L_1)
a	30.5 (0.02L_1)	j	125.5 (0.87L_1)
b	40 (0.1L_1)	k	135 (0.95L_1)
Exterior Cell	48.6 (0.18L_1)	l	144.5 (0.04L_2)
c	59 (0.27L_1)	2nd Cell	157.75 (0.16L_2)
d	68.5 (0.36L_1)	m	163.5 (0.22L_2)
e	76 (0.42L_1)	n	173 (0.31L_2)
f	87.5 (0.53L_1)	o	182.5 (0.39L_2)
g	97 (0.61L_1)	p	192 (0.48L_2)
2nd Web	104.5 (0.68L_1)	q	201.5 (0.57L_2)
h	109 (0.72L_1)	3rd Web (CL bridge)	211 (0.66L_2)

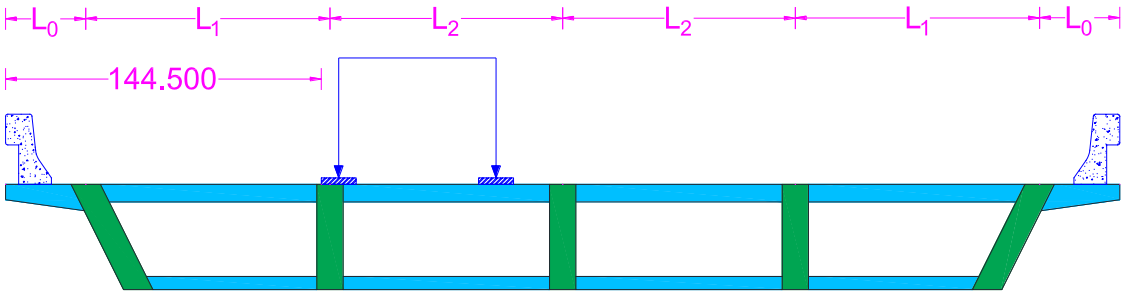

Figure 3.5. Illustration of the axle load case (small box, case-l, unit: in)

Table 3.3. Transverse axle load cases of the large box girder case

Case	Distance between EOD and Face of Tire (in)	Case	Distance between EOD and Face of Tire (in)
Face of Barrier	21 (0.51L_0)	i	211 (0.9L_1)
a	31 (0.68L_0)	j	229 (L_1)
b	49 (L_0)	k	247 (0.1L_2)
c	67 (0.1L_1)	l	265 (0.2L_2)
d	85 (0.2L_1)	2nd Cell	283 (0.3L_2)
Exterior Cell	103 (0.3L_1)	m	301 (0.4L_2)
e	121 (0.4L_1)	n	319 (0.5L_2)
f	139 (0.5L_1)	o	337 (0.6L_2)
g	157 (0.6L_1)	p	355 (0.7L_2)
h	175 (0.7L_1)	3rd Web (CL bridge)	373 (0.8L_2)
2nd Web	193 (0.8L_1)	-	-

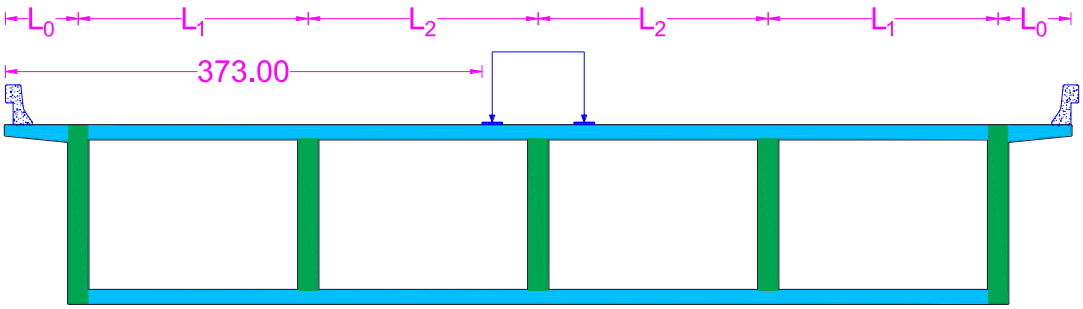

Figure 3.6. Illustration of the axle load case (large box, case-3rd web, unit: in)

3.2.4 Longitudinal load case

With the case study on the longitudinal positions of the axle load has been conducted for the small box girder, it is worth noting the three-span configuration only represents one of the typical span configurations in CA. To ensure that the rigid model strategy is reliable and covers the different span configurations commonly used in CA, case studies on five longitudinal span configurations were performed by extending the refined bridge model of the small box girder, as illustrated in **Figure 3.7**. These span configurations include: Case A – the original span design [**Figure 3.7**(a)]; Case B – single main span [**Figure 3.7**(b)]; Case C – two identical main spans [**Figure 3.7**(c)]; Case D – main span with end spans equal to 75% of the main span [**Figure 3.7**(d)]; and Case E – two identical main spans with end spans equals to 75% of the main span [**Figure 3.7**(e)].

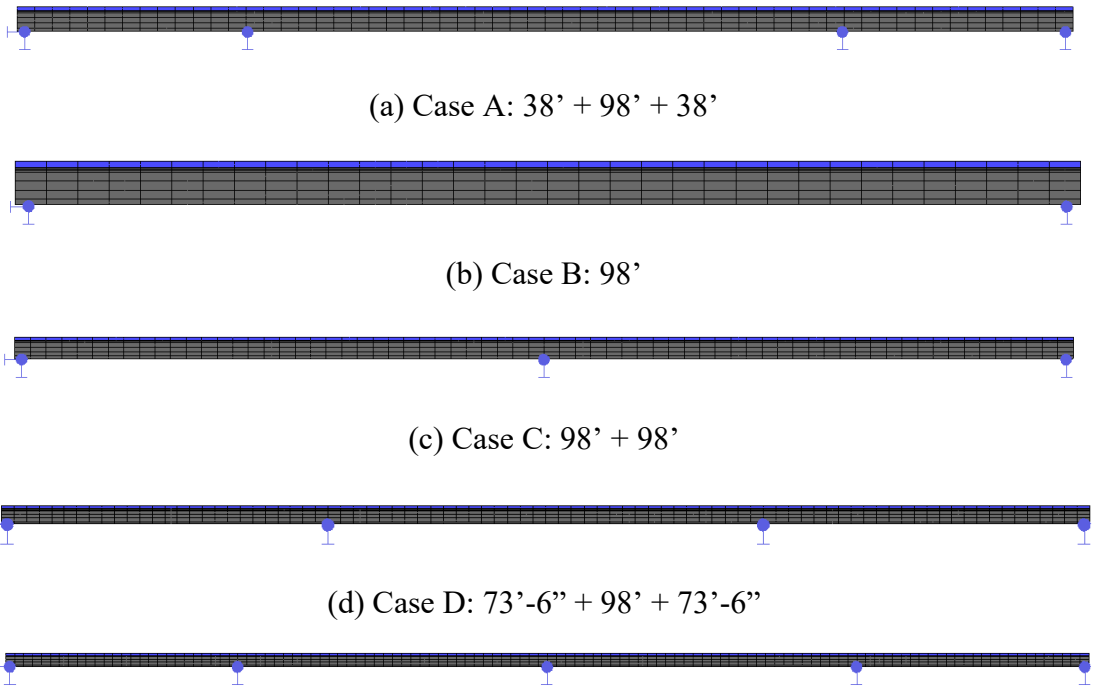

(a) Case A: 38’ + 98’ + 38’

(b) Case B: 98’

(c) Case C: 98’ + 98’

(d) Case D: 73’-6” + 98’ + 73’-6”

(e) Case E: 73’-6” + 98’ + 98’ + 73’-6”

Figure 3.7. Various span configurations commonly used in California

To save the computational efforts, only the mid-main span of Case A and the 0.75*L* end span of Case C were applied with the comprehensive transverse minor load cases, assuming these two longitudinal span cases are more critical, for both the two prototype bridges (refined models). Only the most critical transverse minor cases, which was determined upon completion of the comprehensive transverse load analysis, were applied to the mid-main span and/or 0.75L end span of the rest longitudinal span configurations. The result indicates that the actual most critical load demands occur at the mid-main span and 0.75*L* end span of Case B. Although it contradicts with the original assumption that the mid-main span of Case A and the 0.75*L* end span of Case C are more critical, the differences in load demands are very small and the results of the RSMs can still envelope that of the most critical cases. For consistency, the following analysis are still based on the mid-main span of Case A and the 0.75*L* end span of Case C. Details will be described in the next section.

3.3 Results and Discussion

3.3.1 Data extraction

To compare the results between the RSM and the refined model, the peak magnitude of the scale bar of the load intensity contour, e.g., as shown in **Figure 2.14**, may not the best choice. Because the peak load demand intensity in the ATENA post-process usually occurs within the region of patch axle load, where unreliable spikes of load magnitude often appear at a few element nodes due to the nature of the FE simulation. Instead, the average load demands within the selected influence length *L*, or equivalently the strip width as defined in the approximate method (AASHTO 2017), is more preferrable. In **Figure 3.8**(a), the elements encompassed by the blue frame with a dimension of *L* in the longitudinal direction is the target influence area. **Figure 3.8**(b) represents the integrated transverse moment of the selected elements, where the two circled peak numbers shall be divided by the influence length *L* to yield the peak average moment demands at the given minor patch load case. The average shear demand is treated in the same manner but will be further divided by the thickness of the deck to yield stress. For the validation purpose of the RSM, two lines of elements with a total length *L* varies within 66–70" in the longitudinal direction are deemed as appropriate to obtain the peak average load demands. The slight variation in the length of the influence area is caused by the different mesh size due to the different span lengths of the built bridge models.

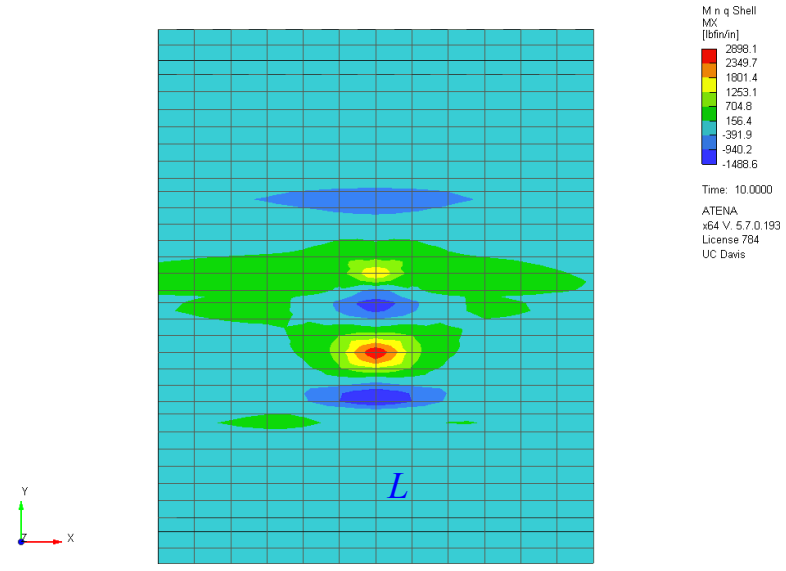

(a) Transverse moment intensity (lbf-in/in)

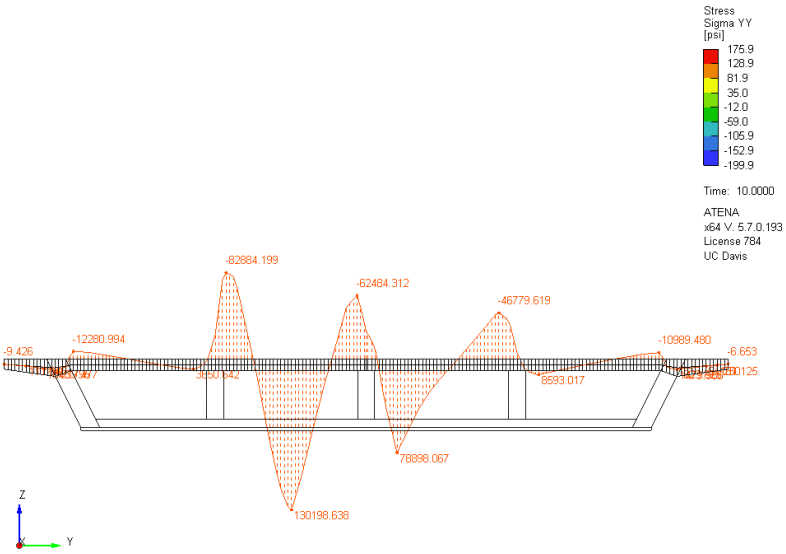

(b) Integrated transverse moment distribution of the selected elements (lbf-in)

Figure 3.8. Concept of average load demand within the influence length *L*

It is important to clarify that only the peak load demands across the entire cross-section of each minor patch load case will be extracted and saved for comparison. The peak load demands do not necessarily occur at the location where the tire patch is applied. Using the small box girder bridge as an example, as illustrated in **Figure 3.9**, the red cross indicates the actual location of the peak load demands, and this position of peak load demands varies depending on different minor patch load cases and the type of load demand (i.e., positive, and negative moment, and shear).

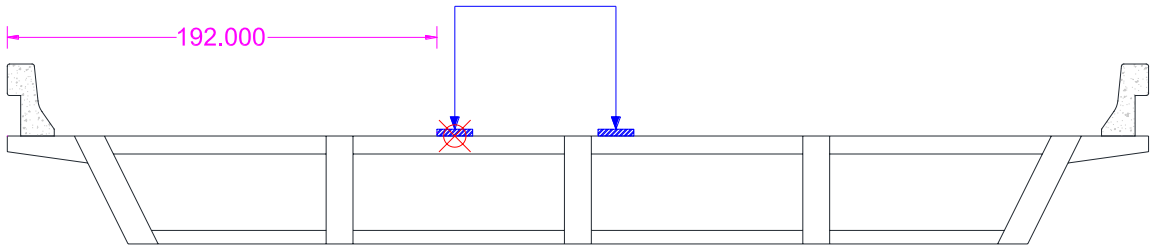

(a) Position of peak $+M_x$ (load case-p, unit: in)

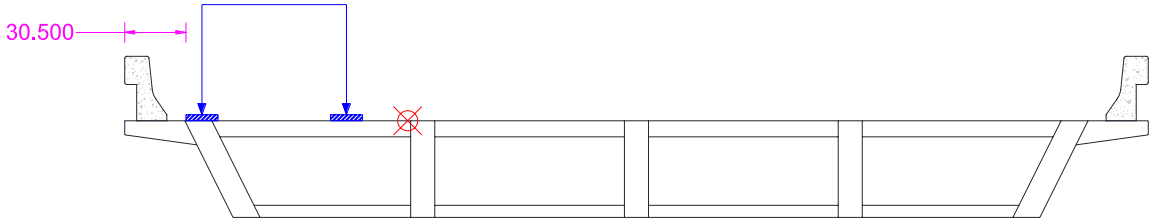

(b) Position of peak $-M_x$ (load case-a, unit: in)

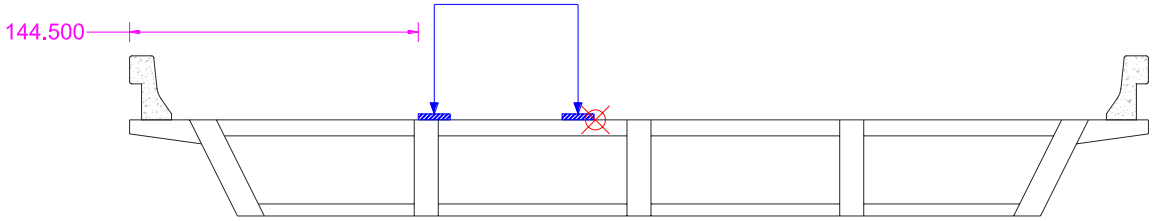

(c) Position of peak Q_{yz} (load case-l, unit: in)

Figure 3.9. Relation between the location of tire patch load and the location of peak load demands

3.3.2 Results comparison

The comparisons between the results from the RSMs and their refined model counterparts are visualized in **Figure 3.10** to **Figure 3.13**. In each subplot, the solid line represents the load demands from the RSM, while the column bars represent the load demands from the refined model. The horizontal axis indicates the distance between the end of deck to the left face of the left tire in inch, and it is consistent with the transverse axle load cases described in **Table 3.2** and **Table 3.3**, for the small and large box girder bridge, respectively. It should also be noted that the given numbers in these plots are the most critical average load demands at each minor axle load case across the entire cross-section, e.g., two circled numbers in **Figure 3.8**(b), but not the load demands fixed to a specific location of the cross-section.

In **Figure 3.10** and **Figure 3.11** for the small box girder bridge, the moment from the RSM seems to envelope the results from the refined model, except a few positions when the patch load is closer to the overhang. However, the shear from the RSM is less satisfying because the difference between two models fluctuates more than that of the moment results. Nevertheless, the RSM still yields larger results in maximum positive moment (4.4% higher), maximum negative moment (18.2% higher) and maximum shear (3.7% higher) than the refined model.

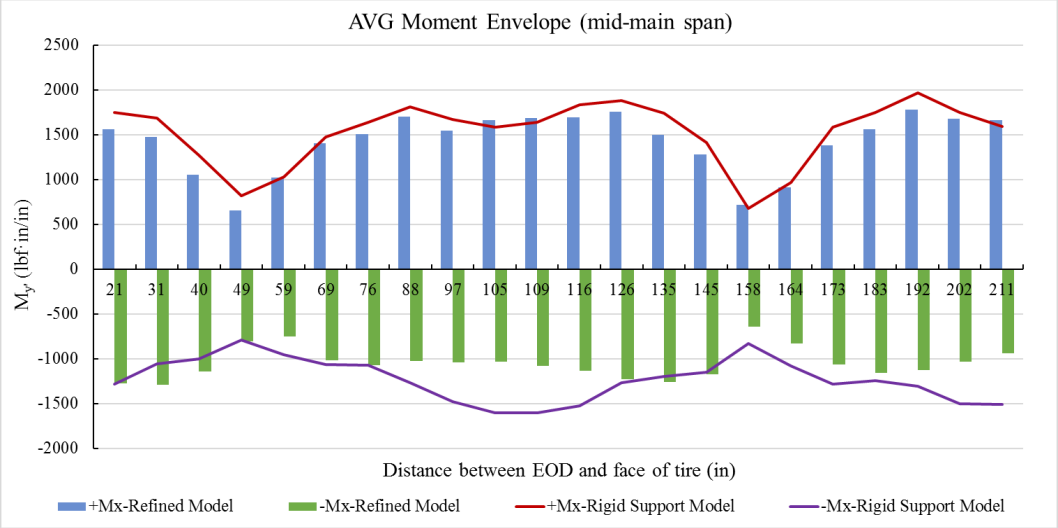

(a) Moment

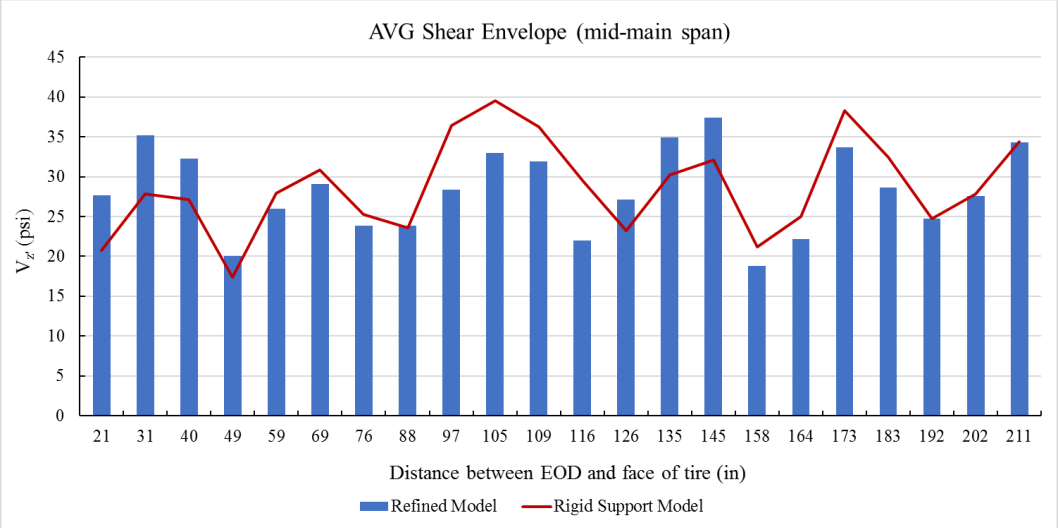

(b) Shear

Figure 3.10. Comparison of peak load demands between the refined model and the RSM (small box girder bridge, mid-main span of Case A)

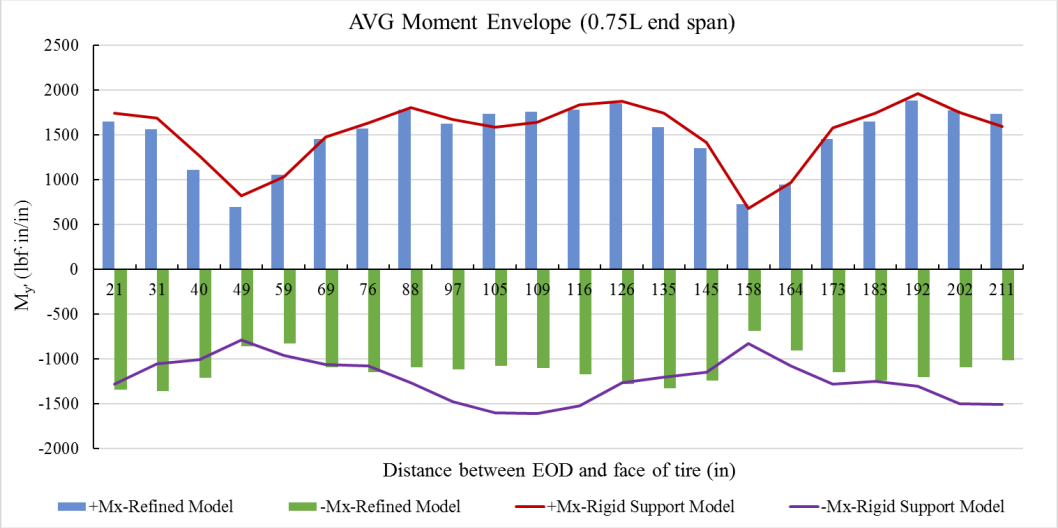

(a) Moment

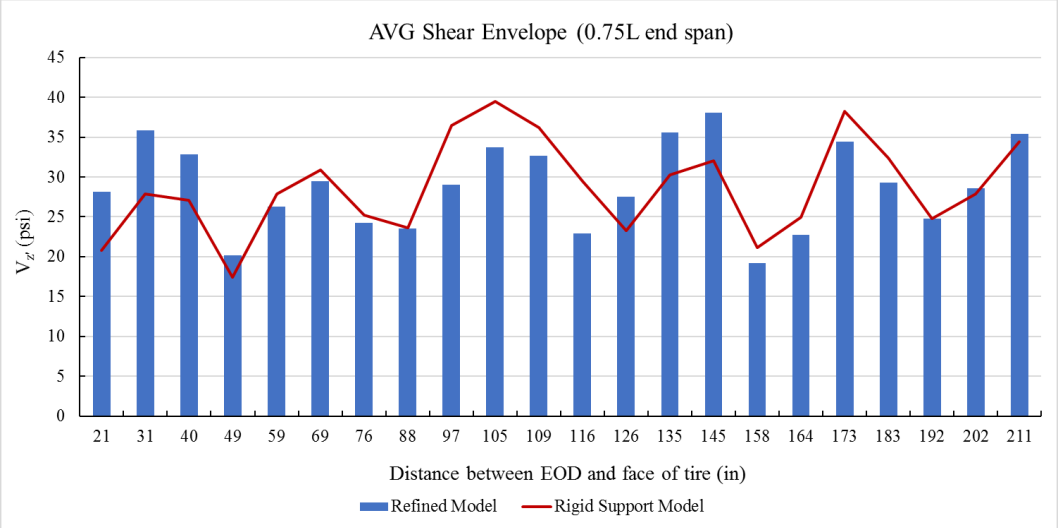

(b) Shear

Figure 3.11. Comparison of peak load demands between the refined model and the RSM (small box girder bridge, 0.75*L* end span of Case C)

In **Figure 3.12** and **Figure 3.13** for the large box girder bridge, a very close results have been observed between the RSM and the refined model. The results from the refined model can mostly envelope that from the refined model for both moment and shear. In short, the RSM yields larger results in both maximum negative moment (7.7% higher) and maximum shear (1.5% higher), but slightly smaller in maximum positive moment (-0.7% smaller) than the refined model. This difference of -0.7% is very small and can even be within the fluctuation of FE approximation due to different mesh size and element type, hence, the result is acceptable.

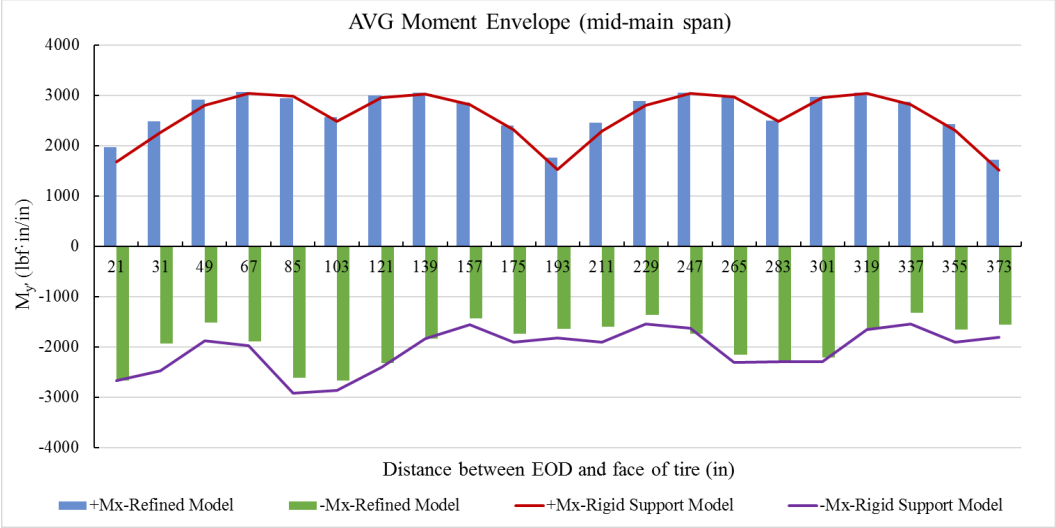

(a) Moment

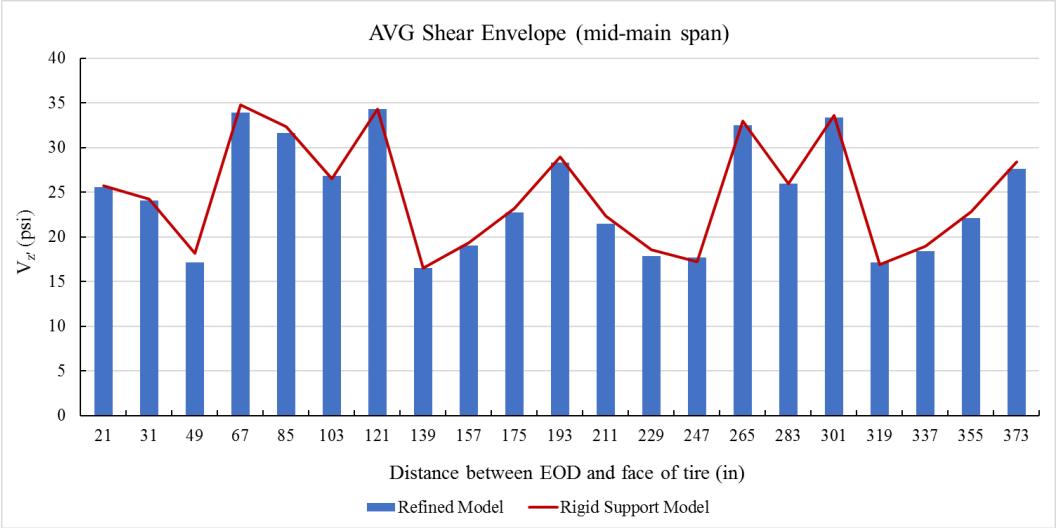

(b) Shear

Figure 3.12. Comparison of peak load demands between the refined model and the RSM (large box girder bridge, mid-main span of Case A)

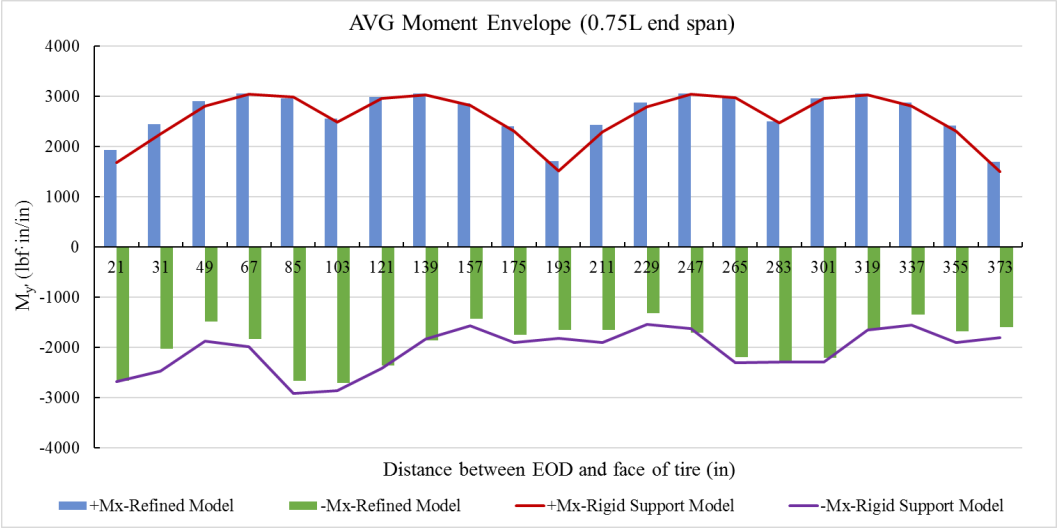

(a) Moment

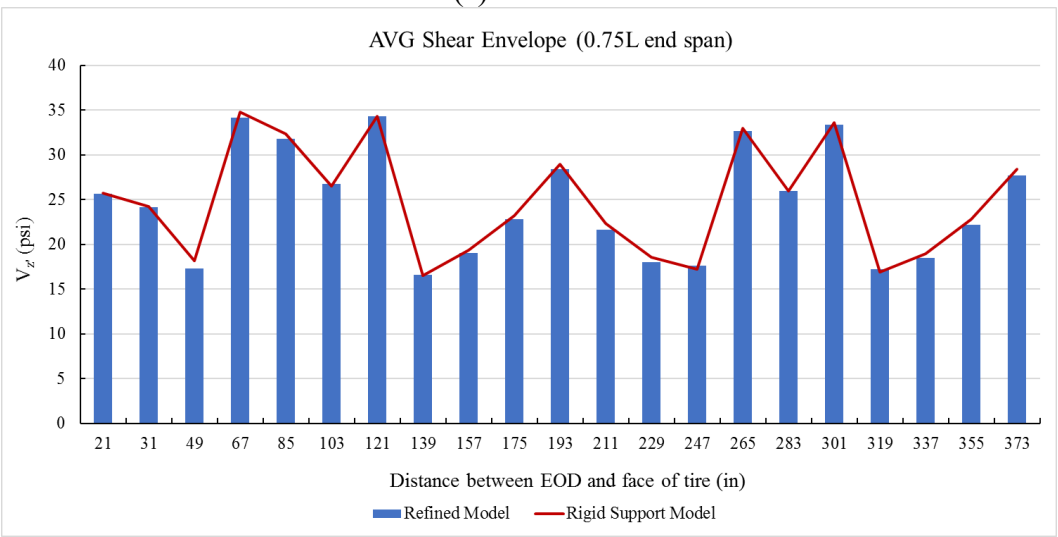

(b) Shear

Figure 3.13. Comparison of peak load demands between the refined model and the RSM (small box girder bridge, 0.75*L* end span of Case C)

On the other hand, upon completion of these two comprehensive transverse axle load cases, the critical minor cases were applied to the mid-main span and/or 0.75*L* end span of the rest longitudinal span configurations, as mentioned in the previous section. Because of the large workload of FE analysis, only the small box girder bridge case was conducted to investigate the influence on the load demands due to different longitudinal span configuration. The comparison of the maximum average load demands between the RSM and the refined models with different longitudinal span configurations are presented in **Figure 3.14** and **Figure 3.15** for mid-main span and 0.75L end span case, respectively. It can be seen that the variation in span configuration does not produce a large difference in the maximum load demands of bridge decks, e.g., the differences in load demands are all within 2% between Case B and Case C. Although the most critical load demands seem to occur at the mid-main span and 0.75*L* end span of Case B, which contradicts with the original assumption that they occur at the mid-main span of Case A and the 0.75*L* end span of Case C, the maximum moment and shear from the different cases based on the refined

model are still below that of the RSM. As a result, it is concluded that the RSM is reliable and more conservative to be used as a simpler alternative to the refined model to conduct production run in the next stage of the project.

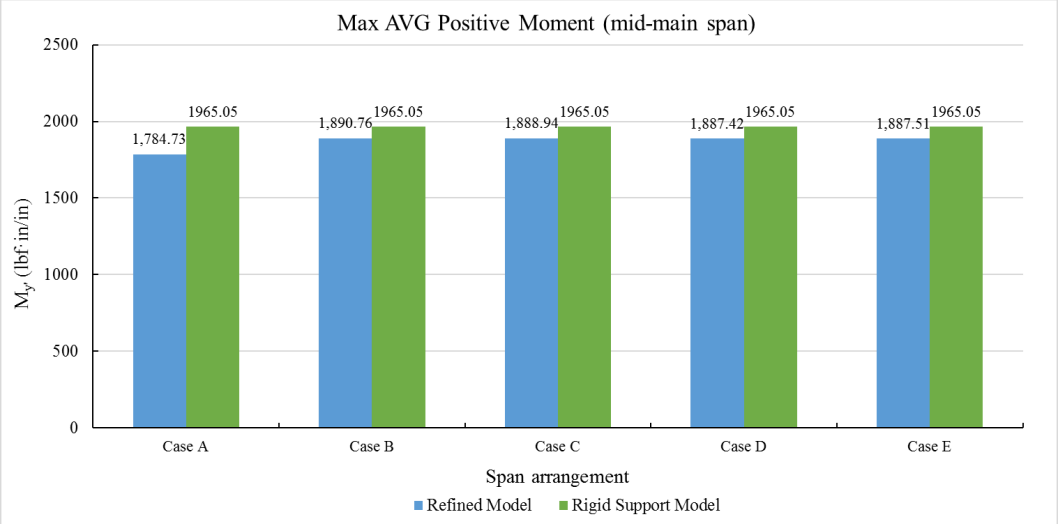

(a) Positive moment

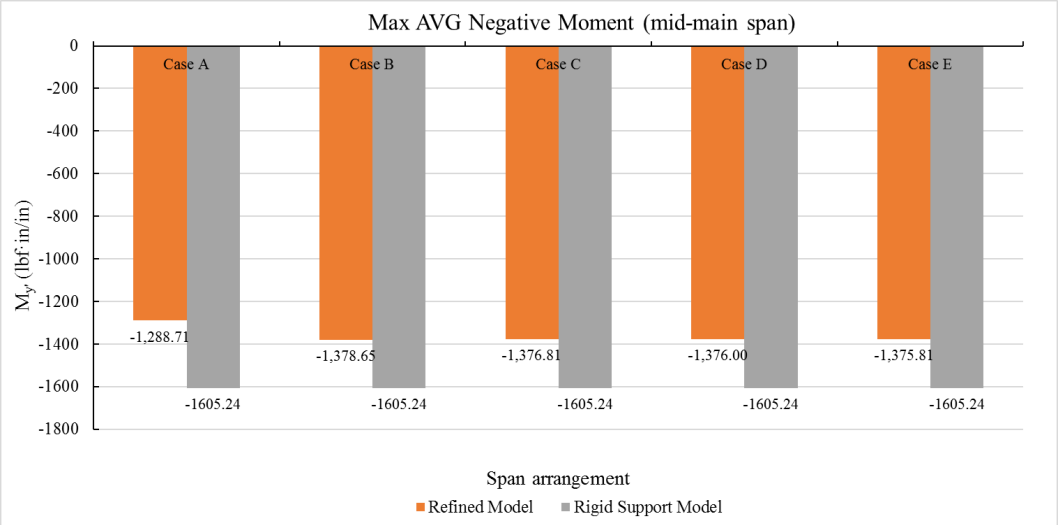

(b) Negative moment

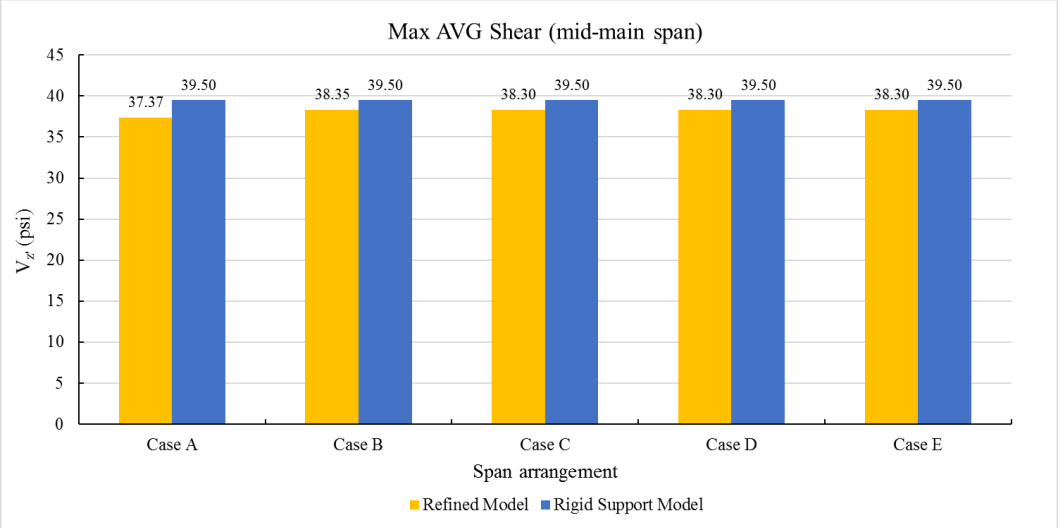

(c) Shear

Figure 3.14. Comparison of maximum load demands between the refined model and the RSM for different span configurations (small box girder bridge, mid-main span)

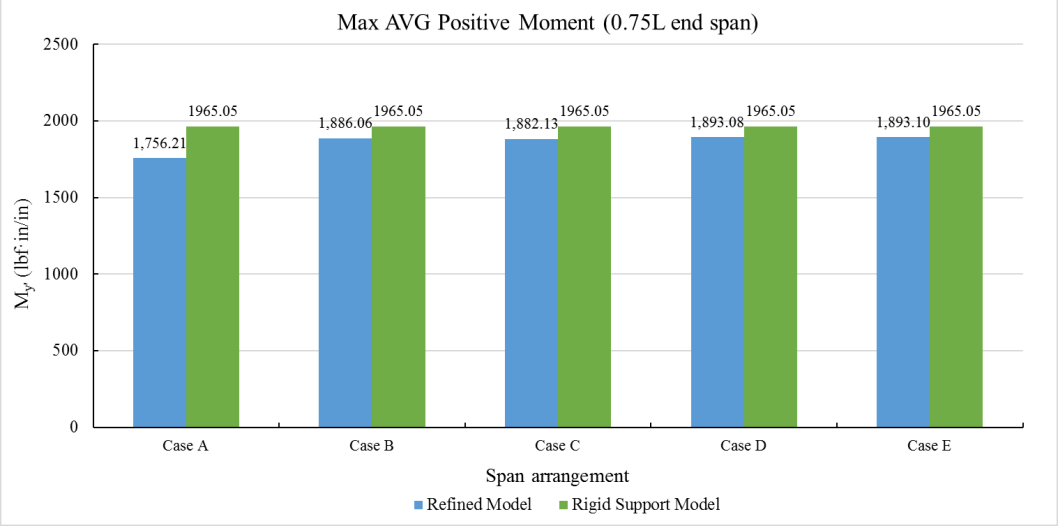

(a) Positive moment

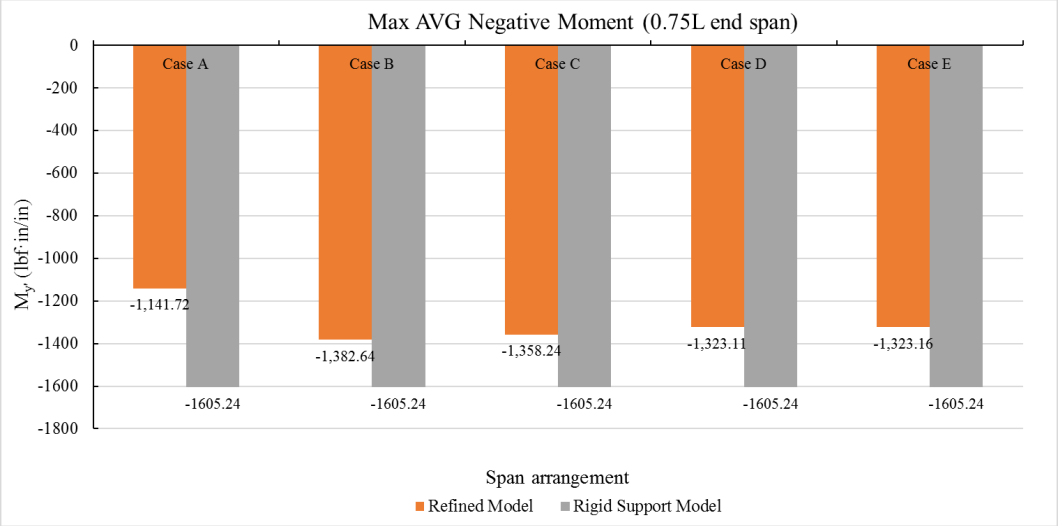

(b) Negative moment

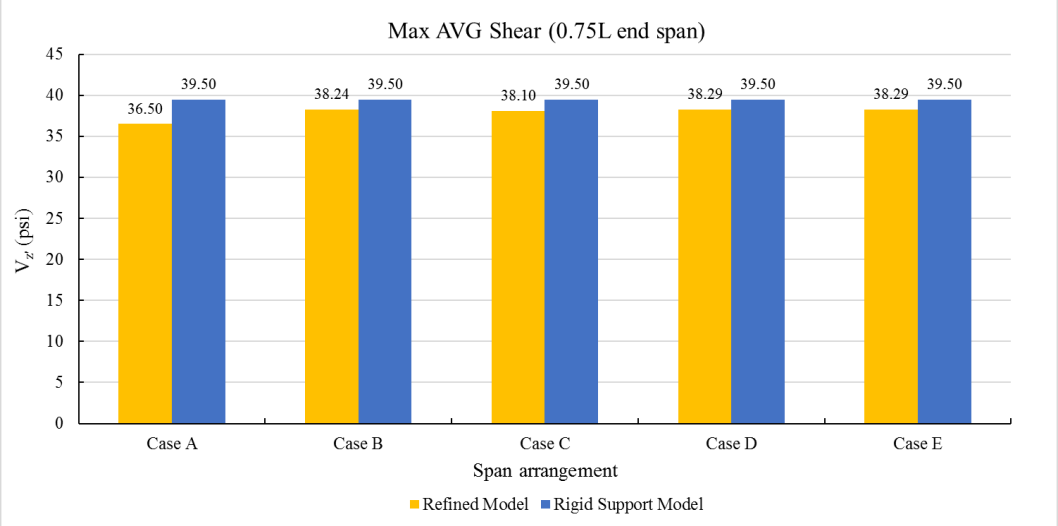

(c) Shear

Figure 3.15. Comparison of maximum load demands between the refined model and the RSM for different span configurations (small box girder bridge, 0.75*L* end span)

3.3.3 Critical positions of load demands

To determine the critical positions of the bridge deck for both moment and shear, as well as to study the influence of cross-sectional geometries on the peak load distribution, the normalized load demand envelopes are plotted and compared in **Figure 3.16** for both the small and large box girder bridges based on the RSM. In each subplot, the horizontal (x) axis represents the relative location of the box girder, i.e., 0 = end of deck (EOD); 0.5 = mid-overhang; 1 = CL 1st web; 1.5 = CL 1st cell; 2 = CL 2nd web; 2.5 = CL 2nd cell; and 3 = CL 3rd web (CL bridge), etc. The vertical axis represents the peak load demand at the relative position of the deck divided by the maximum load demand of the deck. In **Figure 3.16**(a), both cases follow a similar trend of moment distribution, where the critical positive moment usually occurs at the middle of cells (x =1.5 or 2.5) while the critical negative moment occurs at the faces of webs (close to x = 1, 2, or 3). However, the exact location of maximum moment demand slightly varies for the two box cases, and it should depend

on the geometry of the cross-section, e.g., spacing, web thickness, length of overhang, angle of exterior web, etc. Likewise, the normalized shear envelope in **Figure 3.16**(b) shows some similarity between the two cases, where the critical locations of shear are usually close to the web. But the exact location of maximum shear demand varies for the two cases.

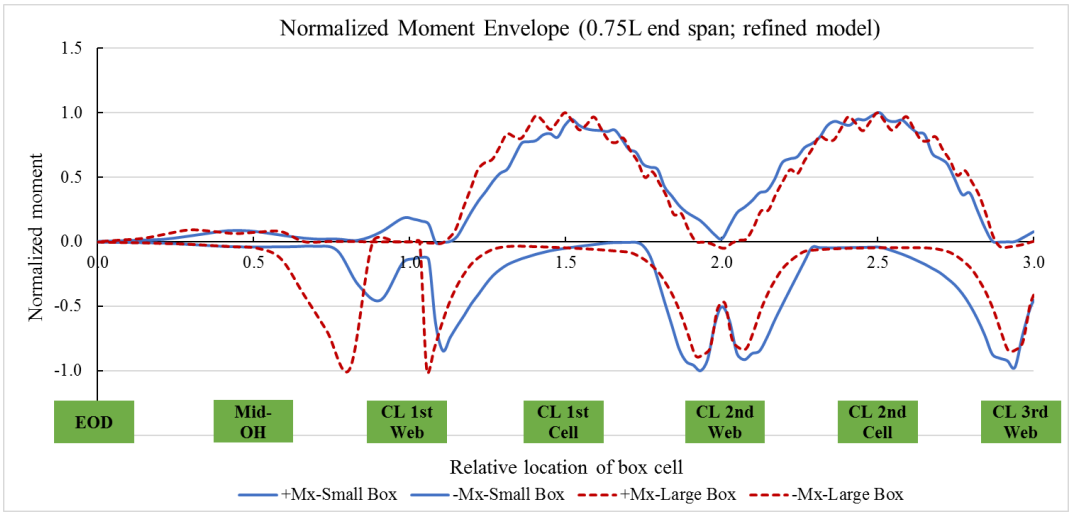

(a) Moment

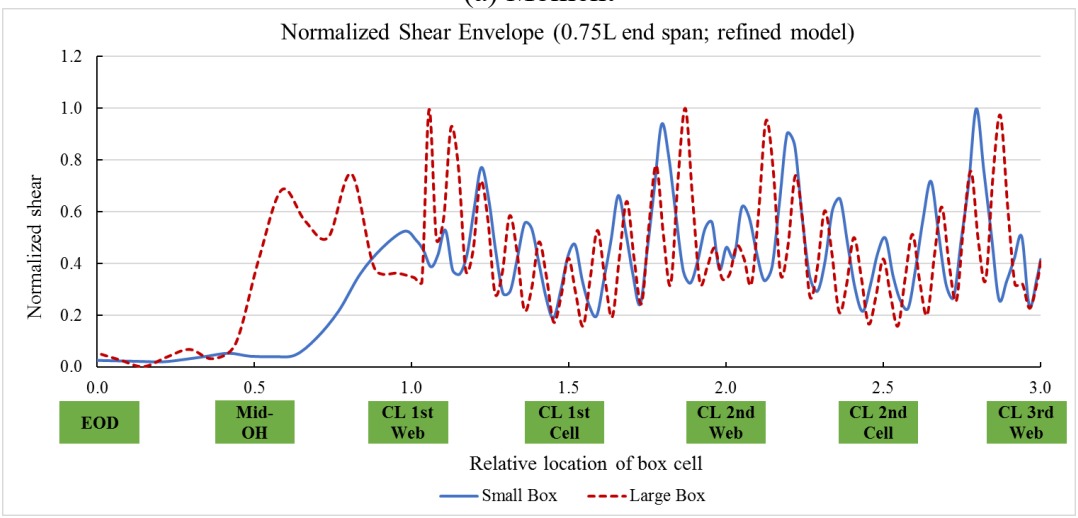

(b) Shear

Figure 3.16. Normalized load demand envelopes of both small and large box girder bridges (RSM)

3.3.4 Deck punching shear

AASHTO (2017) points out that the bridge deck designed by flexural theory has a factor of safety at least 10 times that of the punching shear failure. Hence, the predominant failure mechanism of a well-supported bridge deck slab is the fan-shape like punching shear under the tire patch load, and the failure process is always associated with a complex internal arching effect. To preliminarily examine the shear state in the bridge deck under axle patch load, the shear stress at the assumed failure section of the bridge deck was extracted from the FE models. In **Figure 3.17**, assuming a 45° angle of load development from the top of deck to the bottom under the single

tire patch load, two critical positions were considered, i.e., left and right side of the tire with a distance of half the deck thickness (orange dashed line). Likewise, in the longitudinal direction, the critical local punching shear stress was assumed to occur at half the deck thickness away from the tire patch. In other words, to obtain the average critical shear stress at the assumed failure section, a narrower length of the influence area *L* (strip width) should be considered. As shown in **Figure 3.18**, for example, when the applied tire pressure is 100 psi, the equivalent patch size equals to 16×10", so the length of the selected influence area *L* should be 10" plus 8", where the latter number is the deck thickness, and yields 18". Thus, a finer mesh was assigned to the FE model, and it was reanalyzed to capture the required critical shear stress. In this study, two tire pressure was considered, i.e., 100 psi and 125 psi, corresponding to the tire patch size of 16×10" and 16×8", respectively, for both the small and larger box girder bridges. And the maximum critical shear stresses were obtained as 55.2 psi and 57 psi for the small box girder bridge under the 100 psi and 125 psi tire pressure, respectively, and as 47.6 psi and 49 psi for the large box girder bridge under the 100 psi and 125 psi tire pressure, respectively. It should be noted that all these numbers are nominal shear stresses without the inclusion of load factors.

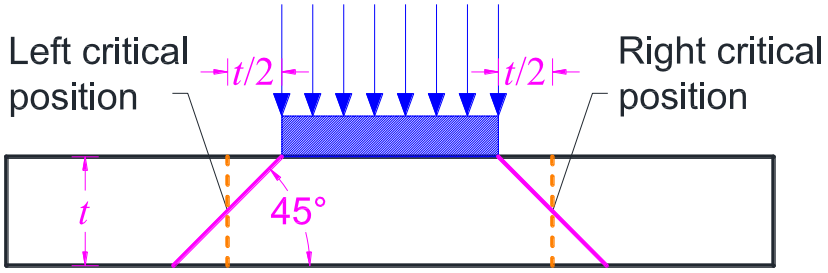

Figure 3.17. Cross-section of deck slab under tire patch load

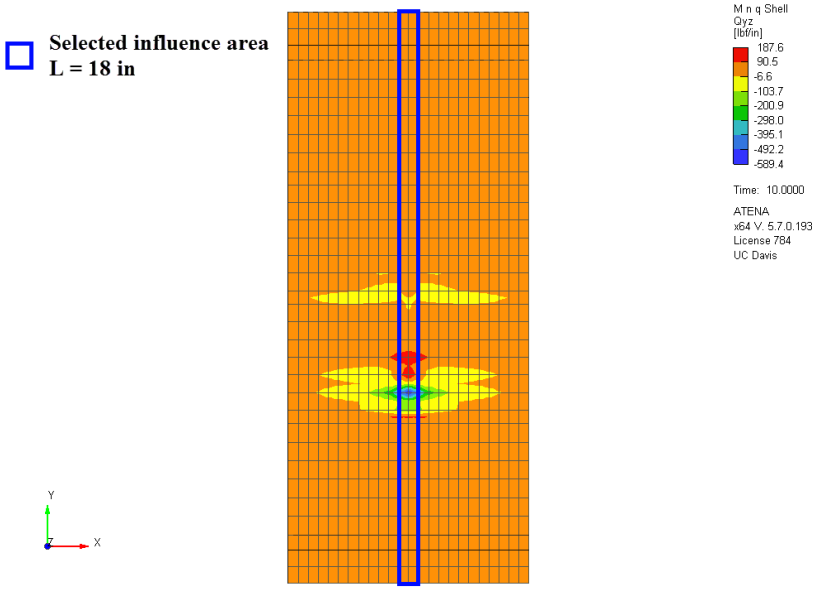

(a) Transverse shear intensity (lbf/in)

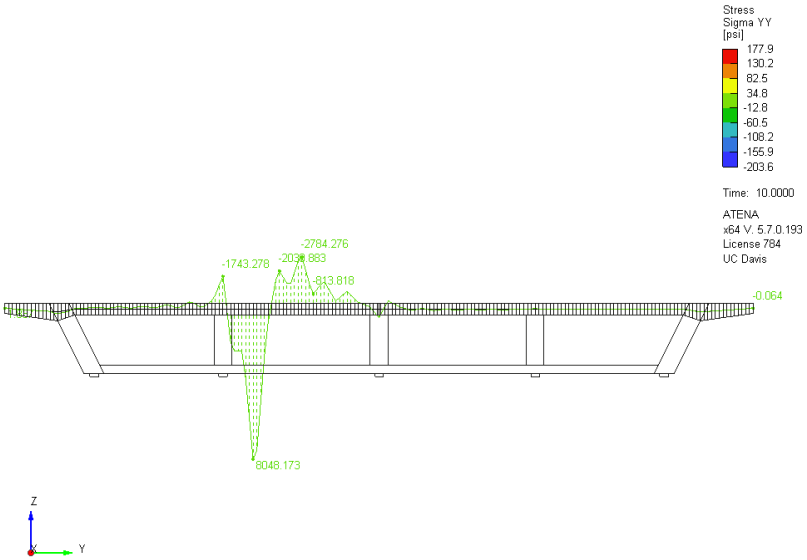

(b) Integrated transverse shear distribution of the selected elements (lbf)

Figure 3.18. Updated FE model with a finer mesh for the punching shear stress at the tire

A general punching shear model (Fang et al. 1990; Graddy et al. 2002) was adopted to estimate the theoretical punching shear capacity of the bridge deck. As presented in **Figure 3.19**(a), this model assumes a rectangular tire footprint and failure planes with the same inclination angle θ. The failure plane propagates downward to the bottom of the deck slab by a thickness of d. **Figure 3.19**(b) illustrates the free-body diagram of the failure plane under applied forces, hence, the punching shear capacity can be easily derived from the equilibrium of these forces as:

$$V_c = 2\left(b_1 + b_2 + \frac{2d}{tan\theta}\right)\frac{d}{tan\theta}f_t \tag{3.1}$$

where b_1 = long side of the tire footprint (in); and b_2 = short side of the tire footprint (in). Additionally, the diagonal tensile strength of concrete can be referred to ACI 318 Table 22.6.5.2 (ACI 2019) as:

$$f_t = (2 + \frac{4}{\beta})\lambda_s\lambda\sqrt{f_c'} \leq 4\lambda_s\lambda\sqrt{f_c'} \tag{3.2}$$

where λ_s = size effect factor = $\sqrt{2/(1+d/10)} \leq 1$; λ = modification factor of lightweight concrete; β = ratio of long to short side of the tire footprint; and f_c' = concrete compressive strength (psi). As a result, the punching shear capacity of the bridge deck based on the general model can be calculated in **Table 3.4** for the two prototype bridge examples, under either 100 psi or 125 psi tire pressure.

For the small box girder bridge deck, a nominal shear stress level of 21.8% (55.2 psi/253 psi) or a nominal load level of 9.4% (16 kip/170 kip) is reached under the 100 psi tire pressure, and a nominal shear stress level of 22.5% (57 psi/253 psi) or a nominal load level of 9.9% (16 kip/162 kip) is reached under the 125 psi tire pressure. Likewise, for the large box girder bridge deck, a nominal shear stress level of 18.8% (47.6 psi/253 psi) or a nominal load level of 6.9% (16 kip/233 kip) is reached under the 100 psi tire pressure, and a nominal shear stress level of 19.4% (49 psi/253 psi) or a nominal load level of 7.2% (16 kip/223 kip) is reached under the 125 psi tire pressure. In both cases, the critical shear stress levels or load levels of the bridge decks are still low with the applied tire patch load, and it seems that the shear capacities of the two example bridges are sufficient under the static vehicle loading.

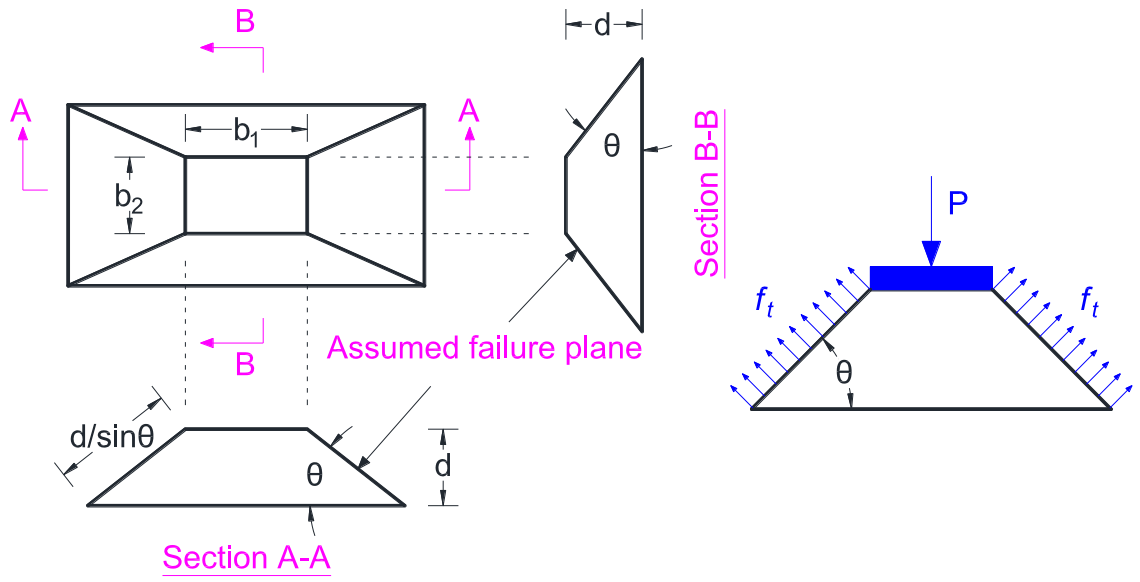

(a) Assumed failure plane in punching shear (b) Forces acting on the failure plane

Figure 3.19. General punching shear model

Table 3.4. Bridge deck parameters and punching shear capacities under 100 psi and 125 psi tire pressures

Parameter	Small Box Girder Prototype		Large Box Girder Prototype	
	100 psi	125 psi	100 psi	125psi
b_1 (in)	16	16	16	16
b_2 (in)	10	8	10	8
β	1.6	2	1.6	2
d (in)	8	8	10	10
[a]θ	45°	45	45	45
f_c' (psi)	4000	4000	4000	4000
f_t' (psi)	253	253	253	253
V_c (kip)	170	162	233	223
[b]f_v (psi)	253	253	253	253

[a]θ was observed as 38°–39° in the experiment (Fang et al. 1990; Graddy et al. 2002) but was selected as 45° for conservatism in this study; [b]f_v = equivalent shear strength at the failure section defined as $V_c/[2d(b_1+b_2+2d)]$ in **Figure 3.17**.

3.4 Summary

To reduce the workload of the original workplan and make it more practical, a rigid support modeling strategy is proposed in this chapter. To validate the accuracy of the RSM, a second prototype bridge with a large box girder was constructed using both the refined modeling and rigid support modeling methods. The updated boundary conditions and mesh setting of the new RSM are discussed and studied. In terms of the load cases, a comprehensive set of transverse minor patch load cases are applied to both the refined model and the RSM for comparison. In addition, five typical longitudinal span configurations in CA are included to ensure that the validation procedure is reliable and can cover the most common bridge types. The concept of the average load demands within the selected influence area is introduced and the results are compared for the two different FE model types based on the small and large box girder bridge examples. It indicates

that the load demands of the proposed RSM can envelope that of the refined model for all the different types of span configuration. Hence, the RSM has been verified as a more efficient and conservative alternative to the complex refined model, and it will be adopted for the production run of this research.

The critical positions of load demands are also presented based on the normalized load demands envelopes of the two prototype box girder bridges. From the data, it can be inferred that the critical positive moment usually occurs at the middle of cells, the critical negative moment usually occurs at the faces of webs, and the critical shear is usually close to the web. Moreover, a general punching shear model is introduced to estimate the local punching shear capacity of the bridge deck. From the shear demands extracted from the two prototype bridge examples, it indicates that the shear capacities of the selected bridge models are sufficient under the static vehicle loading.

4 FATIGUE OF REINFORCED CONCRETE BRIDGE DECKS

This chapter presents the state-of-the-art review on a comprehensive literature survey on available concrete fatigue models in the open literature and a proposed a strategy/methodology framework to incorporate the appropriate concrete fatigue model for practical use as a design method.

Fatigue is a slow process of mechanical degradation of a material when it is confronted with repeated loading (Torrenti et al. 2013). It is an irreversible process of deterioration in the microstructure of the material, in a form of diffuse microvoids or microcracks, and results in a permanent damage of the material. The material can fail under a load level much smaller than its static load-carrying capacity when the number of applied cycles is sufficient. However, repeated loadings with a very high load level, e.g., earthquakes may cause failures in less in than 100 cycles [ACI 215R-74 (Revised 1992/Reapproved 1997)]. These failures are usually referred to as low-cycle fatigue and will not be specifically discussed in this report.

The fatigue strength of concrete is defined as a fraction of its static strength that can be maintained under a given number of loading cycles, which is traditionally addressed through the empirical *S–N* curves (fatigue strength vs. fatigue life in a logarithmic scale) or a Goodman model that takes into account the loading ratio ($R = \sigma_{min}/\sigma_{max}$) (Fu et al. 2003; Cornelissen and Reinhardt 1984). To address the scattering issue in concrete fatigue strength, a deterministic model is proposed in Model Code 10 (2010), which is currently considered as the international reference to calculate the fatigue strength of concrete. To further account for the statistical dispersion of compressive strength of concrete, probabilistic models have also been proposed in estimating the fatigue life (Liang et al. 2017; Saucedo et al. 2013). Moreover, it is evident that fatigue loading causes progressive reduction in elastic modulus of concrete due to the internal micro-cracking (Vicente et al. 2014). Consequently, a progressive stiffness loss can be expected when a concrete member is subjected to fatigue. This has many structural consequences that should be considered in the design, such as the progressive increase of deflection, prestress losses, and the progressive reduction of natural frequency (Vicente et al. 2014).

In RC structures, steel reinforcement is prone to fatigue cracking and failure of its own, which can result in failure and collapse of a structure. Fatigue behavior of reinforcing steel is comparable with that of mild steel used in structural applications and is well-studied in the past (ACI 215 1997). However, behavior of RC member subjected to high cycle fatigue cannot be simply predicted from that of plain concrete and reinforcement alone. This is particularly true when the member is subjected to high shear forces or multiaxial loading (Subramaniam et al. 2002; Subramaniam and Shah 2003). Thus, several studies have been conducted in the literature to address the fatigue behavior of RC beams/slabs and some empirical models exist for the fatigue design of steel reinforcement and prestressing strands embedded in concrete (Perdikaris et al. 1993; AASHTO 2017).

Both AASHTO and the CA Amendments state that fatigue need not be investigated for concrete deck slabs. This recommendation is based on the experimental results obtained from the testing of RC slabs that were designed according to the conventional AASHTO moment and the isotropic reinforcement methods (Batchelor et al. 1978).

4.1 Overview

Two major levels of fatigue models are investigated and reviewed in this report, including fatigue models for plain concrete at the material level, and fatigue models for RC bridge deck slab

at the structural level. For plain concrete, the fatigue behavior subjected to cyclic loading is introduced in terms of residual concrete strength, secant modulus, and concrete strain. Important factors on the fatigue performance of plain concrete are discussed, such as normalized stress level and stress ratio, stress reversal, multi-axial stress state, loading frequency, shape of cyclic loading form, and loading history. Fatigue models from available literatures on plain concrete are reviewed and categorized by different theoretical basis, which include deterministic models, probabilistic models, and energy models. In aspect of the fatigue models for RC bridge deck slab, experimental studies under both static and fatigue load cases are firstly introduced to illustrate the failure mechanism of RC deck slab subjected to tire patch load. Different approaches are then described to estimate the static load capacity of RC deck slab, including various punching shear models and yield line theory. Available semi-empirical fatigue life models in the literatures are summarized to provide the most practical references for the fatigue design of RC deck slabs. Additionally, studies on using numerical method to explore the fatigue failure process of RC deck slab are also introduced, even though the modeling strategy to account for the fatigue degradation is complicated. Finally, two potential frameworks are recommended by the authors to adopt the current fatigue models into practical design, namely, the stress-based method and the force-based method. And a case study within the scope of the force-based method is presented as an example to calculate the fatigue life of typical RC bridge deck slabs in CA with the provided design inputs.

4.2 Background

Many cementitious or reinforced concrete (RC) elements of infrastructures are subjected to repeated loadings, such as airport and highway pavement, highway and railway bridges and bridge decks. They will mostly experience a high-cycle fatigue with an approximate range from 1000 to 10 million cycles during their service life (Hsu 1981). Among these RC elements as described above, RC bridge decks were prone to have fatigue failure after decades of service. Although the fatigue failures of other RC elements are rarely observed in the existing structures, the degradation in structural performance under fatigue loading may lead to many serious problems. For example, the development of internal microcracks of concrete elements under fatigue loading can accumulate to macro-cracks, resulting in a loss of stiffness and strength of the concrete elements. The infiltrated moisture and chloride salt through the concrete cracks may cause the reinforcement to corrode and further weaken the performance of the entire structure (Sun et al. 2002). On the other hand, with the increase of live load because of the heavier modern trucks, existing bridges are expected to carry a larger ratio of live load to dead loads. The repeated load amplitude applied to the bridge components (deck, girder and columns, etc.) will become larger and accelerates the deterioration of materials, which may lead to a shortened service life. Thus, it is important to understand the fatigue behavior at both the material level and the structural level for RC elements. The fatigue effects should also be recognized in the design to ensure that the in-service load ranges of the structural component remain at an appropriate level to accommodate the design life.

This research aims at conducting a comprehensive literature review on the fatigue behavior of RC bridge deck, as well as the available models for design considerations. Because the failure process of RC bridge decks subjected to cyclic loads is usually governed by the degradation of concrete material, the factors that affect the fatigue performance of plain concrete are the main focuses of this discussion. Fatigue models of plain concrete are also collected and categorized from the open literatures, which contain different model types based on the average concrete strength, probability of failure, and dissipated energy. To fully understand the failure mechanism of RC bridge deck under fatigue loading, experimental studies are focused to expose the typical

structural behavior of RC deck slabs under static, fixed pulsating, and moving wheel loading cases. The degraded behavior of RC deck slabs and cracking patterns of concrete are discussed in detail based on the test observations. In addition, different theories are reviewed to explore the failure process of RC deck slabs subjected to tire patch loads, along with the semi-empirical models derived from the test data to predict the fatigue life of RC deck slabs. Numerical methods are also presented as a potential alternative to the time- and cost-consuming experimental studies, despite the complicated modeling of materials to consider the degradation under fatigue loading.

4.3 Fatigue of Plain Concrete

Plain concrete element subject to cyclic loads may fail after a number of cycles, which is referred to as the fatigue life N, although the maximum stress that the concrete element has experienced is less than the concrete strength (compressive or tensile). The fatigue life N of concrete is usually interpreted by a logarithmic relation with the maximum applied normalized stress level S_{max}, with the minimum applied normalized stress level S_{min} remains constant. Herein, S_{max} and S_{min} equals to the maximum and minimum stress level during the repeated loading with respect to the static strength of concrete (compressive or tensile), respectively. If S_{max} is in tension, a positive S_{min} represents a tension-tension cyclic loading, and a negative S_{min} represents a tension-compression cyclic loading and vice versa. This relation is usually referred to as the Wöhler curve, also known as the S-N curve.

For example, as shown in **Figure 4.1**, the series of S-N curves represent the fatigue life expectations under different S_{min} in tension. It can be seen that, with the increase of S_{min}, the fatigue life N increases under the same S_{max}. This type of S-N curves predicted by the deterministic models, reflecting the experimental observations, are most common and has been widely adopted by many researchers (Tepfers and KuttiHsu 1979; Hsu 1981; Cornelissen and Reinhardt 1984; Petkovic et al. 1990; Lohaus et al. 2012; Isojeh et al. 2017). It neglects the variations in the static concrete strength and use either the characteristic or the average concrete strength to determine the normalized stress levels (S_{max} and S_{min}).

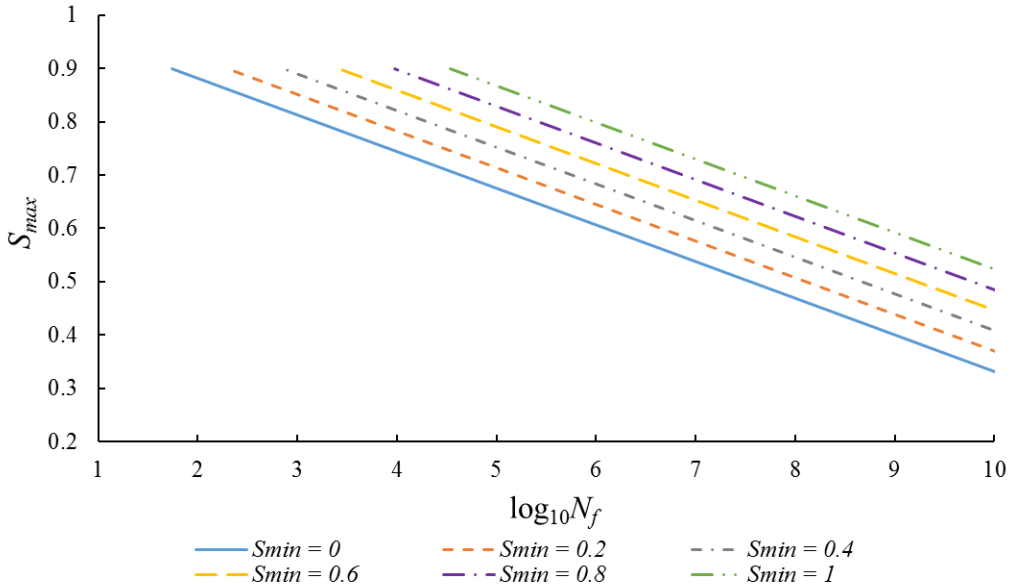

Figure 4.1. Predicted S-N curves for plain concrete in tension (adapted from Cornelissen and Reinhardt 1984)

However, to obtain reliable *S-N* curves for design, a large number of concrete specimens needs to be tested for each stress level, yet significant scatter in *S-N* data is still inevitable due to the variation of concrete strength within the same batch, as well as the stochastic nature of fatigue process (Cornelissen and Reinhardt 1984). This scatter exists in both the static and fatigue strength of concrete and depends on the same parameters, including but not limited to nature and type of the aggregates, concrete mix proportions, water to cement ratio, porosity, curing condition, size of the specimen, loading rate, concrete shrinkage, and creep, etc.

To address the aforementioned scattering issue and to estimate the fatigue life of concrete specimen, the probabilistic concept has been incorporated into the fatigue model by many researchers (McCall 1958; Holmen 1982; Petryna et al. 2002; Saucedo et al. 2013; Liang et al. 2017; Ortega et al. 2018). For example, as shown in **Figure 4.2**, a series of *S-N* curves are presented for different probability of failure (*P*) of concrete, and these are usually called as the *S-N-P* curves. In general, the curve of 50% probability of failure ($P = 0.5$) is adopted to describe the behavior of concrete under fatigue loading.

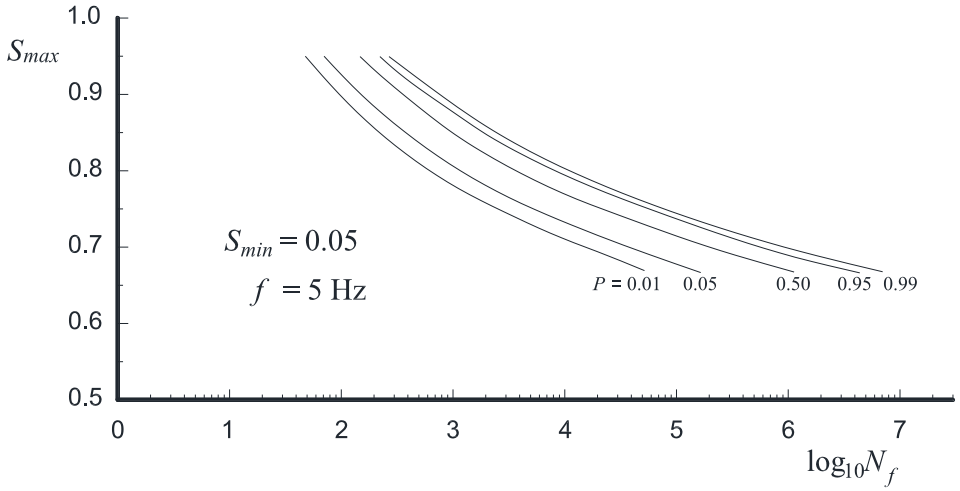

Figure 4.2. Representative *S-N-P* curves based on a linear interpolation for the probability of failure (adapted from Holmen 1982)

4.3.1 Concrete

The development of fatigue in concrete is basically a degenerative process of the material. The energy absorbed by the concrete within each fatigue cycles leads to the diffuse microcracks and it causes the internal damage to accumulate. For concrete material, this energy is referred to as the dissipation energy E_δ within each cycle enclosed by the unloading and reloading path, as shown in **Figure 4.3**. The area between the first loading and the first unloading curve represents the irreversible plastic energy E_{pl} of the concrete. The area under the first unloading curve represents the elastic energy E_{el}. The reloading curve is above the first unloading curve, but with a smaller stiffness than the initial one. The major part of the dissipation energy E_δ is believed to be transformed into thermal energy and the cumulative dissipated energy ΣE_δ is related to the damage process of the concrete (Bode and Marx 2020).

On the other hand, with the development of internal damage of concrete under cyclic loading, the mechanical properties of concrete will vary gradually, including residual concrete strength, secant modulus, and concrete strain.

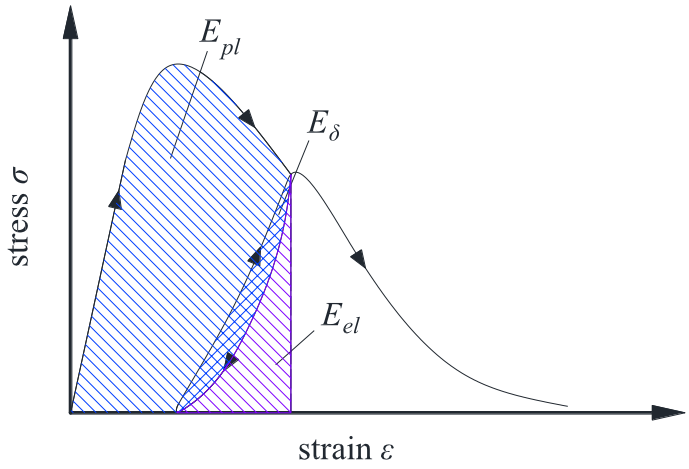

Figure 4.3. Stress-strain behavior of concrete under cyclic loading (adapted from Bode and Marx 2020)

Residual concrete strength

Research aims to investigate the residual concrete strength after a specific number of fatigue cycles is rare. Isojeh et al. (2017) tested a series of concrete cylinders and measured their residual compressive strength before the fatigue failure. It was found that the residual compressive strength of concrete slightly increased at early fatigue cycles, but with a further increase of cycles, an obvious degradation in compressive strength was observed. A similar observation was also noticed in the test of Taliercio and Gobbi (1996) where the residual strength of the specimens survived the target fatigue cycles under uniaxial load reached a larger strength than their static counterparts on average. But those specimens with extra lateral confinement presented a lower post-fatigue compressive strength than their static counterparts. The early increase of the post-fatigue compressive strength maybe due to the further curing of concrete and scatter of concrete material. However, it is generally believed that the fatigue cycles will have a detrimental effect on the residual concrete strength because of the accumulated internal damage (Petryna et al. 2002).

Secant modulus

For concrete specimens tested under fatigue cycles and reached fatigue failure, a common three-stage behavior was observed for the secant modulus of concrete. In **Figure 4.4**, the secant modulus of concrete started to decrease rapidly not long after the fatigue cycles started, and this stage is referred to as the first stage. The decrease rate of the secant modulus then slowed down and reached a relative stable magnitude, this second stage usually accounted for over 70% of the fatigue life N_f of the concrete specimen. When the concrete specimen was close to its fatigue life, the decrease rate of the secant modulus speeded up again until fatigue failure. This three-stage behavior was noticed not only in the compressive concrete fatigue test (Holmen 1982; Petkovic et al. 1990; Gao and Hsu 1998), but also in the flexural and torsional fatigue tests of plain concrete as well (Subramaniam et al. 2000; Subramaniam et al. 2002). In addition, the decrease rate of secant modulus is highly relevant to the maximum stress level applied to the specimen, as presented in **Figure 4.4**. Taliercio and Gobbi (1996) also found out that for specimens under triaxial fatigue load conditions, the greater internal damage caused by a higher stress triaxiality ratio resulted in a more significant drop in the secant modulus.

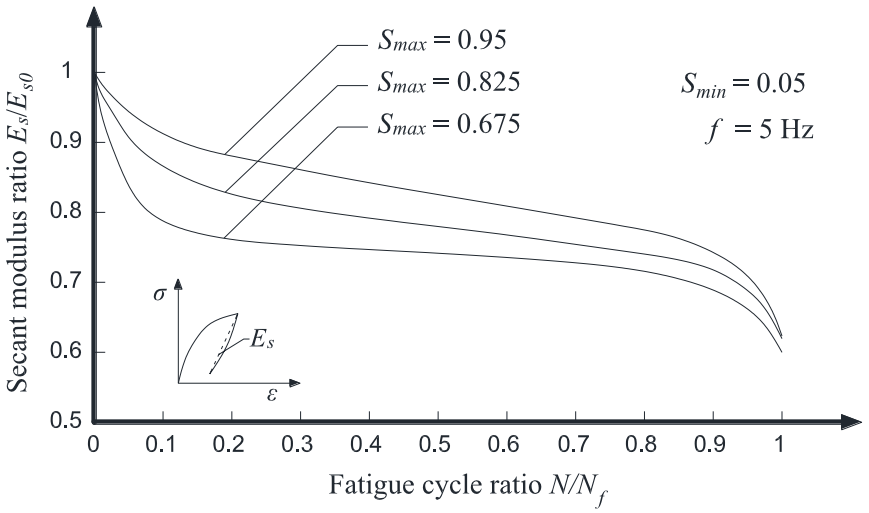

Figure 4.4. Representative change in secant modulus of plain concrete during fatigue cycles (adapted from Holmen 1982)

Concrete strain

Likewise, the permanent strain of concrete performed in a three-stage development during the fatigue cycles, as shown in **Figure 4.5**, but its magnitude always increased as compared to the decreasing trend of secant modulus as presented in **Figure 4.4**. At the first stage (typically within 10-20%N_f), the concrete strain had a nonlinear increase at a decreasing rate due to the closing up of concrete pores and microcracks between aggregates and cement mortar. It was followed by a stable increase with a constant rate in the second stage, while the microcracks within the cement mortar increased. Researchers reported that the duration of the second stage usually stayed within 70-90%N_f (Holmen 1982; Cornelissen and Reinhardt 1984; Taliercio and Gobbi 1996; Isojeh et al. 2017), beyond which the strain increased rapidly again in the third stage until fatigue failure.

Because of the relative stable strain rate within the second stage, some researchers believed it is more reliable to predict the fatigue life of plain concrete by using the "secondary strain rate ε_{sec} (or secondary creep rate)", as illustrated in **Figure 4.5**. As a result, a general equation was proposed by Sparks and Menzies (1973) to estimate the fatigue life N_f as below:

$$N_f = a(\varepsilon_{sec})^{-b} \tag{4.1}$$

where a, b= coefficients calibrated from the test data.

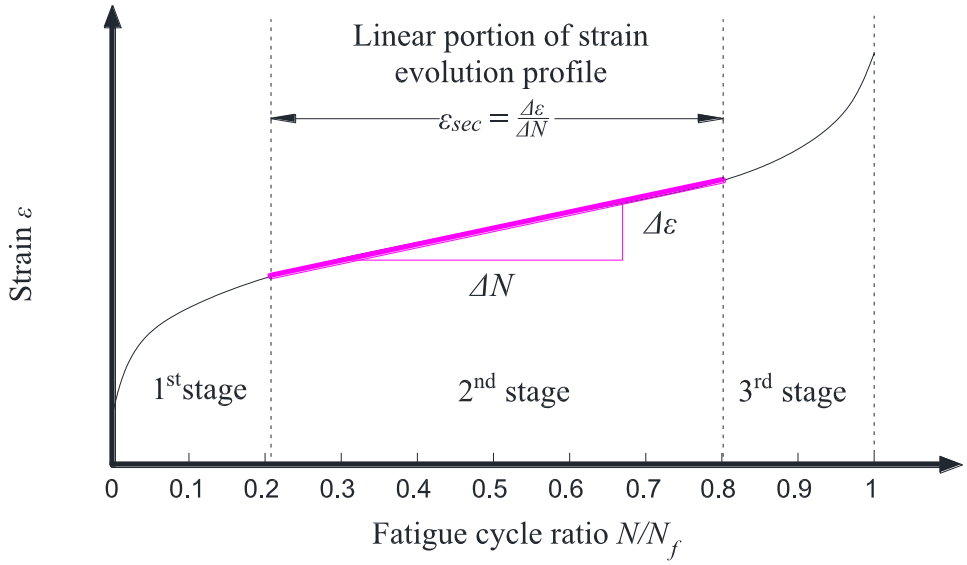

Figure 4.5. Concrete strain development during the fatigue cycles (adapted from Isojeh et al. 2017)

4.3.2 Important parameters of concrete fatigue

Due to the lack of standard test configuration for the plain concrete under fatigue loading, the reported fatigue tests of concrete in the literatures used different test setups, size, and geometry of the concrete specimens. To minimize the influence caused by these testing details, the normalized fatigue parameters are usually preferred in the fatigue models to accommodate the test data from different experiments. In short, the fatigue life of concrete primarily depends on the key parameters as below, which will be discussed in the subsections:

- Normalized stress level and stress ratio (or amplitude)
- Stress reversal
- Multi-axial stress state
- Loading frequency
- Shape of cyclic loading form loading history

Normalized stress level and stress ratio

From test observations in the open literatures, the normalized stress level, both the maximum normalized stress level S_{max}, and the minimum normalized stress level S_{min} play the most important role in the fatigue life of concrete. Test results from Cornelissen and Reinhardt (1984) indicated that for tested concrete specimens under repeated loading, at a given S_{max}, reducing S_{min} resulted in shorter lives of concrete specimens. In other words, a larger stress amplitude, i.e., (S_{max} - S_{min}), means a shorter fatigue life. On the other hand, Aas-Jakobsen (1970) reported that the relationship between S_{max} and S_{min} is linear for concrete specimens failed at 2 million fatigue cycles. And hence, he proposed the famous Aas-Jakobsen's formula to incorporate the stress ratio R, which equals to S_{min}/S_{max}, into the Wöhler curve and yielded the following fatigue model as:

$$S_{max} = 1 - \beta(1 - R)log_{10}N_f \tag{4.2}$$

where β = material parameter (0.0685 per Aas-Jakobsen 1970). This model has been widely adopted by researchers to examine the fatigue life of concrete and a typical illustration of this model is shown in **Figure 4.6**. This model was also further extended by other studies to take more factors into consideration (Hsu 1981; Zhang et al. 1996; Isojeh et al. 2017).

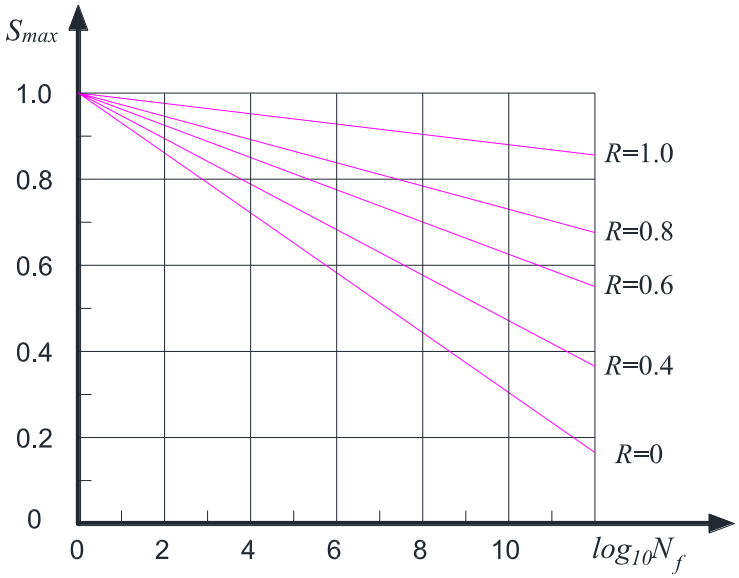

Figure 4.6. Wöhler curves for different values of R (adapted from Tepfers and Kutti 1979)

However, it should be noted that for a very large R number, e.g., $R = 1$, Eq. (4.2) yields a result of $S_{max} = 1$. It basically means that the concrete is under the sustained loading condition instead of the fatigue loading. Tests conducted by Rüsch (1960) indicated that the sustained strength of concrete is time dependent, and the long-term strength may drop down to 75-80% of the short-term static strength due to concrete creep. Therefore, it is generally believed that for $R > 0.75$, the concrete specimen is approaching the sustained loading state and this sustained loading effect should be considered for fatigue models (Tepfers et al. 1973; Hsu 1981; Zhang et al. 1996; Zhang et al. 1998).

Stress reversal

Few experimental studies were reported on the stress reversal effect on the fatigue performance of plain concrete. Cornelissen and Reinhardt (1984) tested a series of plain concrete specimens under both tensile and tensile-compressive fatigue loading. Test results indicated that at a given maximum tensile stress level, when the minimum stress was reversed from tensile to compressive, a considerable reduction of fatigue life was observed. This detrimental effect of stress reversal from tension-tension to tension-compression was also confirmed by Reinhardt and Cornelissen (1984). A modified Goodman diagram is presented herein to visualize the effect due to the stress reversal (Cornelissen and Reinhardt 1984). In **Figure 4.7**, each curve represents the relationship between the maximum and minimum stress level when the specimen can reach a fatigue life of the designated number, e.g., $\log N_f = 3$. The vertical axis indicates the normalized maximum tensile stress level, while the horizontal axis indicates the normalized minimum stress level either in tension or compression. It should be noted that for the tension-tension condition the normalized minimum stress level is based on the tensile strength of concrete, while it is based on the compressive strength of concrete for the tension-compression condition. Apparently in this plot,

the stress reversal will lead to a shorter fatigue life of specimens. To reach the same fatigue life, e.g., $\log N_f = 5$, it is necessary to remain a much lower maximum tensile stress for the tension-compression condition. Although the negative effect caused by the stress reversal on the fatigue life of plain concrete was also confirmed by both Tepfers (1982) and Zhang et al. (1996), they believed that the influence of stress reversal is small.

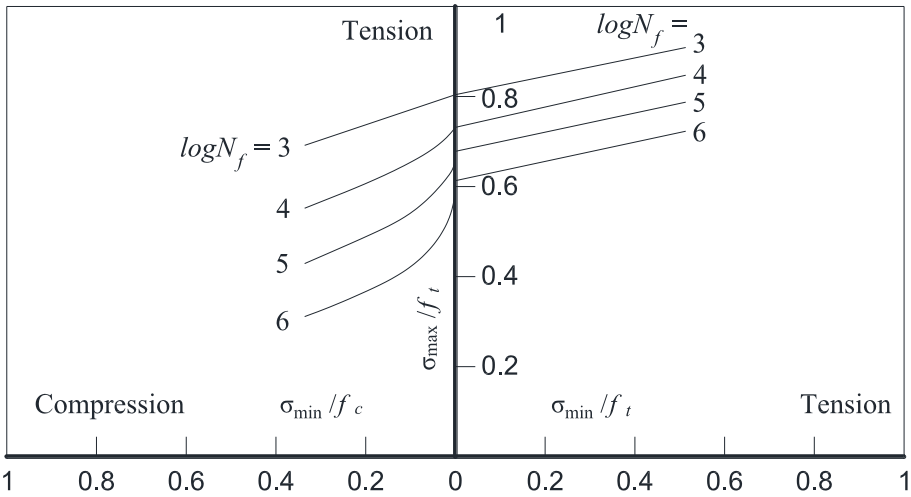

Figure 4.7. Modified Goodman diagram of concrete under stress reversal (adapted from Cornelissen and Reinhardt 1984)

Multi-axial stress state

Limited studies were conducted aiming to investigate the influence of multi-axial stress state on the fatigue behaviors of plain concrete. Although the experimental study conducted by Buyukozturk and Tseng (1984) did not focus on the fatigue life of concrete under biaxial stress state, test results indicated that the lateral confinement contributed to the stiffness of the specimen in the inelastic range during cyclic loading. Su and Hsu (1988) reported that the biaxial compression state detained the internal microcracks of concrete, and hence it prolonged the fatigue life compared to the uniaxial compression state. As shown in **Figure 4.8**, a series of biaxial fatigue strength envelops are plotted covering the fatigue life from one cycle to 10 million cycles with a constant stress ratio $R = 0.05$. Each envelop represents the relationship between the two orthogonally applied normalized stress level, i.e., σ_2/f_c' and σ_3/f_c', at the designated fatigue life of the concrete specimen. It was concluded that a maximum increase of fatigue strength could be achieved at the confining stress ratio σ_2/σ_3 equals to either 0.2 or 0.5 for a target fatigue life of two million cycles. On the other hand, Taliercio and Gobbi (1996) tested a series of concrete specimens under triaxial compressive stress state. Again, test results confirmed that the lateral confinement increased the fatigue life of concrete specimen, but it also caused more internal damage of concrete material and led to a more rapid decrease in the residual modulus.

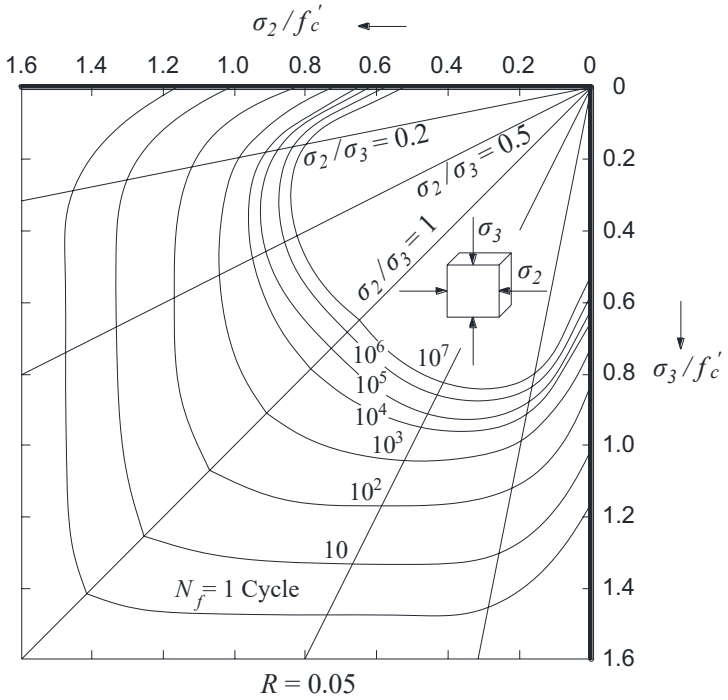

Figure 4.8. Fatigue strength envelope of concrete under biaxial compressive stress state (adapted from Su and Hsu 1988)

Loading frequency

The loading frequency, or the rate of loading during fatigue cycles, is believed to have little effect on the fatigue strength of concrete within the range of approximately 1-15 Hz, provided that the normalized maximum stress level S_{max} is less than 75% [ACI 215R-74 (Revised 1992/Reapproved 1997)]. But for concrete specimens with $S_{max} > 0.75$, the effect due to the loading frequency becomes more significant because of the concrete creep (Sparks and Menzies 1973; Tepfers and Kutti 1979, Zhang et al. 1996). Under a higher stress level, decreasing the rate of loading equals to changing the concrete stress state from the fatigue loading to the sustained loading, hence the long-term effect is non-negligible as described before. In addition, the tests conducted by Ode and Marx (2020) also indicated that more damage was accumulated within each fatigue cycle for concrete specimens under a lower frequency in the aspect of energy dissipation. Furthermore, Zhang et al. (1996) proposed an equation to measure the actual concrete strength f_{cf}' at the applied loading frequency f, and the equation is presented as follows:

$$f_{cf}' = C_f f_c' = (ab^{-logf} + c) f_c' \tag{4.3}$$

where a, b = material parameters = 0.249, 0.920, respectively; and c = coefficient of long-term concrete strength = 0.796. This equation indicates that the long-term concrete strength is approximately 80% of the static strength when the loading frequency approaches zero. Likewise, Hsu (1981) incorporated the time effect and the effect of loading rate into the Aas-Jakobsen's formula to estimate the fatigue life of concrete, and this model will be introduced in detail later in this review study.

Shape of cyclic loading form

As aforementioned, the sustained loading effect will influence the fatigue life of plain concrete because of the creep. In this sense, Zhang et al. (1998) tested a few concrete beam specimens to investigate the relation between the sustained load level and the sustained time to failure. The proposed model was similar to the model firstly introduced by Hsu (1981); however, it also took the shape of cyclic loading forms (square, triangular, trapezoidal and sinusoidal) into consideration by virtue of an equivalent damage assumption (Zhang et al. 1998). A transformation coefficient ω was hence introduced to convert the cyclic period t_0 into an equivalent time t_{max} under the maximum applied fatigue load level S_{max}. In **Figure 4.9**, the shape of the cyclic loading form depends on the shape factor λ, which varies within the range between 0 and 1. **Figure 4.10** provides the values of ω corresponding to different shape factors λ and special stress ratios R', where R' can be represented by the following equations to account for the effect due to stress reversals as well:

$$R' = R = \frac{S_{min}}{S_{max}} \quad for\ R \geq 0$$
$$R' = \left|\frac{f_r}{f_c'}\right| R \qquad for\ R < 0 \tag{4.4}$$

where f_r = modulus of rupture of concrete; and f_c' = concrete compressive strength.

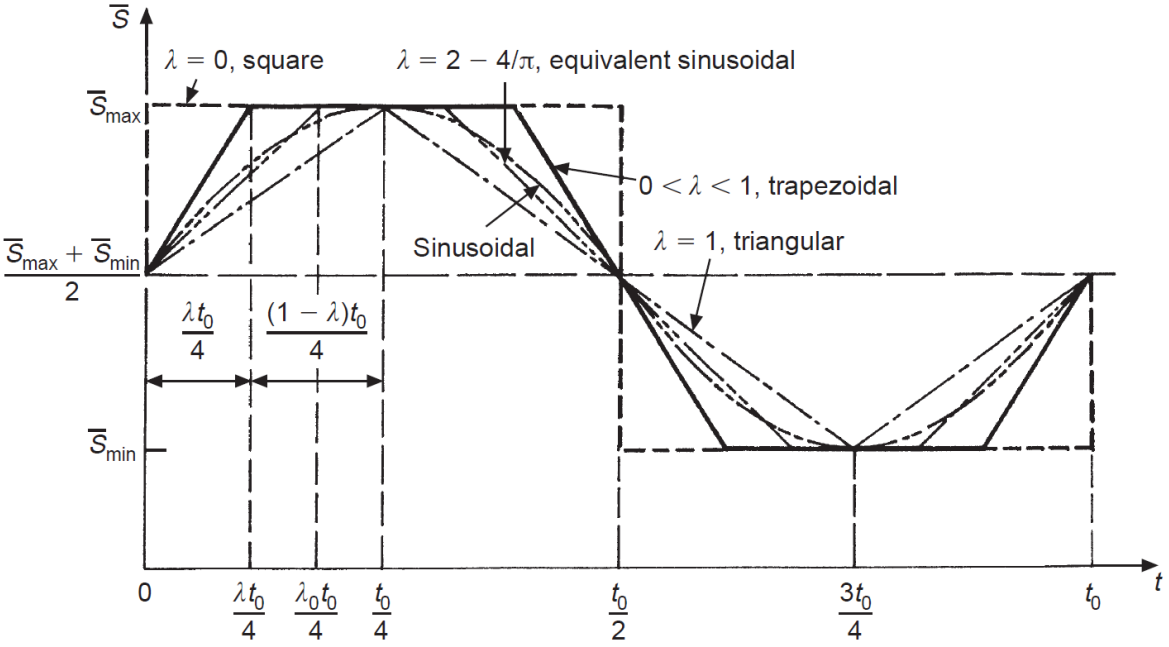

Figure 4.9. Full trapezoidal loading cycles for different λ (Zhang et al. 1998)

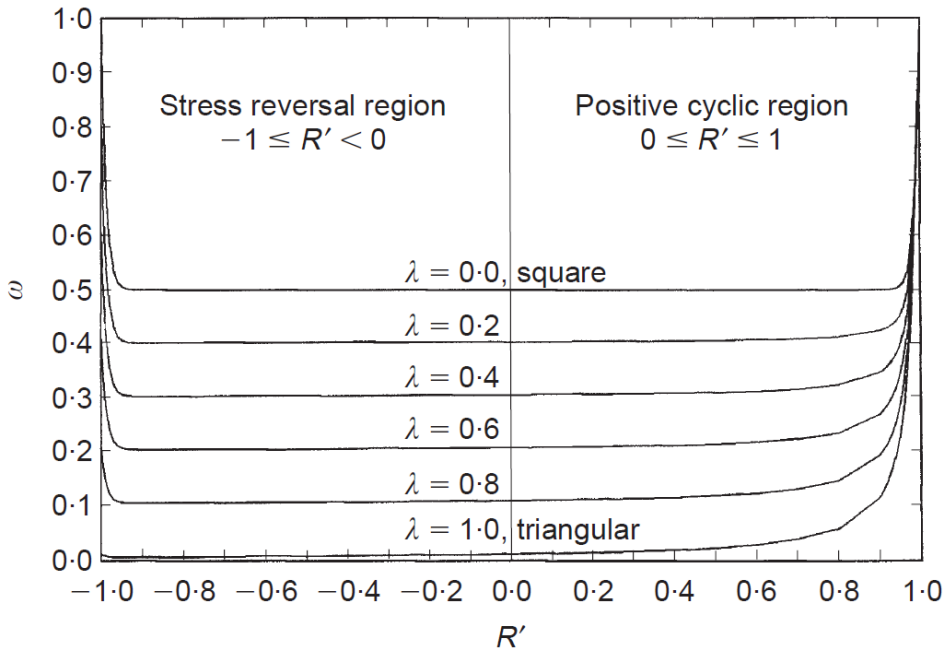

Figure 4.10. Family of ω - R' curves for different λ (Zhang et al. 1998)

Loading history

Most experimental studies reported in the literatures adopted constant fatigue stress amplitudes (range) to test the concrete specimens up to failure. However, this laboratory fatigue loading condition is ideal and against the nature of randomly varying loads applied to the concrete structures in the real world. To approximate more representative fatigue loading conditions, a few tests were carried out to investigate the influence of variable stress amplitudes on the fatigue life of concrete specimens (Hilsdorf and Kesler 1966; Holmen 1982; Cornelissen and Reinhardt 1984; Petkovic et al. 1990). Meanwhile, the Palmgren-Miner (PM) rule (Palmgren 1924; Miner 1945) was often taken as the failure criterion for specimens under a combination of different fatigue stress levels: The PM rule assumes that the damage D of concrete accumulates linearly with the increase of fatigue cycles under constant maximum and minimum stress levels, and it reaches unity when the fatigue failure occurs. In the case of varying stress amplitude conditions, the equivalent damage can be calculated by:

$$D = \sum_{i=1}^{k} \frac{N_i}{N_{fi}} = 1.0 \tag{4.5}$$

where $i = i^{th}$ stress amplitude condition; k = total number of different stress amplitude conditions; N_i = number of fatigue cycles under the i^{th} stress amplitude condition; N_{fi} = number of fatigue cycles to failure under the i^{th} stress amplitude condition. It assumes that the damage caused by each stress amplitude condition can be added linearly to the equivalent damage and it neglects the sequential effect of different stress amplitude conditions. Although this PM rule was widely adopted in many studies, the fatigue life of concrete specimen predicted by the PM rule can be either unsafe (e.g., $D < 1$) or too conservative (e.g., $D > 1$) at specimen failure in different test programs (Hilsdorf and Kesler 1966; Holmen 1982; Cornelissen and Reinhardt 1984). As a result, the concept of non-linear accumulation of damage extended from the PM law was also proposed by some researchers (Torrenti et al. 2013) to account for the sequence of various fatigue stress amplitudes.

4.3.3 Fatigue life models of concrete

The scatter of fatigue life of concrete specimens is significant and unpredictable according to the existing experimental data. For identical concrete specimens in the same batch, the scatter in concrete fatigue life can reach as much as two orders of magnitude or even higher (Ortega et al. 2018). To minimize the variations caused by this scatter of material properties, fatigue models of concrete are usually proposed and calibrated from a large number of test specimens. As aforementioned in the overview, the deterministic model has been mostly adopted to predict the fatigue life of concrete, based on the average concrete fatigue strength. On the other hand, probabilistic models also draw the attention of researchers to take the dispersion of concrete properties into consideration by means of the probability of failure (Holmen 1982; Petryna et al. 2002; Saucedo et al. 2013; Liang et al. 2017; Ortega et al. 2018). Moreover, other alternative approaches have also been investigated, such as the energy-based method (Tepfers et al. 1984; Lei et al. 2017; Song et al. 2018; Bode and Marx 2021) or concrete strain-based method (Sparks and Menzies 1973; Isojeh et al. 2017). Limited by the scope of this project, not all the available fatigue models of concrete in the literatures will be discussed in this review, only those representative models are introduced in the following subsections as key references.

Deterministic model

Most deterministic models widely adopted are based on the Aas-Jakobsen's formula (1970) and use the stress ratio R as the most important variable, as described in Chapter 4.3.2. Extensions or revisions of this formula are proposed by either recalibrating the model coefficients from a larger database or incorporating more parameters (Hsu 1981; Isojeh et al. 2017). Nevertheless, other forms of deterministic models were also proposed by considering the influence due to S_{max} and S_{min} on the fatigue life of concrete, respectively (Cornelissen and Reinhardt 1984; Model of Petkovic et al. 1990; Lohaus et al. 2012). Representative deterministic models of concrete fatigue life are introduced as below:

(1) *Model of Hsu (1981)*

Hsu (1981) extended the Aas-Jakobsen's formula (1970) to include the effect due to the rate of loading, or equivalently the time effect. He also investigated the differences for both low-cycle and high-cycle fatigue loading cases, as well as the boundary between these two cases. The proposed fatigue models are presented in the following:

(a) For low-cycle fatigue ($N = 1 – 10^3$):

$$S_{max} = 1.2 - 0.2R - 0.133(1 - 0.779R)logN_f - 0.053(1 - 0.445R)logt \quad (4.6)$$

(b) For high-cycle fatigue ($N = 10^3 – 10^7$):

$$S_{max} = 1 - 0.0662(1 - 0.556R)logN_f - 0.294logt \quad (4.7)$$

where t = period of one load cycle (sec).

(2) *Model of Isojeh et al. (2017)*

Isojeh et al. 2017 proposed a damage evolution model by combining the models of Hsu (1981), Gao and Hsu (1998) and Zhang et al. (1998) to take parameters including loading frequency, shape of cyclic loading form, stress ratio into consideration. It can also estimate the concrete residual strength and fatigue secant modulus by means of the damage concept assuming the critical damage

value D_{cr} = 0.4 for the secant modulus, and D_{cr} = 0.35 for the residual strength. This damage evolution model can be presented as follows:

$$D = D_{cr} exp[s(S_{max} - u)]N^{v} \tag{4.8}$$

$$u = C_f \left(1 - \gamma_2 log\left(\zeta N_f t\right)\right) \tag{4.9}$$

$$v = 0.434 C_f \left(\beta_2 (1 - R)\right) \tag{4.10}$$

where s = damage parameter (only valid for $0 \leq R \leq 0.5$, more details per Isojeh et al. 2017); t = period of one load cycle (sec); $\gamma_2 = 2.47 \times 10^{-2}$; ζ = transformation coefficient converting the cyclic period t into an equivalent time $T = 0.15$ for sinusoidal cycle (Zhang et al. 1998); C_f is referred to Eq. (4.3). It should be noted that the fatigue failure occurs when $D = D_{cr}$.

(3) *FIB Model Code 2010 (FIB 2010)*

The FIB model code 2010 prescribes the fatigue strength of concrete by the category of pure compression, compression tension and pure tension, respectively. This model is valid for concrete material with a normal strength, or high strength or even ultra-high strength (up to C200). The effects due to the age of concrete, temperature, type of concrete and sustained loading have also been considered.

(a) Pure compression (Lohaus et al. 2012):

For $S_{c,min} > 0.8$, the S-N relations for $S_{c,min} = 0.8$ are valid. For $0 \leq S_{c,min} \leq 0.8$, we can use:

$$logN_1 = \frac{8}{(Y-1)}\left(S_{c,max} - 1\right) \tag{4.11}$$

$$logN_2 = 8 + \frac{8ln(10)}{(Y-1)}\left(Y - S_{c,min}\right) log\left(\frac{S_{c,max} - S_{c,min}}{Y - S_{c,min}}\right) \tag{4.12}$$

with:

$$Y = \frac{0.45 + 1.8 S_{c,min}}{1 + 1.8 S_{c,min} - 0.3 S_{c,min}^2} \tag{4.13}$$

where:

$$\text{if } logN \leq 8, \text{ then } logN = logN_1 \tag{4.14a}$$

$$\text{if } logN > 8, \text{ then } logN = logN_2 \tag{4.14b}$$

with:

$$S_{c,max} = \frac{\left|\sigma_{c,max}\right|}{f_{ck,fat}}$$

$$S_{c,min} = \frac{\left|\sigma_{c,min}\right|}{f_{ck,fat}}$$

$$\Delta S_c = \left|S_{c,max}\right| - \left|S_{c,min}\right|$$

where $S_{c,max}$ = maximum compressive stress level (MPa); $S_{c,min}$ = minimum compressive stress level (MPa); $\sigma_{c,max}$ = maximum compressive stress (MPa); $\sigma_{c,min}$ = minimum compressive stress (MPa); and $f_{ck,fat}$ = fatigue reference compressive strength and may be estimated as:

$$f_{ck,fat} = \beta_{cc}(t)\beta_{c,sus}(t, t_0) f_{ck}(1 - f_{ck}/400) \tag{4.15}$$

in which $\beta_{cc}(t)$ = age coefficient of concrete at the beginning of fatigue loading as:

$$\beta_{cc}(t) = esp\left\{s\left[1 - \left(\frac{28}{t_T}\right)^{0.5}\right]\right\} \tag{4.16}$$

where s = coefficient which depends on the strength class of cement in **Table 4.1**; t_T = temperature-adjusted concrete age in days and could be determined by:

$$t_T = \sum_{i=1}^{n} \Delta t_i exp\left[13.65 - \frac{4000}{273+T(\Delta t_i)}\right] \quad (4.17)$$

where Δt_i = number of days where at a temperature T prevails; $T(\Delta t_i)$ = mean temperature in °C during the time period Δt_i.

Table 4.1. Coefficient s for different types of cement

f_{cm} (MPa)[a]	Strength Class of Cement	s
≤ 60	32.5 N	0.38
	32.5 R, 42.5 N	0.25
	42.5 R, 52.5 N, 52.5 R	0.20
> 60	All classes	0.20

[a]f_{cm} = mean compressive strength in MPa at an age of 28 days.

In addition, $\beta_{c,sus}(t,t_0)$ = coefficient which takes into account the effect of high mean stresses during loading and may be taken as 0.85 for fatigue loading; and f_{ck} = characteristic compressive strength refers to 5% quantile of static strength (**Table 4.2**).

Table 4.2. Characteristic strength f_{ck} of normal weigh concrete (MPa)

Concrete Grade	C12	C16	C20	C25	C30	C35	C40	C45	C50
f_{ck}	12	16	20	25	30	35	40	45	50
$f_{ck,cube}$	15	20	25	30	37	45	50	55	60
Concrete Grade	C55	C60	C70	C80	C90	C100	C110	C120	-
f_{ck}	55	60	70	80	90	100	110	120	-
$f_{ck,cube}$[a]	67	75	85	95	105	115	130	140	-

[a]Characteristic value of cube compressive strength of concrete.

(b) Compression-tension with $\sigma_{ct,max} \leq 0.026|\sigma_{c,max}|$:

$$logN = 9(1 - S_{c,max}) \quad (4.18)$$

(c) Pure tension and tension-compression with $\sigma_{ct,max} > 0.026|\sigma_{c,max}|$:

$$logN = 12(1 - S_{ct,max}) \quad (4.19)$$

with:

$$S_{ct,max} = \sigma_{ct,max}/f_{ctk,min}$$

where $S_{ct,max}$ = maximum tensile stress level; $\sigma_{ct,max}$ = maximum tensile stress (MPa); and $f_{ctk,min}$ = minimum characteristic tensile strength (MPa).

Probabilistic model

Because of the scatter in the concrete static strength and the stochastic nature of fatigue procedure, larger deviations are usually observed between the model predictions and test results by using the deterministic approaches. In the recent years, probabilistic approach of concrete fatigue failure has been developed and become a promising alternative to the deterministic model by some researchers (Petryna et al. 2002; Model of Saucedo et al. 2013; Liang et al. 2017; Ortega et al. 2018). Some representative studies are summarized as below:

(1) *Model of Ortega et al. (2018)*

Ortega et al. (2018) conducted a series of fatigue tests on the self-compacting steel fiber-reinforced concrete specimens, and a two-parameter Weibull distribution was selected to describe the cumulative probability of concrete failure under compressive cyclic load as:

$$F(x) = 1 - exp\{-(x/\eta)^{\beta}\} \tag{4.20}$$

where $x = logN$; η = scale factor (3.72 calibrated from the test data) and β = shape factor (4.56 calibrated from the test data). The scale factor η also approximately represents the order of magnitude (10^{η}) of the fatigue lifetime of concrete specimens. This research also proposed a methodology to establish the minimum number of tests needed to limit the possible error below an admissible value, and it helped determine the design fatigue curve for a given safety level.

(2) *Model of Saucedo et al. (2013)*

Saucedo et al. (2013) proposed a probabilistic fatigue model, based on a three-parameter Weibull cumulative distribution function, to describe the probability of failure (PF) and quantify the dispersion of concrete static strength as follows:

$$PF(\sigma_{f0}) = 1 - \exp\left[-\left(\frac{\sigma_{f_0} - \sigma_{min_0}}{\lambda}\right)^{k}\right] \qquad \sigma_{f_0} \geq \sigma_{min_0} \tag{4.21}$$

where σ_{f0} = intercept of the iso-probability failure curve with the σ_f axis; σ_{min0} = minimum stress below which no failure will occur; λ = scale parameter; and k = shape parameter. For the fatigue life N of concrete specimens, the influence of loading frequency f was also considered, along with the maximum stress σ_{max} and stress ratio R as follows:

$$PF(N; \sigma_{max}, f, R) = 1 - \exp\left\{-\left[\frac{\sigma_{max}\left(\frac{\dot{\sigma_0}}{2f\Delta\sigma}\right)^{\alpha} - \sigma_{min_0}}{\lambda N^{-[b+cln(1+f)](1-R)}}\right]^{k}\right\} \tag{4.22}$$

$\dot{\sigma_0}$ = loading rate of the compressive characterization test; $\Delta\sigma$ = stress range; $\alpha = 0.014$; b and c = coefficients relevant to the loading frequency calibrated from the test data. This model can also be reformed to obtain the fatigue life in terms of the secondary strain rate $\dot{\varepsilon}$ as:

$$PF(\dot{\varepsilon}; \sigma_{max}, f, R) = 1 - \exp\left\{-\left[\frac{\sigma_{max}\left(\frac{\dot{\sigma_0}}{2f\Delta\sigma}\right)^{\alpha} - \sigma_{min_0}}{\lambda N(\dot{\varepsilon})}\right]^{k}\right\} \tag{2.23}$$

Energy model

Lei et al. (2017) proposed an energy-based fatigue model and it assumed that the dissipated energy within each cycle is based on the stress level of concrete as:

$$W_d = \alpha exp(\beta S) \tag{4.24}$$

where α = transient response coefficient of cyclic hysteretic energy (1.899×10^{-11} calibrated from the test data); β = transient response exponent of cyclic hysteretic energy of the test (28.489 calibrated from the test data); and S = stress level of concrete (MPa). This study also believed that the critical energy dissipation W_{dc}, or the accumulated energy dissipation at concrete failure, is a mechanical property of the concrete and independent of the stress level S. It can be estimated as a constant 737kJ/m^3 from the tests conducted by Tepfers et al (1984). Hence, assuming a constant energy dissipation rate during the fatigue cycles, the fatigue life can be calculated by

$$N_f = W_{dc}/W_d \tag{4.25}$$

However, test results from Bode and Marx (2020) indicated that the accumulative energy dissipation of specimen at failure is proportional to the number of fatigue cycles, and a huge

difference existed in the accumulative energy dissipation for specimens under different stress level. This conclusion contradicted with the assumptions adopted by Lei et al. (2017).

4.4 Fatigue of Reinforced Concrete Bridge Decks

The fatigue degradation of RC bridge decks is a complex hybrid process composed of concrete crack and deterioration, degradation of the bond between concrete and steel reinforcements, redistribution of internal stress, and degradation of steel reinforcements, etc. Although AASHTO (2017) does not require the fatigue design of RC deck slabs supported on multi-girders, the fatigue failure of the RC deck slabs is possible and has been confirmed in previous experiments. In addition, the fatigue life of RC deck slabs can be significantly decreased when subjected to moving wheel load, compared to the fixed pulsating load (Sonoda and Horikawa 1982; Perdikaris and Beim 1988).

On the other hand, the most common fatigue failure pattern of RC deck slabs is the punching shear failure, with significant concrete cracks developed at the bottom of the slab, along with the elliptical cracks on the top of the slab closer to the supports (Sonoda and Horikawa 1982). The only exception was reported by Schläfli and Brühwiler (1998) where the fatigue failure due to the fracture of steel rebars was observed for specimens under a high peak fatigue load. However, the tested specimens are slab-like beams with an aspect ratio equals to eight, not representative of the bridge deck slabs. And the load was applied primarily through a four-point bending setup (with no tire footprint), with the beam simply supported at the far ends. This test will not be included in this review because it significantly deviates from the typical test setup of RC bridge deck slabs subjected to patch loads. As a result, the fracture failure of reinforcements, as well the fatigue behavior of reinforcements on the material level (i.e., steel and FRP) will not be discussed herein. Nevertheless, the allowable constant-amplitude fatigue thresholds for different reinforcements are specified in Article 5.5.3 of AASHTO (2017) for other structural components of bridges.

4.4.1 Experimental study

Due to cost and restrictions of laboratory conditions, limited number of experimental efforts have been made to investigate the fatigue behavior of RC bridge decks under the vehicle load. Although some relevant projects have been conducted by either the department of transportations in different countries or the research teams at universities, full-scale field fatigue tests on the RC bridge decks are rare. Nevertheless, it is still important to understand the fatigue behavior of RC bridge decks from the reduced-scale specimens under pulsating load. Hence, some of the most representative experimental studies are reviewed and summarized in this section to disclose the fatigue characteristics of RC bridge decks under fatigue loading.

Deck specimens

The dimension of the concrete bridge deck specimens varies significantly for different testing purposes and highly depends on the scale factor of the experiment. For consistency, the dimensions of tested specimens have been converted to their original design dimensions according to the reported scale factor, e.g., 1/3 for the tests of Sonoda and Horikawa (1982), and Youn and Chang (1998), 1/6.6 for the test of Perdikaris and Beim (1988). The equivalent range of dimensions of the bridge decks are summarized in **Table 4.3**, along with other important details of the tested specimens (Okada et al. 1978; Sonoda and Horikawa 1982; Perdikaris and Beim 1988;

Csagoly and Lybas 1989; Youn and Chang 1998; Graddy et al. 2002; El-Ragaby et al. 2007; Yoshitake et al. 2010; Cuelho and Stephens 2013; Tauskela 2020). It is important to notice that the different steel reinforcement ratios of the concrete bridge deck specimens may result in different failure mechanisms of the bridge deck. In general, concrete bridge decks require sufficient transverse reinforcements as tension-tie bars to develop the so-called arching action that greatly improves the load carry capacity estimated by the flexural theory (Graddy et al. 2002).

Table 4.3. Details of bridge deck specimens under fatigue loading based on the literature

Length (ft)	2.3 – 50	Width (girder spacing) (ft)	5.9 – 12.8
Thickness (in)	6.5 – 8.5	Concrete strength (psi)	3626 – 6685
Top longitudinal reinforcement ratio (%)	0.17 – 0.7	Top transverse reinforcement ratio (%)	0.2 – 0.7
Bottom longitudinal reinforcement ratio (%)	0.3 – 1.32	Bottom transverse reinforcement ratio (%)	0.23 – 1.96

Note: this table is based on 65 tested specimens, including 17 static, 32 fatigue pulsating and 16 moving fatigue specimens.

Test setup

The test setup of RC bridge decks under fixed pulsating load is usually the same as that of the specimens aim to obtain the static load capacity under a concentrated load. In general, the RC bridge deck specimen is casted on steel girders by means of the shear studs to reach a full composite action, as presented in **Figure 4.11**. Diaphragms are placed at the ends of the bridge deck to provide support at the short edges. Interior diaphragms are also necessary for specimens with a long span to width ratio to enhance the lateral restriction of the deck. The patch load is applied by means of the hydraulic actuator connected to the reaction frame, as shown in **Figure 4.12**. Neoprene or steel loading plates with a size close to the truck tire footprint is placed in between the actuator head and the top surface of the deck specimen to simulate the tire contact area in the field. During the fatigue loading process, a sinusoidal pulsating load is usually applied to the center of the tested bridge deck specimen with a frequency mostly ranges within 1–5 Hz as reported in the literatures. Although a multiple-span (more than two steel girders) specimen in transverse direction is more representative of the real bridges, most experiments only focused on the behavior of a single span bridge deck for simplicity (Okada et al. 1978; Sonoda and Horikawa 1982; Youn and Chang 1998; Bakht and Lam 2000; Graddy et al. 2002; El-Ragaby et al. 2007).

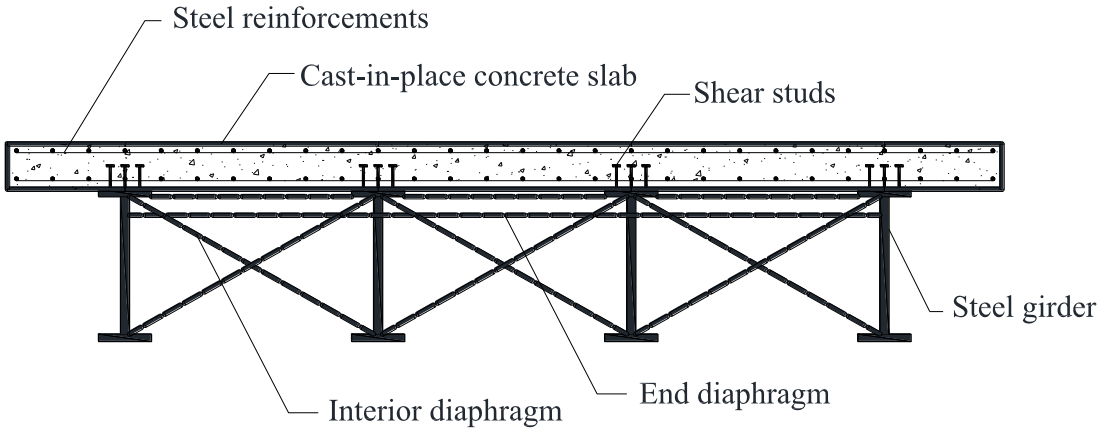

Figure 4.11. Typical cross-section of RC bridge deck specimen (adapted from Fang et al. 1990)

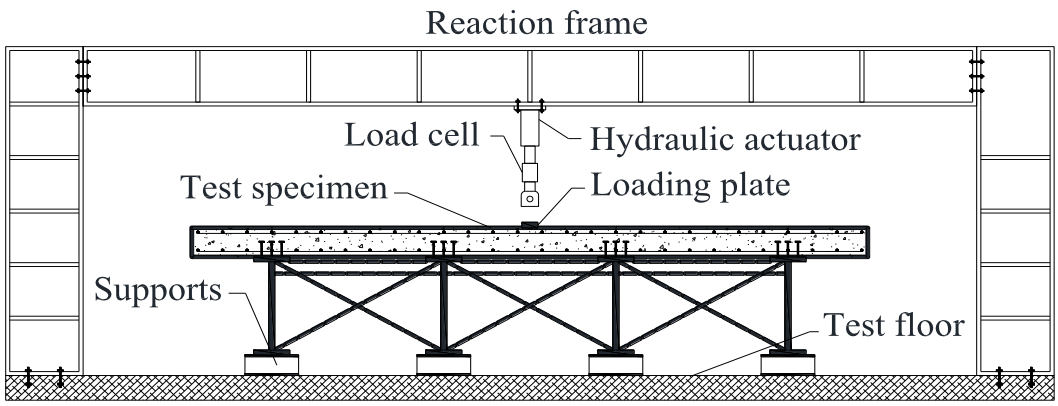

Figure 4.12. Typical loading system for the bridge deck under a concentrated load (adapted from Youn and Chang 1998)

A more advanced loading setup is using either the moving wheels with attached hydraulic device or the pseudo-moving load strategy by changing the position of the actuator. The moving load case is more approximate to the field condition of bridge decks under daily traffic, but very few studies performed tests in this way because of the complexity of the test setup. Okada et al. (1978) carried out a moving load fatigue test on the bridge decks by sliding the slabs in the longitudinal direction and changing the supporting point of the reaction beam in the transverse direction. Likewise, Sonoda and Horikawa (1982) applied the moving load by directly changing the position of the actuator for each fatigue cycle. Perdikaris and Beim (1988) used a custom-built hydraulic cylinder attached to a steel trailer that rolls on a hardened steel plate to simulate the moving wheel load. Cuelho and Stephens (2013) adopted an advanced Automated Bridge Deck Tester (ABDT) for their full-scale bridge deck fatigue test, and the moving load is applied through a single dual-wheel assembly equipped with real truck tires, as presented in **Figure 4.13**(a). Tauskela (2020) used the Rolling Load Simulator (ROLLS) to conduct the fatigue test of a full-scall concrete bridge deck with GFRP and steel reinforcement, this testing apparatus includes a steel supporting structure, the rolling load vehicle (RLV), and a high-power electric motor, as presented in **Figure 4.13**(b). The speed of moving load applied to the bridge deck highly depends on the mechanical capacity of the adopted moving device, and the maximum speed varied within 1.5 – 13.1 ft/sec according to the reported tests.

(a) ABDT (Cuelho and Stephens 2013) (b) ROLLS (Tauskela 2020)

Figure 4.13. Advanced moving load device for the fatigue test of bridge decks

Static test observations

Prior to the fatigue test of deck specimens, it is common to conduct a static test to examine the load carrying capacity of the deck slab and use it as a reference to determine the fatigue load range. As the applied patch load increased, the deflection of the deck increased accordingly. And the behaviors of the applied load vs. slab deflection were highly relevant to the reinforcement ratios of the tested specimens. A higher transverse reinforcement ratio usually led to a stiffer response of the specimen and a higher failure load as well (Perdikaris and Beim 1988). As presented in **Figure 4.14**, the orthotropic specimen almost had a consistent linear behavior before the static failure, while the isotropic specimen performed a more non-linear response with a higher ductility at failure.

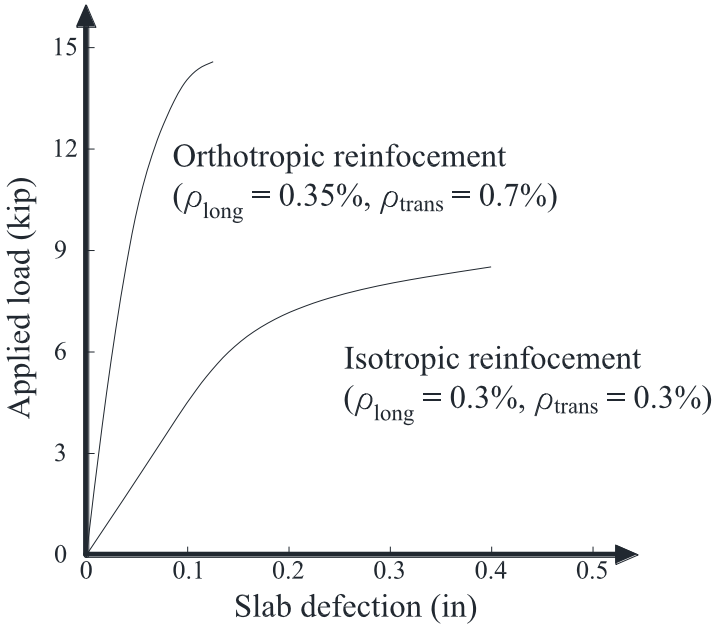

Figure 4.14. Typical load vs. deflection behavior of bridge deck slab under static concentrated load (adapted from Perdikaris and Beim 1988)

In terms of the failure procedure, for a deck slab with a proper reinforcement ratio, with the increase of the applied load, flexural cracks of concrete occurred at the bottom of the slab beneath the loading point and then gradually propagates in both directions. Cracks developed wider with a further increase of load followed by the yielding of bottom reinforcement. In addition, concrete cracks on top of the deck slab appeared later (Sonoda and Horikawa 1982; Fang et al. 1990; El-Ragaby et al. 2007) in an elliptical form around the corners of the slab or close to the edge supports. As shown in **Figure 4.15**, most tested specimens finally failed in a punching shear mode or with a flexural failure pattern to different extents, and a typical fan-shape cracking pattern was often observed. The shape and size of the local punched-in concrete area on top surface of the deck was usually similar to that of the loading plate.

It should also be noted that the failure modes highly depend on the boundary conditions of the slab and the reinforcement ratio. For example, the unreinforced specimens tested by Perdikaris and Beim (1988) failed in flexural mode, while all the other reinforced specimens failed in a punching shear mode. Sonoda and Horikawa (1982) reported a partially flexural failure in addition to the punching shear collapse of the deck slab, because the specimens were simply supported with

no restrictions of the rotation at the slab edges. By contrast, the deck specimens of Youn and Chang (1998) and Fang et al. (1990) used the shear studs welded on the steel girders to reach the full composite action. The rigid connection between the cast-in-place concrete deck slab and the supporting girders ensured the internal arching development of the concrete and thus all specimens failed by punching shear. Furthermore, the steel-free deck slabs tested by Bakht and Lam (2000) had the failure modes of either punching shear, or bending; or a mixed mode of bending and punching shear, depending on the different transverse confining systems that adopted.

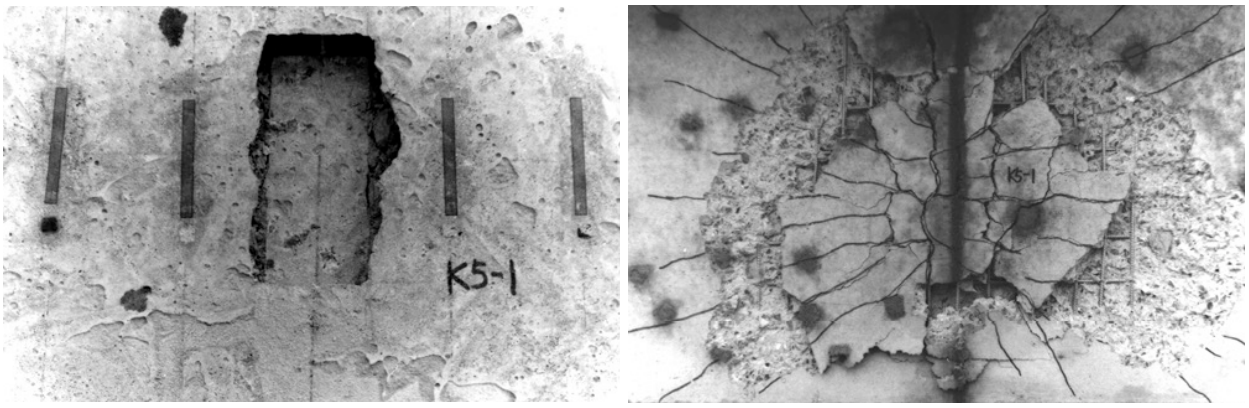

(a) top surface (b) bottom surface

Figure 4.15. Cracking pattern of punching shear failure of the bridge deck slab (Youn and Chang 1998)

Fatigue test observations

The fatigue behavior of concrete deck slab under cyclic loading varies depending on the different fatigue loading scheme. As mentioned above, most tests used the pulsating load applied to a fixed position of the tested slab with either a constant or changing fatigue load range. For example, Okada et al. (1978) and El-Ragaby et al. (2007) both adopted a stepwise fatigue loading strategy to speed up the fatigue degradation of deck slabs to reach failure. While others set the peak fatigue load as a fixed percentage ratio with respect the static ultimate strength of the slab, and it varied within the range of approximately 50 – 90% (Sonoda and Horikawa 1982; Perdikaris and Beim 1988; Youn and Chang 1998; Graddy et al. 2002).

Regardless of the different loading strategy and specimen details, the fatigue behaviors of the tested deck slabs have many similarities. As presented in **Figure 4.16**, all the deck specimens exhibited a gradual increase in deflection at the loaded point with the increase of fatigue cycles, and it also resulted in a stiffness loss to different extent. The variation in stiffness loss may be contributed by the difference in percentage ratios of reinforcement, type of reinforcement, fatigue load range and scatter of concrete material, etc. Meanwhile, the tensile strains of the bottom reinforcements in transverse direction gradually increased because of the concrete degradation under fatigue loading (Okada et al. 1978; Youn and Chang 1998; El-Ragaby et al. 2007). However, this tendency is not always true for the deck slab with a high percentage ratio of transverse reinforcement. Perdikaris and Beim (1988) reported that the measured tensile strain of the transverse reinforcement did not change after 160,000 cycles for the orthotropic deck specimen. Test results of Sonoda and Horikawa (1982) even indicated a decrease of the transverse reinforcement strain during fatigue cycles, and it was possibly due to the redistribution of stresses resulting from both the internal bond slips of reinforcements and the orthotropy of the flexural

rigidity of the slabs. Moreover, the increase of the transverse concrete compressive strain at the top deck surface was observed with the increase of fatigue cycles (El-Ragaby et al. 2007).

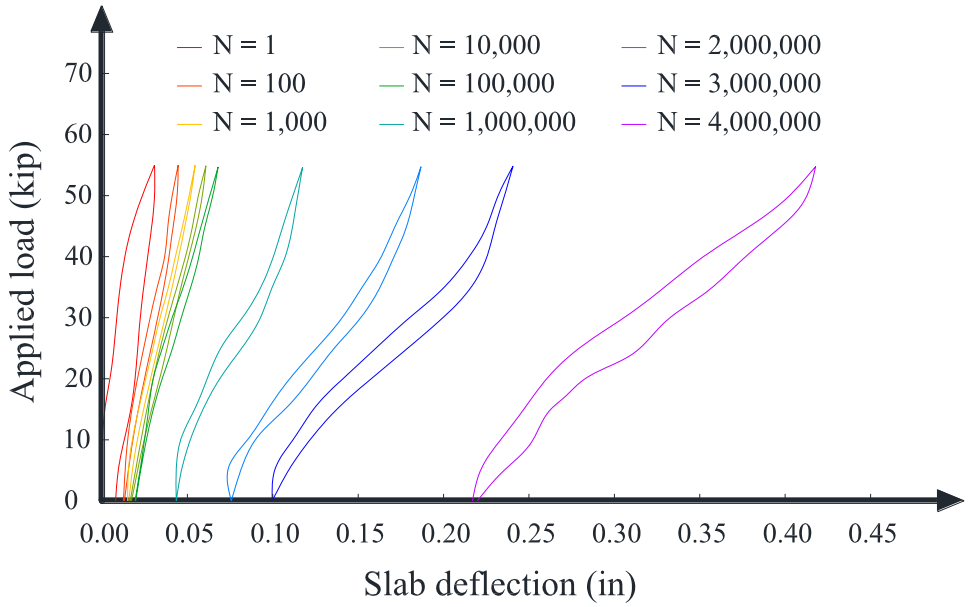

Figure 4.16.Typical slab deflections during the fatigue cycles (adapted from Graddy et al. 2002)

The failure process of bridge deck specimen under fatigue loading is very similar to that of the static case. Flexural cracks of concrete usually occurred firstly at the bottom of the pulsating load position, and it grew wider and spread to a larger circular area as the number of fatigue cycles increased. When the specimen reached a relative stable condition, the crack growth reduced considerably but the crack width continued to increase (Youn and Chang 1998). Aggregate debris or even pieces of concrete might drop from the bottom slab when large concrete cracks formed (Graddy et al. 2002; El-Ragaby et al. 2007). Finally, the deck slab failed in a fan-shape punching shear mode.

For tested specimens under moving wheels or pseudo-moving fatigue loading, the fatigue life significantly drops compared to those pulsating loading cases at fixed positions. Sonoda and Horikawa (1982) reported that the fatigue life of deck specimen under wheel loading could be shorten as much as two orders of magnitude. Likewise, from the test results of specimens subjected to moving wheel load, Perdikaris and Beim (1988) concluded that one wheel load passage is equivalent in damage to about 34 and 1800 load cycles of the pulsating load for the isotropic and orthotropic bridge deck, respectively. On the other hand, because of the longitudinal movement of the wheel load, the entire deck reinforcements were stressed in contrast to the pulsating loading case where only the reinforcement in the vicinity of the loading point was affect. As a result, cracks at the bottom of the deck slab developed transversely along the entire deck length and formed a unique grid-like cracking pattern, as presented in **Figure 4.17**. This cracking pattern was confirmed by Cuelho and Stephens (2013) in their full-scale bridge deck fatigue test under the real truck tires. The alternating crack opening-closing and twisting of the faces of the orthogonal crack as the wheel load moved on the deck significantly accelerated the concrete deterioration and debonding at the interface between concrete and reinforcements, and eventually led to a punching-type failure of the deck (Perdikaris and Beim 1988). This failure mechanism was also observed in the pseudo-moving fatigue test conducted by Okada et al. (1978).

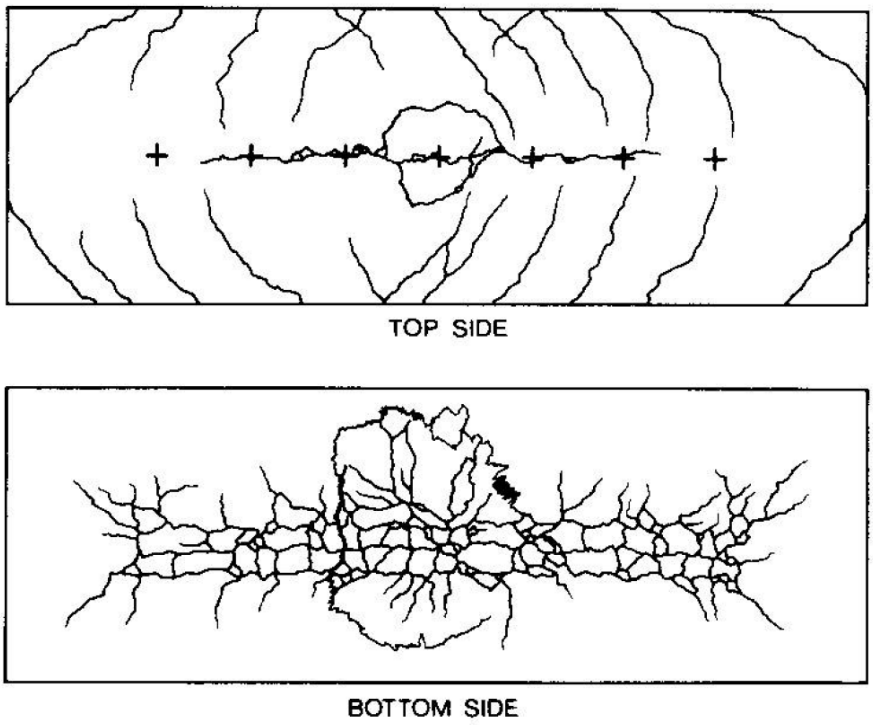

Figure 4.17. Typical cracking pattern of bridge deck slab under moving wheel load (Sonoda and Horikawa 1982)

4.4.2 Models and analytical study

To fully understand the punching shear failure mechanism of bridge deck under both static and different fatigue loading scenarios, and to well explain the internal arching action, analytical efforts have been made by different studies. Most adopted models focus on the punching shear failure mechanism of the deck slab under a concentrated load for the static case. And the yield line theory has also been used to estimate the ultimate strength of the deck as an upper bound. In addition, a few studies investigate the failure procedure of RC bridge deck by means of the numerical models, as well as the degradation behaviors under cyclic loading case. However, the primary method to estimate the fatigue life of bridge deck specimens is still through the semi-empirical models calibrated from the test data points. This section will focus on both the analytical and semi-empirical methodologies that are popular in the literatures to estimate the load carrying capacity and fatigue life of RC bridge decks.

Punching shear models

As aforementioned, the typical failure mode observed in the experiments is the fan-shape punching shear. The idealized model can be illustrated as **Figure 4.18**, where the concrete wedges bound by the shear cracks act as rigid bodies in the radial direction and rotate about the center of rotation (CR). Due to the cracking of concrete, the neutral axis of the slab migrates toward the top surface at the mid span and its position varies along the span of the slab. Meanwhile, the boundary of the slab restricts the rotation tendency of the wedge element which result in the compressive

membrane action or the arching force in the RC deck slab [**Figure 4.18**(b)]. This arching action will significantly enhance the load carrying capacity of the slab.

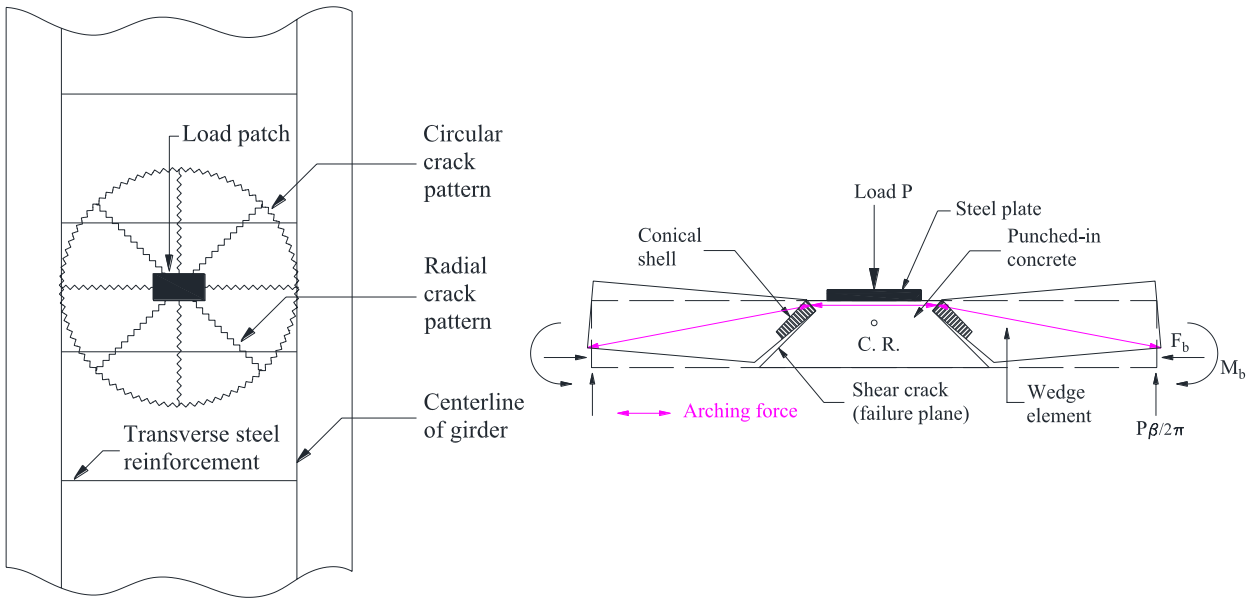

(a) Fan-shape cracking pattern (b) Rigid body rotation of cracked concrete wedges

Figure 4.18. Idealized punching shear failure of concrete slab under a concentrated load (adapted from Hewitt and Batchelor 1975 and Mufti and Newhook 1998)

If it is assumed that only the concrete tensile stress exists at the failure plane, then the trapezoidal punched-in concrete can be isolated as a single rigid body to estimate the punching shear capacity. As presented in **Figure 4.19**, a simple general punching shear model is thus introduced to estimate the theoretical punching shear capacity of bridge deck (Fang et al. 1990). In **Figure 4.19**(a), the concentrated load footprint is assumed as a rectangular shape with the size of $b_1 \times b_2$, and the failure planes have the same inclination angle θ. The failure plane propagates downward to the bottom of the deck slab by a thickness of d. **Figure 4.19**(b) illustrates the free-body diagram of the failure plane under applied forces, hence, the punching shear capacity can be easily derived from the equilibrium of these forces as:

$$V_c = 2\left(b_1 + b_2 + \frac{2d}{tan\theta}\right)\frac{d}{tan\theta} f_t \tag{4.26}$$

where b_1 = long side of tire footprint (in); and b_2 = short side of tire footprint (in). And the tensile strength of concrete on the failure plane can be referred to ACI 318 Table 22.6.5.2 (ACI 2019) as

$$f_t = (2 + \frac{4}{\beta})\lambda_s \lambda \sqrt{f_c'} \leq 4\lambda_s \lambda \sqrt{f_c'} \tag{4.27}$$

where λ_s = size effect factor = $\sqrt{2/(1 + d/10)} \leq 1$; λ = modification factor of lightweight concrete; β = ratio of long to short side of the tire footprint; and f_c' = concrete compressive strength (psi).

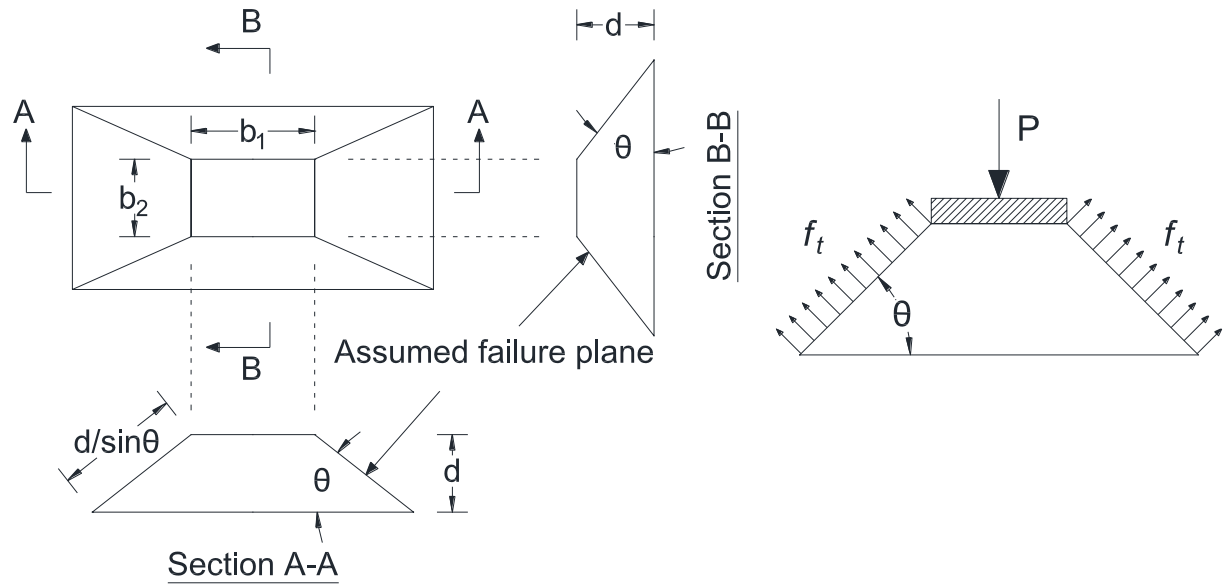

(a) Assumed failure plane in punching shear (b) Forces acting on the failure plane

Figure 4.19. General punching shear model (adapted from Graddy et al. 2002)

However, despite its simplicity and popularity in design and research, this general punching shear model does not quantify the influence of arching force, neither does it incorporate the contribution from reinforcements. Alternatively, another fatigue punching shear model proposed by Matsui (1991) considers the influence of both compressive and tensile reinforcements at the ultimate state of the deck slab. The formation of the fatigue punching shear model proposed by Matsui is described as below:

$$P_{sf} = 2B\left(\tau_{s,max}X_m + \sigma_{t,max}C_m\right) \tag{4.28}$$

$$B = b + 2d_b \tag{4.29}$$

$$\tau_{s,max} = 0.688{f_c}^{'\,0.61} \le {f_c}^{'} = 80\ MPa \tag{4.30}$$

$$\sigma_{t,max} = 0.269{f_c'}^{2/3} \tag{4.31}$$

where B = effective width of the RC bridge deck slab (mm), a = contact length of tire in the transverse direction of bridge (mm) = 2.5b; b = contact width of tire in the longitudinal direction of bridge (mm); H = RC bridge deck thickness (mm); d_b = effective depth of transverse reinforcement at the tension side (mm); ${f_c}^{'}$ = concrete compressive stress at the failure plane (MPa); ${f_t}^{'}$ = tensile stress at the failure plane (MPa); $\tau_{s,max}$ = maximum shear strength of concrete (MPa); $\sigma_{t,max}$ = maximum tensile strength of concrete (MPa); X_m = depth of neutral axis (mm); and C_m = cover depth at the tension side (mm), as illustrated **Figure 4.20**. It should be noted that the original unit system for this model is in metric, hence, both the maximum shear strength and the maximum tensile strength of concrete need to be converted from psi for consistency to yield the punching shear capacity in newtons. However, to accommodate the fatigue life model proposed by Matsui (1991) which will be introduced later, this fatigue punching shear model only includes the contribution from two transverse faces out of the representative four punching shear failure faces, as observed in most experiments (**Figure 4.15**). As a result, a more conservative estimation of the punching shear capacity using this model should be expected.

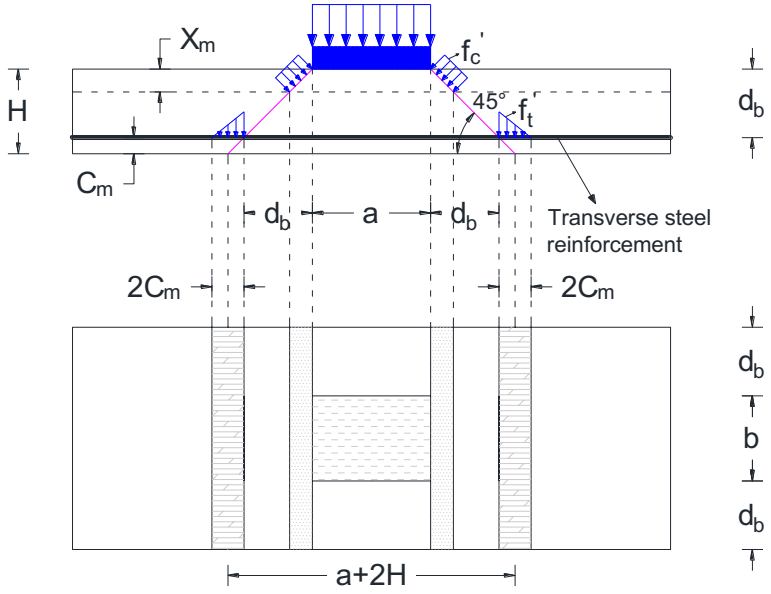

Figure 4.20. The fatigue punching shear model proposed by Matsui (1991)

On the other hand, more advanced models have also been developed for the punching shear failure of bridge deck slabs and incorporate the arching force into the prediction. For example, Hewitt and Batchelor (1975) extended the model of Kinnunen and Nylander (1960) by incorporating the influence of different boundary restrictions via the restraining force F_b and moment M_b, as shown in **Figure 4.18**(b) where β represents the angle of wedge element (sector). Instead of using the punched-in concrete portion, the cracked concrete wedge is focused, and all the forces applied to the wedge are considered, including the compression forces of concrete (e.g., internal arching), forces in the circumferential reinforcement and boundary reactions. In addition, a restraining factor F_R was introduced to quantify the degree of boundary conditions, and it varies within 0–1.0, with 0 represents the simply supported case and the latter represents the ideal infinitely rigid condition. The failure criterion is that punching occurs when the tangential strain at the top of the slab in the vicinity of the root of the shear crack (conical shell) reaches a critical value. A dowel factor equals to 1.2 is included in this model as well to consider the enhancement of deck slab from two-way reinforcements. However, iteration process by computer program is inevitable to determine the punching load with the given failure criterion. Likewise, Mufti and Newhook (1998) adopted a similar methodology by solving the equilibrium state of forces applying to the wedge element but did not include the restraining moment contributed by the boundary conditions. They also took the triaxial compressive state of the conical shell into consideration to estimate a more realistic ultimate concrete strength at failure.

Yield line theory

Due to the predominant failure mode of punching shear for tested deck slabs under the concentrated load, it can be inferred that the actual flexural capacity of the deck slab is larger than its punching shear capacity. The yield line theory, which measures the ultimate flexural strength of a supported slab in the most ideal situation, is usually adopted to predict the upper bound failure loads of the slabs with different boundary conditions. Analytical results from Fang et al. (1990) and Graddy et al. (2002) both confirmed the overestimation of the yield line theory to predict the

load carrying capacity of tested deck specimens. However, Sonoda and Horikawa (1982) reported a very close estimation of the failure load compared to the test results by using the yield line theory. Regardless of the discrepancy in the accuracy of predicted failure loads, it is beneficial to introduce the concept of yield line theory as an alternative to the punching shear models.

The yield line is defined as a crack in a reinforced concrete slab across which the reinforcing bars have yield and along which plastic rotation occurs (Kennedy and Goodchild 2004). For example, if a deck slab is supported between girders, the yield line pattern may be represented by the illustrations as show in **Figure 4.21**. In either case, i.e., two way or one way action, the yield lines depict the boundaries between different rigid regions. These regions rotate about the yield lines, as well as pivot about the axes of rotation which usually locate close to the line of support. Assuming the rigid region rotate an angle of θ_i about its axis of rotation, and the vertical displacement at the loading point equals to δ, then an equilibrium equation in terms of energy can be reached. In other words, the work done by the external load equals to the dissipated energy by rotations about yield lines as below:

$$P\delta = \sum_{i=1}^{n} m_i \, l_i \theta_i \tag{4.32}$$

where P = concentrated load applied to the deck slab; m_i = moment resistance of the slab per unit length at the i^{th} yield line; and l_i = the length of the i^{th} yield line or its projected length onto the axis of rotation of that region. The moment resistance m_i at each yield line can be calculated by using the actual material properties through the classic beam theory. And the rotation angle θ_i can be presented in terms of δ using the geometrical relationship between different rigid regions. Thus, the load carrying capacity of the deck slab can be obtained by solving the Eq. (4.32).

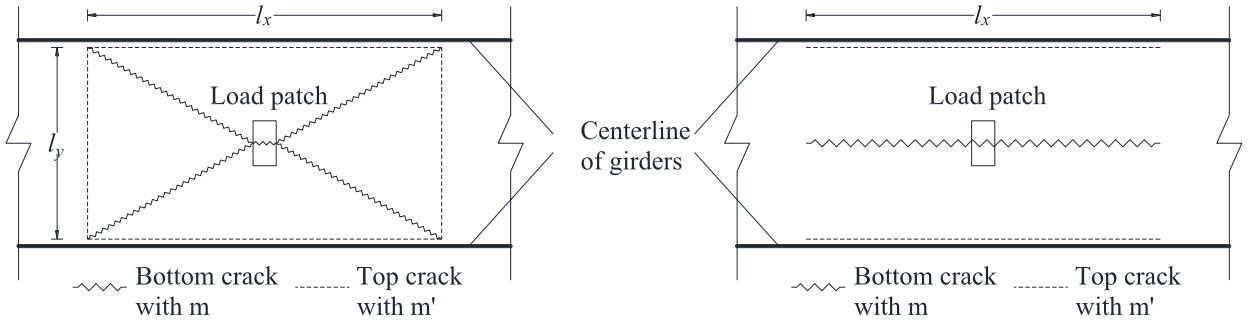

(a) Two-way action (b) One -way action

Figure 4.21. Potential yield line patterns of deck slab under patch load case (adapted from Fang et al. 1990)

However, it should be noted that the yield line pattern needs to be predetermined to formulate the energy equilibrium equation. As a result, the predicted load carrying capacity depends on the selected cracking pattern. And it is possible that the deck slab has various failure pattern corresponding to different failure loads. Kennedy and Goodchild (2004) also recommended a 10% margin on the design load by using the yield line theory to allow for the effects of corner levers in two-way slabs.

Fatigue life models

The fatigue life of RC bridge deck is usually interpretated by a logarithmic relationship with the applied load level P/P_s, or the shear stress level v/v_c, where P = maximum fatigue load applied to the deck slab; P_s = static failure load of the deck slab obtained from test; v = nominal punching

shear stress acting on the failure plane; and v_c = shear strength of the concrete. Because the failure of bridge deck under cyclic loads is highly relevant to the degradation of concrete material, thus, its fatigue characteristics shares many similarities with the fatigue of plain concrete. In other words, scatter is inevitable in the fatigue life of identical bridge deck specimens subjected to the same loading condition, and it has been confirmed by experimental studies (Perdikaris and Beim 1988; Youn and Chang 1998; Graddy et al. 2002). To this end, a large database of test results is necessary to yield a reliable fatigue life model. However, due to the limited number of fatigue tests on the deck slabs, the proposed fatigue life models in the literatures so far are barely satisfying to accommodate to different deck specimens. And neither of these models considers the influence due to loading frequency and duration or discrepancy in material properties. Nevertheless, these models are still presented herein as references.

(1) *Model of Sonoda and Horikawa (1982)*

Sonoda and Horikawa (1982) tested RC deck slabs with either isotropic or orthotropic reinforcement arrangement, subjected to both fixed pulsating and pseudo-moving loading cases. The total number of deck slabs is 20 with a selected fatigue load levels ranging from 50 – 85% with respect to the static load carrying capacity. The fatigue life model was proposed with an upper bound of load cycles equals to two million as below:

$$\frac{P}{P_s} = 1.08 - 0.086 log N_f \quad \text{for isotropic slabs under fixed pulsating loading} \quad (4.33)$$

$$\frac{P}{P_s} = 1.14 - 0.093 log N_f \quad \text{for orthotropic slabs under fixed pulsating loading} \quad (4.34)$$

$$\frac{P}{P_s} = 0.93 - 0.076 log N_f \quad \text{for isotropic slabs under moving loading} \quad (4.35)$$

$$\frac{P}{P_s} = 0.99 - 0.102 log N_f \quad \text{for orthotropic slabs under moving loading} \quad (4.36)$$

(2) *Model of Matsui (1991)*

Matsui (1991) (as referenced by Yoshitake et al. 2010) proposed a semi-empirical equation to estimate the fatigue life of RC deck slabs subjected to moving wheel load as below:

$$log\left(\frac{P}{P_{sf}}\right) = -0.07835 log N_f + log C \quad (4.37)$$

where P_{sf} = fatigue punching shear capacity as introduced in Eq. (4.28) and C = service coefficient equals to 1.23 and 1.52 for wet and dry conditions, respectively. This equation is only valid for N_f greater than 10,000 cycles.

(3) *Model of Youn and Chang (1998)*

Youn and Chang (1998) conducted both the static and fixed pulsating tests at the different positions of the deck slabs. Although they applied a fixed peak fatigue load level of either 59% or 65% based on the average punching shear strength obtained from the static test, the fatigue model is calibrated from the actual load percentage ratio with respect to the various punching shear strengths at different loading positions. They concluded an endurance limit of $0.55P_s$ to reach the recommended fatigue life of 2 million cycles, and the model is presented as follows:

$$log\left(\frac{P}{P_s}\right) = -0.066 log N_f + log 1.4461 \quad (4.38)$$

(4) *Model of El-Ragaby et al. (2007)*

El-Ragaby et al. (2007) tested five full-scale deck slabs reinforced with either GFRP or steel reinforcements under a stepwise fatigue loading scheme with an increasing peak fatigue load. To extend the database, the PM rule (as introduced in Chapter 4.3.2) was adopted to obtain the

equivalent fatigue life of specimens under different peak fatigue loads. A parabolic semi-logarithmic function based on the model of Matsui (1991) was proposed through regression analysis to include the characteristics of fatigue life pattern under higher fatigue load levels as well as follows:

$$\frac{P}{P_s} = 0.0034\left(logN_f\right)^2 - 0.11873\left(logN_f\right) + 1.0752 \quad (4.39)$$

Finite element simulation

The full-scale fatigue tests of RC bridge decks are usually complicated, time consuming and expensive, let alone a large database is always necessary to propose a reliable fatigue model. As an alternative to the experiment, numerical studies have also been made on the simulation of deck slabs subjected to fatigue loading by means of the finite element method (FEM). Some of the representative research is presented in this section.

For example, Maekawa et al. (2006a) extended the direct path-integral scheme (Maekawa et al. 2006b) to the full three-dimensional (3D) analysis of fatigue failure and applied this method to the fatigue life simulation of RC decks subjected to moving wheel loads. A computational constitutive model of concrete was used to consider the effect of concrete degradation due to crack development, time-dependent elastoplastic fracture, and fatigue damage (Maekawa and El-Kashif 2004). In addition, a 3D multi-directional non-orthogonal fixed crack approach was proposed for the fatigue simulation by using the composition method (Maekawa et al. 2003). In this study, a simply supported RC deck slab was modeled representing the tested specimen from Maeda and Matsui (1984) under moving wheel loads, as presented in **Figure 4.22**. The analysis indicated a significant decrease of fatigue life in two or three order of magnitudes for the case under the moving wheel loads compared to the fixed pulsating case. The results of sensitivity study also inferred that the predominant factors in fatigue degradation of RC deck slab are the shear transfer fatigue along cracks, and the bond decay (tension-stiffness). Moreover, the effect of boundary conditions was investigated, and it confirmed that the fixed translational boundary can increase the slab fatigue life compared to the free translational boundary.

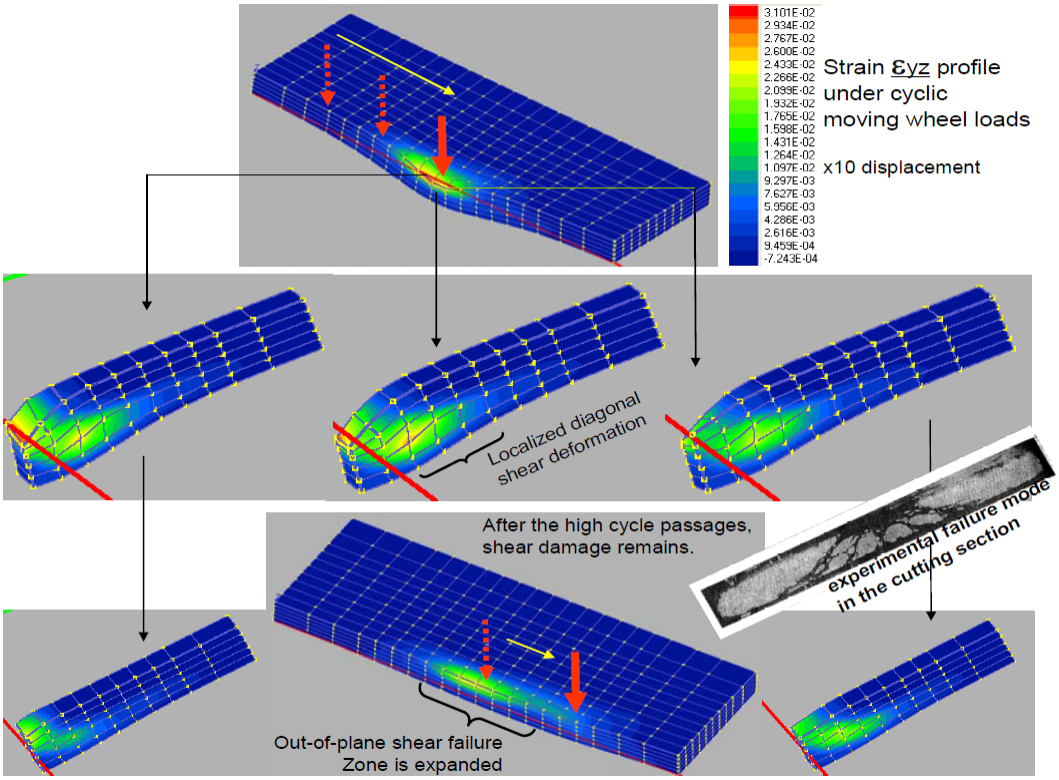

Figure 4.22. Visualized FE results of transverse (magnified) deformation of RC deck slab under moving wheel load (Maekawa et al. 2006a)

Suthiwarapirak and Matsumoto (2006) constructed a FE model of the bridge deck slab based on the experiment of Okada et al. (1978). The concept of crack bridging degradation was adopted to explain the crack initiation and propagation of concrete during cyclic loading, which leads to the fatigue failure of the deck slab. The concrete smeared crack element with a multiple fixed crack concept was used to represent the cementitious material and the rod element with a bilinear stress-strain relationship was used to represent the steel reinforcement. This model successfully reproduced the crack development and damage accumulation of the concrete material and can estimate the fatigue life of the deck slab, as illustrated in **Figure 4.23**. However, it overestimated the fatigue life of deck slab subjected to moving wheel loads. This overestimation is probably caused by the model assumptions that both the fatigue degradation of the shear stress and the bond degradation between the reinforcement and concrete were not considered in the numerical simulation.

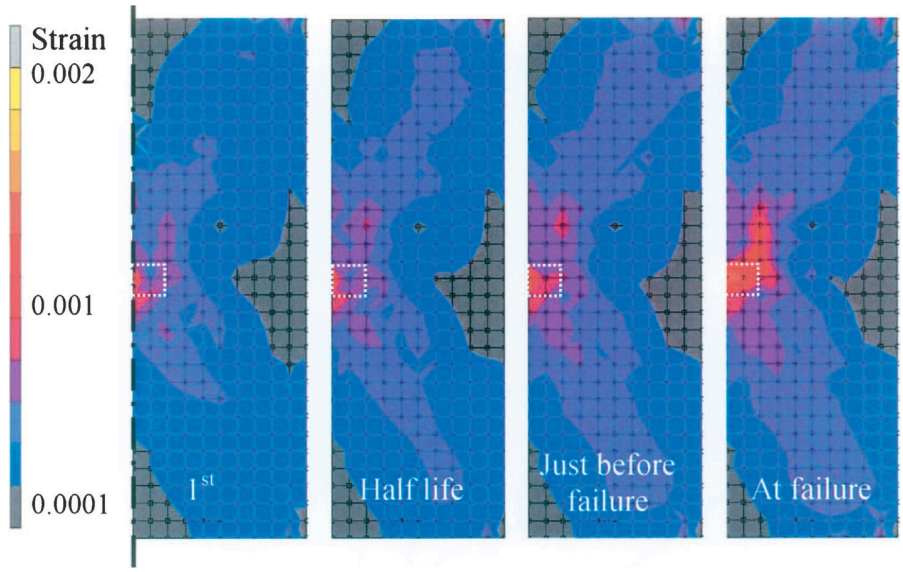

Figure 4.23. Damage accumulation at the bottom of the deck slab during fatigue cycles (Suthiwarapirak and Matsumoto 2006)

Moreover, Drar and Matsumoto (2016) extended the FE modeling strategy of Suthiwarapirak and Matsumoto (2006) by incorporating the bond-slip effect between the reinforcing bar and the surround concrete. RC deck slabs were modeled referring to the experiments conducted by Shakushiro et al. (2011) with either deformed bars or plain bars. The numerical simulation reached a good agreement with the test results, in terms of slab displacement vs. number of fatigue cycles, fatigue life, cracking pattern and strain development of steel reinforcements. A typical comparison between the predicted cracking patterns at the bottom of the RC deck slab and the test observations is presented in **Figure 4.24**. In addition, all the analyzed slab models failed in a punching shear mode with an inner cracking orientation of 45°in the transverse direction, which was consistent with the test results. The FE model analysis also indicated that the RC deck slab reinforced with plain bars has a larger displacement and a shorter fatigue life than that reinforced with deformed bars.

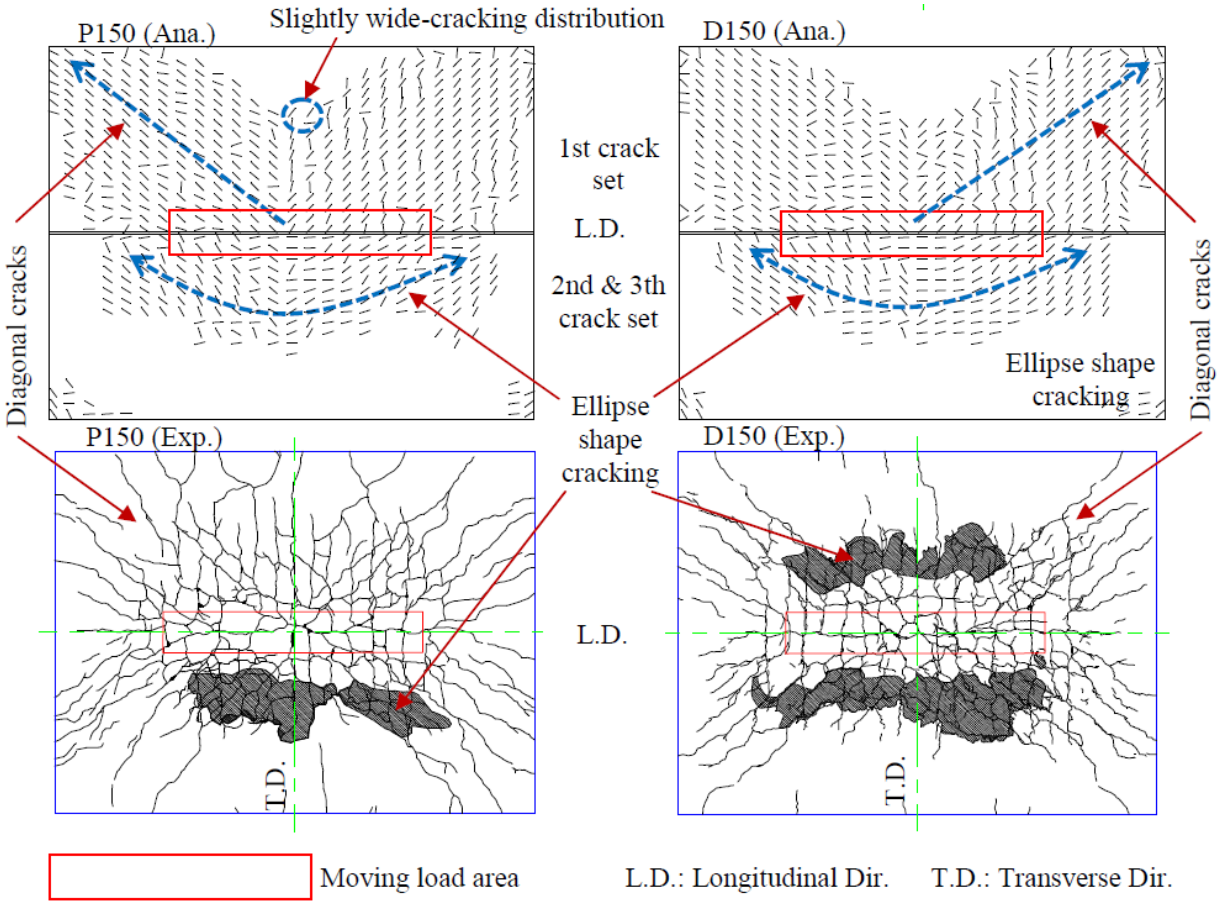

Figure 4.24. Cracking patterns at the bottom of the RC deck slab at the failure load (Drar and Matsumoto 2016)

4.5 Summary

4.5.1 Remarks

A thorough state-of-the-art literature review on the fatigue behavior of reinforced concrete bridge deck is presented in this report, including both the material and structural level. For plain concrete subjected to cyclic loading, the internal damage accumulates due to the applied load loops in terms of the dissipated energy. With a constant fatigue stress range, the material properties of concrete gradually degrade, including a declining tendency of concrete strength and stiffness, accompanied by an increase in the permanent concrete strain. It is believed that the major factors contributed to the fatigue life of concrete include, but not limited to, the normalized stress level, stress reversal, lateral confinement, concrete creep, loading frequency, loading duration, shape of cyclic loading form and loading history. A normalized stress level of $S_{max} > 0.75$ is critical for the concrete material since it approaches the long-term strength of concrete, at which the effect of loading frequency is also more significant. In addition, the sustained loading effect on the fatigue performance of concrete is not negligible for a stress ratio $R > 0.75$. Furthermore, representative concrete fatigue models are reviewed and categorized by different methodologies, which includes the deterministic model, the probabilistic model, and the energy model. These models can be adopted as good references for the fatigue design of RC bridge decks if a stress-based approach is focused.

At the structural level, both experimental and analytical studies on the fatigue characteristics of RC bridge decks are summarized. In general, RC deck slab subjected to cyclic loading has a gradual increase in the deflection at the patch load point, accompanied by a decrease in the deck stiffness. The degradation behavior of the RC deck slab is primarily caused by the accumulated damage in concrete closer to the loading position, where cracks occur and propagate in both longitudinal and transverse directions. A typical punching shear failure mode is usually observed with a fan-shape cracking pattern for fixed pulsating load or grid-like cracking pattern for moving wheel load. Due to the limited number of research effort, as well as the complex failure mechanism of bridge deck, a simple yet reliable model for the fatigue design of RC bridge decks is still lacking. Nevertheless, the existing representative models are still summarized based on either the punching shear failure mechanism with/without arching action, or the yield line theory. The force-based semi-empirical models are also collected from the literature to predict the fatigue life of RC deck slabs, although these models are only based on a very small test database. Moreover, some of the FE modeling strategies are introduced to analyze the fatigue behavior of bridge decks under cyclic loading, as an alternative to the experimental method. These numerical simulations require complex modeling and material definitions, as well as huge computational efforts to yield reliable results. However, the numerical method still deserves more investigation in the future since it helps understand the failure mechanism of bridge decks subjected to fatigue loading, and it can also extend the current test database.

4.5.2 Recommendations

Based on the literature review as described above, there is no doubt that the fatigue process of reinforced concrete bridge decks subjected to cyclic loading is complicated. The fatigue failure is the result comprehensively influenced by multiply factors such as damage accumulation of concrete through microcracks, triaxial compressive stress state within the internal arching, stress redistribution between concrete and steel reinforcements, restriction stiffness of deck supports, type of service load (e.g., stationary or moving load), and loading duration, etc. The proposed fatigue models of plain concrete are still debatable and require the probability theory to consider the scattering of fatigue life in general. In addition, the environmental exposure of bridge decks may significantly affect their fatigue life through the deterioration of materials, e.g., freeze and thaw cycles, corrosion due to deicing salt, aging, etc. As a result, the fatigue models of RC bridge deck reviewed in this review are far from being applicable and practical in deck fatigue design. However, they do provide important insights for the expected fatigue life of bridge deck if the on-site fatigue test is not available. Derived from the current literature review, two frameworks of methodology can be considered in the subsequent research to estimate the fatigue life of RC bridge deck based on these models:

1. *Stress-based method*: Calculate the concrete stress level S_{max} under the critical vehicle load on the failure plane of the punching shear model (**Figure 4.19**), using either analytical or numerical method, and estimate the fatigue life of bridge deck using the models introduced in Chapter 4.3.3. A possible but not exclusive framework of this approach can be illustrated in **Figure 4.25**.

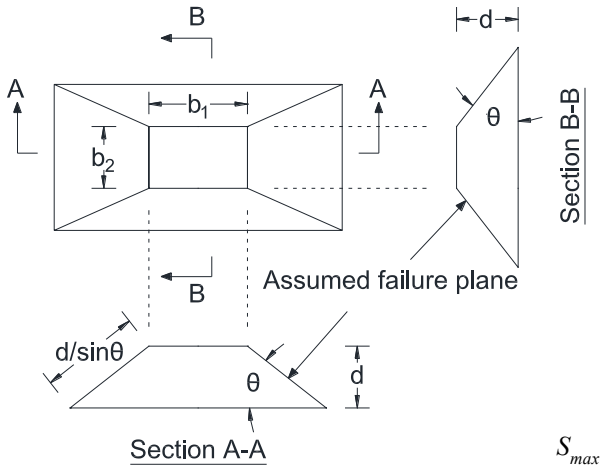

Calculate the maximum concrete stress S_{max} under the repeated vehicle load at the assumed failure plane, e.g., as shown in the left figure, using either

When S is determined, the fatigue life of this local structural component can be estimated by the existing models. For example, the most widely adopted deterministic model proposed by Hsu (1981) can be a possible choice in this case, as presented below:

$$S_{max} = 1 - 0.0662(1 - 0.556R)logN_f - 0.294logt$$

Figure 4.25. Example framework of the stress-based method

However, this stress-based method can be extremely conservative since the stress redistribution, internal arching, and reinforcement of the deck slab are not considered. A more appropriate alternative is using these concrete fatigue models as material input to conduct an independent FE analysis, as described in Chapter 4.4.2, followed by the definition of an appropriate failure criteria, e.g., either load-controlled failure, or deformation-controlled failure, and then estimate the fatigue life of the entire deck structure.

2. *Force-based method*: Calculate the static load carrying capacity P_s of bridge deck using either the punching shear model or the yield line theory. Calculate the critical vehicle load P applied to the bridge deck and estimate its fatigue life using the models introduced in Chapter 4.4.2. A possible but not exclusive framework of this approach can be illustrated in **Figure 4.26.** .

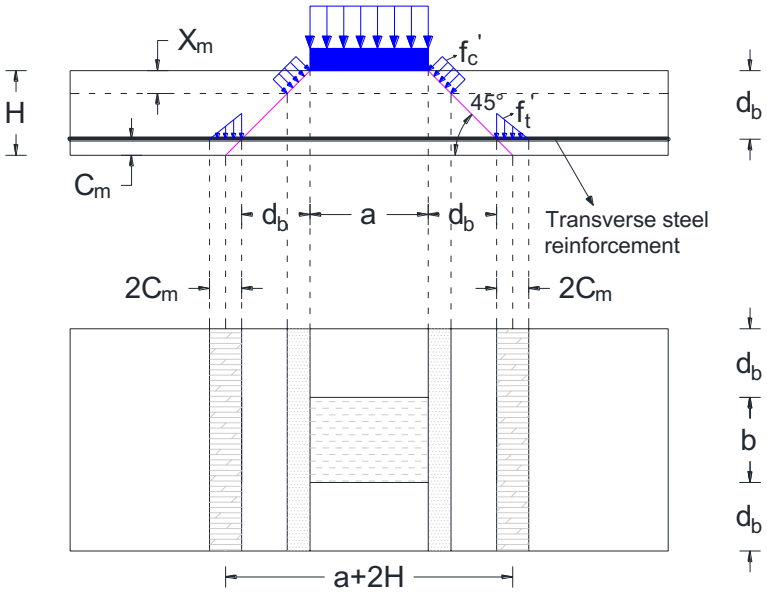

The model of Matsui (1991) as introduced in Chapter 4.4.2, for example, is an appropriate approach to estimate the fatigue punching shear capacity P_{sf} of RC bridge deck, by incorporating the contribution from two transverse failure planes (as shown in the figure above). When P_{sf} is determined, the fatigue life of the deck can be predicted by the semi-empirical fatigue model proposed by Matsui (1991) as well in

Figure 4.26. Example framework of the force-based method

The accuracy of the force-based method highly depends on the selection of the model to estimate the local static load carrying capacity P_s, and its corresponding semi-empirical fatigue model. A tryout case study was conducted to investigate the difference in the required RC bridge deck thickness using the different static and fatigue model combinations, as described in the Appendix. A short observation of the tryout case study contains: (1) the adoption of both the static model and fatigue model of Matsui (1991), i.e., case S1F1, yields a minimum deck thickness of 7.5 in to achieve the target service life of 75 years; and (2) the adoption of the general punching shear model (Graddy et al. 2002) and the fatigue model of El-Ragaby et al. (2007), i.e., case S2F2, shows that the fatigue might not be an issue for the RC deck when a minimum deck thickness of 7 in is explored as per the MTD 10-20 (Caltrans 2008) because the target service life of 75 years can be reached at a deck thickness of 4.875 in. This tryout case study indicates the high variability of the predicted deck fatigue life while using different model combinations, hence, any potential adoption of these models in bridge deck design requires a sophisticated consideration and highly relies on the experience and judgement of engineers.

These two frameworks are proposed for future studies by the authors of this report based on the current literature review. However, they have not been verified by any laboratory test or on-site investigation. Additionally, the models mentioned in the frameworks are intended for the illustration purpose only and they can be replaced by other alternative models that believed to be

more reliable. Since the fatigue issue of either concrete material or RC bridge deck is of interest to many civil engineers, it is possible to conduct more research in the future to examine these two proposed frameworks. Experimental study aiming at measuring the fatigue life of RC bridge decks subjected to realistic moving vehicle loads is always the best approach to deepen the understanding in this research area.

5 CASE STUDIES OF LOAD DEMANDS UNDER VARIOUS PARAMETERS

Currently, various deck types such as cast-in-place reinforced concrete, precast post-tensioned concrete, steel, wood or composite decks are recognized in Caltrans Bridge Design Practice and are used over the State of California. Nevertheless, cast-in-place reinforced concrete decks are among the most common deck types in Caltrans, owing to their relatively lower cost, as well as ease of construction. During this task, the common types of RC deck/support systems with various structural configurations will be considered by means of a few parametric studies to determine the scope of production run of refined deck analysis.

5.1 Parameter Ranges for Bridges in Inventory

In Chapter 4, it was verified that the RSM can conservatively envelope the load demand results from the true refined model, hence, this modeling shortcut will be adopted for the production run of the bridge decks with various girder spacings. However, before the initiation of the production run, it is important to determine the ranges of representative parameters of the bridge decks in CA. Caltrans provides a bridge database covering the design details of 93 box girder bridges in CA, although the number of bridges in the database is extremely small compared to the total number of bridges existing in the state, it helps to understand the correlation between different design parameters. The parameter ranges of bridges in the database are summarized in **Table 5.1**. To conduct the refined deck analysis based on the proposed rigid support modeling approach, the presented parameter ranges should be well considered, and yet the number of combinations using various parameters in the table can be huge and impractical for a production run as well. For example, assuming a series of different girder spacings are used within the given range, i.e., 5', 10', 15', 20', and another series of different structural depth are selected, i.e., 3', 6', 9', 12', the possible number of different bridge configuration can be as many as 16. The number of combinations can increase to thousands when more parameters as listed in the table are included.

Table 5.1. Summary of typical parameter ranges of bridges in the database

Parameter	Range	Parameter	Range
Max span length (ft)	59 – 290	Structural depth (ft)	3 – 11.5
Girder spacing (ft)	5.32 – 19.67	Total deck width (ft)	27.5 – 245.5
Top deck thickness (in)	6.75 – 10.43	Soffit thickness (in)	5.5 – 10.43
Single overhang width (ft)	2 – 7.08	Overhang/spacing	0.1 – 0.65
No. of cells	2 – 26	No. of spans	1 – 13

To understand the correlations among some of the parameters in the table, regression analysis was performed, and the results are visualized in **Figure 5.1**. Some conclusions can be drawn from these plots: (1) the structural depth (girder depth) is linearly proportional to the maximum span length; (2) the larger the girder spacing, the higher the structural depth; (3) the girder spacing is not related to the deck width; (4) the larger the girder spacing, the thicker the top deck and soffit thickness; and (5) the soffit thickness is linearly proportional to the top deck thickness. Because the RSM has a continuous support length of 220 ft, and all the vertical deflections of the girders are restrained, so the girder depth for analysis cannot be simply determined from the derived equation as shown in **Figure 5.1**(a). In addition, it seems that the top deck and soffit thickness can be estimated by the girder spacing with the derived equations [**Figure 5.1**(d) and (e)], and this conclusion is consistent with Caltrans MTD 10-20 (Caltrans 2017) where the thickness of the deck

and soffit slab are specified based on the girder spacing. As a result, the choice of different bridge configurations can narrow down to the choices of girder spacing, girder depth, and number of cells, and these will be discussed in the following sections.

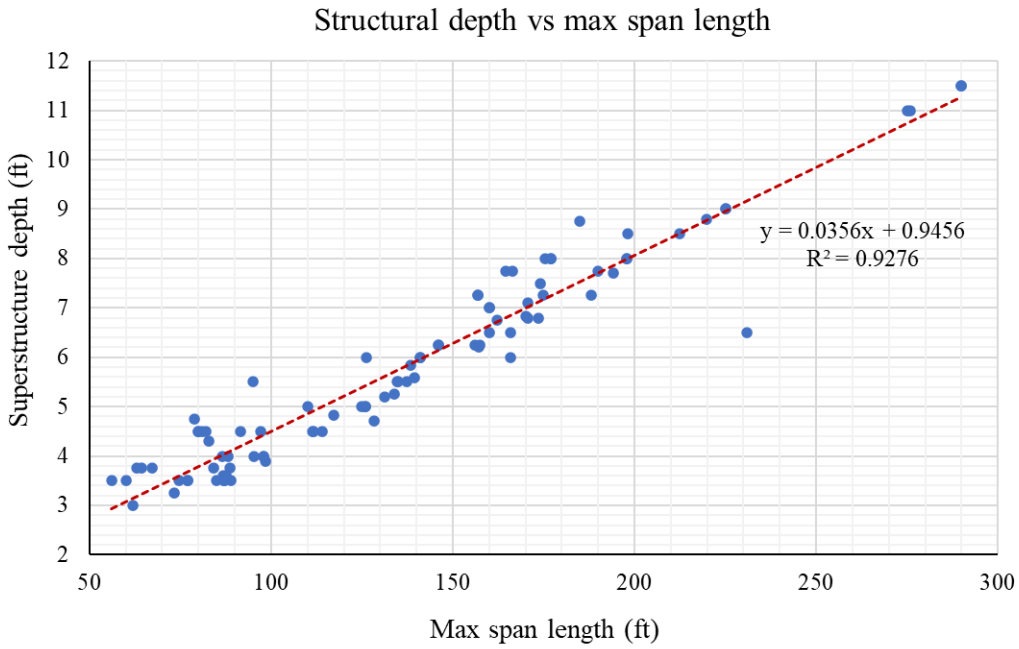

(a) Structural depth vs. max span length

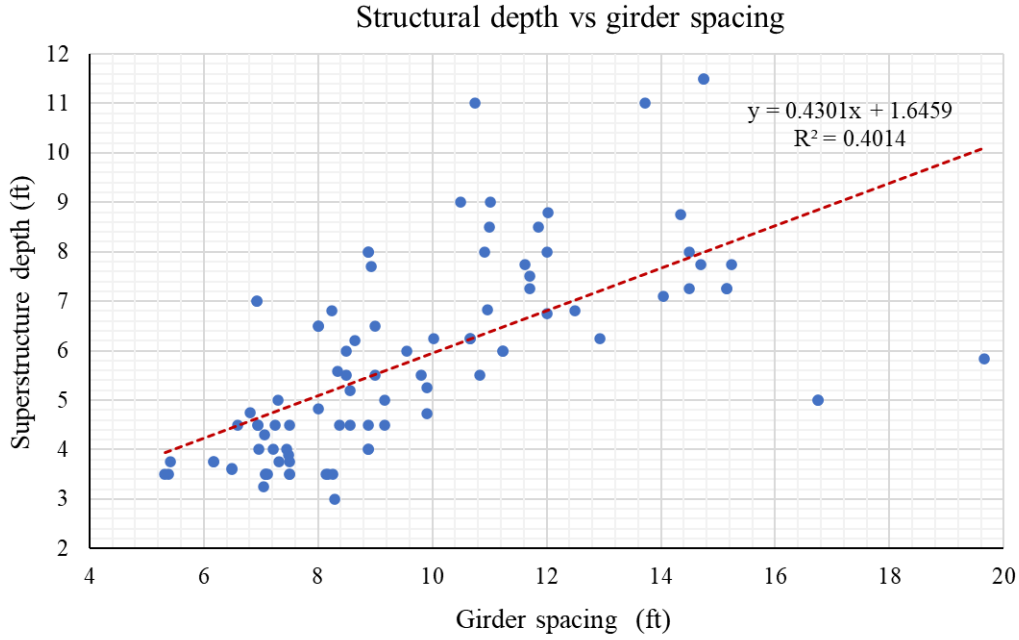

(b) Structural depth vs. girder spacing

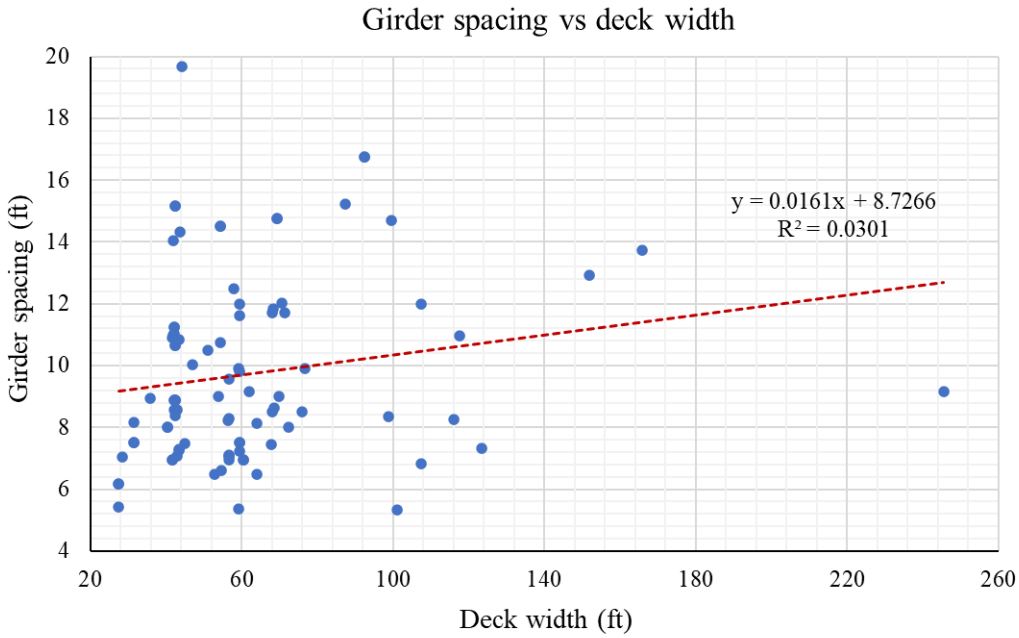

(c) Girder spacing vs. deck width

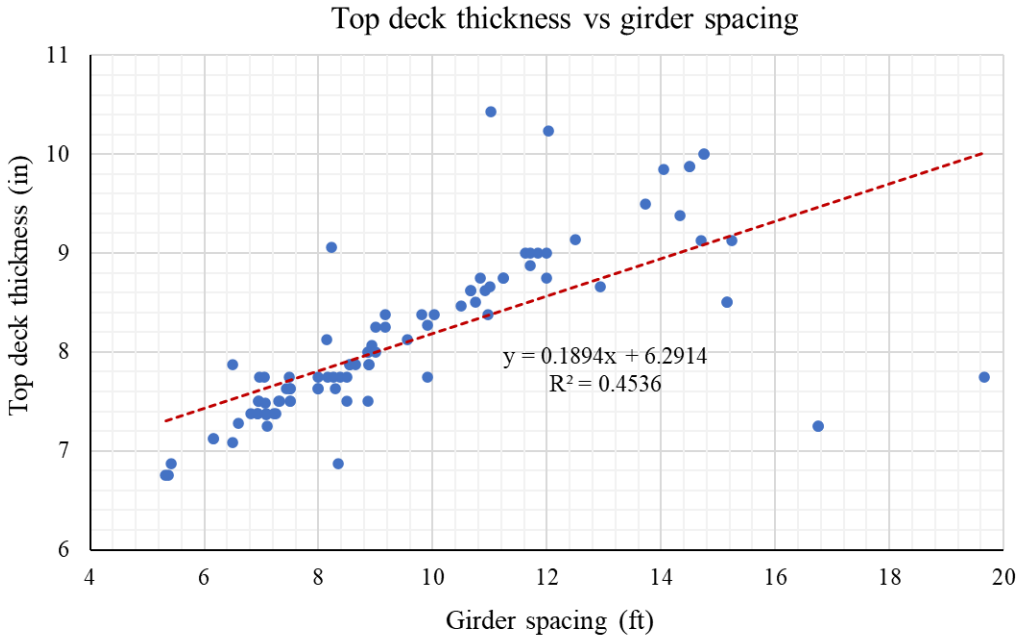

(d) Top deck thickness vs. girder spacing

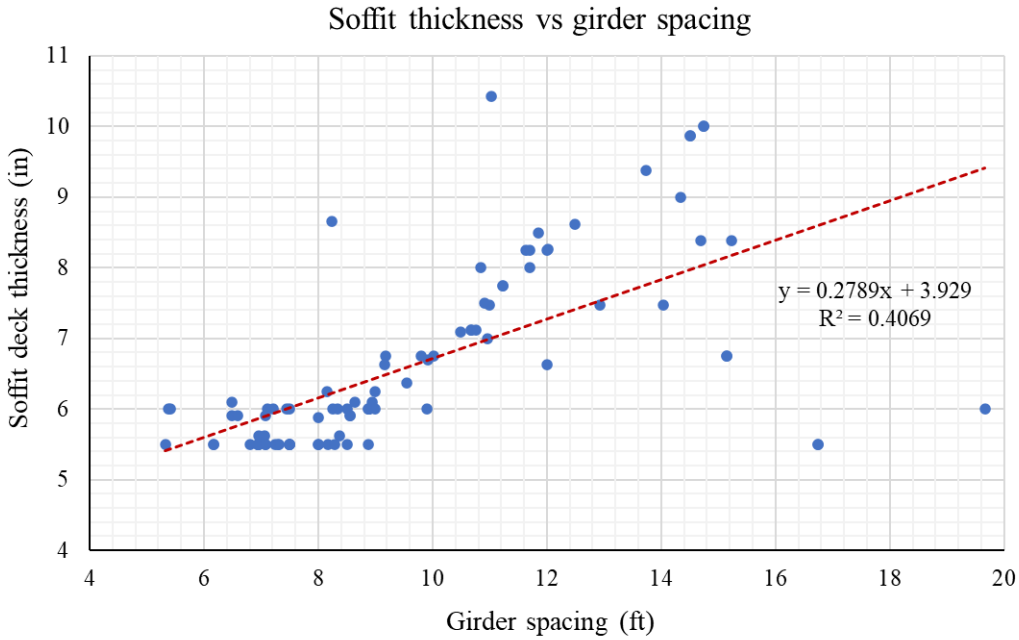

(e) Soffit thickness vs girder spacing

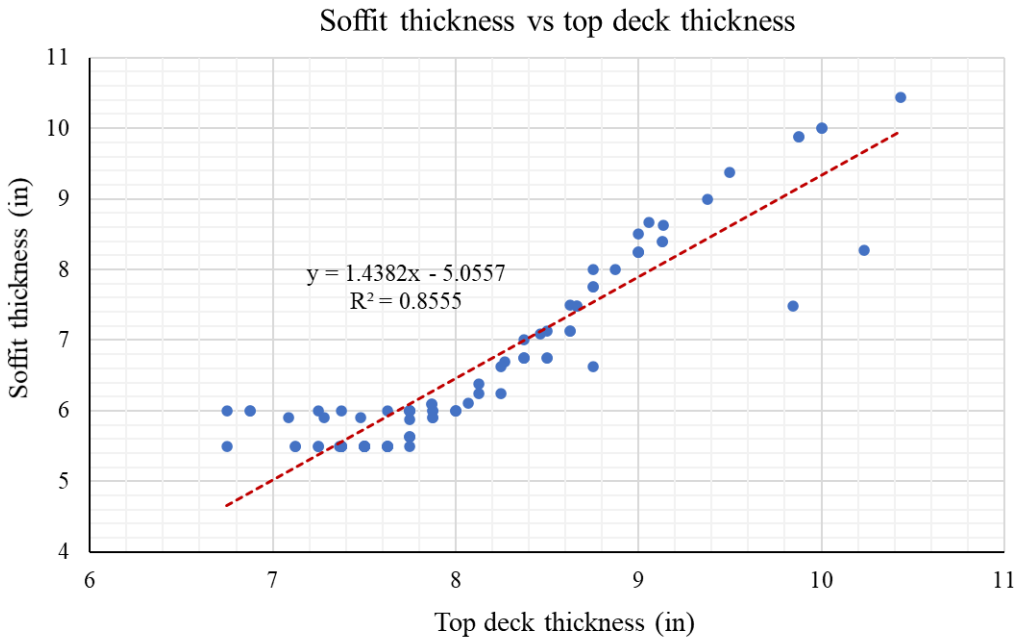

(f) Soffit thickness vs. top deck thickness

Figure 5.1. Correlations between design parameters of the box girder bridges in the database

5.2 Influence due to Girder Depth

Because the girder depth is an important parameter in the refined bridge deck analysis, a case study was conducted to investigate its influence on the load demands of bridge decks using the rigid support modeling strategy. The larger box girder prototype bridge model (RSM) was further revised to lower its original girder depth 11'-6" down to 2'-6" to measure the difference in the

critical load demands. To save computational efforts, only the most critical minor cases under the 100-psi tire patch load of HL-93 single axle were analyzed, and the tire patch load was applied at the mid-span of the RSM. The maximum average load demands within an influence area with L = 66" (see **Figure 3.8** for the definition of L), are summarized and compared for both the original and low depth cases, as described in **Table 5.2** to

Table 5.4. In each table, the maximum difference (%) is highlighted in red. It can be seen that the change in bridge depth results in some significant differences, the lower depth leads to smaller positive moment (-7.04%), yet higher negative moment (21.89%) and shear (3.94%). This result makes sense because a smaller web depth results in a higher vertical/lateral stiffness of the web, such that the web draws more negative moment and shear at the joint/connection, while the positive moment at mid-girder spacing drops down accordingly. And hence, the selection of an appropriate girder depth for the production run requires thorough consideration.

Table 5.2. Comparison for maximum average positive moment (L = 66")

Cases	Max Avg. $+M_x$ (lbf-in/in, depth = 2'-6")	Max Avg. $+M_x$ (lbf-in/in, depth = 11'-6")	Diff. (%)
Face of Barrier	1671.56	1677.35	-0.35
[a]Case-c	2911.67	3042.70	-4.31
[a]Case-d	2838.70	2984.44	-4.88
Exterior Cell	2316.91	2492.24	-7.04
2nd Web	1515.27	1520.53	-0.35
2nd Cell	2308.36	2478.91	-6.88
3rd Web (CL bridge)	1502.32	1507.14	-0.32

[a]Two critical minor cases for load demand, the same for the following two tables

Table 5.3. Comparison for maximum average negative moment (L = 66")

Cases	Max Avg. $-M_x$ (lbf-in/in, depth = 2'-6")	Max Avg. $-M_x$ (lbf-in/in, depth = 11'-6")	Diff. (%)
Face of Barrier	-2728.67	-2673.97	2.05
Case-c	-2411.30	-1978.18	21.89
Case-d	-3353.18	-2917.50	14.93
Exterior Cell	-3232.03	-2862.64	12.90
2nd Web	-1856.64	-1823.52	1.82
2nd Cell	-2582.45	-2289.92	12.77
3rd Web (CL bridge)	-1837.00	-1802.91	1.89

Table 5.4. Comparison for maximum average shear (L = 66")

Cases	Max Avg. V_z (psi, depth = 2'-6")	Max Avg. V_z (psi, depth = 11'-6")	Diff. (%)
Face of Barrier	26.25	25.73	2.02
Case-c	36.18	34.81	3.94
Case-d	33.35	32.30	3.26
Exterior Cell	26.92	26.51	1.55
2nd Web	29.08	28.95	0.48
2nd Cell	26.40	25.94	1.75
3rd Web (CL bridge)	28.54	28.40	0.49

5.3 Influence due to Cross-Slope

The cross slope of the bridge is an important parameter not covered in the bridge girder database. To fill this gap, a case study was conducted on the extreme 10º cross-slope case to estimate its influence on the load demands. According to AASHTO 3.6.3 and 3.6.4 (AASHTO 2017), braking force and centrifugal force should be applied horizontally at a distance 6' above the roadway surface. Such that the centroid of a HL-93 truck is assumed as 6' above the deck surface as well. The free body diagram of the single axle load can be presented in **Figure 5.2**, where R_1 = reaction of the left tire (kip); R_2 = reaction for the right tire; F_1 = friction force of the left tire; F_2 = friction force of the right tire; W = self-weight of the single axle.

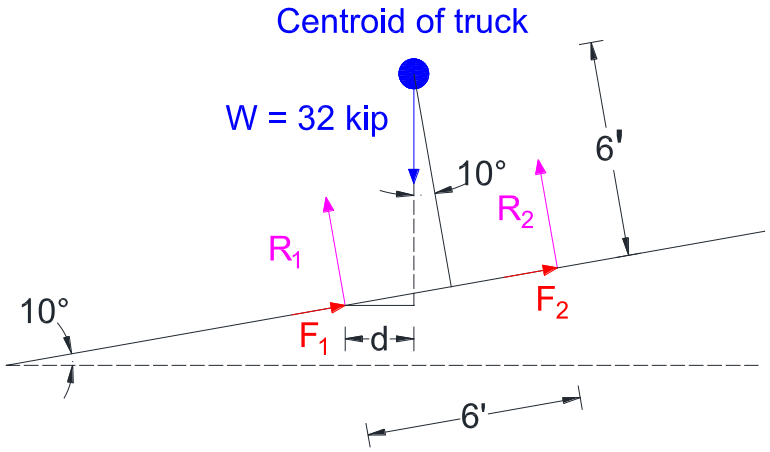

Figure 5.2. FBD of HL-93 axle load on a 10° cross-slope

The moment arm of the self-weight with respect to the center of the left tire is given as:

$$d = \left(\frac{6}{2} - 6tan10°\right) cos10° = 1.91' \tag{5.1}$$

Take the moment about the center of the left tire and it yields:

$$\sum M_1 = -Wd + 6R_2 = 0 \tag{5.2}$$

$$R_2 = 32 \times \frac{1.91}{6} = 10.19\ kip \tag{5.3}$$

Construct the equilibrium equation in vertical direction and it yields:

$$\sum F_y = (R_1 + R_2)cos10° - 32 = 0 \tag{5.4}$$

$$R_1 = \frac{32}{cos10}° - R_2 = 22.30\ kip \tag{5.5}$$

As a result, the size of the tire print changes to 16×13.94" for R_1 and 16×6.4" for R_2 assuming the same 100 psi tire pressure (width of tire print keeps unchanged as 16", as shown in **Figure 5.3**). Based on the RSM of the larger box girder prototype bridge, the most critical transverse positions of the axle patch load were analyzed for the 10° cross-slope case. The sequence of the large (R_1) and small tire print (R_2) was also considered to produce the maximum load demands. The results comparison between the zero and 10° cross-slope cases are summarized in

Table 5.5. It can be seen that the 10° cross-slope significantly increases the load demand in both the positive moment and shear of the deck slab, while the negative moment demand doesn't change much. However, the observed large difference in load demands is caused by the extreme 10° cross-slope, the most common cross-slope ranging within 1.5º – 2º only produces a small difference. Thus, the cross-slope will not be considered in the production run for simplicity.

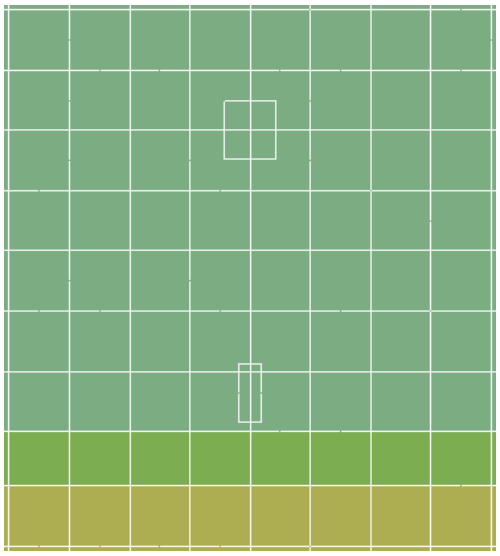

Figure 5.3. Example of the two tire prints with different sizes under 10° cross-slope

Table 5.5. Comparison of the critical avg. load demands between zero and 10° cross-slope case for the large box girder example (L = 66")

Load Demand	Zero Cross-Slope	10° Cross-Slope	Diff. (%)
Max avg. $+M_x$ (lbf-in/in)	3042.70	4154.11	36.53
Max avg. $-M_x$ (lbf-in/in)	-2917.50	-2826.80	-3.11
Max avg. V_z (psi)	34.81	41.62	19.57

5.4 Influence due to Length of Influence Area

As described above in Chapter 3.3.1, the average load demands within the influence area were adopted for the validation of the RSMs, as well as the different cases studies that followed. The selected 66" – 70" range of the length L was deemed as sufficient for the validation purpose, however, it can be inappropriate for a production run. A smaller L will always lead to a larger load demand, and the extreme case is when L approaches zero, the load demand approaches the peak number on the color bar of the load demand contour [**Figure 2.14**] and it is mesh sensitive. To quantify the relationship between the total load carried by the deck influence area vs. the length of the influence area, the maximum integrated load demands within the influence area are extracted from the two prototype RSMs, with a length of the influence area varying within 20" – 320". The results for both the small and larger box girder prototype bridges are summarized in **Table 5.6** and **Table 5.7**, respectively, subjected to the HL-93 patch tire load applied at CL bridge with 100 ksi tire pressure. In both tables, the load demand ratio is the maximum integrated load demands of the influence area divided by the maximum integrated load demands of the entire bridge deck. It indicates the percentage ratio of the applied tire patch load that the selected influence area can carry. In **Figure 5.4** and **Figure 5.5**, the development of the load demand ratios vs. the length of the influence area has also been visualized for both the small and large box girder case, respectively.

Table 5.6. Load demand ratio at different length of the influence area (small box girder)

Length of influence area L (in)	Max $+M_x$ (lbf-in)	Load demand ratio (%)	Max $-M_x$ (lbf-in)	Load demand ratio (%)	Max V_z (lb)	Load demand ratio (%)
20	50168	39.55	-40101	27.95	9614	37.24
40	82748	65.23	-74131	51.67	16103	62.38
60	102246	80.60	-99465	69.33	20122	77.95
80	113936	89.82	-116862	81.46	22642	87.71
100	120666	95.12	-128201	89.36	24173	93.64
120	124365	98.04	-135278	94.29	25059	97.08
140	126266	99.54	-139504	97.24	25544	98.95
160	127142	100.23	-141899	98.91	25789	99.90
180	127464	100.48	-143160	99.79	25897	100.32
200	127508	100.51	-143750	100.20	25931	100.45
220	127428	100.45	-143964	100.35	25928	100.44
240	127309	100.36	-143985	100.36	25910	100.37
260	127190	100.26	-143918	100.32	25888	100.29
280	127090	100.19	-143822	100.25	25868	100.21
300	127012	100.12	-143729	100.18	25851	100.14
320	126955	100.08	-143649	100.13	25838	100.09
Entire Deck	126855	100.00	-143465	100.00	25814	100.00

Note: all the results are under the axle load case-CL bridge; results beyond 100% might be caused by the local stress fluctuation of the FE approximation.

Table 5.7. Load demand ratio at different length of the influence area (large box girder)

Length of influence area L (in)	Max $+M_x$ (lbf-in)	Load demand ratio (%)	Max $-M_x$ (lbf-in)	Load demand ratio (%)	Max V_z (lb)	Load demand ratio (%)
20	46871	41.41	-43923	22.78	8544	34.81
40	77680	68.64	-82146	42.61	14153	57.66
60	96061	84.88	-112275	58.23	17707	72.14
80	106816	94.38	-134887	69.96	20090	81.85
100	112690	99.57	-151483	78.57	21687	88.36
120	115558	102.10	-163542	84.82	22746	92.67
140	116649	103.07	-172263	89.34	23441	95.51
160	116746	103.15	-178550	92.61	23895	97.36
180	116335	102.79	-183067	94.95	24188	98.55
200	116134	102.61	-186295	96.62	24376	99.32
220	115846	102.36	-188586	97.81	24492	99.79
240	115481	102.03	-190193	98.64	24562	100.07
260	115104	101.70	-191305	99.22	24602	100.24
280	114752	101.39	-192058	99.61	24621	100.31
300	114440	101.12	-192553	99.87	24628	100.34
320	114174	100.88	-192865	100.03	24627	100.34
Entire Deck	113178	100.00	-192808	100.00	24544	100.00

Note: all the results are under the axle load case-CL bridge; results beyond 100% might be caused by the local stress fluctuation of the FE approximation.

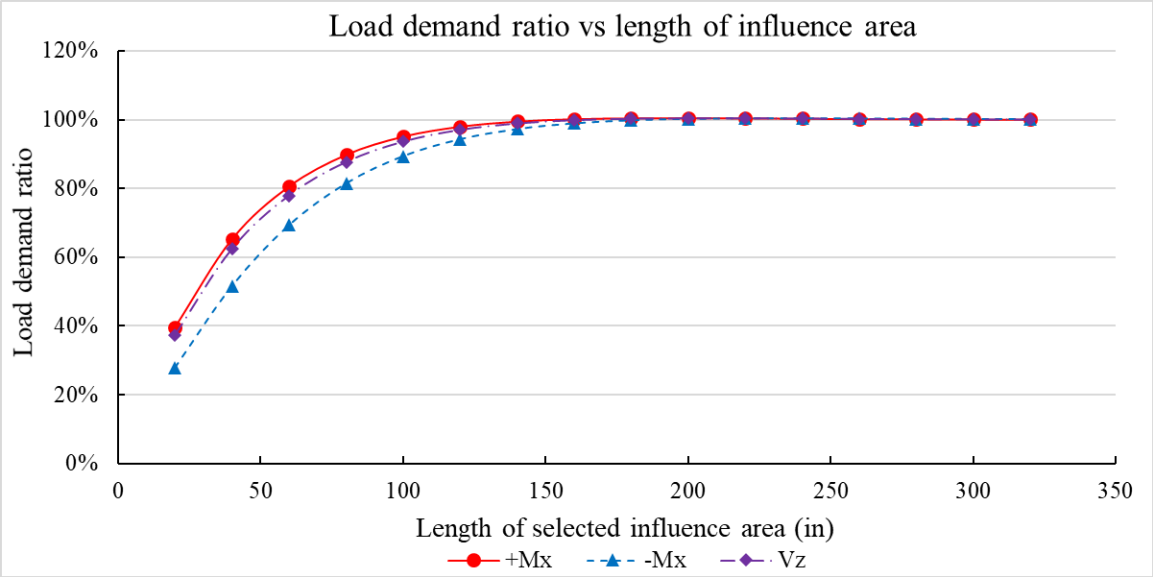

Figure 5.4. Load demand ratio vs length of influence area (small box girder)

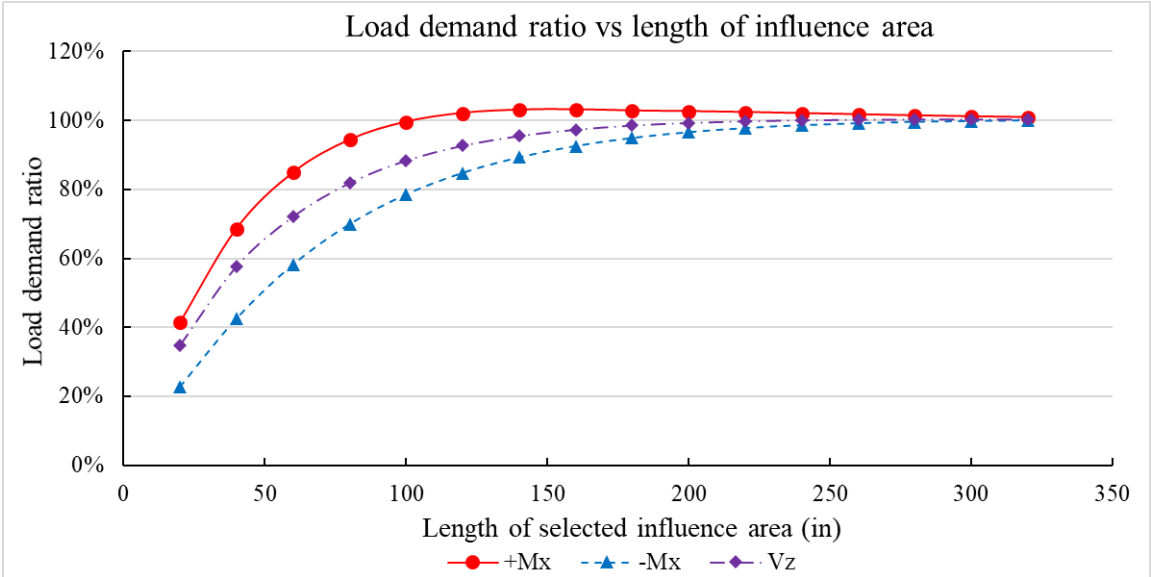

Figure 5.5. Load demand ratio vs length of influence area (large box girder)

It can be seen that with the increase of the length L, the load demand ratio gradually increases and is approaching 100%, but the increase rate steadily drops down to zero. If the 95% load demand ratio is deemed as the threshold beyond which the further increase in L does not noticeably affect the load demands, then the effective L = 100" for $+M_x$, L = 120" for $-M_x$ and L = 100" for V_z of the small box girder case, and L = 80" for $+M_x$, L = 180" for $-M_x$ and L = 140" for V_z of the large box girder case. By comparison, the width of the primary strip specified in AASHTO Table 4.6.2.1.3-1 (AASHTO 2017), equivalent to the length of the influence area, is L = 84.6" for $+M_x$; and L = 74.6" for $-M_x$ of the small box girder case, and L = 125" for $+M_x$; and L = 93" for $-M_x$ of the large box girder case. On the other hand, as mentioned in Chapter 3.3.4, the punching shear failure perimeter equals to the tire print dimension plus the thickness of the deck. Such that if the punching shear failure is more critical than the flexural failure, the effective length of the influence

area L should be 18" for the small box girder, and 20" for the large box girder. The selection of an appropriate length L requires great deliberation and will significantly affect the load demands obtained from the refined FE models. In this study, a fixed L = 20" of the bridge RSMs with different girder spacings was recommended to yield load demands from the production run for both consistency and conservatism.

5.5 Summary

This chapter summarizes the ranges of the main parameters in the box girder bridge design from the provided bridge database in CA, and the relationships among some of the parameters are derived from regression analysis. Based on the RSM determined for the production run, the governing parameters can be narrowed down to the girder spacing, girder depth, and number of cells when the load demands of bridge decks are the focus. Case studies on the influence on the deck load demands due to girder depth, cross-slope, and length of the influence area were also conducted. The result indicates that the change in the girder depth can significantly affect the load demands of bridge decks, in other words, the frame action in the box girder should be considered to yield the most accurate results. In addition, the cross-slope also has a positive influence on the load demands of bridge decks, and this effect can be significant when the cross-slope equals to 10º. However, for a typical range of 1.5–2º, its influence is negligible. Furthermore, the selection of the length of the influence area L (or strip width as defined per AASHTO) can lead to a very different result in the average load demands within that area. A longer L means a smaller average load demands and is also less conservative. Provided that punching shear failure is typically the predominant failure mode of bridge decks subjected to concentrated tire patch loads, a length of influence area L = 20" is recommended, corresponding to the approximate location where punching shear failure usually occurs, to ensure conservatism in the production run.

6 PRODUCTION RUN OF REFINED DECK ANALYSIS

6.1 Initial Workplan

The inclusion of the bridge girders in the FE model, i.e., consideration of frame action, yields a more representative bridge deck behavior under the vehicle load and it has a significant influence on the load demands of bridge decks, as discussed in the previous chapter. Although the adoption of the RSM with girders has significantly decreased the workload of FE modeling by excluding the span configurations, the possible variation in the girder depth still requires a big database of FE models to cover all the possible design cases. To this end, after a comprehensive discussion with the TAC team, a matrix has been proposed to yield the load demands of bridge decks using the RSM without girders for simplicity. Meanwhile, the two existing prototype box girder bridges using the true refined modeling method with girders and considering critical span configurations will be modified and analyzed as the controlled groups to obtain some tangible results under the most representative situations. The analysis matrix containing all the geometric details of interest on the bridge models is summarized in **Table 6.1**.

Table 6.1. Deck slab rigid support (no girder) analysis matrix

Spacing (ft)	No. of Cell	MTD 10-20 Deck Thickness (in)	Clear Overhang Width (ft)	Total Deck Width (ft)	Type 732 Barrier (in)	Max No. of Design Lanes
4	4	7	2	21	17	1
6	4	7.125	3	31	17	2
9	4	8.125	3	43	17	3
12	4	9.125	4	57	17	4
15	4	10.375	4	69	17	5
9	2	7.125	3	25	17	1
15	2	10.375	4	39	17	2

Although some updates or revisions may be applied later to reflect the findings in the FE analysis, the workplan of the production run is preliminarily determined as the following:

(1) Run the deck slab rigid support (no girder) analysis based on the matrix to spot check the AASHTO Appendix A4 (AASHTO 2017) for the current design specifications:
   - Use the length of influence area *L* (strip width) = 20”
   - Only capture the shear stress for spacing = 9’ and 15’
   - Run the entire length of truck or the truck axle
   - Capture raw data
   - Apply impact and multiple presence factors to the raw data

(2) Utilizing the existing two prototype bridge models (longitudinal Case C with 2 spans), run the true refined analysis for both the small and large box girder bridges. Compare the raw refined model results to the raw matrix results for spacing = 9’ and 15’;

(3) Revise the existing two prototype bridge models into 2-cell for the true refined analysis. Compare the raw refined results to the raw matrix results for spacing = 9’ and 15’;

(4) Focus on HL-93 and P-15 loading;

(5) Use a tire pressure of 125 psi;

(6) Capture the average shear stress within the deck thickness;

(7) No deck cross slope;

(8) Investigate available fatigue models and assess shear stress limits;

(9) If time permits, repeat Item (2) and (3) for "I" girder; and
(10) If time permits, run other vehicle types.

This workplan aims to reach a balance between the accuracy or reliability of the FE models and the heavy modeling workload, as well as gain useful raw data from the true refined models for comparison. The higher 125 psi tire pressure preferred in this production run is consistent with the ever-growing trend of using super single tires on trucks in CA.

6.1.1 Case study on type of truck load

It is important to determine whether the truck axle or the entire truck should be applied to the RSM to yield the load demands. The first RSM without girders was constructed with a spacing of 15", and the representative minor axle patch load cases (HL-93 axle), namely, (1) face of barrier; (2) exterior cell; (3) 2nd web; (4) 2nd cell; and (5) 3rd web (CL bridge) in **Table 3.3** were firstly applied to the model to yield the average load demands within a 20" strip. Likewise, the same five minor cases were also applied to the same RSM but using the entire HL-93 truck to obtain the load demands of decks for comparison. The yielded result of the two different truck load types indicates a growth of 3.4% in max positive moment, 0.9% in max negative moment, but the same max shear by using the entire HL-93 truck.

On the other hand, the P-15 truck was studied to spot check the difference between the entire P-15 truck and the P-15 axle load. Unlike the HL-93 truck, the P-15 truck is very long and has many axles (**Figure 6.1**), such that it is necessary to firstly check if the load demands at different axles of the P-15 truck in the RSM have significant differences. For this purpose, the entire P-15 truck was placed at two transverse positions of the RSM, i.e., (1) face of barrier; and (2) CL bridge. As shown in **Figure 6.2**, the critical load demands at each axle were extracted and compared to examine the difference caused by the different longitudinal position on the RSM. The normalized load demands at different axles are summarized and compared in **Table 6.2** and **Table 6.3**, and it can be seen that the different longitudinal positions of axles on the RSM does not cause a significant difference in the load demands. Hence, the load demands at the first axle in the rear of the full P-15 truck load case (rear-1) were compared to the single P-15 axle load case. Again, the five representative transverse minor cases were analyzed, and the load demands were compared for both the entire P-15 truck and the truck axle only cases. The result indicates a growth of 4.3% in max positive moment, 5.6% in maximum negative moment, but the same maximum shear by using the entire P-15 truck.

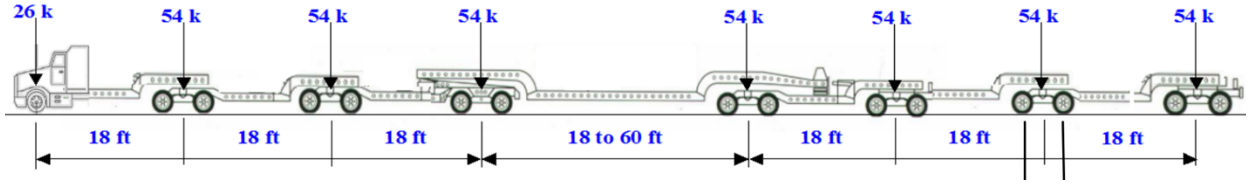

Figure 6.1. Illustration of CA P-15 truck load (CA Amendments 2014)

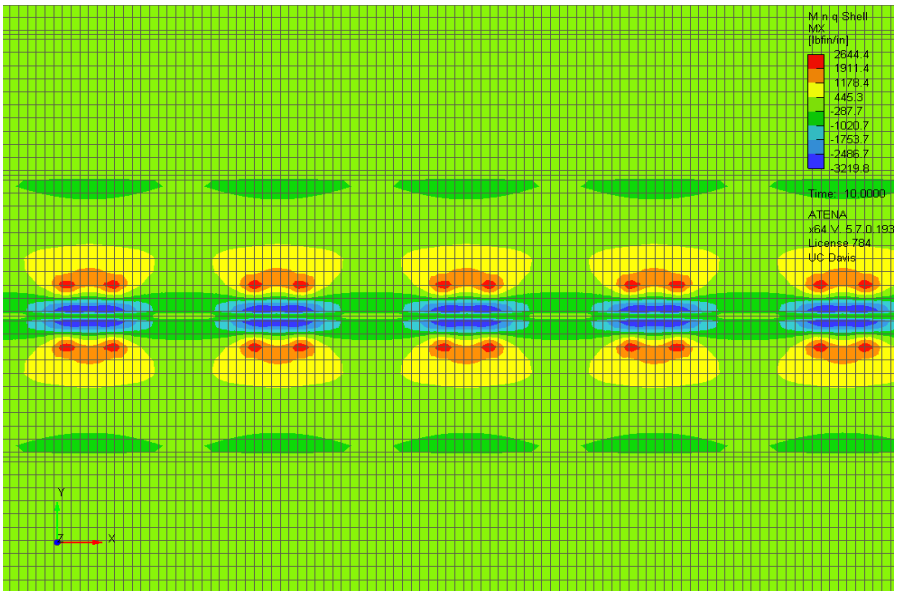

Figure 6.2. Example of transverse moment result of the entire P-15 truck placed at CL bridge of the RSM (lbf·in/in)

Table 6.2. Normalized load demands at different axles of the P-15 truck (face of barrier)

Face of Barrier	Front-2	Front-3	Front-4	Rear-1	Rear-2	Rear-3	Rear-4
Avg. Max. $+M_x$ (lbf·in/in)	99.77%	96.75%	98.60%	98.59%	96.71%	98.97%	100.00%
Avg. Max. $-M_x$ (lbf·in/in)	99.82%	97.27%	98.82%	98.82%	97.29%	100.00%	96.29%
Avg. Max. Q_{yz} (psi)	99.97%	98.21%	99.91%	99.91%	98.22%	100.00%	98.15%

Table 6.3. Normalized load demands at different axles of the P-15 truck (CL bridge)

CL Bridge (Normalized)	Front-2	Front-3	Front-4	Rear-1	Rear-2	Rear-3	Rear-4
Avg. Max. $+M_x$ (lbf·in/in)	100.00%	97.97%	99.68%	99.68%	97.97%	97.97%	98.68%
Avg. Max. $-M_x$ (lbf·in/in)	100.00%	97.22%	98.75%	98.75%	97.22%	99.96%	96.93%
Avg. Max. Q_{yz} (psi)	100.00%	98.04%	99.65%	99.66%	98.04%	99.96%	98.14%

From the case study on the type of truck load, the advantage of using the entire truck to apply the vehicle load is marginal and it only produces a slightly more critical results in moment by approximately 5%. Hence, it is determined that using the entire truck is unnecessary for the RSM. Instead, the axle patch load should be adopted for the following production run to save the computational effort and reduce the post-processing workload.

6.1.2 Methodology of load combinations

The biggest challenge in the production run is the load combinations of different vehicles. Although the concept of influence line or influence surface has often been used to determine the critical position of the load where the load demands at the point of interest reaches its maximum, the situation can be very complicated for a 3D bridge deck model under more than one truck/axle load. Many commercial software packages provide the function of automatically generating the

influence line/surface of the target beam/plate, but ATENA does not have such a built-in module. Of course, the influence surface of the bridge deck can be obtained by using the Müller-Breslau's principle, which describes that the influence line/surface resembles the deflection that the structure displays after releasing the restriction on the point of interest and applying a corresponding unit displacement/rotation at that point. However, this step needs to be repeated for every point of interest, and calculation of the structural deformations for all the situations is time intensive. Alternatively, a "brute force" method can also be used to generate the influence line/surface. It requires the structural analysis of the model independently for a unit load applied at every single element node of the structural surface. The load demands of any point with respect to the position of the unit load can be mapped to form the influence line/surface (Adams et al. 2019). This method is computational inefficient when the structural surface has a fine mesh, and relatively few influence lines/surfaces are required.

Neither of the two introduced method will be adopted in this research to determine the influence surface of the bridge deck, because it still needs trial and error to determine the exact locations of trucks to yield the most critical load demands at the point of interest with the given influence surface. In this study, an approximate linear interpolation and superposition method was proposed to estimate the maximum load demands of bridge decks under multiple axle loads. The workflow of this linear interpolation methodology can be described as the following steps, using the load combination of two trucks (two pairs of axle loads) as an example:

(1) Apply the single pair of axle patch loads to the mid-span of the RSM and move it transversely from the end of deck to the CL bridge with a fixed distance, e.g., 5%×spacing. Extract and save all the load demands at each cut (point of interest) across the entire section within the 20" strip independently at each transverse load case. In other words, the load demand envelope of each cut across the cross-section can be mapped from this analysis. For the load demand envelope of the cuts beyond the CL bridge, a simple mirroring operation can be performed because of the structural symmetry;
(2) Select any point of interest by its transverse coordinate, and it is not necessary the position of the cut. If the position is in between two consecutive cuts, a linear interpolation can be conducted to yield an approximate magnitude of the load demand;
(3) Virtually fix the position of the 1st pair of axle loads, i.e., 1' away from the face of barrier, and virtually place the 2nd pair of axle loads next to it with a minimum spacing of 4' as specified in AASHTO (AASHTO 2017);
(4) Calculate the load demand at the point of interest by combining the effect caused by each truck. This effect has already been collected from step (1) for each transverse position of the axle load. For the position of virtual axle load in between two consecutive transverse cases, a linear interpolation will be conducted to obtain the approximate load demand at the point of interest. Save the load demand as the result of this load combination;
(5) Virtually move the 2nd pair of axle loads transversely toward the other end of the deck with a preset distance, e.g., 2". Calculate and save the combined load demand at the point of interest of this load combination;
(6) Repeat step (5) until the 2nd pair of axle loads reaches the minimum spacing of 1' from the barrier on the other side of the deck;
(7) Virtually move the 1st pair of axle loads transversely toward the other end of the deck with the same preset distance in step (5) and virtually place the 2nd pair of axle loads next to it as that in step (3);
(8) Repeat steps (5) – (7); and

(9) Yield the maximum load demand at the point of interest, as well as the relative positions of the two pairs of axle loads at the critical condition.

This algorithm was successfully programmed using Python and conducted for both the one truck case and two truck case. And the visualized raw results without any factor are presented in **Figure 6.3** for the two truck case, where y is the transverse coordinate of the RSM, y = 144" is the CL 1st cell, y = 228" is the interior face of the 2nd web, and y = 408" is the interior face of the 3rd web. The transverse axis in each subplot represents the distance between EOD and left tire of the 1st pair of axle loads. Of course, the program can yield the maximum load demand at any position of the cross-section, and it can also be further extended to the case of three or more trucks. The accuracy of this linear interpolation and superposition methodology highly depends on the number of transverse load cases in step (1), a more precise result can be anticipated with a shorter moving distance of the axle loads but at the cost of higher computational efforts.

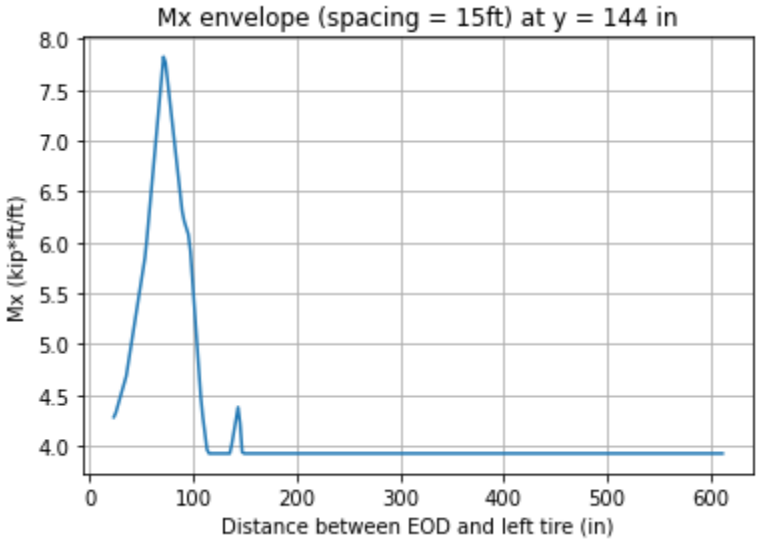

(a) Positive moment envelope at y = 144" (CL 1st cell)

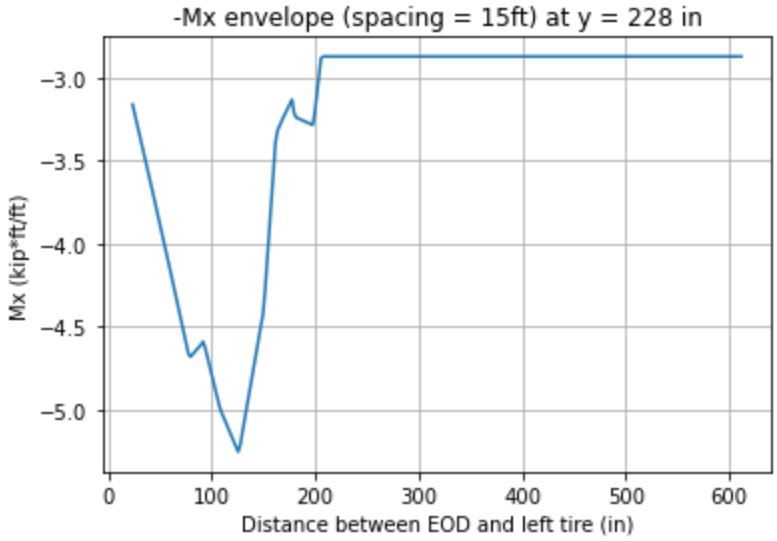

(b) Negative moment envelope at y = 228" (interior face of the 2nd web)

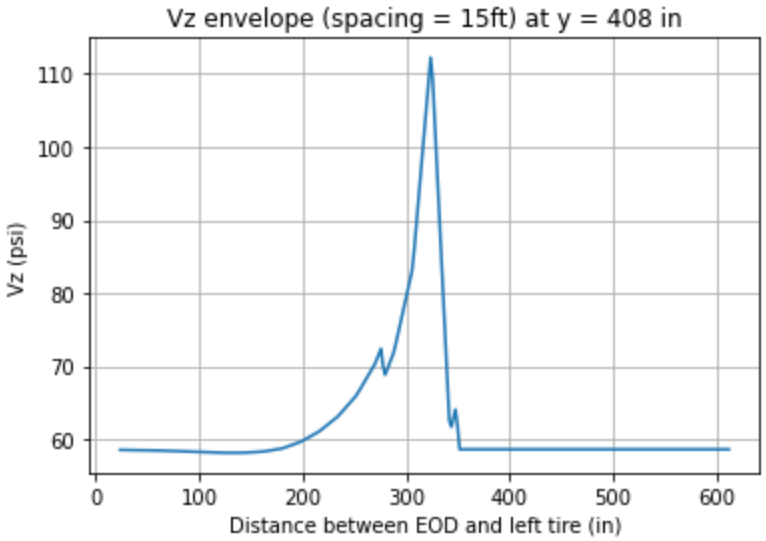

(c) Shear envelope at y = 408” (interior face of the 3rd web)

Figure 6.3. Visualized load demand at the point of interest under the two trucks combination in Python

6.1.3 Summary

This section elaborates the workplan of the production run which covers both the RSMs without girders, and the true refined FE models. The analysis matrix along with the necessary model details are provided to guide the FE modeling procedure. The case study on the type of truck load was conducted, and it is confirmed that the longitudinal positions of different axles of the P-15 truck barely affect the critical load demands of bridge decks. In addition, the entire truck only produces roughly 5% more load demands than a corresponding single axle load for both the HL-93 and P-15 truck case based on the RSM. Hence, it is determined that only the axle load will be adopted for the production run. Moreover, the methodology of load combinations of multiple trucks is introduced, and the algorithm and calculation examples are presented using the Python program. It verifies that the proposed linear interpolation and superposition approach is an efficient and practical alternative to the more complicated methods based on the concept of influence line/surface following either the Müller-Breslau's principle or the “brute force” approach.

This also concludes the research conducted during the first phase of the project. The content in the subsequent phase focuses on production run. Changes in the RSM analysis matrix and strategies for production run was made as outcomes of discussion and agreement with Caltrans TAC team to accommodate the research needs with the progress of the project.

6.2 Production Run using RSM under HL-93

The aim of this part of the study is to consider all possible combinations of placing one HL-93 truck on the bridge deck, to find the maximum values of $+M$, $-M$, $+V$, and $-V$ for each case, and to identify the place or locations where these maximum values occur. Designing a bridge deck to accommodate two HL-93 trucks involves a vast number of possible combinations, making it

challenging to identify the most critical scenarios for design purposes. **Table 6.4** presents the updated matrix of the deck slab analysis with rigid supports (no girder) upon final discussion with the Caltrans TAC team. According to this table, the deck slabs with 4 ft and 6 ft girder spacing have a minimum thickness of 8 in, while the deck slab with 9 ft girder spacing has a minimum thickness of 8.125 in. One truck was modeled for the deck slab with 4 ft girder spacing and the deck slab with 9 ft girder spacing and 2 cells, while two trucks combinations were used for the remaining deck slabs.

Table 6.4. Deck slab rigid support (no girder) analysis matrix

Girder Spacing (ft)	No. of Cell	BDM 9.4 Oct2021 Deck Thickness (in)	Clear Overhang Width (ft)	Total Deck Width (ft)	Type 732 Barrier (in)	Max No. of Design Lanes
4	4	8	2	21	17	1
6	4	8	3	31	17	2
9	4	8.125	3	43	17	2
12	4	9.125	4	57	17	2
15	4	10.375	4	69	17	2
9	2	8.125	3	25	17	1
15	2	10.375	4	39	17	2

In the first phase of this part of the study, to determine the maximum values of +M, -M, +V, and -V for every possible scenario and the locations in which the greatest values occurred, all possible configurations of placing one truck on the deck of the bridge were taken into account. In the second part of this study, we attempted to locate the critical point for $+M$, $-M$, $+V$, and $-V$ which is required in the design of the bridge deck by putting two trucks on the deck of the bridge and moving them transversely across the bridge according to the planned combinations. **Table 6.5** indicates 129 combinations for one truck, 397 combinations for two trucks, and 3 other combinations, adding up to a total of 529 combinations.

Table 6.5. Comprehensive analysis of truck combinations: examining a diverse range of case

Number of Trucks	Examined Cases	Number of Combinations
One truck	Case 1	129
Two trucks	Case 2, 3, 3.5, and 4	397
Total Number of combinations (considering one and two trucks)	All Cases	526 + 3 =529

1) **Case 1**: A single truck is initially positioned at the end of the deck. It is then moved transversely in increments equal to 10% of the distance between girders for each bridge, continuing until the second axle load crosses the bridge centerline;
2) **Case 2**: Two trucks are positioned at the deck's end with a 4 ft separation. In each subsequent step, the second truck is shifted transversely by 10% of the girder spacing until it reaches the opposite end of the bridge;
3) **Case 3**: Two trucks are initially placed at the deck's end, separated by 4 ft. In each step, both trucks are simultaneously shifted transversely by 10% of the girder spacing until the second truck reaches or passes the bridge's centerline;
4) **Case 3.5**: This is to account for the distance considered between the two trucks in Cases 3 and Case 4. In this case, the average distance of Cases 3 and 4 is applied for each girder spacing,

while the remaining combinations are kept the same as in Cases 3 and 4. Two trucks are initially placed at the deck's end, separated by this average distance. In each step, both trucks are simultaneously shifted transversely by 10% of the girder spacing until the second truck reaches or passes the bridge's centerline; and

5) **Case 4**: Two trucks are positioned at the deck's end, with a separation equal to the girder spacing for each deck slab. Both trucks are then moved simultaneously in increments of 10% of the girder spacing until the second truck reaches or passes the bridge's centerline.

To conduct a comprehensive analysis of the deck slab with rigid support (i.e., modeling without girders), a matrix-based study was performed to verify compliance with AASHTO Appendix A4 standards. Comparative evaluations were carried out between the refined results and the matrix results, with particular attention to the spacing values provided in **Table 6.4**. The axle load adopted for the production run was determined using the deck RSM.

The investigation primarily considered HL-93 (16 kip) loading, with a tire pressure of 125 psi and a tire patch dimension of 10×12.8 in. A strip width of 20 in was used, and special emphasis was placed on capturing shear stresses within the deck thickness. Additional loading scenarios, including HL-93, P-15, and EV3, were also analyzed using a tire pressure of 125 psi and no deck cross slope, with the objective of evaluating average shear stresses within the slab. Overall, the study sought to examine structural performance under various loading conditions and to refine the models for improved accuracy.

For the bridge deck slab modeling, the GID and ATENA programs were employed. A longitudinal deck length of 220 ft was selected, with widths and thicknesses varying as specified in **Table 6.4**. In the RSMs, the girders were assumed to be rigidly fixed. A master–slave connection was established between the upper surface of the deck and the applied patch load, which was represented by dummy patch loads in the model. The barrier was not modeled; therefore, the patch load was positioned at the mid-span in the longitudinal direction and at the deck edge in the transverse direction.

6.2.1 Summary of FE Model Details for the RSM Production Run

Two structural materials were used in the construction of the RSM. The concrete used a "solid elastic" material definition, which exhibited linear elastic behavior. This constitutive model requires an elastic modulus and Poisson ratio in its definition, and all concrete was assumed to be a typical 4000 psi grade with a modulus of elasticity of 3600 ksi and a Poisson ratio of 0.2. The so called "rigid supports" were also modeled as a "solid elastic" material, but with a modulus of elasticity 10 times larger than steel (290,000 ksi), which is a typical modeling technique to ensure rigid behavior. An example of this implementation is shown in Figure 6.4**.**

Figure 6.4. Example RSM cross-section showing bridge deck (blue) and rigid supports (pink) with pin support boundary conditions (red triangles).

The concrete slabs were modeled as 3D shell elements, with mesh dimensions of 10 in (longitudinal) by 12 in (transverse) in the plan view. The meshing in the thickness direction was handled in the shell definition so that all slabs, regardless of thickness, were divided into 4 equal sized layers. This created a uniform slab mesh independent of other model parameters (i.e. rigid support and dummy load locations).

As mentioned in previous sections, the tire patches were applied using an GID element type called "dummy surface", which is a 2D element with zero mass or stiffness, but to which loads can be applied. The number and location of tire patch loads will be addressed in their respective vehicle sections, but all patches were based on a 125-psi tire pressure acting over the full patch size. The dummy surfaces were slaved to the top surface of the deck to allow for easy iteration of the tire locations.

6.2.2 One HL-93 truck

In the analysis of the bridge deck slab under the HL-93 loading condition with a single truck, the truck is initially positioned at the deck's end. In each step, it is incrementally moved 10% of the girder spacing specified in **Table 6.6** until the second patch load, represented by a truck tire, surpasses the centerline of the deck width (**Figure 6.5**).

As a representative example, in modeling a 4 ft girder spacing deck slab with four cells, at first, the truck is positioned at the end of the deck, then it is moved transversely as 10% of the girder spacing (4×12×0.1 = 4.8 in). In this way, a total of 10 combinations is created until one of the patch loads (truck tires) crosses the centerline of the bridge. The remaining analyses for the other girder spacing cases are provided in Appendix C.

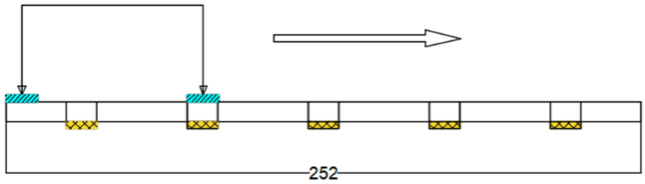

Figure 6.5. The placement of HL-93 load on deck slab with 4-ft girder spacing (first combination)

Table 6.6. Total number of combinations created for 4 ft girder spacing with one truck

No	Girder Spacing (ft)	Distance from Face of Tire to EOD (in)
1	4	0
2		4.8
3		9.6
4		14.4
5		19.2
6		24
7		28.8
8		33.6
9		38.4
10		43.2

Moment and shear diagrams for a 4 ft girder spacing are provided for each scenario, and corresponding moment, shear, and associated envelopes are presented in **Figure 6.6** – **Figure 6.9**.

Figure 6.6. Moment diagrams for deck slab with 4 ft girder spacing and single truck

Figure 6.7. Shear diagrams for deck slab with 4 ft girder spacing and single truck

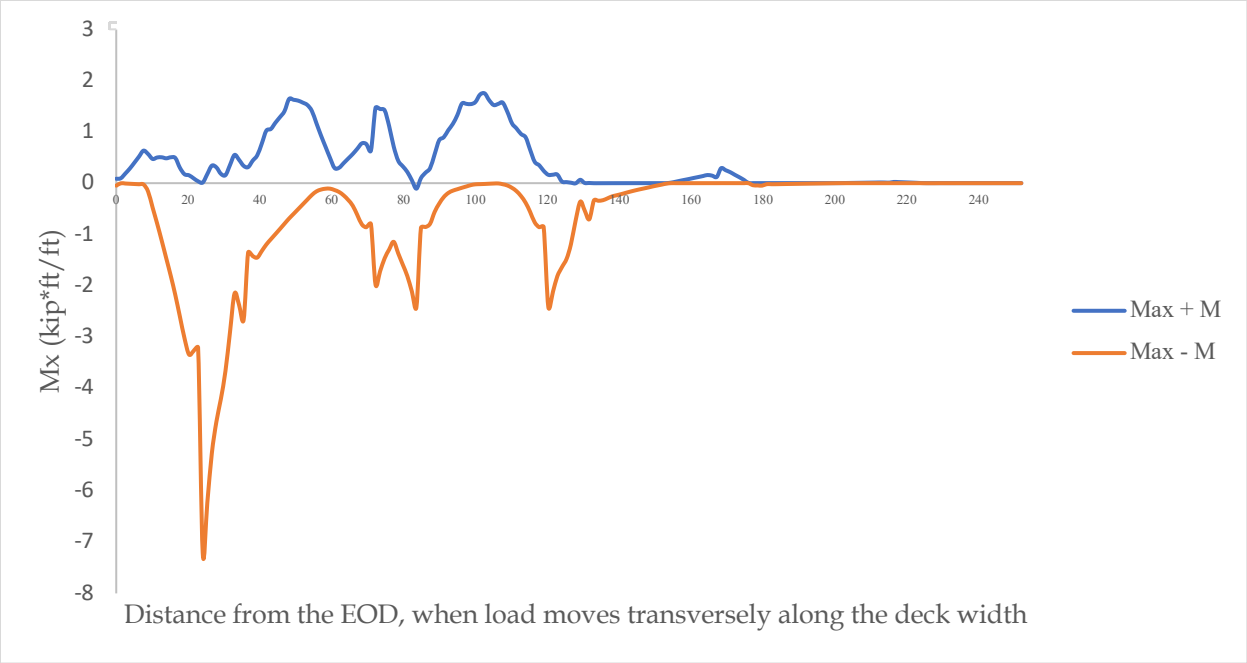

Figure 6.8. Moment envelope for deck slab with 4 ft girder spacing and single truck

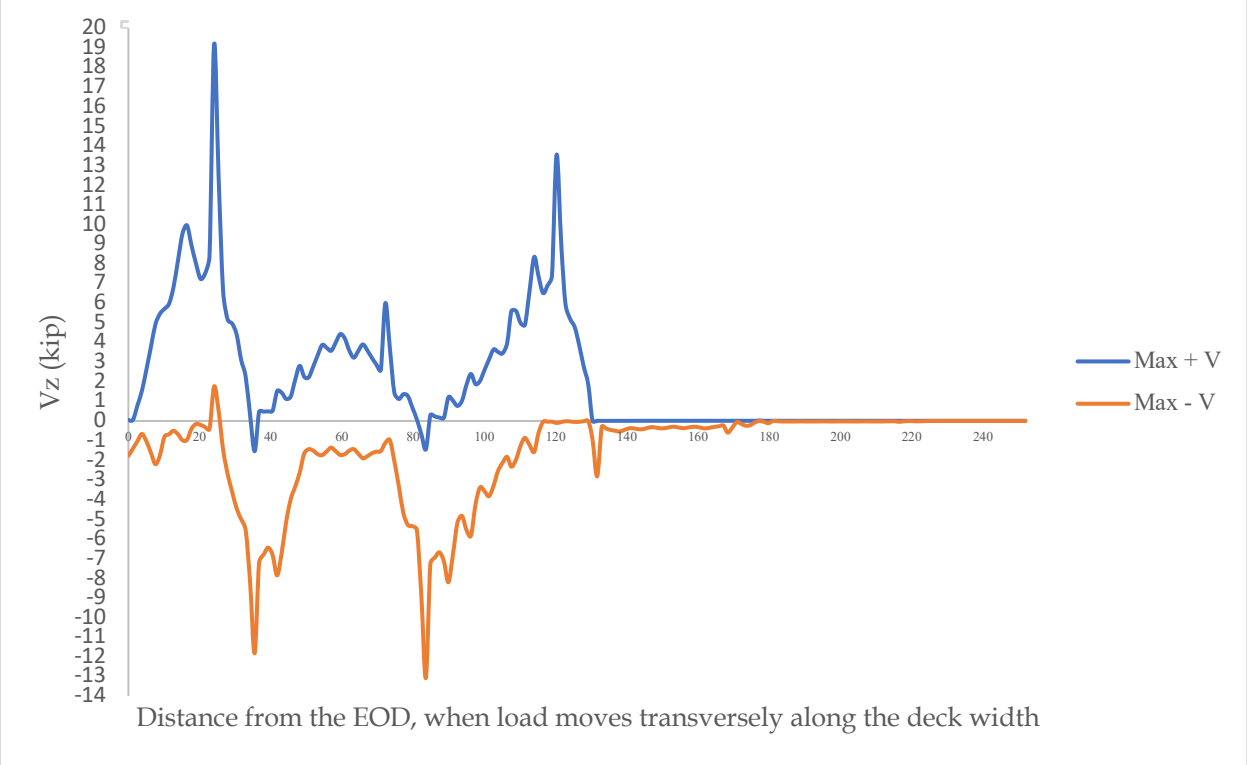

Figure 6.9. Shear envelope Figure for deck slab with 4 ft girder spacing and single truck

In **Figure 6.6**, it was discovered that the maximum positive moment for a 4 ft girder spacing deck slab occurred when the load patch was located 24 in away from the end of the slab, with a value of approximately 1.75 kip-ft/ft, and the maximum negative moment occurred when the truck patch load was located at the end of the slab, with a value of approximately -7.22 kip-ft/ft. In

Figure 6.7, it was discovered that the maximum positive shear for a 4 ft girder spacing deck slab occurred when the load patch was located 9.6 inches away from the end of the slab, with a value of approximately 19.16 kip, and the maximum negative shear occurred when the truck patch load was located at 14.4 inch away from the end of the slab, with a value of approximately -13.08 kip.

Comparisons: In **Table 6.7** and **Table 6.8**, the crucial positions of positive and negative moments, as well as positive and negative shear, relative to the truck's location for each girder spacing, are detailed. The row data from the Rigid Support Model is represented as "RSM" in the tables throughout the following chapters, including positive and negative moments and shear. The RSM(1+IM).m values represent only the factored positive and negative moments by multiplying the corresponding RSM values with a Dynamic Load Allowance factor of 1.33 and a Multiple Presence factor of 1.2. **Table 6.7** and **Table 6.8** present the outcomes specifically identifying the positions where the maximum values are achieved.

When examining the results for the maximum positive moment, it becomes apparent that as the distance between the girders increases, the maximum positive moment also increases. However, this increase is found to occur at a slower rate as the thickness of the deck increases.

Notably, in the cases in which girder spacing is 4 ft, the location of the maximum positive moment occurs between the second and third girder, while for all other girder spacing, the maximum positive Moment is located between the first and second girder. This information highlights the importance of the girder spacing and deck thickness on the distribution of loads and the resulting maximum moment.

Upon examining the results for the maximum negative moment for various deck configurations with differing girder spacing, it is evident that the maximum values are achieved when the load is applied at the end of the deck. Notably, the precise location at which the maximum values are attained aligns with the point at which the overhang commences.

This finding also showed that the overhang length plays a crucial role in the distribution of forces and ultimately impacts the magnitude of the moment generated in the structure. Therefore, careful consideration must be given to the overhang length in the design process to ensure the optimal distribution of forces and prevent any potential issues that may arise due to excessive moments. **Figure 6.10** displays the location at which the maximum negative moment is obtained.

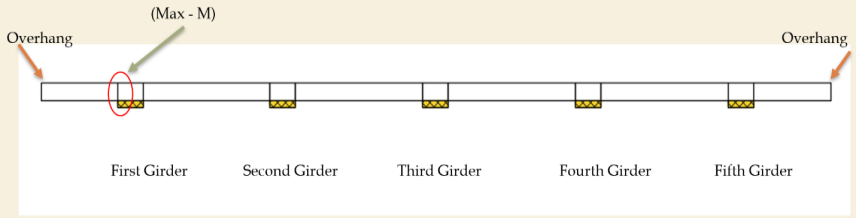

Figure 6.10. Visualization of maximum negative moment location

Analysis of **Tables 6.9** and **6.10** indicates that the maximum negative moment occurs when the truck is positioned at the end of the deck, whereas the maximum positive moment is observed when the truck is placed between the first and second girder (first span). For Case 1, the analysis showed that both the maximum positive and negative moments occurred within the initial span when the overhang was not considered. However, when the overhang is taken into account, the negative moment shifts to the root of the overhang.

Table 6.7. Maximum values and their respective locations for 4-cell deck slabs (load placed at the overhang)

Girder Spacing (ft)	Position of Truck (Distance from Face of Tire to EOD, ft)	Max.	RSM Values	RSM(1+IM)m Values	Exact Location of Max Values (Distance from Face of Tire to EOD, ft)	Total Deck Width	CL of Deck
4	4 ft (48 in)	+M (kip-ft/ft)	1.78	2.84	4.54 ft (54.45 in)	21 ft (252 in)	10.5 ft (125 in)
	4.4 ft (52.8 in)	-M (kip-ft/ft)	-2.53	-4.04	6 ft (72.19 in)		
	0.8 ft (9.6 in)	+V (kip/ft)	11.5	-	7 ft (83.58 in)		
	7.2 ft (86.4 in)	-V (kip/ft)	-7.71	-	7 ft (83.58 in)		
6	5.4 ft (64.8 in)	+M (kip-ft/ft)	2.37	3.78	6 ft (72.9 in)	31 ft (372 in)	15.5 ft (186 in)
	7.2 ft (86.4 in)	-M (kip-ft/ft)	-3.4	-5.43	9 ft (108.4 in)		
	7.8 ft (93.6 in)	+V (kip/ft)	9.25	-	9 ft (108.4 in)		
	9.97 ft (119.6 in)	-V (kip/ft)	-9.31	-	9.97 ft (119.6 in)		
9	7.2 ft (86.4 in)	+M (kip-ft/ft)	2.89	4.61	8 ft (95.94 in)	43 ft (516 in)	21.5 ft (258 in)
	9 ft (108 in)	-M (kip-ft/ft)	-4.29	-6.85	2.1 ft (14.5.2 in)		
	1.8 ft (21.6 in)	+V (kip/ft)	11.3	-	3 ft (36.32 in)		
	7.2 ft (86.4 in)	-V (kip/ft)	- 10.42	-	13 ft (155.6 in)		
12	9.6 ft (115.2 in)	+M (kip-ft/ft)	3.47	5.54	10 ft (120.3 in)	57 ft (684 in)	28.5 ft (342 in)
	7.2 ft (86.4 in)	-M (kip-ft/ft)	-6	-9.58	16 ft (192.5 in)		
	2.4 ft (28.8 in)	+V (kip/ft)	12.6	-	4 ft (48.13 in)		
	16.8 ft (201.6 in)	-V (kip/ft)	- 7.9	-	17 ft (202.8 in)		
15	10.5 ft (126 in)	+M (kip-ft/ft)	3.73	5.95	11 ft (133.1 in)	69 ft (828 in)	34.5 ft (414 in)
	10.5 ft (126 in)	-M (kip-ft/ft)	-6.99	-11.16	19 ft (228.8 in)		
	12 ft (144 in)	+V (kip/ft)	9.8	-	19.1 ft (228.8 in)		
	21 ft (252 in)	-V (kip/ft)	-5.7	-	20 ft (241.3 in)		

Table 6.8. Maximum values and their respective locations for 2-cell deck slabs (load placed at the overhang)

Girder Spacing (ft)	Position of Truck (Distance from Face of Tire to EOD, ft)	Max.	RSM Values	RSM(1+IM)m Values	Exact Location of Max Values (Distance from Face of Tire to EOD, ft)	Total Deck Width	CL of Deck
9	6.3 ft (75.6 in)	+M (kip-ft/ft)	3	4.79	7.2 ft (85.93 in)	25 ft (300 in)	12.5 ft (150 in)
	9 ft (108 in)	-M (kip-ft/ft)	-4.71	-7.52	12 ft (144.7 in)		
	1.8 ft (21.6 in)	+V (kip/ft)	12.1	-	3 ft (36.19 in)		
	7.2 ft (86.4 in)	-V (kip/ft)	-9.8	-	12.9 ft (155.3 in)		
15	10.5 ft (126 in)	+M (kip-ft/ft)	3.73	5.95	10.8 ft (129.3 in)	39 ft (468 in)	19.5 ft (234 in)
	10.5 ft (126 in)	-M (kip-ft/ft)	-7.63	-12.18	4.1 ft (49.4 in)		
	12 ft (144 in)	+V (kip/ft)	12.03	-	19 ft (228.1 in)		
	15 ft (180 in)	-V (kip/ft)	-10.05	-	20 ft (239.9 in)		

Table 6.9. Maximum values and their respective locations for 4-cell deck slabs (load placed in the span)

Girder Spacing (ft)	Position of Truck (Distance from Face of Tire to EOD, ft)	Max.	RSM Values	RSM(1+IM)m Values	Exact Location of Max Values (Distance from Face of Tire to EOD, ft)	Total Deck Width	CL of Deck
4	4 ft (48 in)	+M (kip-ft/ft)	1.78	2.84	4.54 ft (54.45 in)	21 ft (252 in)	10.5 ft (125 in)
	4.4 ft (52.8 in)	-M (kip-ft/ft)	-2.53	-4.04	6 ft (72.19 in)		
	0.8 ft (9.6 in)	+V (kip/ft)	11.5	-	7 ft (83.58 in)		
	7.2 ft (86.4 in)	-V (kip/ft)	-7.71	-	7 ft (83.58 in)		
6	5.4 ft (64.8 in)	+M (kip-ft/ft)	2.37	3.78	6 ft (72.9 in)	31 ft (372 in)	15.5 ft (186 in)
	7.2 ft (86.4 in)	-M (kip-ft/ft)	-3.4	-5.43	9 ft (108.4 in)		
	7.8 ft (93.6 in)	+V (kip/ft)	9.25	-	9 ft (108.4 in)		
	9.97 ft (119.6 in)	-V (kip/ft)	-9.31	-	9.97 ft (119.6 in)		
9	7.2 ft (86.4 in)	+M (kip-ft/ft)	2.89	4.61	8 ft (95.94 in)	43 ft (516 in)	21.5 ft (258 in)
	9 ft (108 in)	-M (kip-ft/ft)	-4.29	-6.85	2.1 ft (14.5.2 in)		
	1.8 ft (21.6 in)	+V (kip/ft)	11.3	-	3 ft (36.32 in)		
	7.2 ft (86.4 in)	-V (kip/ft)	- 10.42	-	13 ft (155.6 in)		
12	9.6 ft (115.2 in)	+M (kip-ft/ft)	3.47	5.54	10 ft (120.3 in)	57 ft (684 in)	28.5 ft (342 in)
	7.2 ft (86.4 in)	-M (kip-ft/ft)	-6	-9.58	16 ft (192.5 in)		
	2.4 ft (28.8 in)	+V (kip/ft)	12.6	-	4 ft (48.13 in)		
	16.8 ft (201.6 in)	-V (kip/ft)	- 7.9	-	17 ft (202.8 in)		
15	10.5 ft (126 in)	+M (kip-ft/ft)	3.73	5.95	11 ft (133.1 in)	69 ft (828 in)	34.5 ft (414 in)
	10.5 ft (126 in)	-M (kip-ft/ft)	-6.99	-11.16	19 ft (228.8 in)		
	12 ft (144 in)	+V (kip/ft)	9.8	-	19.1 ft (228.8 in)		
	21 ft (252 in)	-V (kip/ft)	-5.7	-	20 ft (241.3 in)		

Table 6.10. Maximum values and their respective locations for 2-cell deck slabs (load placed in the span)

Girder Spacing (ft)	Position of Truck (Distance from Face of Tire to EOD, ft)	Max.	RSM Values	RSM(1+IM)m Values	Exact Location of Max Values (Distance from Face of Tire to EOD, ft)	Total Deck Width	CL of Deck
9	6.3 ft (75.6 in)	+M (kip-ft/ft)	3	4.79	7.2 ft (85.93 in)	25 ft (300 in)	12.5 ft (150 in)
	9 ft (108 in)	-M (kip-ft/ft)	-4.71	-7.52	12 ft (144.7 in)		
	1.8 ft (21.6 in)	+V (kip/ft)	12.1	-	3 ft (36.19 in)		
	7.2 ft (86.4 in)	-V (kip/ft)	-9.8	-	12.9 ft (155.3 in)		
15	10.5 ft (126 in)	+M (kip-ft/ft)	3.73	5.95	10.8 ft (129.3 in)	39 ft (468 in)	19.5 ft (234 in)
	10.5 ft (126 in)	-M (kip-ft/ft)	-7.63	-12.18	4.1 ft (49.4 in)		
	12 ft (144 in)	+V (kip/ft)	12.03	-	19 ft (228.1 in)		
	15 ft (180 in)	-V (kip/ft)	-10.05	-	20 ft (239.9 in)		

6.2.3 Two HL-93 trucks

Table 6.11 illustrates the existence of two-truck combinations with 6 ft, 9 ft, 12 ft, and 15 ft girder spacing, featuring 4 cells, as well as in 9 ft and 15 ft girder spacing with 2 cells. Given the multitude of potential combinations in the two-truck analysis, Cases 2, 3, 3.5, and 4 have been introduced to systematically explore critical locations and encompass all conceivable scenarios. **Table 6.11** provides an overview of the total number of combinations for each case. Notably, Case 1, as indicated in Table 6.11, pertains to a single-truck scenario, extensively discussed in the previous section. In Case 2, two trucks are positioned at the deck's end with a 4 ft separation. In each subsequent step, the second truck is incrementally moved by 10% of the girder spacing until it reaches the opposite end. For Case 3, two trucks are initially situated at the deck's end side by side with a 4 ft spacing. Subsequently, in each step, both trucks are simultaneously shifted by 10% of the girder spacing until the second truck either reaches or surpasses the center line of bridge. In Case 3.5, two trucks are placed at the average distance between 4 ft and the girder spacing of each deck slab. In the ensuing step, both trucks are simultaneously moved by 10% of the girder spacing until the second truck reaches or exceeds the center line of bridge. In Case 4, two trucks are located at the deck's end, with a separation equivalent to the girder spacing for each deck slab. In each step, these two trucks are simultaneously moved by 10% of the girder spacing until the second truck arrives or surpasses the bridge's center line**.**

Table 6.11. The total number of combinations generated for each case with one and two trucks

Girder Spacing (ft)	No. of Cell	Truck Case	Case Description	Total Combinations
4	4	Case 1	Single truck	19
6	4	Case 1	Single truck	21
		Case 2	1 stationary at the end of the girder, second truck moving away	31
		Case 3 (4 ft apart)	2 trucks move together from EOD (until centerline of the deck)	25
		Case 3.5 (5 ft apart)	2 trucks move together from EOD (until centerline of the deck)	13
		Case 4 (6 ft apart)	2 trucks move together from EOD (until centerline of the deck)	12
9	4	Case 1	Single truck	22
		Case 2	1 stationary at the end of the girder, second truck moving away	32
		Case 3 (4 ft apart)	2 trucks move together from EOD (until centerline of the deck)	16
		Case 3.5 (6.5 ft apart)	2 trucks move together from EOD (until centerline of the deck)	15
		Case 4 (9 ft apart)	2 trucks move together from EOD (until centerline of the deck)	13
12	4	Case 1	Single truck	21
		Case 2	1 stationary at the end of the girder, second truck moving away	34
		Case 3 (4 ft apart)	2 trucks move together from EOD (until centerline of the deck)	18

		Case 3.5 (8 ft apart)	2 trucks move together from EOD (until centerline of the deck)	16
		Case 4 (12 ft apart)	2 trucks move together from EOD (until centerline of the deck)	15
15	4	Case 1	Single truck	22
		Case 2	1 stationary at the end of the girder, second truck moving away	36
		Case 3 (4 ft apart)	2 trucks move together from EOD (until centerline of the deck)	19
		Case 3.5 (9.5 ft apart)	2 trucks move together from EOD (until centerline of the deck)	17
		Case 4 (15 ft apart)	2 trucks move together from EOD (until centerline of the deck)	15
9	2	Case 1	Single truck	12
15	2	Case 1	Single truck	12
		Case 2	1 stationary at the end of the girder, second truck moving away	16
		Case 3 (4 ft apart)	2 trucks move together from EOD (until centerline of the deck)	9
		Case 3.5 (9.5 ft apart)	2 trucks move together from EOD (until centerline of the deck)	7
		Case 4 (15 ft apart)	2 trucks move together from EOD (until centerline of the deck)	5

As an example, the following results are presented for the 9 ft girder spacing case under 2 trucks (Cases 2, 3, 3.5, and 4). The remaining analyses for the other girder spacing cases are provided in Appendix C.

Case 2 (9 ft)

For modeling two trucks in a 9 ft girder spacing deck slab in which two trucks are moved apart from each other (**Figure 6.11**), for the first combination the first truck is placed at the end of the deck, and the second truck is placed 4 ft away from it. For the second combination, the second truck is placed at (4×12) + (9×12×0.1) = 58.8 in away from the first truck and continues moving transversely until the second truck reaches to the other end of the bridge deck. In this case, 32 combinations are created. The moment envelope is illustrated below.

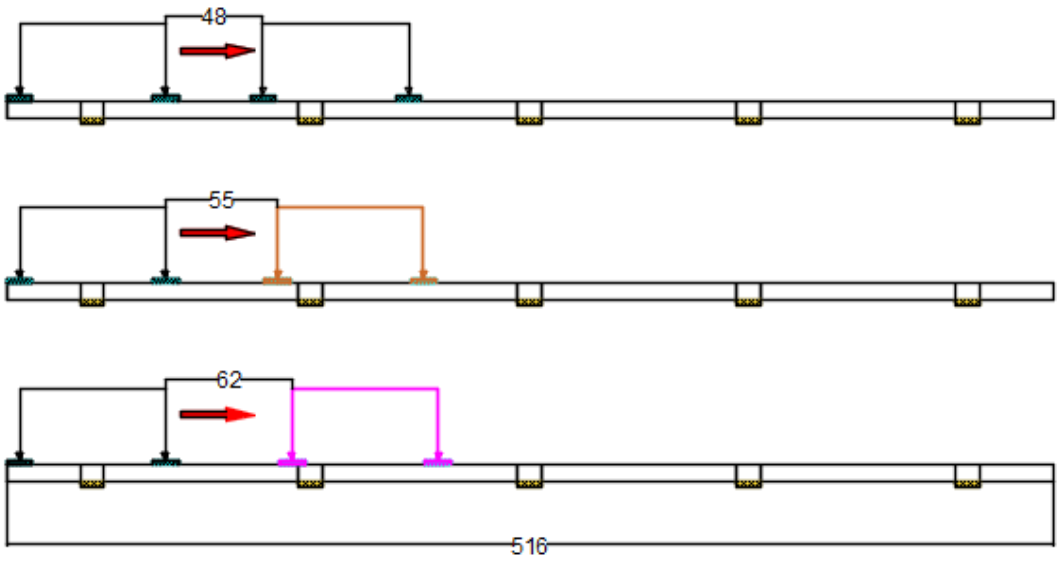

Figure 6.11. The placement of two HL-93 truck load on the deck slab with 9 ft girder spacing (first three combinations of Case 2, unit: in)

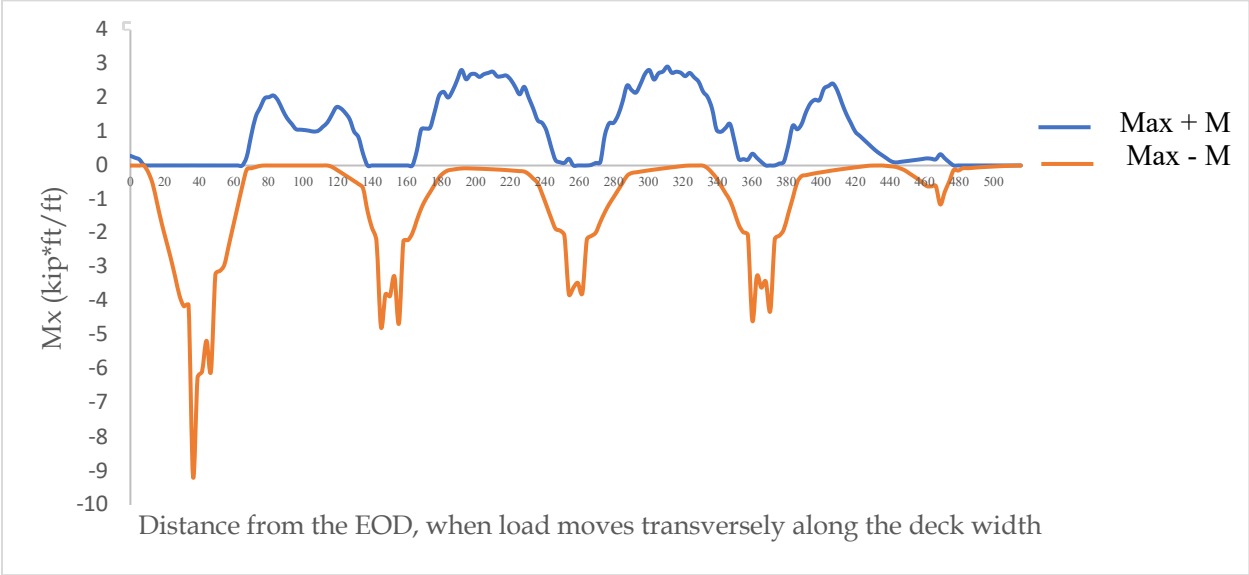

Figure 6.12. Moment envelope for deck slab with 9 ft girder spacing and two truck (Case 2)

Case 3 (9 ft)

For modeling two trucks in a 9 ft girder spacing deck slab in which two trucks are moved simultaneously, for the first combination the first truck is placed at the end of the deck, and the second truck is placed 4 ft away from the first truck. For the second combination, the first truck is placed at 9×12×0.1 = 10.8 in away from the end of the deck. The second truck is placed at 4 ft away from the first truck and continues moving transversely until the second tire of the second truck passed the center line of the deck (**Figure 6.13**). In this case a total of 16 combinations is created. In this case 16 combinations are created. The moment envelope is illustrated below.

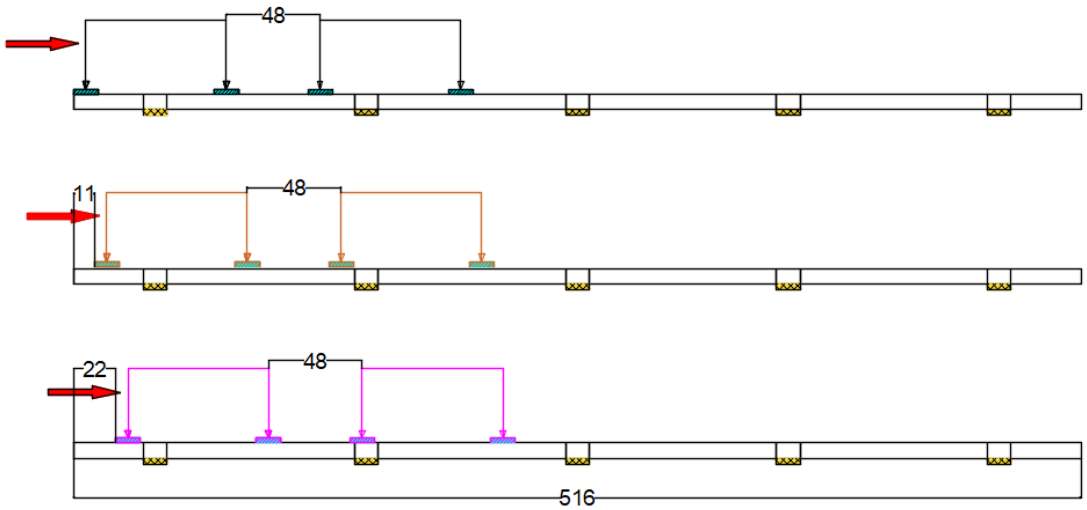

Figure 6.13. The placement of two HL-93 truck load on the deck slab with 9 ft girder spacing (first three combinations of Case 3, unit: in)

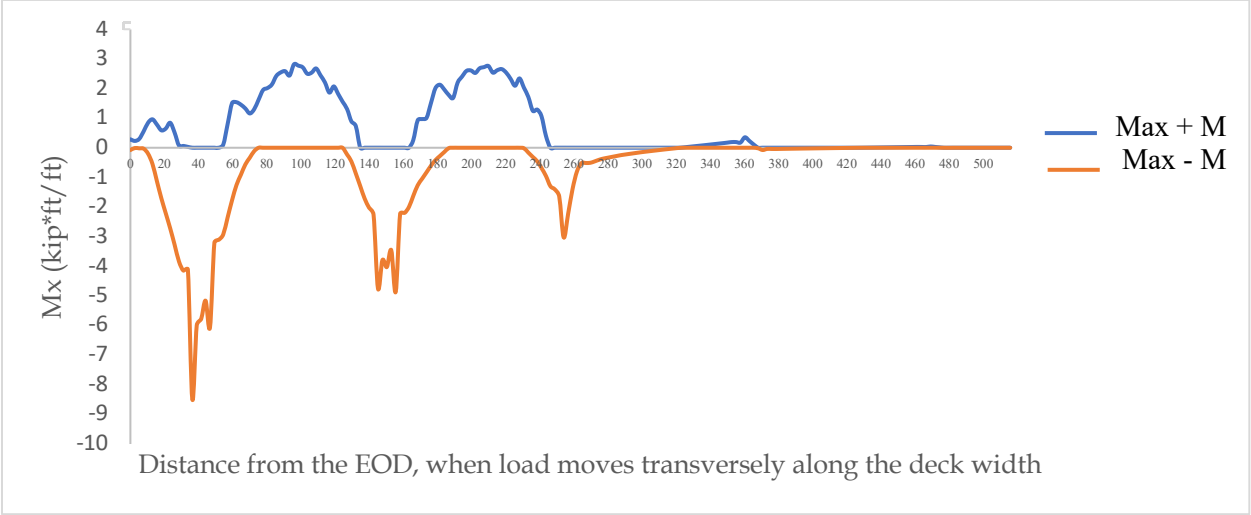

Figure 6.14. Moment envelope for deck slab with 9 ft girder spacing and two truck (Case 3)

Case 3.5 (9 ft)

For modeling two trucks in a 9 ft girder spacing deck slab in which two trucks are moved simultaneously, for the first combination the first truck is placed at the end of the deck, and the second truck is placed 6.5 ft. away from the first truck. For the second combination, the first truck is placed at 9×12×0.1 = 10.8 in away from the end of the deck. The second truck is placed at 9 ft. away from the first truck and continues moving transversely until the second tire of the second truck passed the center line of the deck (**Figure 6.15**). In this case 15 combinations are created.

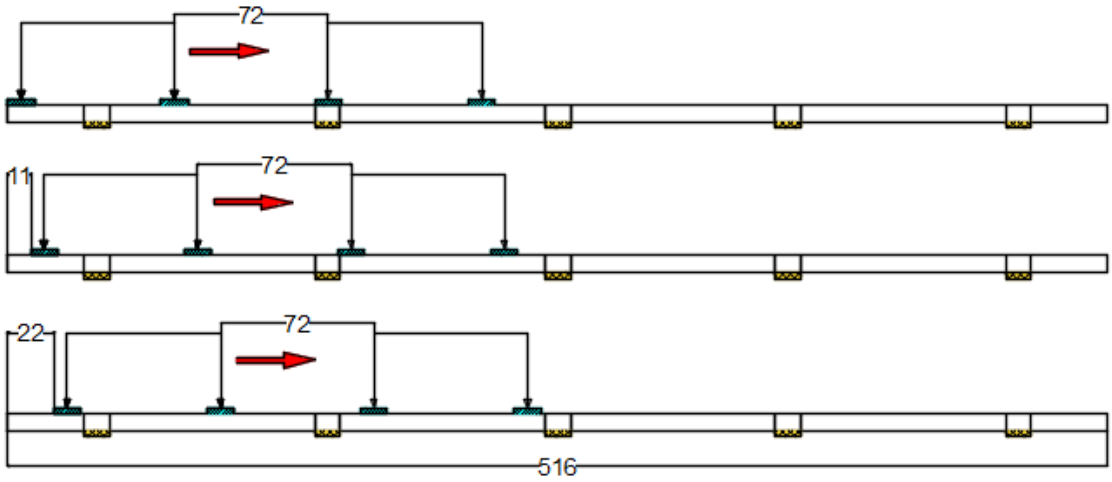

Figure 6.15. The placement of two HL-93 truck load on the deck slab with 9 ft girder spacing (first three combinations of Case 3.5, unit: in)

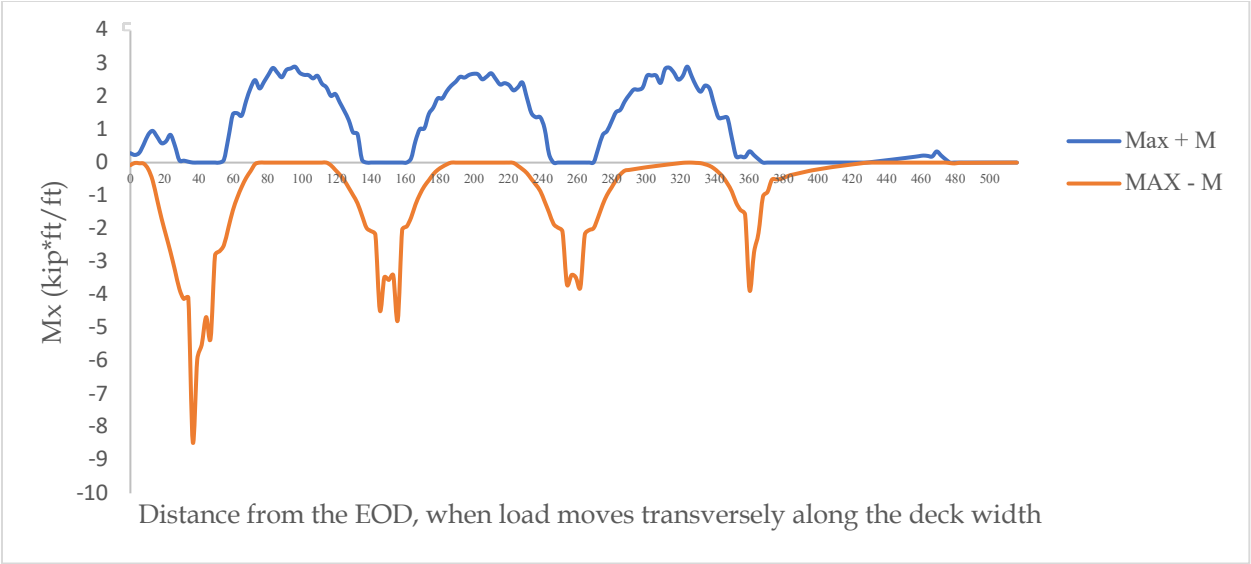

Figure 6.16. Moment envelope for deck slab with 9 ft girder spacing and two truck (Case 3.5)

Case 4 (9 ft)

For modeling two trucks in a 9 ft girder spacing deck slab in which two trucks are moved simultaneously, for the first combination the first truck is placed at the end of the deck, and the second truck is placed 9 ft away from the first truck. For the second combination, the first truck is placed at 9×12×0.1 = 10.8 in away from the end of the deck. The second truck is placed at 9 ft. away from the first truck and continues moving transversely until the second tire of the second truck passed the center line of the deck (**Figure 6.17**). In this case 13 combinations are created.

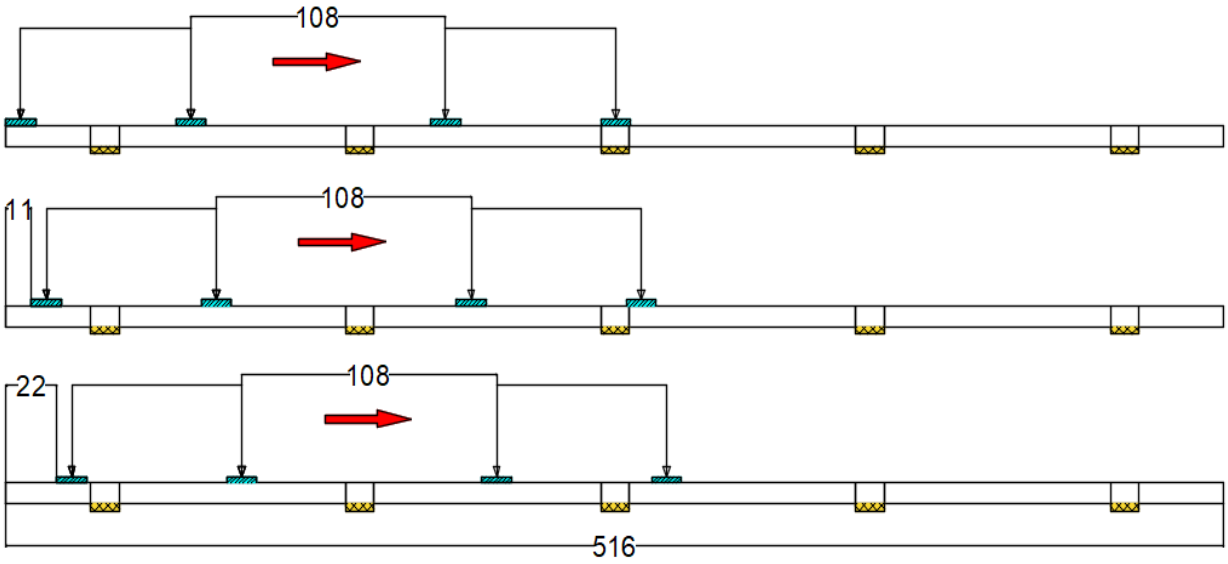

Figure 6.17. The placement of two HL-93 truck load on the deck slab with 9 ft girder spacing (first three combinations of Case 4, unit: in)

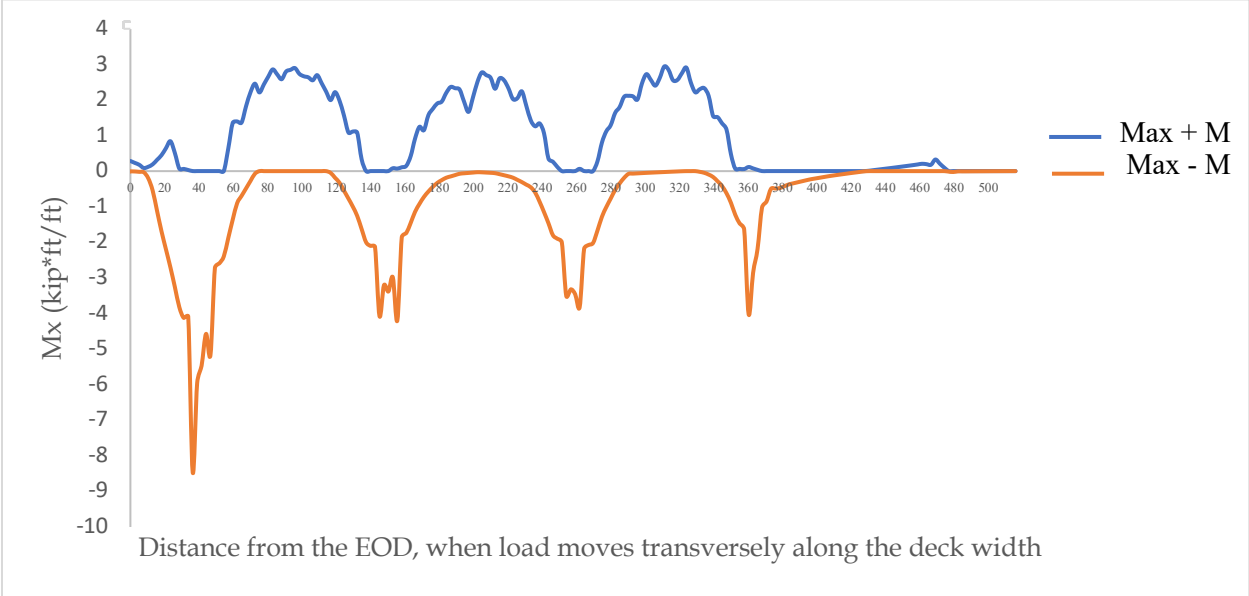

Figure 6.18. Moment envelope for deck slab with 9 ft girder spacing and two truck (Case 4)

6.2.4 Summary of all cases

The outcomes of each scenario, detailing both positive and negative moments as well as positive and negative shear forces, are summarized in the **Table 6.12** to **Table 6.21**. The tables also specify the positions of trucks and pinpoint the exact locations where maximum values occur. The Multiple Presence factor is equal to 1.00 for two-truck cases per AASHTO (2017). Using the outcomes of the deck slab with a girder spacing of 6 ft as an example, it is evident that the maximum positive and negative moments are observed in Case 1, while the maximum positive and negative shear values are found in cases 3 and 2, respectively.

Table 6.12. The results for one and two trucks – 6 ft (negative moments at overhang)

Case No.	Girder Spacing (ft, Truck Load)	Position of 1st Truck: Distance from Face of Tire to EOD, ft (in)	Position of 2nd Truck: Distance from 1st Truck (in)	Max.	RSM Values	RSM(1+IM)m Values	Exact Location of Max.: Distance from Face of Tire to EOD, ft (in)	Total Deck Length
1	6 (one truck)	5.4 ft (64.8 in)	No second Truck	+M (kip-ft/ft)	2.29	3.65	6.2 ft (74.77 in)	31 ft (372 in)
		0		-M (kip-ft/ft)	-7.57	-12.08	3.1 ft (37.4 in)	
		7.8 ft (93.6 in)		+V (kip/ft)	9.25	-	9 ft (108.4 in)	
		9.97 ft (119.6 in)		-V (kip/ft)	-9.31	-	9.97 ft (119.6 in)	
2	6 (two trucks move apart)	0	12.4 ft (148.8 in)	+M (kip-ft/ft)	2.46	3.27	19 ft (228.1in)	
		0	18 ft (215.5 in)	-M (kip-ft/ft)	-7.57	-10.07	3.1 ft (37.4in)	
		0	13.6 ft (163.2 in)	+V (kip/ft)	8.81	-	21 ft (252.4in)	
		0	10 ft (119.6 in)	-V (kip/ft)	-10.06	-	9.97 ft (119.6in)	
3	6 (two trucks move simultaneously)	8.4ft (100.8 in)	4 ft	+M (kip-ft/ft)	2.46	3.27	18.85 ft (226.2in)	
		0		-M (kip-ft/ft)	-7.59	-10.09	3.1 ft (37.4in)	
		14ft (167.5 in)		+V (kip/ft)	10.05	-	21 ft (252.4in)	
		3.6ft (43.2 in)		-V (kip/ft)	-9.81	-	9.97 ft (119.6in)	
3.5	6 (two trucks move simultaneously)	7.2 ft (86.4 in)	5 ft	+M (kip-ft/ft)	2.39	3.18	18.85 ft (226.2.in)	
		0		-M (kip-ft/ft)	-7.6	-10.11	3.1 ft (37.4.6in)	
		1.75 ft (21.6 in)		+V (kip/ft)	8.98	-	9 ft (108.4 in)	
		4.2 ft (50.4 in)		-V (kip/ft)	-9.24	-	10 ft (119.6in)	
4	6 (two trucks move simultaneously)	5.4 ft (64.8 in)	6 ft	+M (kip-ft/ft)	2.38	3.17	6 ft (72.9.in)	
		0		-M (kip-ft/ft)	-7.6	-10.11	3.1 ft (37.4.6in)	
		1.75 ft (21.6 in)		+V (kip/ft)	9.07	-	21 ft (252.4 in)	
		4.2 ft (50.4 in)		-V (kip/ft)	-9.21	-	22 ft (263.6in)	

Table 6.13. The results for one and two trucks – 6 ft (negative moments within span)

Case No.	Girder Spacing (ft, Truck Load)	Position of 1st Truck: Distance from Face of Tire to EOD, ft (in)	Position of 2nd Truck: Distance from 1st Truck (in)	Max.	RSM Values	RSM(1+IM)m Values	Exact Location of Max.: Distance from Face of Tire to EOD, ft (in)	Total Deck Length
1	6 (one truck)	5.4 ft (64.8 in)	No second Truck	+M (kip-ft/ft)	2.29	3.78	6 ft (72.9 in)	31 ft (372 in)
		7.2 ft (86.4 in)		-M (kip-ft/ft)	-3.4	-5.43	9 ft (108.4 in)	
		7.8 ft (93.6 in)		+V (kip/ft)	5.58	-	9 ft (108.4 in)	
		9.97 ft (119.6 in)		-V (kip/ft)	-5.58	-	9.97 ft (119.6 in)	
2	6 (two trucks move apart)	0	12.4 ft (148.8 in)	+M (kip-ft/ft)	2.46	3.27	19 ft (228.1in)	
		0	4.6 ft (55.2 in)	-M (kip-ft/ft)	-2.93	-3.90	9 ft (108.4 in)	
		0	13.6 ft (163.2 in)	+V (kip/ft)	8.81	-	21 ft (252.4in)	
		0	10 ft (119.6 in)	-V (kip/ft)	-10.06	-	9.97 ft (119.6in)	
3	6 (two trucks move simultaneously)	8.4ft (100.8 in)	4 ft	+M (kip-ft/ft)	2.46	3.27	18.85 ft (226.2in)	
		6.6 ft (79.2 in)		-M (kip-ft/ft)	-3.66	-4.87	9 ft (108.4 in)	
		14ft (167.5 in)		+V (kip/ft)	10.05	-	21 ft (252.4in)	
		3.6ft (43.2 in)		-V (kip/ft)	-9.81	-	9.97 ft (119.6in)	
3.5	6 (two trucks move simultaneously)	7.2 ft (86.4 in)	5 ft	+M (kip-ft/ft)	2.39	3.18	18.85 ft (226.2.in)	
		6.6 ft (79.2 in)		-M (kip-ft/ft)	-3.65	-4.85	9 ft (108.4 in)	
		1.75 ft (21.6 in)		+V (kip/ft)	8.98	-	9 ft (108.4 in)	
		4.2 ft (50.4 in)		-V (kip/ft)	-9.24	-	hear	
4	6 (two trucks move simultaneously)	5.4 ft (64.8 in)	6 ft	+M (kip-ft/ft)	2.38	3.17	6 ft (72.9.in)	
		6.6 ft (79.2 in)		-M (kip-ft/ft)	-3.61	-4.80	9 ft (108.4 in)	
		1.75 ft (21.6 in)		+V (kip/ft)	9.07	-	21 ft (252.4 in)	
		4.2 ft (50.4 in)		-V (kip/ft)	-9.21	-	22+B16:H23 ft (263.6 in)	

Table 6.14. The results for one and two trucks – 9 ft (negative moments at overhang)

Case No.	Girder Spacing (ft, Truck Load)	Position of 1st Truck: Distance from Face of Tire to EOD, ft (in)	Position of 2nd Truck: Distance from 1st Truck (in)	Max.	RSM Values	RSM(1+IM)m Values	Exact Location of Max.: Distance from Face of Tire to EOD, ft (in)	Total Deck Length
1	9 (one truck)	7.2 ft (86.4 in)	No second Truck	+M (kip-ft/ft)	2.83	4.52	8 ft (95.94 in)	43 ft (516 in)
		0		-M (kip-ft/ft)	-8.44	-13.47	3 ft (36.32 in)	
		1.8 ft (21.6 in)		+V (kip/ft)	6.78	-	3 ft (36.32 in)	
		7.2 ft (86.4 in)		-V (kip/ft)	-6.25	-	13 ft (155.6 in)	
2	9 (two trucks move apart)	0	28.3 ft (339.6 in)	+M (kip-ft/ft)	2.93	3.90	35 ft (420.1 in)	
		0	18.4 ft (220.8 in)	-M (kip-ft/ft)	-9.18	-12.21	3 ft (36.32 in)	
		0	18.4 ft (220.8 in)	+V (kip/ft)	14.45	-	3 ft (36.32 in)	
		0	28.3ft (339.6 in)	-V (kip/ft)	-10.88	-	41.5 ft (479.7 in)	
3	9 (two trucks move simultaneously)	6.3 ft (75.6 in)	4 ft	+M (kip-ft/ft)	2.9	3.86	16.2 ft (194.5 in)	
		0		-M (kip-ft/ft)	-8.5	-11.31	3 ft (36.32 in)	
		1.8 ft (21.6 in)		+V (kip/ft)	11.3	-	3 ft (36.32 in)	
		7.2 ft (86.4 in)		-V (kip/ft)	-12.78	-	13 ft (155.6 in)	
3.5	9 (two trucks move simultaneously)	8.1 ft (97.2 in)	6.5 ft	+M (kip-ft/ft)	2.9	3.86	27 ft (324.1 in)	
		0		-M (kip-ft/ft)	-8.45	-11.24	3 ft (36.32 in)	
		1.75 ft (21.6 in)		+V (kip/ft)	11.35	-	3 ft (36.32 in)	
		0.9 ft (10.8 in)		-V (kip/ft)	-11.05	-	13 ft (155.6 in)	
4	9 (two trucks move simultaneously)	4.5 ft (54 in)	9 ft	+M (kip-ft/ft)	2.93	3.90	26 ft (311.2 in)	
		0		-M (kip-ft/ft)	-8.47	-11.27	3 ft (36.32 in)	
		1.75 ft (21.6 in)		+V (kip/ft)	11.33	-	3 ft (36.32 in)	
		7.2 ft (86.4 in)		-V (kip/ft)	-10.22	-	13 ft (155.6 in)	

Table 6.15. The results for one and two trucks – 9 ft (negative moments within span)

Case No.	Girder Spacing (ft, Truck Load)	Position of 1st Truck: Distance from Face of Tire to EOD, ft (in)	Position of 2nd Truck: Distance from 1st Truck (in)	Max.	RSM Values	RSM(1+IM)m Values	Exact Location of Max.: Distance from Face of Tire to EOD, ft (in)	Total Deck Length
1	9 (one truck)	7.2 ft (86.4 in)	No second Truck	+M (kip-ft/ft)	2.83	4.52	8 ft (95.94 in)	43 ft (516 in)
		9 ft (108 in)		-M (kip-ft/ft)	-4.29	-6.85	12.1 ft (145.2 in)	
		1.8 ft (21.6 in)		+V (kip/ft)	6.78	-	3 ft (36.32 in)	
		7.2 ft (86.4 in)		-V (kip/ft)	-6.25	-	13 ft (155.6 in)	
2	9 (two trucks move apart)	0	28.3 ft (339.6 in)	+M (kip-ft/ft)	2.93	3.90	35 ft (420.1 in)	
		0	4 ft (48 in)	-M (kip-ft/ft)	-4.75	-6.32	12.1 ft (145.2 in)	
		0	18.4 ft (220.8 in)	+V (kip/ft)	14.45	-	12.1 ft (36.32 in)	
		0	28.3ft (339.6 in)	-V (kip/ft)	-10.88	-	41.5 ft (479.7 in)	
3	9 (two trucks move simultaneously)	6.3 ft (75.6 in)	4 ft	+M (kip-ft/ft)	2.9	3.86	16.2 ft (194.5 in)	
		3.6 ft (43.2 in)		-M (kip-ft/ft)	-4.63	-6.16	12.1 ft (145.2 in)	
		1.8 ft (21.6 in)		+V (kip/ft)	11.3	-	3 ft (36.32 in)	
		7.2 ft (86.4 in)		-V (kip/ft)	-12.78	-	13 ft (155.6 in)	
3.5	9 (two trucks move simultaneously)	8.1 ft (97.2 in)	6.5 ft	+M (kip-ft/ft)	2.9	3.86	27 ft (324.1 in)	
		3.6 ft (43.2 in)		-M (kip-ft/ft)	-4.47	-5.95	12.1 ft (145.2 in)	
		1.75 ft (21.6 in)		+V (kip/ft)	11.35	-	3 ft (36.32 in)	
		0.9 ft (10.8 in)		-V (kip/ft)	-11.05	-	13 ft (155.6 in)	
4	9 (two trucks move simultaneously)	4.5 ft (54 in)	9 ft	+M (kip-ft/ft)	2.93	3.90	26 ft (311.2 in)	
		9 ft (108 in)		-M (kip-ft/ft)	-4.36	-5.80	12.1 ft (145.2 in)	
		1.75 ft (21.6 in)		+V (kip/ft)	11.33	-	3 ft (36.32 in)	
		7.2 ft (86.4 in)		-V (kip/ft)	-10.22	-	13 ft (155.6 in)	

Table 6.16. The results for one and two trucks – 12 ft (negative moments at overhang)

Case No.	Girder Spacing (ft, Truck Load)	Position of 1st Truck: Distance from Face of Tire to EOD, ft (in)	Position of 2nd Truck: Distance from 1st Truck (in)	Max.	RSM Values	RSM(1+IM) m Values	Exact Location of Max.: Distance from Face of Tire to EOD, ft (in)	Total Deck Length
1	12 (one truck)	9.6 ft (115.2 in)	No second Truck	+M (kip-ft/ft)	3.47	5.54	10 ft (120.3 in)	57 ft (684 in)
		1.2 ft (14.4 in)		-M (kip-ft/ft)	-7.63	-12.18	4 ft (48.13 in)	
		2.4 ft (28.8 in)		+V (kip/ft)	7.56	-	4 ft (48.13 in)	
		16.8 ft (201.6 in)		-V (kip/ft)	-4.74	-	17 ft (202.8 in)	
2	12 (two trucks move apart)	0	4 ft (48 in)	+M (kip-ft/ft)	3.33	4.43	10 ft (127.2 in)	
		0	4 ft (48 in)	-M (kip-ft/ft)	-10.15	-13.50	4 ft (48.13 in)	
		0	5.2 ft (62.4 in)	+V (kip/ft)	10.73	-	4 ft (48.13 in)	
		0	41.2 ft (494.4 in)	-V (kip/ft)	-12.24	-	53 ft (635.9 in)	
3	12 (two trucks move simultaneously)	3.6 ft (43.2 in)	4 ft	+M (kip-ft/ft)	3.62	4.81	10 ft (120.3 in)	
		0		-M (kip-ft/ft)	-10.15	-13.50	4 ft (48.13 in)	
		4.8 ft (57.6 in)		+V (kip/ft)	14.55	-	16 ft (192.5 in)	
		19.2 ft (230.4 in)		-V (kip/ft)	-11.72	-	28.9 ft (347.2 in)	
3.5	12 (two trucks move simultaneously)	9.6 ft (115.2 in)	8 ft	+M (kip-ft/ft)	3.46	4.60	10 ft (120.3 in)	
		0		-M (kip-ft/ft)	-9.86	-13.11	4 ft (48.13 in)	
		2.4 ft (28.8 in)		+V (kip/ft)	12.66	-	4 ft (48.13 in)	
		15.6 ft (187.2 in)		-V (kip/ft)	-10.31	-	29 ft (347.2 in)	
4	12 (two trucks move simultaneously)	9.6 ft (115.2 in)	12 ft	+M (kip-ft/ft)	3.48	4.63	10 ft (120.3 in)	
		0		-M (kip-ft/ft)	-9.9	-13.17	4 ft (48.13 in)	
		2.4 ft (28.8 in)		+V (kip/ft)	12.66	-	4 ft (48.13 in)	
		10.8 ft (129.6 in)		-V (kip/ft)	-8.85	-	29 ft (347.2 in)	

Table 6.17. The results for one and two trucks – 12 ft (negative moments within span)

Case No.	Girder Spacing (ft, Truck Load)	Position of 1st Truck: Distance from Face of Tire to EOD, ft (in)	Position of 2nd Truck: Distance from 1st Truck (in)	Max.	RSM Values	RSM(1+IM)m Values	Exact Location of Max.: Distance from Face of Tire to EOD, ft (in)	Total Deck Length
1	12 (one truck)	9.6 ft (115.2 in)	No second Truck	+M (kip-ft/ft)	3.47	5.54	10 ft (120.3 in)	57 ft (684 in)
		7.2 ft (86.4 in)		-M (kip-ft/ft)	-6	-9.58	16 ft (192.5 in)	
		2.4 ft (28.8 in)		+V (kip/ft)	7.56	-	4 ft (48.13 in)	
		16.8 ft (201.6 in)		-V (kip/ft)	-4.74	-	17 ft (202.8 in)	
2	12 (two trucks move apart)	0	4 ft (48 in)	+M (kip-ft/ft)	3.33	4.43	10 ft (127.2 in)	
		0	6.4 ft (76.8 in)	-M (kip-ft/ft)	-5.03	-6.69	19 ft (228.8 in)	
		0	5.2 ft (62.4 in)	+V (kip/ft)	10.73	-	4 ft (48.13 in)	
		0	41.2 ft (494.4 in)	-V (kip/ft)	-12.24	-	53 ft (635.9 in)	
3	12 (two trucks move simultaneously)	3.6 ft (43.2 in)	4 ft	+M (kip-ft/ft)	3.62	4.81	10 ft (120.3 in)	
		7.2 ft (86.4 in)		-M (kip-ft/ft)	-7.33	-9.75	19 ft (228.8 in)	
		4.8 ft (57.6 in)		+V (kip/ft)	14.55	-	16 ft (192.5 in)	
		19.2 ft (230.4 in)		-V (kip/ft)	-11.72	-	28.9 ft (347.2 in)	
3.5	12 (two trucks move simultaneously)	9.6 ft (115.2 in)	8 ft	+M (kip-ft/ft)	3.46	4.60	10 ft (120.3 in)	
		7.2 ft (86.4 in)		-M (kip-ft/ft)	-6.77	-9.00	19 ft (228.8 in)	
		2.4 ft (28.8 in)		+V (kip/ft)	12.66	-	4 ft (48.13 in)	
		15.6 ft (187.2 in)		-V (kip/ft)	-10.31	-	29 ft (347.2 in)	
4	12 (two trucks move simultaneously)	9.6 ft (115.2 in)	12 ft	+M (kip-ft/ft)	3.48	4.63	10 ft (120.3 in)	
		7.2 ft (86.4 in)		-M (kip-ft/ft)	-6.17	-8.21	19 ft (228.8 in)	
		2.4 ft (28.8 in)		+V (kip/ft)	12.66	-	4 ft (48.13 in)	
		10.8 ft (129.6 in)		-V (kip/ft)	-8.85	-	29 ft (347.2 in)	

Table 6.18. The results for one and two trucks – 15 ft (negative moments at overhang)

Case No.	Girder Spacing (ft, Truck Load)	Position of 1st Truck: Distance from Face of Tire to EOD, ft (in)	Position of 2nd Truck: Distance from 1st Truck (in)	Max.	RSM Values	RSM(1+IM)m Values	Exact Location of Max.: Distance from Face of Tire to EOD, ft (in)	Total Deck Length
1	15 (one Truck)	10.5 ft (126 in)	No second Truck	+M (kip-ft/ft)	3.73	5.95	11 ft (133.1 in)	69 ft (828 in)
		0		-M (kip-ft/ft)	-7.7	-12.29	4.2 ft (49.94 in)	
		12 ft (144 in)		+V (kip/ft)	5.88	-	19.1 ft (228.8 in)	
		21 ft (252 in)		-V (kip/ft)	-3.42	-	20 ft (241.3 in)	
2	15 (Two trucks move apart)	0	35.5 ft (426 in)	+M (kip-ft/ft)	3.97	5.28	44 ft (530.5 in)	
		0	4 ft (48 in)	-M (kip-ft/ft)	-9.33	-12.41	4.9 ft (58.26 in)	
		0	5.5 ft (66 in)	+V (kip/ft)	10.59	-	19 ft (228.8 in)	
		0	44.5 ft (534 in)	-V (kip/ft)	-10.67	-	50 ft (599.2 in)	
3	15 (Two trucks move simultaneously)	16.5 ft (198 in)	4 ft	+M (kip-ft/ft)	4.38	5.83	27 ft (324.5 in)	
		6 ft (72 in)		-M (kip-ft/ft)	-9.69	-12.89	19.1 ft (228.8 in)	
		7.5 ft (90.2 in)		+V (kip/ft)	13.17	-	19.1 ft (228.8 in)	
		25.5 ft (306 in)		-V (kip/ft)	-8.06	-	35 ft (420.4 in)	
3.5	15 (Two trucks move simultaneously)	16.5 ft (198 in)	9.5 ft	+M (kip-ft/ft)	4.38	5.83	27 ft (324.5 in)	
		7.5 ft (90.2 in)		-M (kip-ft/ft)	-9.69	-12.89	19.5 ft (233 in)	
		7.5 ft (90.2 in)		+V (kip/ft)	13.18	-	19 ft (228.8 in)	
		10.5 ft (126.2 in)		-V (kip/ft)	-7.33	-	20 ft (241.3 in)	
4	15 (Two trucks move simultaneously)	10.5 ft (126 in)	15 ft	+M (kip-ft/ft)	3.73	4.96	11.1 ft (133.1 in)	
		0		-M (kip-ft/ft)	-7.73	-10.28	4.2 ft (49.94 in)	
		12 ft (144 in)		+V (kip/ft)	9.81	-	19.1 ft (228.8 in)	
		15 ft (180 in)		-V (kip/ft)	-6.1	-	35 ft (420.4 in)	

Table 6.19. The results for one and two trucks – 15 ft (negative moments within span)

Case No.	Girder Spacing (ft, Truck Load)	Position of 1st Truck: Distance from Face of Tire to EOD, ft (in)	Position of 2nd Truck: Distance from 1st Truck (in)	Max.	RSM Values	RSM(1+IM)m Values	Exact Location of Max.: Distance from Face of Tire to EOD, ft (in)	Total Deck Length
1	15 (one Truck)	10.5 ft (126 in)	No second Truck	+M (kip-ft/ft)	3.73	5.95	11 ft (133.1 in)	69 ft (828 in)
		10.5 ft (126 in)		-M (kip-ft/ft)	-6.99	-11.16	19 ft (228.8 in)	
		12 ft (144 in)		+V (kip/ft)	5.88	-	19.1 ft (228.8 in)	
		21 ft (252 in)		-V (kip/ft)	-3.42	-	20 ft (241.3 in)	
2	15 (Two trucks move apart)	0	35.5 ft (426 in)	+M (kip-ft/ft)	3.97	5.28	44 ft (530.5 in)	
		0	4 ft (48 in)	-M (kip-ft/ft)	-6.54	-8.70	19 ft (228.8 in)	
		0	5.5 ft (66 in)	+V (kip/ft)	10.59	-	19 ft (228.8 in)	
		0	44.5 ft (534 in)	-V (kip/ft)	-10.67	-	50 ft (599.2 in)	
3	15 (Two trucks move simultaneously)	16.5 ft (198 in)	4 ft	+M (kip-ft/ft)	4.38	5.83	27 ft (324.5 in)	
		7.5 ft (90 in)		-M (kip-ft/ft)	-9.41	-12.52	19 ft (228.8 in)	
		7.5 ft (90.2 in)		+V (kip/ft)	13.17	-	19.1 ft (228.8 in)	
		25.5 ft (306 in)		-V (kip/ft)	-8.06	-	35 ft (420.4 in)	
3.5	15 (Two trucks move simultaneously)	10.5 ft (126 in)	9.5 ft	+M (kip-ft/ft)	3.73	4.96	27 ft (324.5 in)	
		10.5 ft (126.2 in)		-M (kip-ft/ft)	-7.33	-9.75	19 ft (228.8 in)	
		7.5 ft (90 in)		+V (kip/ft)	13.18	-	19 ft (228.8 in)	
		10.5 ft (126 in)		-V (kip/ft)	-7.33	-	20 ft (241.3 in)	
4	15 (Two trucks move simultaneously)	10.5 ft (126 in)	15 ft	+M (kip-ft/ft)	3.73	4.96	11.1 ft (133.1 in)	
		9 ft (108.2 in)		-M (kip-ft/ft)	-7.29	-9.70	19 ft (228.8 in)	
		12 ft (144 in)		+V (kip/ft)	9.81	-	19.1 ft (228.8 in)	
		15 ft (180 in)		-V (kip/ft)	-6.1	-	35 ft (420.4 in)	

Table 6.20. The results for one and two trucks – 15 ft with two cells (negative moments at overhang)

Case No.	Girder Spacing (ft, Truck Load)	Position of 1st Truck: Distance from Face of Tire to EOD, ft (in)	Position of 2nd Truck: Distance from 1st Truck (in)	Max.	RSM Values	RSM(1+IM)m Values	Exact Location of Max.: Distance from Face of Tire to EOD, ft (in)	Total Deck Length
1	15 with two cells (one truck)	10.5 ft (126 in)	No second Truck	+M (kip-ft/ft)	3.73	5.95	10.8 ft (129.3 in)	39 ft (468 in)
		0 ft (0 in)		-M (kip-ft/ft)	-8.33	-13.30	4.1 ft (49.4 in)	
		12 ft (144 in)		+V (kip/ft)	12.03	-	19 ft (228.1 in)	
		6 ft (72 in)		-V (kip/ft)	-7.31	-	5 ft (58.8 in)	
2	15 with two cells (two trucks move apart)	0	20.5 ft (246 in)	+M (kip-ft/ft)	4.04	5.37	44 ft (530.5 in)	
		0	4 ft (48 in)	-M (kip-ft/ft)	-10	-13.30	4.9 ft (58.26 in)	
		0	5.5 ft (66 in)	+V (kip/ft)	13.54	-	19 ft (228.8 in)	
		0	20 ft (239.9 in)	-V (kip/ft)	-14.14	-	50 ft (599.2 in)	
3	15 with two cells (two trucks move simultaneously)	1.5 ft (18 in)	4 ft	+M (kip-ft/ft)	4.24	5.64	12.15 ft (145.8 in)	
		6 ft (72.2 in)		-M (kip-ft/ft)	-10.56	-14.04	19 ft (228.1 in)	
		7.5 ft (90 in)		+V (kip/ft)	17.04	-	19 ft (228.1 in)	
		10.5 ft (126 in)		-V (kip/ft)	-15.38	-	20 ft (239.9 in)	
3.5	15 with two cells (two trucks move simultaneously)	6 ft (72 in)	9.5 ft	+M (kip-ft/ft)	3.76	5.00	28.4 ft (341 in)	
		0		-M (kip-ft/ft)	-8.4	-11.17	4.2 ft (49.4 in)	
		1.5 ft (18 in)		+V (kip/ft)	10.8	-	19 ft (228.1 in)	
		4.5 ft (54 in)		-V (kip/ft)	-12.59	-	20 ft (239.9 in)	
4	15 with two cells (two trucks move simultaneously)	6 ft (72 in)	15 ft	+M (kip-ft/ft)	3.71	4.93	27.63 ft (331.6 in)	
		0		-M (kip-ft/ft)	-8.35	-11.11	4.2 ft (49.4 in)	
		6 ft (72 in)		+V (kip/ft)	8.2	-	34 ft (409.2 in)	
		0		-V (kip/ft)	-12	-	20 ft (239.9 in)	

Table 6.21. The results for one and two trucks – 15 ft with two cells (negative moments within span)

Case No.	Girder Spacing (ft, Truck Load)	Position of 1st Truck: Distance from Face of Tire to EOD, ft (in)	Position of 2nd Truck: Distance from 1st Truck (in)	Max.	RSM Values	RSM(1+IM)m Values	Exact Location of Max.: Distance from Face of Tire to EOD, ft (in)	Total Deck Length
1	15 with two cells (one Truck)	10.5 ft (126 in)	No second Truck	+M (kip-ft/ft)	3.73	5.95	10.8 ft (129.3 in)	39 ft (468 in)
		10.5 ft (126 in)		-M (kip-ft/ft)	-7.63	-12.18	4.1 ft (49.4 in)	
		12 ft (144 in)		+V (kip/ft)	12.03	-	19 ft (228.1 in)	
		15 ft (180 in)		-V (kip/ft)	-7.31	-	20 ft (239.9 in)	
2	15 with two cells (two trucks move apart)	0	20.5 ft (246 in)	+M (kip-ft/ft)	4.04	5.37	44 ft (530.5 in)	
		0	4 ft (48 in)	-M (kip-ft/ft)	-7.13	-9.48	19 ft (228.1 in)	
		0	5.5 ft (66 in)	+V (kip/ft)	13.54	-	19 ft (228.8 in)	
		0	20 ft (239.9 in)	-V (kip/ft)	-14.14	-	50 ft (599.2 in)	
3	15 with two cells (two trucks move simultaneously)	1.5 ft (18 in)	4 ft	+M (kip-ft/ft)	4.24	5.64	12.15 ft (145.8 in)	
		12 ft (144 in)		-M (kip-ft/ft)	-9.22	-12.26	20 ft (239.9 in)	
		7.5 ft (90 in)		+V (kip/ft)	17.04	-	19 ft (228.1 in)	
		10.5 ft (126 in)		-V (kip/ft)	-15.38	-	20 ft (239.9 in)	
3.5	15 with two cells (two trucks move simultaneously)	6 ft (72 in)	9.5 ft	+M (kip-ft/ft)	3.76	5.00	28.4 ft (341 in)	
		9 ft (108 in)		-M (kip-ft/ft)	-8.08	-10.75	19 ft (228.1 in)	
		1.5 ft (18 in)		+V (kip/ft)	10.8	-	19 ft (228.1 in)	
		4.5 ft (54 in)		-V (kip/ft)	-12.59	-	20 ft (239.9 in)	
4	15 with two cells (two trucks move simultaneously)	6 ft (72 in)	15 ft	+M (kip-ft/ft)	3.71	4.93	27.63 ft (331.6 in)	
		6 ft (72 in)		-M (kip-ft/ft)	-5.12	-6.81	19 ft (228.1 in)	
		6 ft (72 in)		+V (kip/ft)	8.2	-	34 ft (409.2 in)	
		0		-V (kip/ft)	-12	-	20 ft (239.9 in)	

The summarized results of the maximum values obtained for each girder spacing in the deck slab are presented in **Table 6.22**. When comparing the results of RSM(1+IM)m moment values both for at the overhang and in the span, it is evident that Case 1 dominates for the majority of the deck, regardless of the girder spacing. However, Case 3 controlling the negative moment, can be observed in decks with a girder spacing of 12 and 15 ft, with four cells, as well as in decks with a girder spacing of 15 ft and two cells. When comparing these values to those of Case 1, the difference is minimal, with a maximum deviation of 10%. This change in governing load case was of interest during internal TAC discussions, so additional models with 10 ft and 11 ft girder spacings were added to the study.

Table 6.22. Governing cases under HL-93 (16 kip; 125 psi) based on RSM(1+IM)m values

Girder Spacing (ft)	No. of Cell	Positive Moment	Negative Moment at Overhang	Negative Moment within span	Positive Shear	Negative Shear
4	4	Case 1	Case 1	Case 1	Case 1	Case 1
6	4	Case 1	Case 1	Case 1	Case 3	Case 2
9	4	Case 1	Case 1	Case 1	Case 2	Case 3
12	4	Case 1	Case 3	Case 3	Case 3	Case 2
15	4	Case 1	Case 3	Case 3	Case 3	Case 2
9	2	Case 1	Case1	Case1	Case 1	Case 1
15	2	Case 1	Case 3	Case 3	Case 3	Case 3

Based on the additional models, the transition from Case 1 governing to Case 3 governing was located between a 9 ft girder spacing and a 10 ft girder spacing, as shown in **Table 6.23**. This change is likely due to the layout of the tires in Case 3. The center-to-center distance of tires on one axel is 6 ft, and the center to center spacing of tires on adjacent vehicles in Case 3 is 4 ft, meaning that starting at a girder spacing of 9 ft it becomes possible to fit three tires in one girder spacing with two tires relatively close to a single girder. The maximum moments for each girder spacing have also been summarized in **Table 6.24**.

Table 6.23. Expanded governing cases under HL-93 (16 kip and 125 psi) based on RSM(1+IM)m values

Girder Spacing (ft)	No. of Cell	Positive Moment	Negative Moment at Overhang	Negative Moment within span	Positive Shear	Negative Shear
4	4	Case 1	Case 1	Case 1	Case 1	Case 1
6	4	Case 1	Case 1	Case 1	Case 3	Case 2
9	4	Case 1	Case 1	Case 1	Case 2	Case 3
10	4	Case 1	–[a]	Case 3	–	–
11	4	Case 1	–	Case 3	–	–
12	4	Case 1	Case 3	Case 3	Case 3	Case 2
15	4	Case 1	Case 3	Case 3	Case 3	Case 2
9	2	Case 1	Case1	Case1	Case 1	Case 1
10	2	Case 1	–	Case 3	–	–
15	2	Case 1	Case 3	Case 3	Case 3	Case 3

[a]Not applicable

Table 6.24. Summary of maximum moments due to HL-93 loading by girder spacing

Girder Spacing (ft)	Distance - Edge of Tire to Edge of Deck	M_{Max} (kip-ft/ft)	RSM (kip-ft/ft)	1+IM	m	RSM(1+IM)m (kip-ft/ft)	Governing Load Case
4	4 ft (48 in)	+M	1.78	1.33	1.2	2.84	1
	4.4 ft (52.8 in)	-M	-2.53	1.33	1.2	-4.04	1
6	5.4 ft (64.8 in)	+M	2.37	1.33	1.2	3.78	1
	7.2 ft (86.4 in)	-M	-3.45	1.33	1.2	-5.51	1
9	7.2 ft (86.4 in)	+M	2.89	1.33	1.2	4.61	1
	9 ft (108 in)	-M	-4.78	1.33	1.2	-7.63	1
10	9 ft (108 in)	+M	3.07	1.33	1.2	4.90	1
	2 ft (24 in)	-M	-6.53	1.33	1	-8.69	3
11	14.3 ft (171.6 in)	+M	3.39	1.33	1.2	5.41	1
	11 ft (132 in)	-M	-7.58	1.33	1	-10.08	3
12	9.6 ft (115.2 in)	+M	3.47	1.33	1.2	5.54	1
	3.6 ft (43.2 in)	-M	-8.25	1.33	1	-10.97	3
15	10.5 ft (126 in)	+M	3.73	1.33	1.2	5.95	1
	6 ft (72 in)	-M	-9.69	1.33	1	-12.89	3
6 (2 cells)	5.4 ft (64.8 in)	+M	2.44	1.33	1.2	3.89	1
	5.4 ft (64.8 in)	-M	-3.41	1.33	1.2	-5.44	1
9 (2 cells)	6.3 ft (75.6 in)	+M	3	1.33	1.2	4.79	1
	9 ft (108 in)	-M	-4.71	1.33	1.2	-7.52	1
10 (2 cells)	9 ft (108 in)	+M	3.12	1.33	1.2	4.98	1
	2 ft (24 in)	-M	-5.62	1.33	1	-7.47	3
15 (2 cells)	10.5 ft (126 in)	+M	3.73	1.33	1.2	5.95	1
	6 ft (72 in)	-M	-10.56	1.33	1	-14.04	3

The punching shear capacity is evaluated here according to the theory described in Chapter 3 using Eq. (3.1) where b_1 = 12.8 in for the long side of the tire footprint and b_2 = 10 in for the short side of the tire footprint. The diagonal tensile strength of concrete is calculated using Eq. (3.2) as:

$$f_t = \left(2 + \frac{4}{12.8/10}\right) \times \sqrt{4000} = 324.1 \text{ ps} \leq 4\sqrt{4000} = 253 \text{ psi} \qquad (6.1)$$

Table 6.25. Comparison of punching shear capacity

Girder Spacing, S (ft)	Slab Thickness, d (in)	Linear Shear from RSM Output		RSM Shear Stress	Total Shear Force from RSM, V_c		b_1'	b_2'	Calculated Shear Stress using Eq. (3.1)	RSM/ Calculated
		(kip/ft)	(lbs/in)	(lbs/in^2)	(kip)	(lbs)	b_1+d	b_2+d	(lbs/in^2)	
4	8	11.5	958.3	119.79	157	157000	20.8	18	252.9	0.47
6	8	10.1	837.5	104.69	157	157000	18	8	377.4	0.28
9	8.125	14.5	1204.2	148.21	160.5	160500	8.125	8.125	607.8	0.24
12	9.125	14.6	1212.5	132.88	189.5	189500	9.125	9.125	569.0	0.23
15	10.375	13.2	1097.5	105.78	228.5	228500	10.375	10.375	530.7	0.20
9 (2 cells)	8.125	12.1	1008.3	124.10	160.5	160500	8.125	8.125	607.8	0.20
15 (2 cells)	10.375	17.0	1420.0	136.87	228.8	228800	10.375	10.375	531.4	0.26

Based on the shear values in

Table 6.25, it is clear that the calculated shear capacity using Eq. (3.1) significantly exceeds the shear demand obtained from the RSM modeling results, with a margin ranging from 20 to 47%. This suggests that the shear stress is considerably lower than the diagonal tensile strength of concrete. **Figure 6.19** depicts the region of the slab that undergoes an impact when subjected to the tire patch loading. Based on these results, the shear demand from subsequent vehicle loads is expected to remain negligible; therefore, this study will focus primarily on the moment demands.

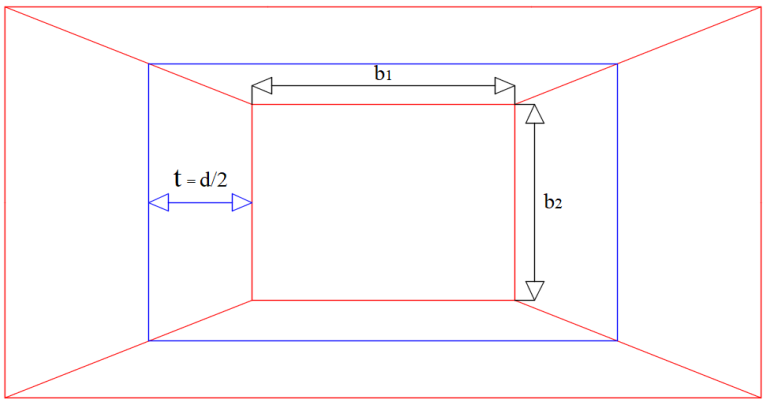

Figure 6.19. Visualization of impact zone: mapping slab region affected by tire patch loading

6.3 Production Run using RSM under P-15

After completing the analysis of HL-93 truck combinations for both single and two trucks, the subsequent focus of this project shifted to the examination of the P-15 truck. **Figure 6.20** provides details regarding the arrangement of the P-15 truck tires and the distances between them. The loading calculation for the P-15 model truck is set at 27 kips per axle, equivalent to 6.75 kips per tire. Since the P-15 vehicles have two axles much closer together than the HL-93 vehicles, 4 ft versus 14 ft respectively, both axles were included in the analysis. The tire pressure was consistent across all vehicle types at 125 psi, resulting in a patch size of 52 in² (10×5.4") for the P-15 vehicle.

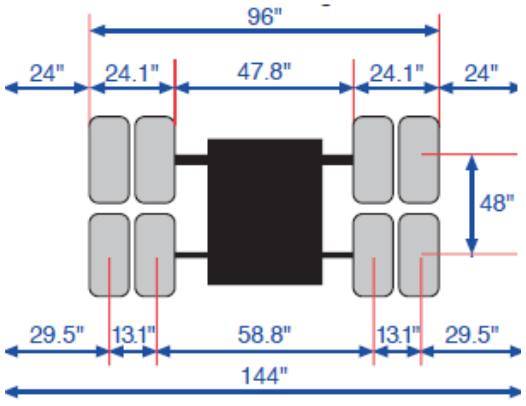

Figure 6.20. P-15 truck tire arrangement and spacing

The Dynamic Load Allowance (IM) and Multiple Presence Factor (m) vary among HL-93, P-15, and EV3 trucks. Specifically, the Dynamic Load Allowances for HL-93, P-15, and EV3 trucks are designated as 1.33, 1.25, and 1.33, respectively. Correspondingly, the Multiple Presence

Factors for HL-93, P-15, and EV3 trucks (one-lane loaded) are specified as 1.2, 1.00, and 1.00, respectively. Detailed information for each is outlined in **Table 6.26**.

Table 6.26. Caltrans truck loading specification summary

Vehicle Type	Loading Specification	Application of Live Loads	Applicable Limit States	Live Load Factors (Not Used)	Dynamic Load Allowance (*IM*)	Multiple Presence Factor (*m*)	Tire Pressure Used (psi)
HL-93	AASHTO LRFD	Multiple Lanes (loading per AASHTO LRFD Specification	Strength I	1.75	33% (Design truck only)	1 loaded lane = 1.20 2 loaded lanes = 1.00 3 loaded lanes = 0.85 >3 loaded lanes = 0.65	125
			Service I	1.00			
CA P15	AASHTO LRFD	Two Lanes Max	Strength II	1.35	25%	1 loaded lane = 1.00 2 loaded lanes = 1.00	125 (8 tires)
SHV	SM&I LRFR	Multiple Lanes (loading per AASHTO LRFD Specification	Strength	1.45	33%	1 loaded lane = 1.20 2 loaded lanes = 1.00 >2 loaded lanes = 1.00	125
			Service	1.00			
EV	SM&I LRFR	Two Lanes Total (single lane EV Vehicle plus one Legal 3S-2	Strength	1.30	33%	1.00	125
~~Fatigue (HL-93)~~	~~AASHTO LRFD~~	~~One Lane Tota~~	~~Fatigue I~~	~~1.75~~	~~15%~~	~~1.00~~	~~80 or 125?~~
~~Fatigue (P9)~~	~~AASHTO LRFD~~	~~One Lane Tota~~	~~Fatigue II~~	~~1.00~~	~~15%~~	~~1.00~~	~~80 or 125?~~

Similar to the HL-93 analysis, the positioning of the truck on the bridge deck can vary depending on the modeled combination. To streamline the modeling of the P-15 truck and minimize workload, we opted to place the truck at the critical locations identified in the HL-93 analysis. The total number of combinations for each girder spacing is provided in **Table 6.27**.

To verify the assumption that the controlling load position would be consistent with the HL-93 cases, girder spacings with more than one governing case were considered since the maximum positive and negative moments may occur under different scenarios. In some cases, the controlling position shifted slightly, but this was due to the difference in the patch width and the fact that the position is reported based on the edge of the tire and not the centroid of the patches. This discrepancy is illustrated in **Figure 6.21**. To ensure the maximum and minimum values were found for every span configuration, local maxima and minima were checked for each girder spacing. **Figure 6.22** shows the results for a 4 ft girder spacing, 4-cell configuration. From the figure it is clear that both the maximum and minimum moments occurred when the first tire patch was placed 48 in from the edge of the deck since both the maximum and minimum moments are

smaller in magnitude when the load is moved in either direction. This logical step allowed many models to be skipped without compromising the certainty of the results.

Table 6.27. Comprehensive overview of combinations for each girder spacing for P-15 truck

Girder Spacing (ft)	No. of Cell	Truck Case	Moments	Total Combinations
4	4	Case 1	Positive Moment	1
		Case 1	Negative Moment	1
6	4	Case 1	Positive Moment	1
		Case 1	Negative Moment	1
9	4	Case 1	Positive Moment	2
		Case 1	Negative Moment	2
12	4	Case 1	Positive Moment	1
		Case 3 (4 ft apart)	Negative Moment	17
15	4	Case 1	Positive Moment	1
		Case 3 (4 ft apart)	Negative Moment	19
9	2	Case 1	Positive Moment	1
		Case 1	Negative Moment	1
15	2	Case 1	Positive Moment	1
		Case 3 (4 ft apart)	Negative Moment	8
Total Number of Combinations				57

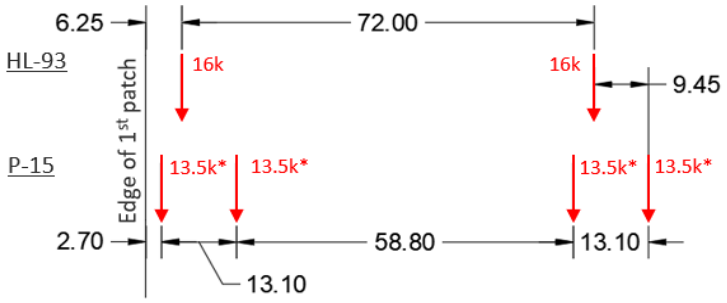

Figure 6.21. Comparison of HL-93 and P-15 resultant force locations w.r.t. edge of first patch

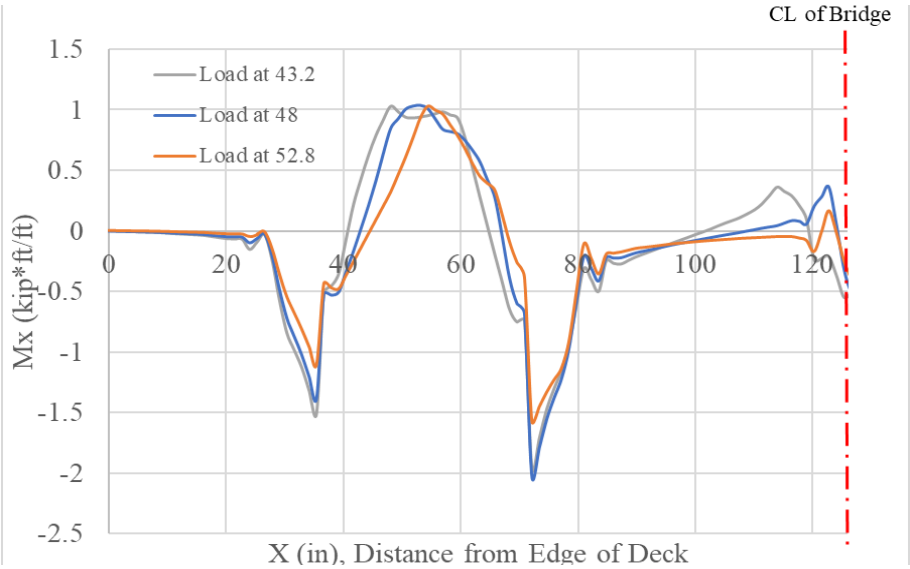

Figure 6.22. Partial moment envelope for 4 ft girder spacing, 4-cell

The results of the P-15 analysis are shown in **Table 6.28**. Similar to the HL-93 run, the governing load case switched from Case 1 to Case 3 between the 9 ft and 10 ft girder spacings. One difference is that the positive moment is also controlled by Case 3 for the 15 ft girder spacing in both the 4-cell and 2-cell configurations.

Table 6.28. Summary of maximum moments due to P-15 loading by girder spacing

Girder Spacing (ft)	Distance - Edge of Tire to Edge of Deck	Max. Moment (kip-ft/ft)	RSM (kip-ft/ft)	1+IM	m	RSM(1+IM)m (kip-ft/ft)	Governing Load Case
4	4 ft (48 in)	+M	1.03	1.25	1	1.29	1
	4 ft (48 in)	-M	-2.03	1.25	1	-2.54	1
6	5.4 ft (64.8 in)	+M	1.69	1.25	1	2.11	1
	5.4 ft (64.8 in)	-M	-3.2	1.25	1	-4.00	1
9	7.2 ft (86.4 in)	+M	2.7	1.25	1	3.38	1
	9 ft (108 in)	-M	-4.95	1.25	1	-6.19	1
10	9 ft (108 in)	+M	2.84	1.25	1	3.55	1
	1 ft (12 in)	-M	-5.04	1.25	1	-6.30	3
11	14.3 ft (171.6 in)	+M	3.2	1.25	1	4.00	1
	11 ft (132 in)	-M	-7.22	1.25	1	-9.03	3
12	9.6 ft (115.2 in)	+M	3.4	1.25	1	4.25	1
	7.2 ft (86.4 in)	-M	-8.48	1.25	1	-10.60	3
15	10.5 ft (54 in)	+M	4.51	1.25	1	5.64	3
	4.5 ft (54 in)	-M	-10.94	1.25	1	-13.68	3
6 (2 cells)	5.4 ft (64.8 in)	+M	1.79	1.25	1	2.24	1
	5.4 ft (64.8 in)	-M	-3.16	1.25	1	-3.95	1
9 (2 cells)	6.3 ft (75.6 in)	+M	2.61	1.25	1	3.26	1
	9 ft (108 in)	-M	-4.96	1.25	1	-6.20	1
10 (2 cells)	9 ft (108 in)	+M	2.84	1.25	1	3.55	1
	1 ft (12 in)	-M	-5.07	1.25	1	-6.34	3
15 (2 cells)	4.5 ft (54 in)	+M	4.52	1.25	1	5.65	3
	4.5 ft (54 in)	-M	-11.92	1.25	1	-14.90	3

Due to the P-15 truck having two patch loads on each side, an additional combination for 9 ft girder spacing was introduced, as illustrated in **Figure 6.26**. In this case, the truck is positioned based on the distance from the deck's end to the middle of the two tire patches, whether on the right or left side. A comparison of results revealed that the difference is negligible when locating the truck based on the distance to the tire face for a 9 ft girder spacing deck slab. Consequently, adopting the location method akin to the HL-93 truck, based on the distance from the deck's end to the tire face, is deemed appropriate.

The positioning of the P-15 truck for girder spacings of 4 ft, 6 ft, 9 ft, 12 ft, and 15 ft with four cells, as well as 9 ft and 15 ft girder spacings with two cells, is illustrated in **Figure 6.23** to **Figure 6.33**.

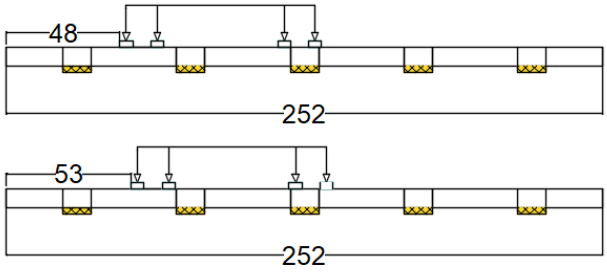

Figure 6.23. Location of P-15 truck for 4 ft girder spacing deck slab (Case 1, unit: in)

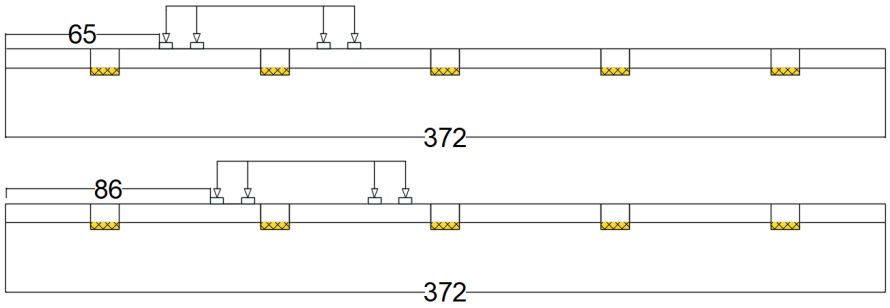

Figure 6.24. Location of P-15 truck for 6 ft girder spacing deck slab (Case 1, unit: in)

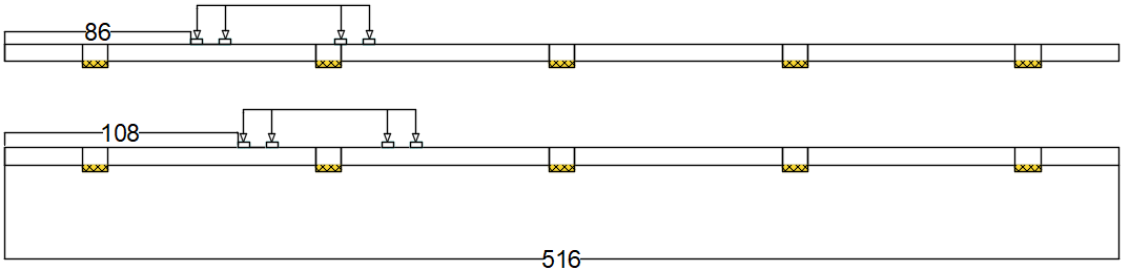

Figure 6.25. Location of P-15 truck for 9 ft girder spacing deck slab (Case 1, unit: in)

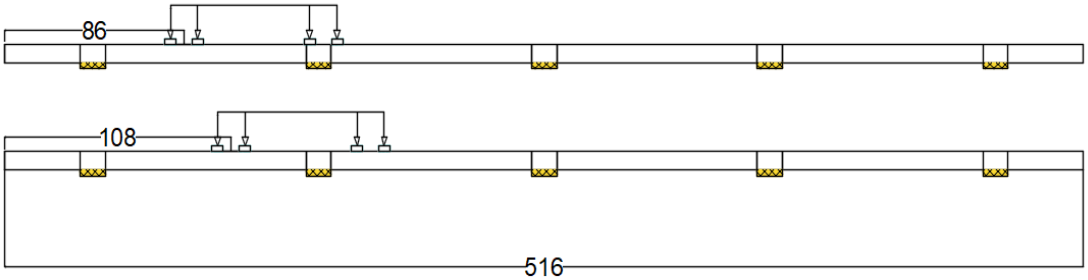

Figure 6.26. Location of P-15 truck for 9 ft girder spacing deck slab (Case 1, load located at the centerline of two patch load, unit: in)

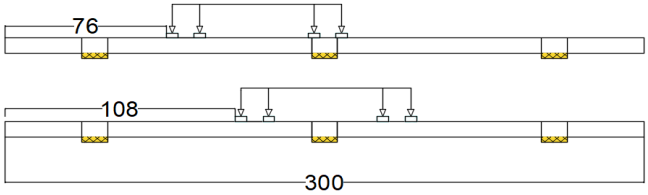

Figure 6.27. Location of P-15 truck for 9 ft girder spacing deck slab (2 cells, Case 1, unit: in)

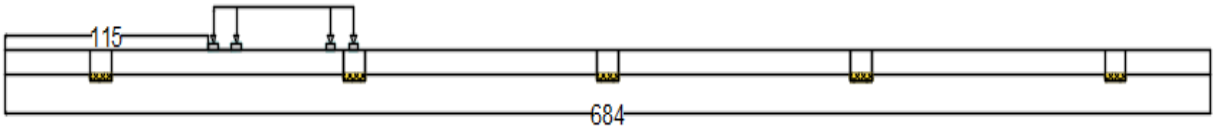

Figure 6.28. Location of P-15 truck for 12 ft girder spacing deck slab (Case 1, unit: in)

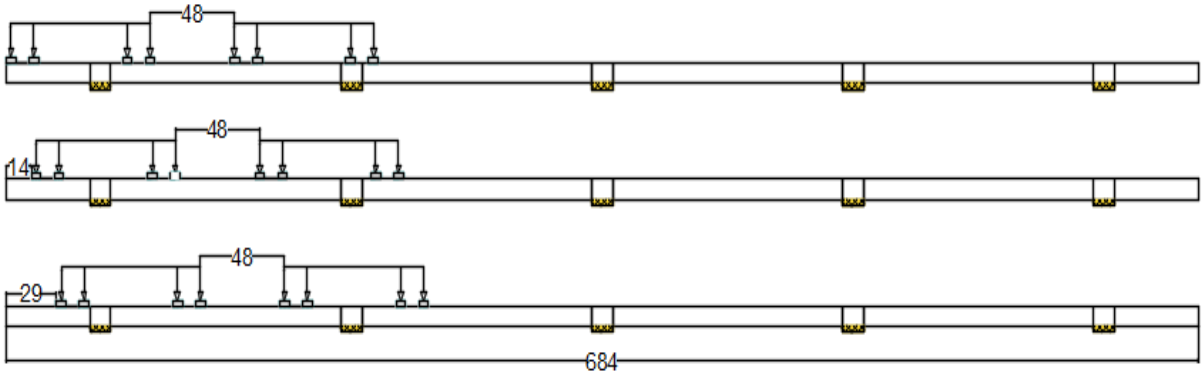

Figure 6.29. Location of P-15 truck for 12 ft girder spacing deck slab (Case 3, unit: in)

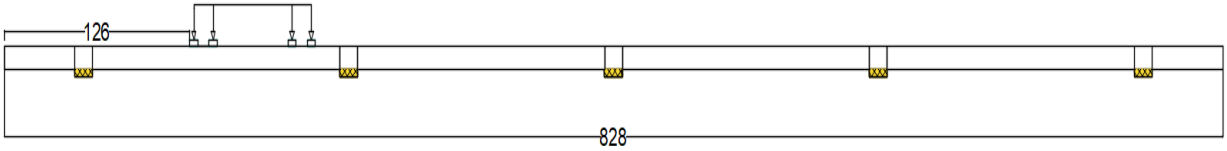

Figure 6.30. Location of P-15 truck for 15 ft girder spacing deck slab (Case 1, unit: in)

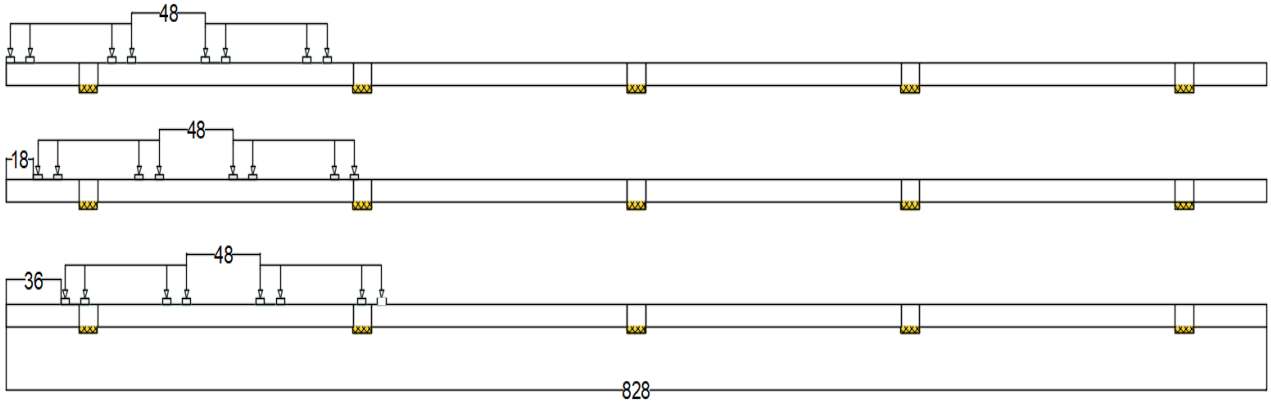

Figure 6.31. Location of P-15 truck for 15 ft girder spacing deck slab (Case 3, unit: in)

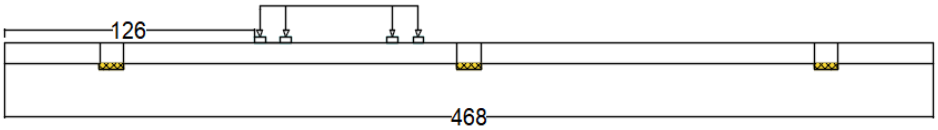

Figure 6.32. Location of P-15 truck for 15 ft girder spacing deck slab (2 cells, Case 1, unit: in)

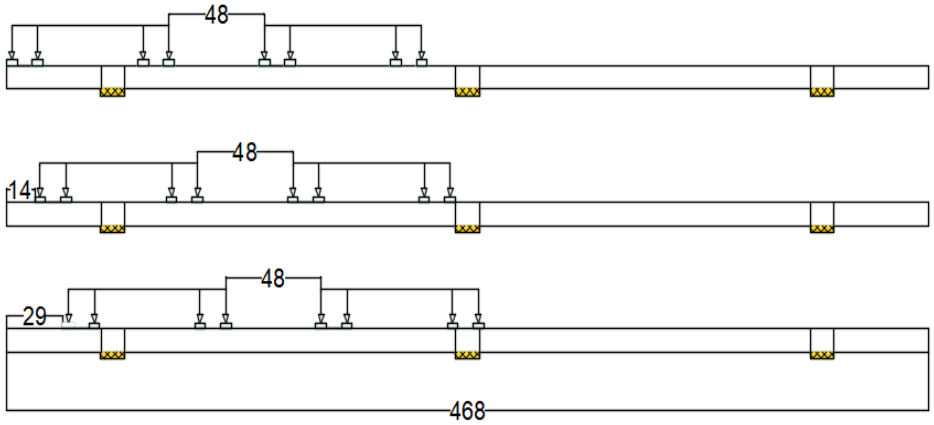

Figure 6.33. Location of P-15 truck for 15 ft girder spacing deck slab (2 cells, Case 3, unit: in)

A P-15 vehicle has a larger combined axle weight than an HL-93 vehicle. However, having two P-15 trucks side by side and carrying a load that exceeds 48 kip is currently not allowed. This rule ensures that the operational limit of 48 kip is maintained, which is crucial for safety and structural integrity. It balances current safety limits, set at 48 kip, with a thoughtful overdesign in the planning stages to possibly increase to 54 kip in the future. To accommodate this potential change in allowance, the P-15 vehicles used in this study were all assumed to have the full 54 kip double axle weight, even when two vehicles are considered side by side. This approach is taken to make sure structures or vehicles remain safe and durable even under the heaviest expected loads, even though there's no immediate need for the higher capacity. The discussion underlines the need for policies and designs to be flexible enough to adjust to future demands while also making sure not to harm important structures. Moreover, it covers specific planning for different types of vehicles, showing a deep understanding of the various situations that could impact how much weight structures can safely handle. It illustrates the complex but essential balance of technical accuracy, planning for the future, and careful management required in engineering and policymaking, highlighting the challenges in preparing for both today's and tomorrow's infrastructure needs in simpler terms.

6.4 Production Run using RSM under SHV

The next load pattern considered was the special hauling vehicle (SHV), which consists of more closely spaced axles than any other vehicle in this study. There are multiple variations of axle configurations for SHVs, shown in **Figure 6.34**, in addition to the Notional Rating Load in **Figure 6.35**, which was selected for use in this study. The notional case has the most axles with the closest spacings making it the largest load demand and therefore the conservative choice for use. Based on the 125 psi standard tire pressure, two different sized tire patches were used. The 17-kip axles had 10 by 6.8 in tire patches, and the 8-kip axles had 10 by 3.2 in tire patches.

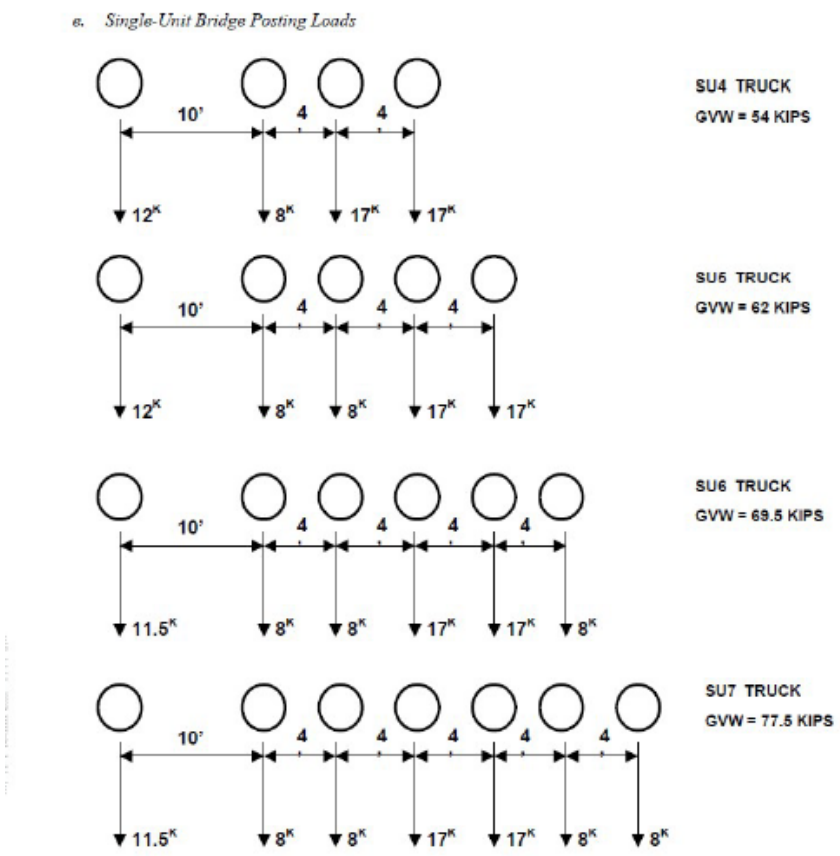

Figure D6A-7—Bridge Posting Loads for Single-Unit SHVs that Meet Federal Bridge Formula B

Figure 6.34. SHV axle configuration variants

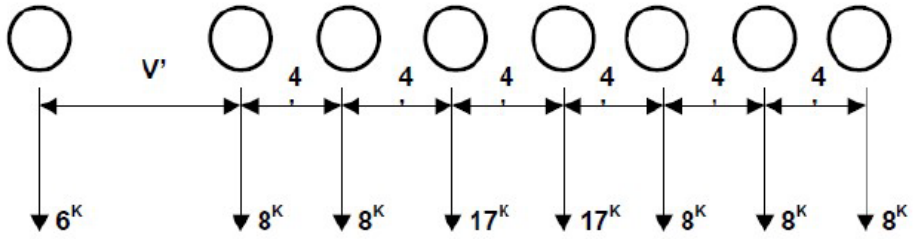

V=VARIABLE DRIVE AXLE SPACING—6'0" TO 14'0". SPACING TO BE USED IS THAT WHICH PRODUCES MAXIMUM LOAD EFFECTS.

AXLES THAT DO NOT CONTRIBUTE TO THE MAXIMUM LOAD EFFECTS UNDER CONSIDERATION SHALL BE NEGLECTED.

MAXIMUM GVW = 80 KIPS

AXLE GAGE WIDTH = 6'0"

Figure D6A-6—Notional Rating Load (NRL) for Single-Unit SHVs that Meet Federal Bridge Formula B

Figure 6.35. Notional Rating Load for SHV

Prior to starting the production run for the SHV, some exploratory models were run. There are no other trucks with more than two axles at a 4 ft spacing were considered, so several models were constructed to test the influence of more than two axles at a 4-ft spacing. At one extreme, a model was run with the full set of 8 axles, and at the other extreme, a model consisting of only one 17-kip axle was run. The largest positive and negative moments were compared between these two models, the results of which are summarized in **Table 6.29**. For both the positive and negative moments, the full notional load produced significantly larger demands and so it was decided to use the full notional load for the production run of the SHV.

Table 6.29. Summary of moments comparing the SHV full notional load to a single axle

Moment	Full Notional Load	Single 17-kip Axle	Single/Full
$+M_{max}$ (kip-ft/ft)	2.89	1.99	0.69
$-M_{min}$ (kip-ft/ft)	-3.26	-1.62	0.50

The SHV production run was accelerated by using the same local maxima and minima approach focused on the previously discovered governing load positions, reducing the total number of models required. The results of the SHV analysis are summarized in **Table 6.30**. The pattern of the controlling combination changing from Case 1 to Case 3 between 9 ft and 10 ft girder spacings remained consistent for the SHV results.

Table 6.30. Summary of maximum moments due to SHV loading by girder spacing

Girder Spacing (ft)	Distance - Edge of Tire to Edge of Deck	M_{max} (kip-ft/ft)	RSM (kip-ft/ft)	1+IM	m	RSM(1+IM)m (kip-ft/ft)	Governing Load Case
4	3.6 ft (43.2 in)	+M	1.42	1.33	1.2	2.27	1
	4.4 ft (52.8 in)	-M	-1.44	1.33	1.2	-2.30	1
6	6 ft (72 in)	+M	1.623	1.33	1.2	2.59	1
	6 ft (72 in)	-M	-2.29	1.33	1.2	-3.65	1
9	7.2 ft (86.4 in)	+M	2.17	1.33	1.2	3.46	1
	9 ft (108 in)	-M	-3.39	1.33	1.2	-5.41	1
10	9 ft (108 in)	+M	2.45	1.33	1.2	3.91	1
	2 ft (24 in)	-M	-4.65	1.33	1	-6.18	3
11	14.3 ft (171.6 in)	+M	2.5	1.33	1.2	3.99	1
	11 ft (132 in)	-M	-5.84	1.33	1	-7.77	3
12	9.6 ft (115.2 in)	+M	2.9	1.33	1.2	4.63	1
	3.6 ft (43.2 in)	-M	-7.04	1.33	1	-9.36	3
15	10.5 ft (126 in)	+M	3.68	1.33	1.2	5.87	1
	6 ft (72 in)	-M	-9.91	1.33	1	-13.18	3
6 (2 cells)	5.4 ft (64.8 in)	+M	1.45	1.33	1.2	2.31	1
	5.4 ft (64.8 in)	-M	-2.02	1.33	1.2	-3.22	1
9 (2 cells)	6.3 ft (75.6 in)	+M	2	1.33	1.2	3.19	1
	9 ft (108 in)	-M	-3.55	1.33	1.2	-5.67	1
10 (2 cells)	9 ft (108 in)	+M	2.47	1.33	1.2	3.94	1
	2 ft (24 in)	-M	-5.21	1.33	1	-6.93	3
15 (2 cells)	10.5 ft (126 in)	+M	3.68	1.33	1.2	5.87	1
	6 ft (72 in)	-M	-10.8	1.33	1	-14.36	3

6.5 Production Run using RSM under EV3

In the single EV3 vehicle configuration is depicted in **Figure 6.36**, each of the three axles carries two patch loads. The heaviest axle on the EV3 has a load distribution of 15.5 kips per tire and therefore requires a 10 in by 12.4 in tire patch to maintain the 125 psi tire pressure used in this study. For Case 3 loading, that is 2 vehicles side by side with 4 ft center to center between adjacent tires, the second vehicle is not also an EV3. Instead, the second vehicle is a Type 3S2 support vehicle which has 31 kips distributed over a double axle, resulting in twice as many tires with half the contact area per tire (10 by 6.2 in) compared to the EV3. Since the two vehicles have different axle spacings, several models were run to determine which axles should be aligned to cause the maximum moment effect. It was determined that aligning middle axles of each vehicle caused the largest effects.

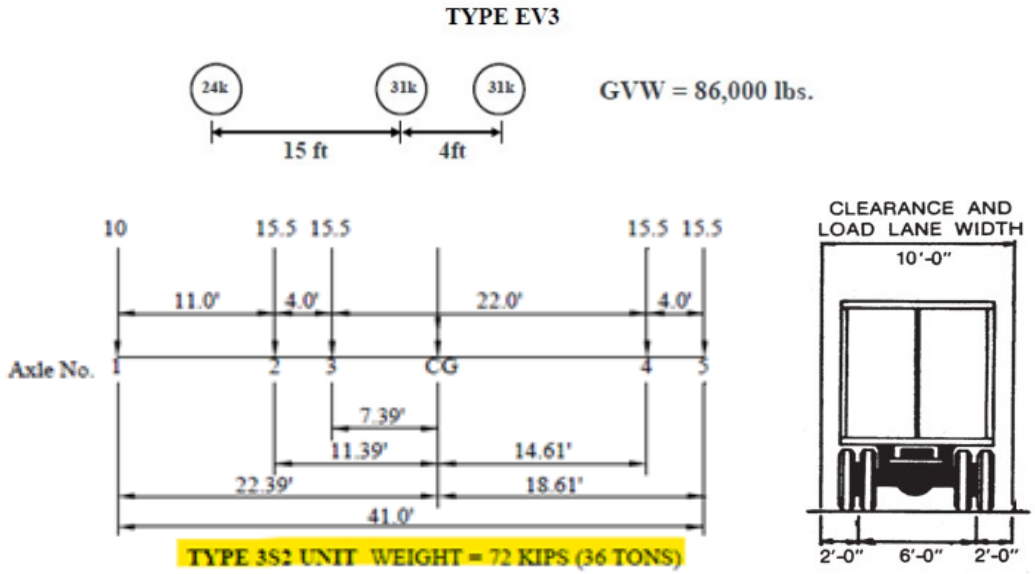

Figure 6.36. EV3 (top) and 3S2 (bottom) truck axle configurations

Similar to the P-15 production run, the EV3 run was accelerated by using the same local maxima and minima approach focused on the previously discovered governing load positions. The results of the EV3 analysis are summarized in **Table 6.31** based on the combinations for each girder spacing in **Table 6.32**. A similar pattern emerged in the governing load case switching from Case 1 to Case 3 between the 9 ft and 10 ft spacings and similar to the P-15 cases, the positive moment for the 15 ft spacing was also governed by Case 3.

Table 6.31. Summary of maximum moments due to EV3 loading by girder spacing

Girder Spacing (ft)	Distance - Edge of Tire to Edge of Deck	M_{max} (kip-ft/ft)	RSM (kip-ft/ft)	1+IM	m	RSM(1+IM)m (kip-ft/ft)	Governing Load Case
4	4 ft (48 in)	+M	1.8	1.33	1	2.39	1
	4.4 ft (52.8 in)	-M	-2.55	1.33	1	-3.39	1
6	5.4 ft (64.8 in)	+M	2.56	1.33	1	3.40	1
	7.2 ft (86.4 in)	-M	-3.65	1.33	1	-4.85	1
9	7.2 ft (86.4 in)	+M	3.55	1.33	1	4.72	1
	9 ft (108 in)	-M	-6.28	1.33	1	-8.35	3

10	9 ft (108 in)	+M	3.71	1.33	1	4.93	1
	6 ft (72 in)	-M	-6.81	1.33	1	-9.06	3
11	14.3 ft (171.6 in)	+M	4.15	1.33	1	5.52	1
	12.1 ft (145.2 in)	-M	-8	1.33	1	-10.64	3
12	9.6 ft (115.2 in)	+M	4.42	1.33	1	5.88	1
	7.2 ft (86.4 in)	-M	-8.94	1.33	1	-11.89	3
15	6 ft (72 in)	+M	5.42	1.33	1	7.21	3
	7.5 ft (90 in)	-M	-11.11	1.33	1	-14.78	3
6 (2 cells)	5.4 ft (64.8 in)	+M	2.63	1.33	1	3.50	1
	5.4 ft (64.8 in)	-M	-3.67	1.33	1	-4.88	1
9 (2 cells)	6.3 ft (75.6 in)	+M	3.52	1.33	1	4.68	1
	9 ft (108 in)	-M	-5.74	1.33	1	-7.63	1
10 (2 cells)	9 ft (108 in)	+M	3.77	1.33	1	5.01	1
	6 ft (72 in)	-M	-5.8	1.33	1	-7.71	3
15 (2 cells)	10.5 ft (126 in)	+M	5.42	1.33	1	7.21	1
	10.5 ft (126 in)	-M	-11.94	1.33	1	-15.88	3

Table 6.32. Comprehensive overview of combinations for each girder spacing for EV3 truck

Girder Spacing (ft)	No. of Cell	Truck Case	Moments	Total Combinations
4	4	Case 1	Positive Moment	3
		Case 1	Negative Moment	3
6	4	Case 1	Positive Moment	3
		Case 1	Negative Moment	3
9	4	Case 1	Positive Moment	3
		Case 1	Negative Moment	3
12	4	Case 1	Positive Moment	3
		Case 3 (4 ft apart)	Negative Moment	3
15	4	Case 1	Positive Moment	3
		Case 3 (4 ft apart)	Negative Moment	3
9	2	Case 1	Positive Moment	3
		Case 1	Negative Moment	3
15	2	Case 1	Positive Moment	3
		Case 3 (4 ft apart)	Negative Moment	3

6.6 Comparison among HL-93, P-15, SHV and EV3

With the moment demands for the HL-93, EV3 and P-15 trucks documented, the results can be compared. All three vehicle types exhibited similar behavior with location of the maximum and minimum moments. The maximum positive moments generally occurred at or near the mid span of the first (exterior) girder spacing. The minimum negative moments also generally occurred at the face of the first interior girder. The moment demands from all vehicles are summarized in the table below. **Table 6.33** displays the results of RSM(1+IM)m and RSM values for maximum positive and negative moments for each truck within the categories of HL-93, P-15, and EV3.

Table 6.33. Moment comparisons among HL-93, P-15 and EV3 at critical locations

Girder Spacing (ft)	M_{max} (kip-ft/ft)	HL-93		P-15		EV3		SHV	
		RSM	RSM(1+IM)m	RSM	RSM(1+IM)m	RSM	RSM(1+IM)m	RSM	RSM(1+IM)m
4	+M	1.78	2.84	1.03	1.29	1.80	2.39	1.42	2.27
	-M	-2.53	-4.04	-2.03	-2.54	-2.55	-3.39	-1.44	-2.30
6	+M	2.37	3.78	1.69	2.11	2.56	3.40	1.62	2.59
	-M	-3.45	-5.51	-3.20	-4.00	-3.65	-4.85	-2.29	-3.65
9	+M	2.89	4.61	2.70	3.38	3.55	4.72	2.17	3.46
	-M	-4.78	-7.63	-4.95	-6.19	-6.28	-8.35	-3.39	-5.41
10	+M	3.07	4.90	2.84	3.55	3.71	4.93	2.45	3.91
	-M	-6.53	-8.69	-5.04	-6.30	-6.81	-9.06	-4.65	-6.18
11	+M	3.39	5.41	3.20	4.00	4.15	5.52	2.50	3.99
	-M	-7.58	-10.08	-7.22	-9.03	-8.00	-10.64	-5.84	-7.77
12	+M	3.47	5.54	3.40	4.25	4.42	5.88	2.90	4.63
	-M	-8.25	-10.97	-8.48	-10.60	-8.94	-11.89	-7.04	-9.36
15	+M	3.73	5.95	4.51	5.64	5.42	7.21	3.68	5.87
	-M	-9.69	-12.89	-10.94	-13.68	-11.11	-14.78	-9.91	-13.18
6 (2 cells)	+M	2.44	3.89	1.79	2.24	2.63	3.50	1.45	2.31
	-M	-3.41	-5.44	-3.16	-3.95	-3.67	-4.88	-2.02	-3.22
9 (2 cells)	+M	3.00	4.79	2.61	3.26	3.52	4.68	2.00	3.19
	-M	-4.71	-7.52	-4.96	-6.20	-5.74	-7.63	-3.55	-5.67
10 (2 cells)	+M	3.12	4.98	2.84	3.55	3.77	5.01	2.47	3.94
	-M	-5.62	-7.47	-5.07	-6.34	-5.80	-7.71	-5.21	-6.93
15 (2 cells)	+M	3.73	5.95	4.52	5.65	5.42	7.21	3.68	5.87
	-M	-10.56	-14.04	-11.92	-14.90	-11.94	-15.88	-10.80	-14.36

6.6.1 HL-93 vs. P-15

The positive moment demands of the HL-93 and P-15 vehicles are compared in **Figure 6.37** and **Figure 6.38**. Based on the figures, it is evident that HL-93 exhibits higher values in all girder spacings, except for the 15 ft girder spacing with 4 and 2-cell moments without the dynamic load or multiple presence factors (dashed lines). In all cases the HL-93 positive moments are larger when the design factors are considered (solid lines).

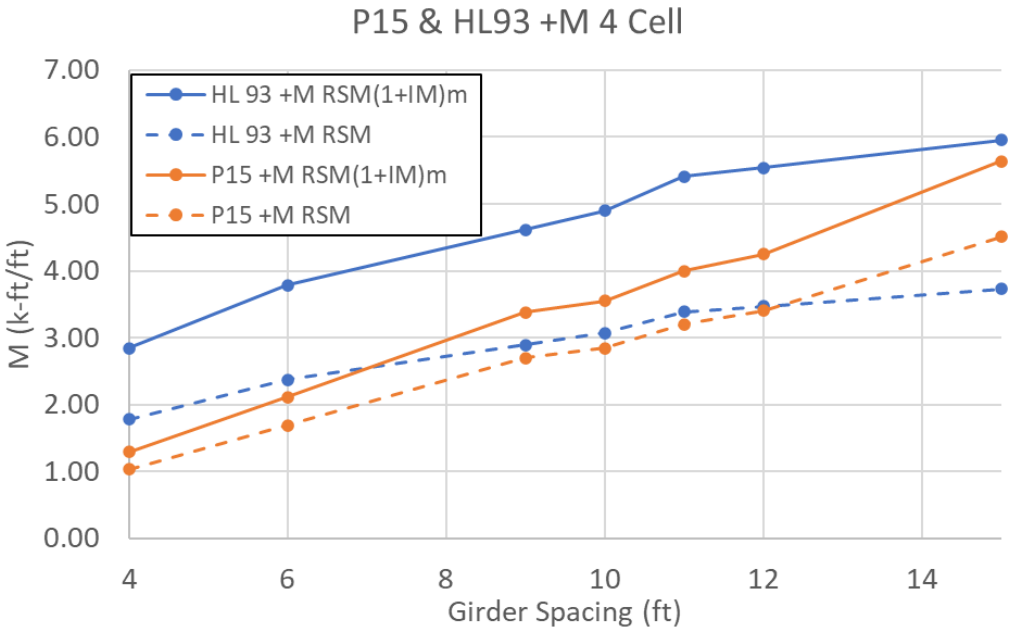

Figure 6.37. Maximum positive moments based on critical locations (4 cells)

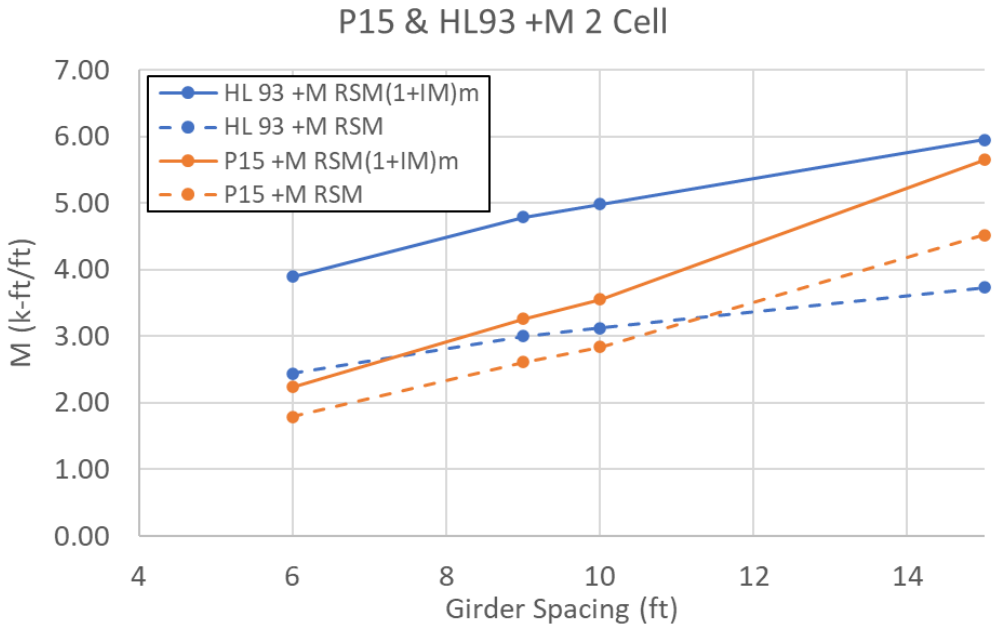

Figure 6.38. Maximum positive moments based on critical locations (2 cells)

A similar comparison can be made for the negative moment demands in **Figure 6.39** and **Figure 6.40**. For the negative moments, the trend is the same with and without consideration for the design factors. In both cases, the P-15 vehicles produce slightly larger moments for spans greater than 12 ft. This difference is small, with the largest difference being 6% for a 15 ft span. This is small enough to be considered a negligible difference. Based on these comparisons it can be concluded that if only HL-93 vehicles are considered in the analysis, the P-15 case can also be considered covered.

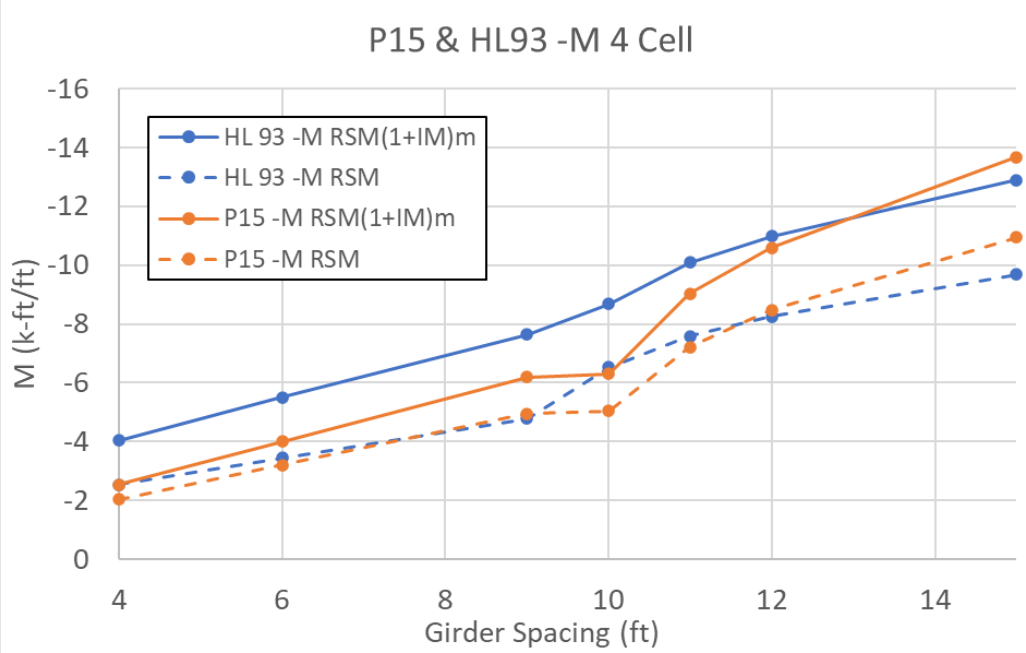

Figure 6.39. Negative moments based on critical locations (4 cells)

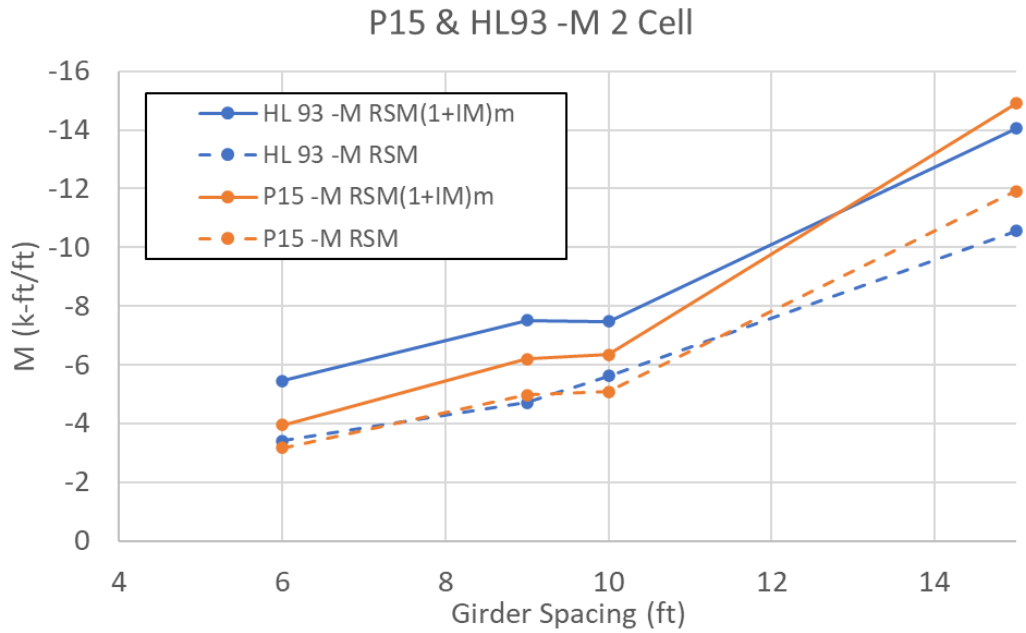

Figure 6.40. Negative moments based on critical locations (2 cells)

6.6.2 HL-93 vs. SHV

The positive moment demands of the HL-93 and SHV vehicles are compared in **Figure 6.41** and **Figure 6.42**. Based on the figures, it is evident that HL-93 exhibits higher values in all girder spacings, with (solid line) and without the multiple presence and dynamic load factors (dashed line) considered. There is a noticeable trend here, similar to P-15 vehicle, in that the SHV demands start to close in on the HL-93 demands at larger spacings.

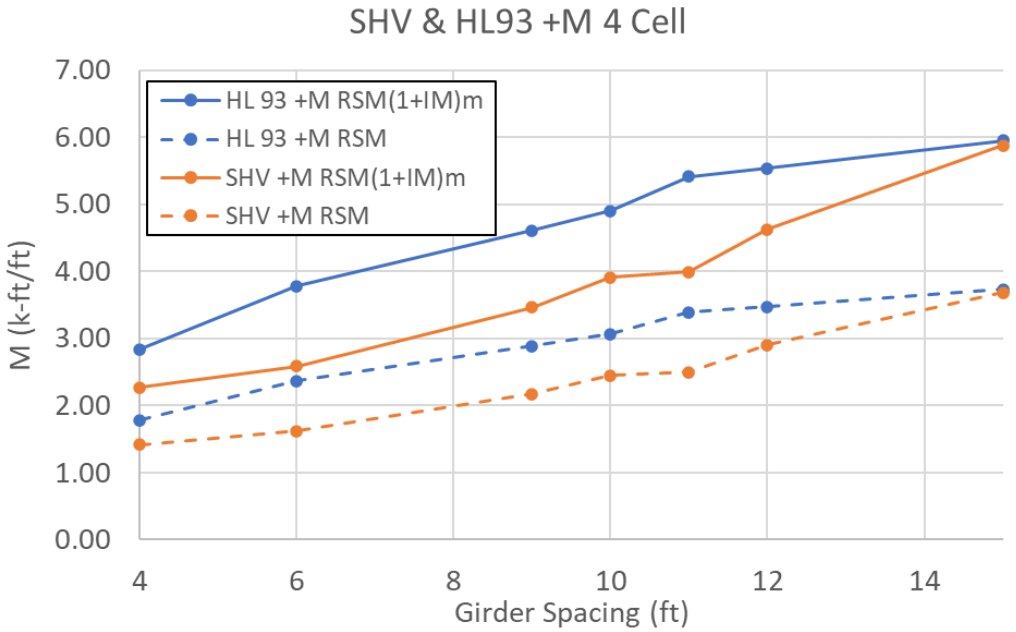

Figure 6.41. Positive moments based on critical locations (4 cells)

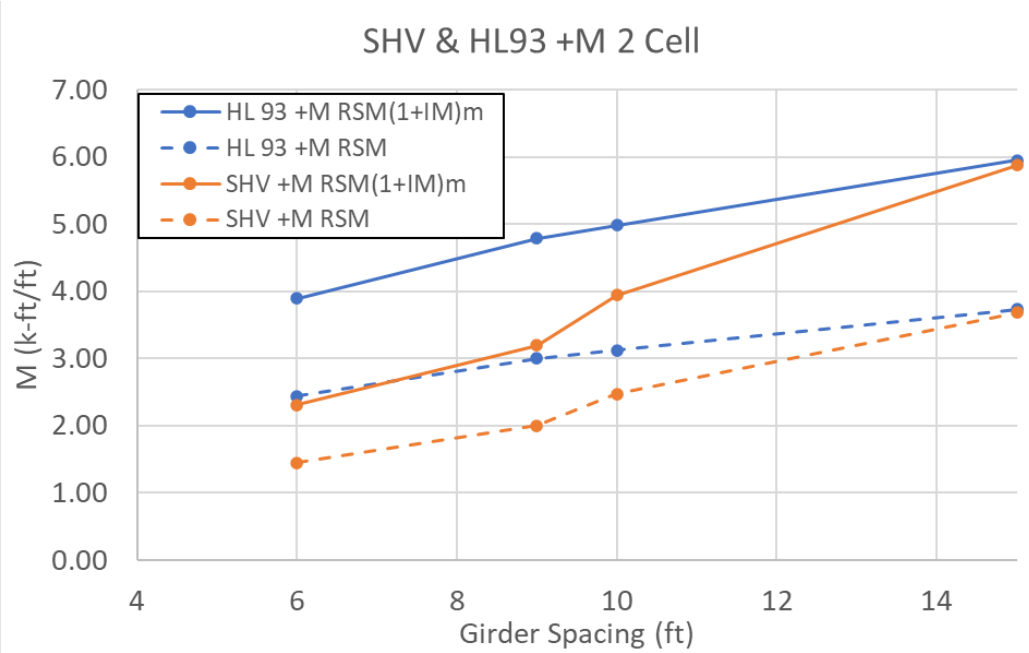

Figure 6.42. Positive moments based on critical locations (2 cells)

The results are similar for the negative moment demands shown in **Figure 6.43** and **Figure 6.44**. The HL-93 values govern for all but the 15-ft girder spacing, where the SHV moments are larger. This difference is so small (< 2%) that it can be considered negligible. However, it is worth noting here that a 15-ft girder spacing was the upper bound considered for this study, but if larger spacings are necessary, vehicles other than the HL-93 truck may control the moment demands.

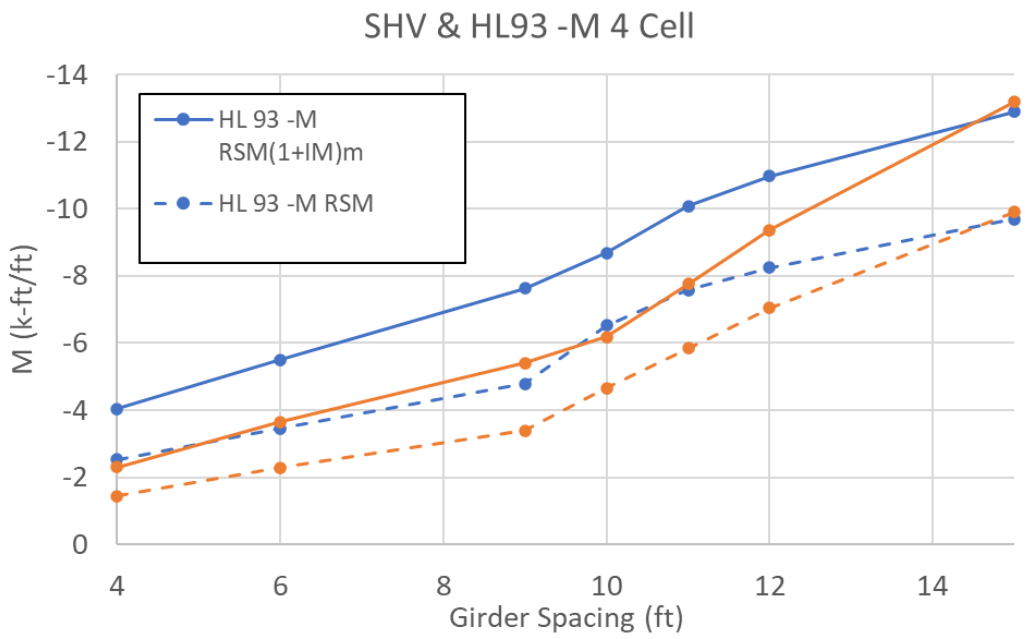

Figure 6.43. Negative moments based on critical locations (4 cells)

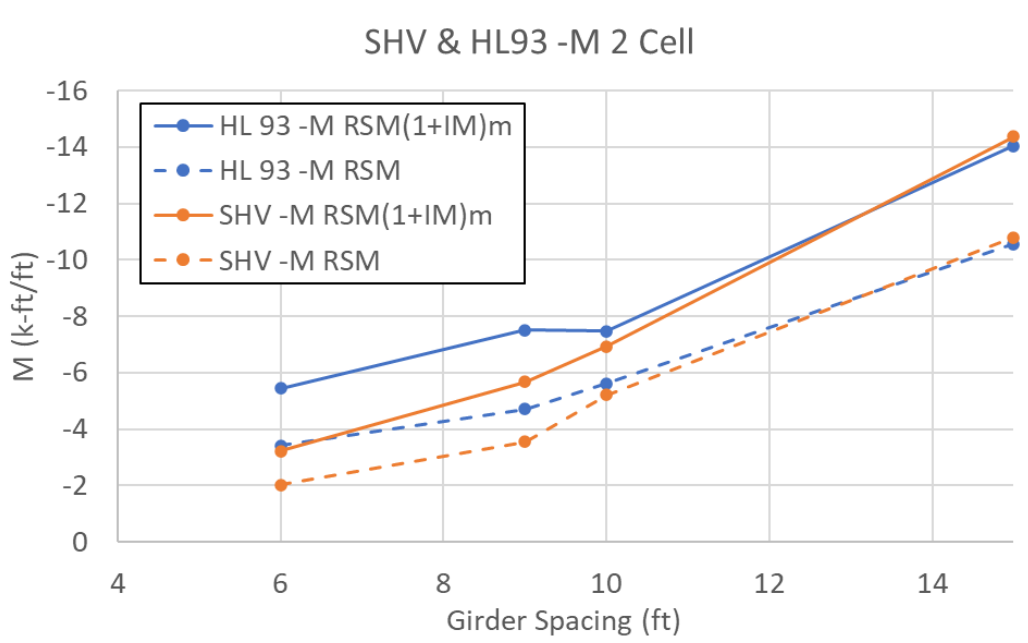

Figure 6.44. Negative moments based on critical locations (2 cells)

6.6.3 HL-93 vs. EV3

The positive moment demands for the EV3 and HL-93 cases are compared in **Figure 6.45** and **Figure 6.46**. From the graphs it is evident there are many spans where the EV3 vehicles have similar or slightly greater demands than the HL-93 cases. The disparity grows with larger spans, with the largest difference being 21%.

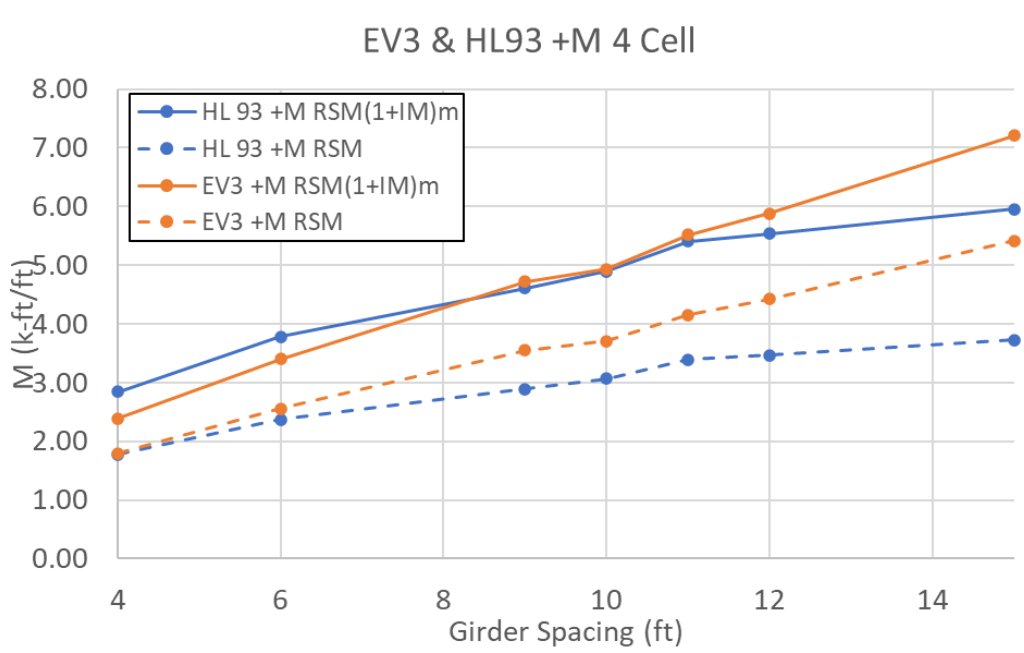

Figure 6.45. Positive moments based on critical locations (4 cells)

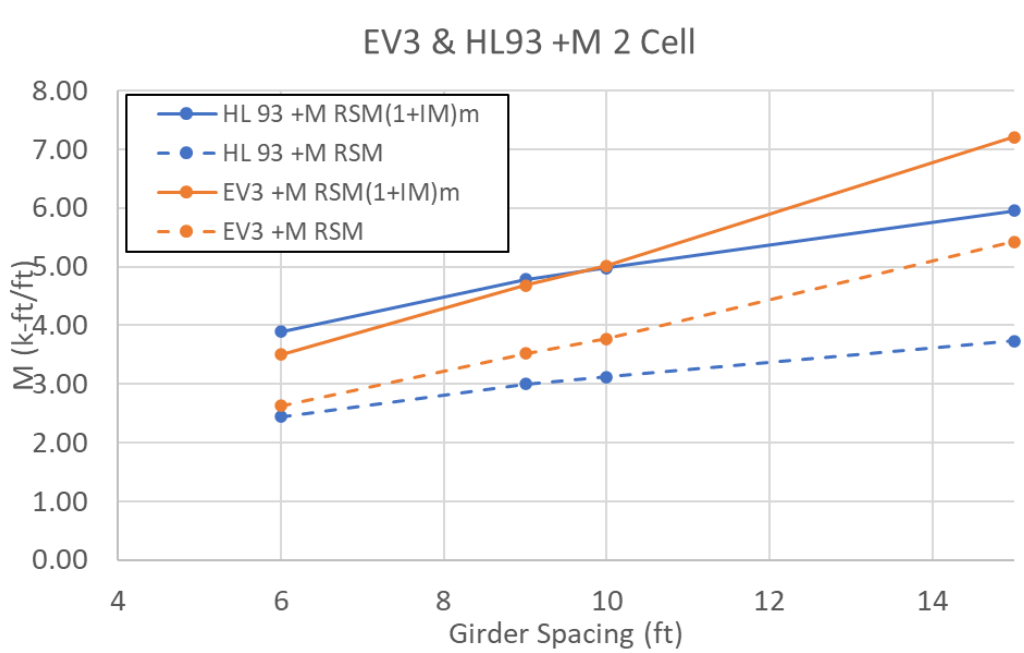

Figure 6.46. Positive moments based on critical locations (2 cells)

A similar trend is evident for the negative moment demands shown in **Figure 6.47** and **Figure 6.48**, where the EV3 demands start to exceed the HL-93 results around an 8 ft or 9 ft span length. Here the largest difference is 15% at the largest span length of 15 ft. Since these differences can exceed 10%, they should be considered significant which means that EV3 demands merit special consideration on top of the standard HL-93 case in design. This comparison does not account for LRFD load factors. Since the LRFD factors for the two vehicle types are different, that would add another layer of complication in the design process. The LRFD live load factor for the HL-93 case

is 1.75 while the factor for EV3 is only 1.30. If the EV3 and HL-93 values are normalized based on the HL-93 moment for the largest difference, they would be 1.21 and 1.0 respectively. Then, multiplying the EV3 value of 1.21 by the LRFD factor the normalized factored value would be 1.57, while the HL-93 value would be 1.75. This means that when using LRFD design methodology, the demands from HL-93 will always exceed the EV3 case, even for these longer spans.

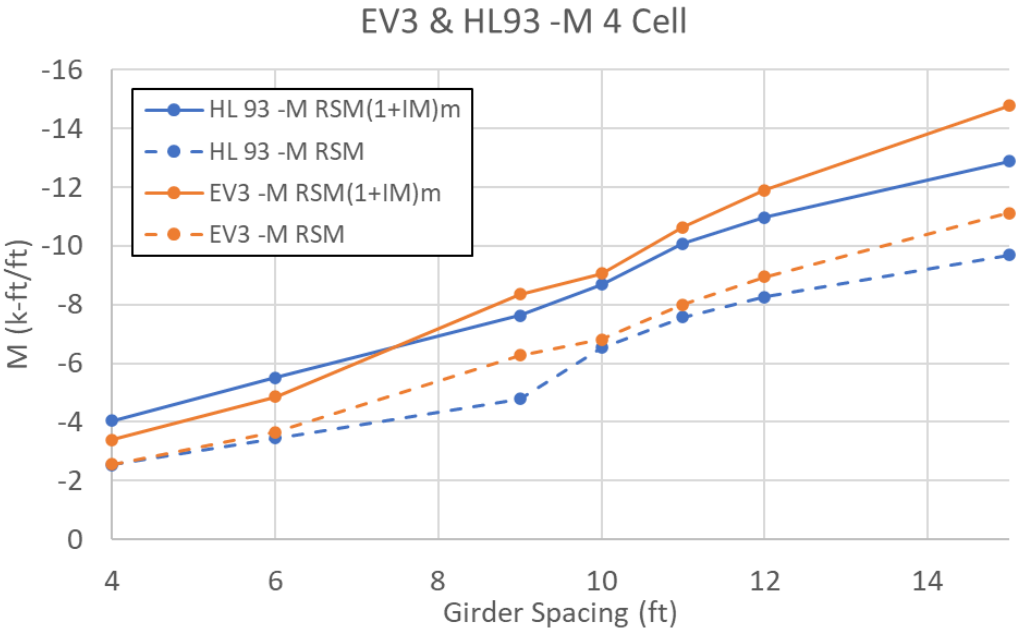

Figure 6.47. Negative moments based on critical locations (4 Cells)

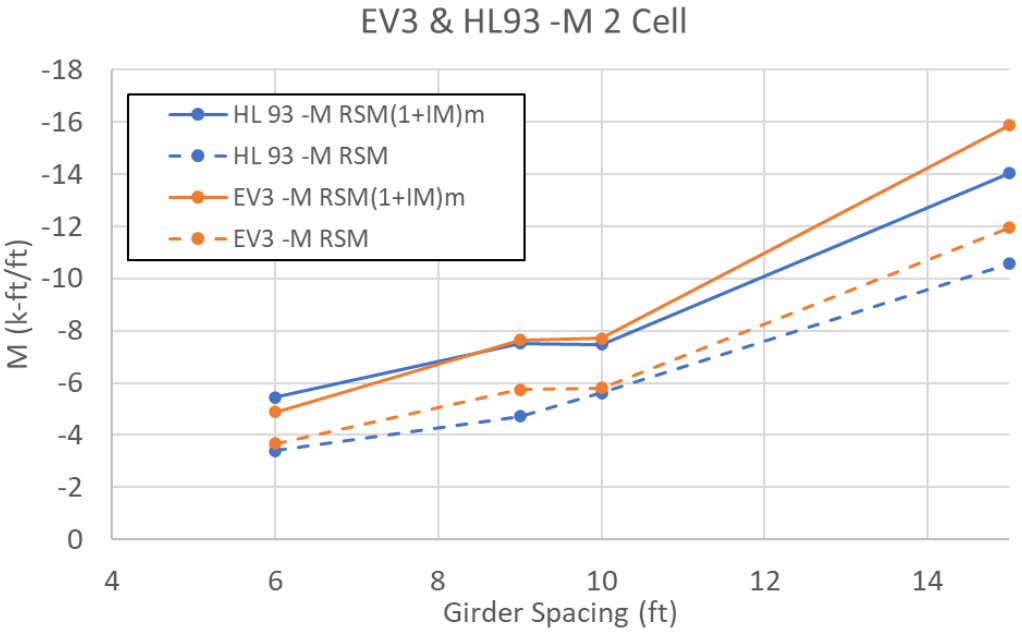

Figure 6.48. Negative moments based on critical locations (2 Cells)

6.7 Post-production Run RSM Verification

At the conclusion of the production run, several more detailed models were created to serve as a "sanity check" for the RSM results. These models were also created using the ATENA and GiD software packages, using similar methodology to the RSM but with some geometric simplifications removed. The girder spacings selected for these models were 9 ft (4-cell) and 15 ft (4-cell). The 9 ft spacing was selected because it severed as a median bridge size during internal discussions and the 15 ft spacing was because that is where the largest difference in demand between the HL-93 and EV3 vehicles was detected. For these models, the girders, soffits, and bent caps were added and were tested in a continuous two 98 ft span configuration. The bridge supports were pin-roller-roller. The tire patch sizes and material properties were kept the same as the RSM. These models were not meant to be exhaustive, so the controlling load case (i.e. Case 1 with one truck or Case 3 with two trucks) was assumed to be the same as the corresponding RSM model.

The results of the verification model and comparison to the corresponding RSM models are included in **Table 6.34**. Since the verification models included actual bridge spans, the labels 0.5L and 0.25L indicate the longitudinal position of the loads. Based on these two longitudinal load positions, the variation in the negative moment is negligible (< 5% variation). In all three loading and span combinations, the verification models showed reasonable agreement (maximum variation of 16%) with the RSM results for positive moments. The negative moments showed much larger variations between the models. In all cases the verification models reported much lower negative moments than the RSM. This difference was larger than a factor of two. The load position causing the maximum moment also changed under the verification models. However, this was expected since the bridge girders had significantly more joint flexibility than the rigid supports, which was discussed in Section 5.2.

Table 6.34. Summary comparison of maximum moments from RSM and verification models

	Girder Spacing (ft)	Distance - Edge of Tire to Edge of Deck	M_{max}	RSM (kip-ft/ft)	*1+IM*	*m*	IMMRSM (kip-ft/ft)	Controlling Case	R
HL-93	9 (RSM)	7.2 ft (86.4 in)	+M	2.89	1.33	1.2	4.61	1	0.99
		9 ft (108 in)	-M	-4.78	1.33	1.2	-7.63	1	2.66
	9 (Verification)	9 ft (108 in)	+M	2.91	1.33	1.2	4.64	1*	-
		10.8 ft (129.2 in) - 0.5L	-M	-1.8	1.33	1.2	-2.87	1*	-
		10.8 ft (129.2 in) - 0.25L	-M	-1.71	1.33	1.2	-2.73	1*	-
EV3	9 (RSM)	7.2 ft (86.4 in)	+M	3.55	1.33	1	4.72	1	1.16
		9 ft (108 in)	-M	-6.28	1.33	1	-8.35	3	2.75
	9 (Verification)	7.2 ft (86.4 in)	+M	3.07	1.33	1	4.08	1*	-
		8.1 ft (97.2 in) - 0.5L	-M	-2.28	1.33	1	-3.03	3*	-
		8.1 ft (97.2 in) - 0.25L	-M	-2.31	1.33	1	-3.07	3*	-
EV3	15 (2 cells, RSM)	10.5 ft (126 in)	+M	5.42	1.33	1	7.21	1	0.91
		10.5 ft (126 in)	-M	-11.94	1.33	1	-15.88	3	2.83
	15 (2 cells, Verification)	7.5 ft (90 in)	+M	5.98	1.33	1	7.95	1*	-
		7.5 ft (90 in) - 0.5L	-M	-4.22	1.33	1	-5.61	3*	-

*Load case was matched for verification models

R = RSM/Refined Model Results > 1.0 means RSM is conservative

There are several key takeaways from the verification models. First is that they confirm that the RSM moment demands are either reasonably accurate (positive moments) or skew conservative (higher demands for negative moments) relative to a model with more "realistic" stiffness. These models also confirmed that the location of the maximum positive and negative moments occur near mid-girder spacing and at the face of the interior girders, respectively. Additionally, it confirms that ignoring the longitudinal stiffness of the bridge deck was a reasonable assumption. However, these models highlight that the negative moments may be very sensitive to the stiffness of and/or the exact manner in which the rigid supports were modeled. In future studies, there should be some additional investigation into adding an intermediate element between the bridge deck and the rigid support. A common modeling technique would be to include a stiff rubber pad between the concrete and the rigid support, similar to how physical beam tests are conducted. Alternatively, a small concrete haunch, not necessarily the full girder height, with a typical chamfer may alleviate some of the artificial stress concentration at the edge of the rigid support.

6.8 Summary

The analysis presented in this study provides significant insights into the structural behavior of bridge decks under various loading conditions, as summarized by the detailed examination of moment values across different girder spacings and loading scenarios. The key findings from our research are as follows:

- The positioning of one truck can drastically influence the moment values, with maximum negative moments occurring at the deck's end and maximum positive moments between the first and second girders. This variation emphasizes the importance of considering truck placement in bridge design to ensure structural integrity;
- If the design lanes are allowed to extend into the deck overhangs, special consideration should be given to the negative moment at the exterior girders;
- Maximum magnitude negative moments excluding the overhangs generally occurred at the face of the first interior girder;
- In the 2 trucks scenario, Case 1 emerged as the dominant scenario for girder spacings less than 9 ft. However, for decks with larger girder spacings, especially those greater than 10 ft with four and two cells, Case 3 also showed significance in negative moment generation;
- The HL-93 loading standard generally produced higher positive moment values across all girder spacings, indicating its adequacy for positive moment considerations in bridge design. Nonetheless, for specific girder spacings (15 ft with 4 and 2 cells), a slight deviation suggests the potential need for adjustments based on actual loading conditions;
- For maximum negative moments, the HL-93 loading standard was appropriate for most girder spacings, with other vehicles producing marginally larger moments at larger girder spacings; and
- The comparison between the EV3 truck and HL-93 loading scenarios for 9 ft girder spacing highlighted the EV3's higher moment values, necessitating the inclusion of such specialized loading conditions in bridge design considerations to accommodate extreme loads.

The visual representations in **Figure 6.37** to **Figure 6.48** support the quantitative findings, offering a clear depiction of the impact of different loading standards and truck configurations on bridge deck moment values.

In conclusion, this study underscores the complexity of accurately predicting bridge deck responses to vehicular loads and the necessity for a nuanced approach in bridge design. The findings advocate for the adoption of diverse loading conditions, including specialized vehicles like the EV3 truck, in structural analysis to ensure bridges are designed with adequate safety margins. Moreover, the slight deviations observed in moment values across various scenarios indicate the potential for optimizing bridge design by tailoring the analysis to specific girder spacings and loading conditions. This research contributes to the body of knowledge in bridge engineering by offering a detailed assessment of moment distribution under different loading conditions, thereby facilitating more informed design decisions to enhance bridge safety and longevity.

7 ASSESSMENT OF EXISTING AASHTO A4 DESIGN

Quantitatively assess the impact of approximate analysis methods on the accuracy and reliability of the existing AASHTO LRFD bridge deck design specifications and California Amendments. A recent investigation conducted on a typical Californian bridge design demonstrated that the California P-15 Permit truck load analysis using the traditional distribution factors lead to a conservative shear demand up to 14%, when compared to the results of a refined FE analysis (Abughneam 2019). Furthermore, the results of the traditional analysis were reported to be highly conservative (up to 77%) in the case of substructure demands, when compared with the results of an FEM used for simultaneous analysis of the super and substructure (Abughneam 2019). As the results of a properly implemented refined analysis are more accurate compared to that of the approximate methods, it is well-expected that refined methods of analysis lead to a less conservative design, which has a reliability index closer to the target value (Adams et al. 2019). Therefore, during this task, a quantitative assessment will be conducted on the accuracy and reliability of the current deck design using approximate analysis method as specified in the AASHTO LRFD specification with the California Amendments. The approximate analysis method results will be evaluated against the results obtained through the refined analysis method using finite element computer modeling developed in Chapter 3. The truck loadings to be considered for this assessment will be the 16-kip axle point load, the HL-93, and the California P-15 truck.

7.1 Independent Study by Modjeski and Masters, Inc.

A Caltrans research project on concrete bridge deck behavior is being conducted, and as part of that work, the basis for the deck design moments contained in Appendix A4 of the AASHTO LRFD Bridge Design Specifications (BDS) is needed to better understand the values being used to design typical bridge decks. As there does not appear to be detailed documentation available describing the assumptions that were used to develop the table of values contained in Appendix A4, an analysis was undertaken to determine the assumptions by replicating values in the table. The results of the analysis closely match the table values, and indicate what assumptions were used in the development of the original Appendix A4. Below is the list of assumptions adopted in this study:

- The flexibility of longitudinal girders supporting the deck was neglected;
- Wheel loads were simplified as concentrated forces and correspond to the 32-kip truck axle;
- The width of traffic lanes was taken as 12.0 ft, and wheel loads were not closer than 2.0 ft from the edges of traffic lanes, and bridge railing;
- Effective strip widths to determine design moments per foot of deck were taken from AASHTO LRFD BDS Section 4.6.2.1.3;
- In addition, this work aligned with the next assumptions listed in Appendix A4;
- Multiple presence factors and the dynamic load allowance were included in the design values;
- Cross sections for analysis were established considering a minimum of 3 girders and a width of at least 14.0 ft between centerlines of exterior girders. Stated minimum and maximum overhang widths and a railing system width of 21.0 in were also used;
- Moments for deck overhangs were excluded from the analysis.

The maximum live load moment for design was determined considering two broad cases of analysis: Case (a) and Case (b). These correspond to the minimum and maximum overhang dimensions, respectively, stipulated in Appendix A4. Within each broad case, additional cases of analysis were considered by increasing the number of girders in the cross section. For the number of girders, a lower bound of 3 was used, consistent with Appendix A4, and a practical upper bound of 5 was believed reasonable for this work. Note that the likelihood of simultaneously having multiple lanes contributing to a given response decreases with the number of lanes, and that influence-line ordinates tend to quickly reduce in magnitude with distance from the location of the selected response. The peak value of all analysis cases was taken as the value for design. The schematic in **Figure 7.1** summarizes the analysis cases considered in this study.

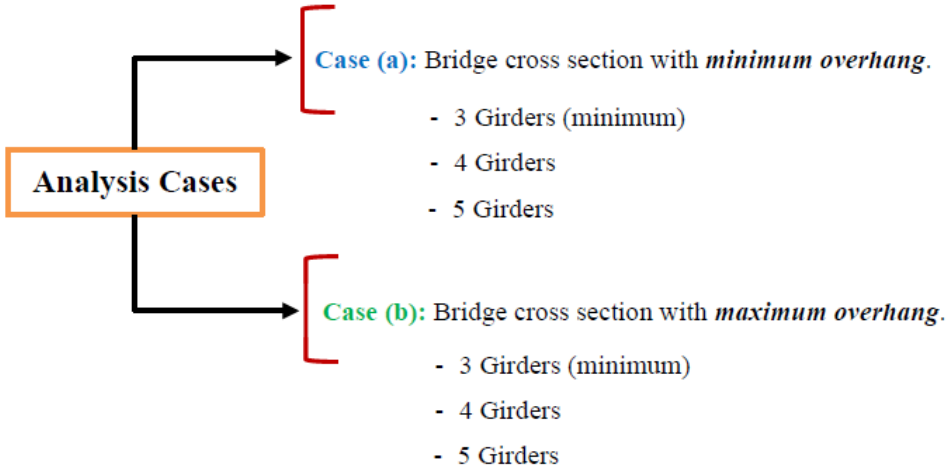

Figure 7.1. Analysis cases for maximum live load moment

Influence lines across the bridge width were developed using Lusas and employed to determine maximum responses. Longitudinal girders were treated as infinitely rigid, and therefore, the problem was reduced to the analysis of a prismatic continuous beam on rigid supports, with span lengths equivalent to the girder spacing. This work only examined a girder spacing of 9'-6".

Due to the uncertainty in the location where the maximum response would develop, several locations had to be considered. For instance, for positive moment, response functions (i.e., influence lines) were constructed at 0.4 of the span length, for spans adjacent to overhangs, and at midspan for the remaining interior spans (**Figure 7.2**). For negative moments at girder centerline, response functions at different girder locations were built, without including girders adjacent to overhangs. In the case of negative moments at a distance away from the centerline of girders, response function locations at both sides of a given girder were considered.

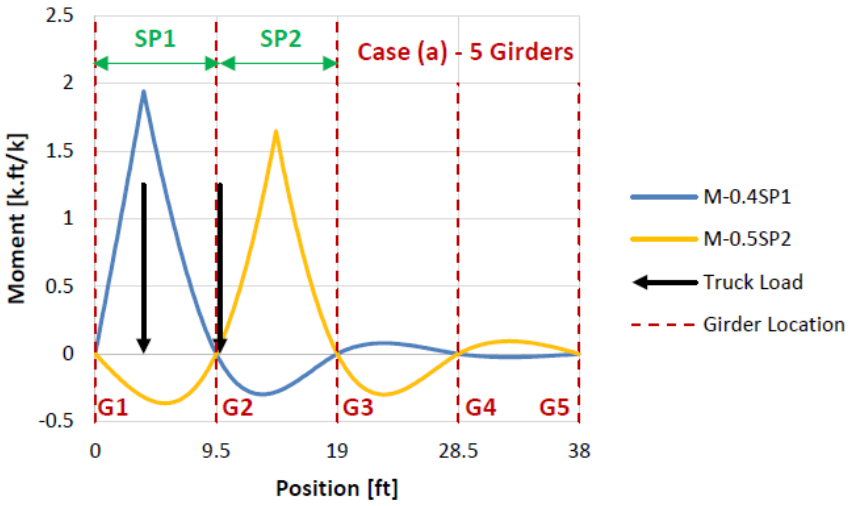

Figure 7.2. Influence lines for positive moment and governing truck configuration, Case (a) – 5 Girders

The number of traffic lanes per analysis case was determined as the integer part of the ratio between the clear deck width and 12 ft. To maximize the response of interest, they were transversely moved. As an initial attempt and for simplicity, only two locations were considered: 1) traffic lanes aligned to the left of the cross-section, and 2) traffic lanes centered. As will be shown later, this was enough to achieve a reasonable approximation to AASHTO values.

Wheel loads are those of a 32-kip truck axle and were applied as concentrated point loads. For every location of traffic lanes, wheel loads were also transversely moved considering a design lane of 10 ft, and a minimum distance to the edge of the traffic lane of 2 ft. Six discrete positions within a traffic lane were used.

As previously mentioned, a design response is the peak value of all the analyses that need to be considered. They include multiple presence factors (A. BDS. T. 3.6.1.1.2-1) and the dynamic load allowance (A. BDS. T. 3.6.2.1-1). Design values per foot of deck width were obtained with the effective strip width (A. BDS. T. 4.6.2.1.3-1) that corresponds to the response being determined (e.g., positive moment → +M strip width in A. BDS. T. 4.6.2.1.3-1). **Table 7.1** below shows the comparison between AASHTO and calculated values for positive moment and negative moment at 0.0" and 6.0", for a girder spacing of 6', 9'-6" and 15'. The small differences displayed suggest that assumptions and approach described in this document may be comparable to those employed for the determination of AASHTO values.

Table 7.1. Comparison between AASHTO and calculated design values

S	Positive Moment		Diff. (%)	Negative Moment @ 0.0"		Diff. (%)	Negative Moment @ 6.0"		Diff. (%)
	AASHTO	Calculated		AASHTO	Calculated		AASHTO	Calculated	
6'	4.83	4.87	0.80	-4.88	-4.78	-2.09	-3.50	-3.39	-3.01
9'-6"	6.59	6.53	-0.95	-7.15	-7.10	-0.68	-5.46	-5.25	-3.82
15'	9.47	9.36	-1.12	-13.09	-13.04	-0.37	-11.37	-11.14	-2.00

7.2 Comparison between RSM Modeling Results with M&M Study

As illustrated in Table 7.2, disparities exist between RSM and those developed by M&M. In our models, we incorporated deck slabs with girder spacings of 4 ft, 6 ft, 9 ft, 12 ft, and 15 ft. Conversely, the M&M model focused on girder spacings of 6 ft, 9.5 ft, and 15 ft for deck slabs. This reveals the initial distinction in girder spacing between 9 ft in our models and 9.5 ft in the M&M model.

Table 7.2. Comparison between RSM and M&M study

Moment	M&M location based on RSM model in this study					Take the closest combination based on M&M				
	S (ft)	No. of Girder	Overhang Width (ft)	Truck Location (ft)	Distance between 2 Trucks (ft)	S (ft)	No. of Girder	Overhang Width (ft)	Truck Location (ft)	Distance between 2 Trucks (ft)
Positive Moment	6.0	5	1.75	5.9	-	6.0	5	3	6	-
Negative Moment @0.0”	6.0	4	1.75	6.3	-	6.0	5	3	6.6	-
Negative Moment @6.0”	6.0	4	1.75	6.7	-	6.0	5	3	6.6	-
Positive Moment	9.5	5	1.75	7.3	-	9.0	5	3	7.2	-
Negative Moment @0.0”	9.5	3	5.9375	5	3.7	9.0	3	3	5.4	3.7
Negative Moment @6.0”	9.5	3	5.9375	4.2	3.7	9.0	3	3	4.5	3.7
Positive Moment	15.0	3	1.75	10.3	-	15.0	3	4	10.5	-
Negative Moment @0.0”	15.0	3	1.75	9.5	8.6	15.0	3	4	9	8.6
Negative Moment @6.0”	15.0	3	1.75	9.5	8.6	15.0	3	4	9	8.6

Another discrepancy lies in the number of girders considered. Our model employs 5 and 3 girders for calculation, while the M&M model, particularly for a 6 ft girder spacing deck slab, utilizes 4 girders to compute negative moments. Furthermore, variations in overhang width exist between our model and the M&M model. Our model derives overhang width from Table 1, whereas M&M adopts values such as 1.75 ft for 6 ft and 15 ft deck slabs and 5.9375 ft for 9.5 ft girder spacing deck slabs.

Divergences extend to truck locations as well. In our model, the truck is incrementally moved 10% of the deck width at each step, aligning with values obtained from the closest location based on the M&M model.

Additionally, differences arise in the distance between two trucks. For a 6 ft girder spacing deck slab, our model considers the second truck locations based on cases 2, 3, 3.5, and 4, whereas

M&M does not model two trucks for this scenario. For a 9 ft deck slab, our model sets the distance between two trucks at 4 ft in Case 3, while M&M designates it as 3.7 ft for a 9.5 ft girder spacing deck slab. Likewise, for the 15 ft girder spacing case, our model assumes a distance of 9.5 ft between two trucks, whereas M&M opts for 8.6 ft. To reconcile this distinction in the distance between the two trucks, we developed an additional set of three models, addressing and accommodating this particular variation.

The outputs from M&M and our model are compiled in **Table 7.2**. Upon comparing the results with those of M&M, it became apparent that the maximum moments consistently occurred at very close distances in our modeling, sometimes even at the same point. This result further illustrates the close proximity of the X_M (X_M indicates the location at which the maximum moment occurs) values in our findings. **Figure 7.3** illustrates the X_M location.

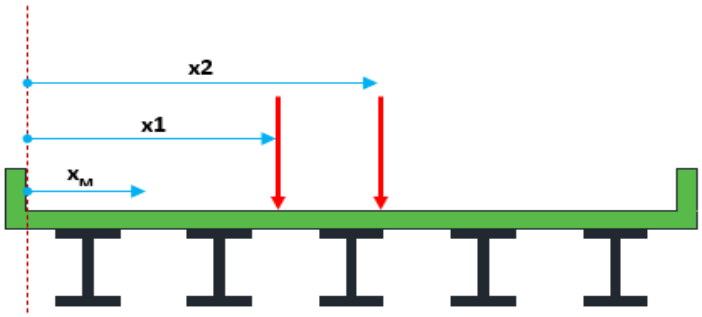

Figure 7.3. The X_M location based on M&M study

Table 7.3. Contrasting the outcomes of the M&M study with our model's results

	M&M		Based on RSM model in this study	
Girder Spacing	M_{max}	X_M	M_{max}	X_M
6.0 ft	(k-ft/ft)	(ft)	(k-ft/ft)	(ft)
Positive Moment	4.87	2.4	3.69	2.5
Negative Moment @ 0.0"	-4.78	6	-5.43	5.53
Negative Moment @ 6.0"	-3.39	6.5	-5.43	5.53
Girder Spacing	M_{max}	X_M	M_{max}	X_M
9.5 ft	(k-ft/ft)	(ft)	(k-ft/ft)	(ft)
Positive Moment	6.53	3.8	4.63	4.5
Negative Moment @ 0.0"	-7.1	9.5	-5.79	9.4
Negative Moment @ 6.0"	-5.25	9	-6.58	9.4
Girder Spacing	M_{max}	X_M	M_{max}	X_M
15.0 ft	(k-ft/ft)	(ft)	(k-ft/ft)	(ft)
Positive Moment	9.36	6	6	6.3
Negative Moment @ 0.0"	-13.04	15	-11.05	14.5
Negative Moment @ 6.0"	-11.14	14.5	-11.05	14.5
Additional, non-controlling cases:				
Positive Moment	6.42	10.25	-	-
Negative Moment @ 0.0"	-12.55	19.25	-	-
Negative Moment @ 6.0"	-10.59	18.75	-	-

Table 7.4. Comparison of moment values between RSM and AASHTO A4 values

S (ft)	Positive Moment		Diff. (%)	Negative Moment @0 in		Diff. (%)	Negative Moment @6 in		Diff. (%)
	AASHTO	Calculated		AASHTO	Calculated		AASHTO	Calculated	
4	4.68	2.84	-39.32%	-2.68	-4.04	50.75%	-1.74	-4.04	132.18%
6	4.83	3.78	-21.74%	-4.88	-5.43	11.27%	-3.5	-5.43	55.14%
9	6.29	4.52	-28.14%	-6.81	-6.85	0.59%	-5.13	-6.85	33.53%
12	8.01	5.54	-30.84%	-10.28	-9.75	-5.16%	-8.51	-9.75	14.57%
15	9.47	5.95	-37.17%	-13.09	-12.56	-4.05%	-11.37	-12.56	10.47%
9 (2 cells)	6.29	4.79	-23.85%	-6.81	-7.52	10.43%	-5.13	-7.52	46.59%
15 (2 cells)	9.47	5.95	-37.17%	-13.09	-12.26	-6.34%	-11.37	-12.26	7.83%

Upon comparing our findings with those presented in Table A4 of the AASHTO, it became evident that there exists a 20 to 40% variance in the maximum positive moments. Concerning the negative moments, a decreasing trend is observed in the results. As we can say, as the span between the girders increases, the values tend to converge toward one another for maximum negative moment.

When examining the computed outcomes with AASHTO A4-1, it became evident that there was a difference between the values. The factors contributing to these differences are outlined below:

- A potential factor contributing to the variation is the longitudinal flexibility of the deck. Since the infinite deck's decreased flexibility in the longitudinal direction, it results in a stiffer deck and subsequently lower positive moments and higher negative moments compared to the values provided in the A4 table;
- Another possible reason for this difference is the difference in the truck loading assumptions. According to AASHTO, trucks are restricted within its lane, with wheel loads maintained at a minimum distance of 2.0 ft from the edges of traffic lanes and bridge railings. However, in our study, trucks have the freedom to move laterally, disregarding lane restriction considerations (2^{nd} truck was moved laterally at 10% of the girder spacing); and
- Upon careful examination of the results obtained from the M&M modeling outputs, a clear pattern emerges combinations involving one truck exhibit the highest values for both maximum positive and negative moments for small girder spacing (s=6 ft). Two trucks exhibit highest values for negative moment for larger girder spacing (s=9.5 ft and 15 ft). There appears to be no necessity to model combinations involving three trucks.

8 PROPOSED CA-A4 AMENDMENTS

Following the production run via a comprehensive parametric study in the previous tasks, a streamlined design procedure following the same format as the existing AASHTO LRFD A4 design is proposed in this chapter. The updated design (CA-A4 Amendments) will be of great interest to production design while also allowing for a fast sanity check of a design that is entirely based on a complex analysis such as 3D finite element analysis. This updated design procedure will assist the Caltrans Technical Committee to recommend potential articles and changes to be included in the next round of the California Amendments to the AASHTO LRFD 9th Edition. Sections where potential changes are envisioned by the research team include Section 9 (Deck and Deck systems), Section 4 (Structural Analysis and Evaluation), and possibly Section 5 (Concrete Structures). These recommendations can be drafted in the required AASHTO format and can include commentary and supporting graphics at an appropriate level of detail and scaled for readability in the future.

8.1 Description of a Typical Production Run

As a recap, the adopted Rigid Support Model (RSM) exhibited acceptable differences in results compared to the 3D solid finite element model but had substantial computational time savings and a fraction of the data storage requirements. The key features of the RSM model are summarized again below:

- The deck was modeled using a 3D shell element;
- The girders were modeled as "rigid supports" meaning that they were represented using extremely stiff steel plates that were continuously (pin) supported in the longitudinal direction;
- The longitudinal stiffness of the deck was assumed to be negligible, so the bridge length was taken as approximately 200 times the transverse bridge width;
- The load was placed at the longitudinal center of the bridge and moved transversely to determine moment demand in the deck;
- For the HL-93 loading, the effect of multiple axels was negligible. To reduce the modeling and computational time, only one 32-kip axel was used in the load configuration;
- Lanes were allowed to shift from the edge of the deck to the centerline of the deck. No barrier was accounted for in the analysis. This provides a conservative result, but it should also be noted that the negative moment in the deck at the exterior girder was excluded from the results. The overhang and adjacent slab region should be designed in compliance with AASHTO A13.4.1; and
- The deck was limited to linear elastic behavior.

For a given girder spacing (S) and vehicle combination, the load was placed at the edge of the deck and moved in $0.1S$ increments. Every cross-section considered was symmetric at the centerline of deck, so beyond the centerline of the cross-section the moment envelope is also symmetric.

Upon completion of the runs, the internal forces on a 20-inch-wide strip of deck centered on the patch loads were tabulated in excel and compiled for every load position. These internal forces were then used to assemble a moment envelope for minimum and maximum moments. Negative moments in the exterior girders were not considered. In every case, the maximum negative

moment came from the face of either the first or second interior girder. For the positive moments, the region bounded by 0.4*S* from the centerline of the exterior girder was excluded from consideration. For the HL-93 load case, 1 and 2 design lanes were considered where the total cross-section was wide enough to accommodate more than 1 design lane. For the case where two lanes were used, a vehicle was placed in each lane at the minimum 4 ft width between adjacent vehicle tires and the axles were aligned to create the highest concentration of force.

The maximum and minimum moment and shear were recorded for each cross-section and girder number combination. For comparison with the AASHTO A4-1 table, the governing moments were plotted against the A4-1 values in **Figure 8.1**.

8.2 Proposed Changes to Existing AASHTO A4 Design Table

After completing the HL-93 production run of extensive models, and verifying that the moment demands of the P-15, SHV, and EV3 vehicles did not generally produce significantly larger moment demands than the HL-93 vehicle, the governing moments for each girder spacing were compared to the equivalent values in the AASHTO A4-1 table. It was found that the production run resulted in generally higher negative moments and lower positive moments than the existing A4-1 values.

The goal of the production run was to get a better estimated moment distribution for the deck to compare to the existing design table AASHTO A4-1. There is little original documentation about the development of the A4 table, so the Modjeski and Masters (M&M) report, attempted to reverse engineer what AASHTO's likely assumptions were. Below is a comparison of M&M's conclusions to the assumptions made of the production run presented in this report (**Table 8.1**).

Table 8.1. Comparison of key model assumptions to M&M Report on A4 table assumptions

Item	M&M Finding on A4 Table	RSM Model Assumption
1	Moment demands in the slab are dominated by one way behavior, so longitudinal stiffness was neglected.	Moment demands in the slab are dominated by one way behavior, so longitudinal stiffness was neglected.
2	2 wheel loads were accounted for as point loads equal to half the axel weight (16 kips).	Two 16 kips wheel loads assigned as patches on tire contact area corresponding to 125 psi.
3	12 ft wide traffic lanes were adopted, with tire positions allowed to move within the lanes. Two lane positions were considered, one justified to the left edge of the cross-section and a second centered on the cross-section, were sufficient to capture the moment envelope.	Wheel patch loads were not restricted to traffic lanes. Loads were moved transversely at 0.1*S* increments from the edge of the overhang to centerline of bridge for a more comprehensive envelope.
4	The developed moment was distributed over an effective strip width as defined in AASHTO LRFD BDS 4.6.2.1.3.	The effective strip width was taken as 20 inches.
5	The multiple presence factor (m) and dynamic load allowance (IM) were incorporated into table values.	The multiple presence factor (m) and dynamic load allowance (IM) were incorporated into table values.

6	Negative moments in the overhang and edge girder were excluded and must be considered in a separate analysis.	Negative moments in the overhang and edge girder were excluded and must be considered in a separate analysis.
7	3, 4, and 5 girder configurations were considered for deck cross-section.	3 and 5 girders were considered were considered for deck cross-section.
8	Positive moments were considered only >0.4 times span length away from edge girders.	Positive moments were considered starting from the first inflection point towards center span from the exterior girder.

8.3 Comparison of Results AASHTO A4 vs HL-93 Production Run

8.3.1 Maximum negative moments

The maximum negative moments from the RSMs are compared to the A4 table values in **Figure 8.1**. The RSM negative moments were located at the face of the girder which corresponds to the A4 – 6 in plot in the figure. The A4 value at 0 inches from the centerline of the girder was also plotted to show the existing maximum values for a complete comparison. The difference in location of the maximum negative moments was caused by the rigid supports creating a drop in the magnitude of the moment at the center of the support ("girder") with the largest moments occurring at the edge of the support. For all but the highest girder spacing, the RSM 4-cell model maximum moments had larger magnitudes than the A4 model. For the 15 ft deck spacing, the 4-cell model dipped below the existing A4 value, but the 2-cell model exceeded the A4 value. This shows that the RSMs consistently showed higher negative moment demands than the existing A4 table values. Another key observation of the below plot is that there is a change in slope of both the A4 table values and the RSM curves in the 9 to 10 ft girder spacing range. This is due to the relative width of a truck axle to the clear distance between girders. For girder spacing < 6ft, it is impossible to fit both sets of tires inside one girder spacing or a second truck next to the first. This change in slope led to considering the curves in two distinct regions delineated by the 9 ft deck span length.

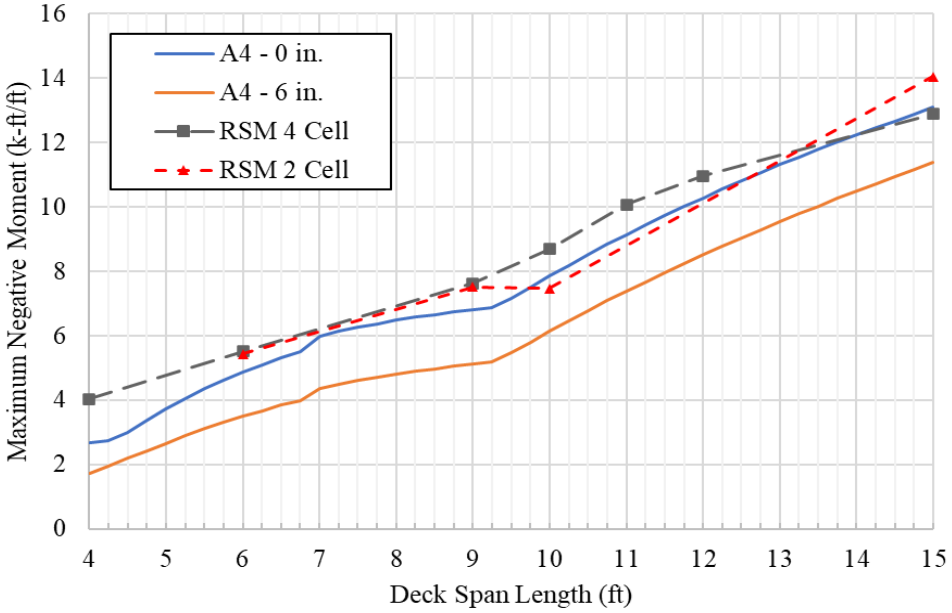

Figure 8.1. 2-cell and 4-cell maximum negative moment comparison of RSM models to A4 table

To further clarify the maximum difference between the RSM models and the A4 table, the largest RSM values, including both 4-cell and 2-cell cases, for each girder spacing were plotted as a single curve in **Figure 8.2**. On average, the RSM moment was 0.98 k-ft/ft larger than the A4 table value, with an increase as a percent relative to the A4 value ranging from 23% for largest girder spacings and 132% for the smaller girder spacings. Based on discussion with the Technical Advisory Committee (TAC) team, it was decided that instead of using the RSM values directly to update the A4 table, using an equation fit to the new data was preferable. To this end, the RSM data was broken down into two regions delineated by the 9 ft mark, and a linear regression analysis was performed on each subset of data. The proposed curve is shown in **Figure 8.3** overlaid onto the RSM results. The bilinear function fits the data well with R^2 values of 0.999 and 0.996 for each linear segment, respectively. This should not be interpreted as extremely high accuracy though, as it is easy to obtain high R^2 values for such small datasets that are reasonably linear.

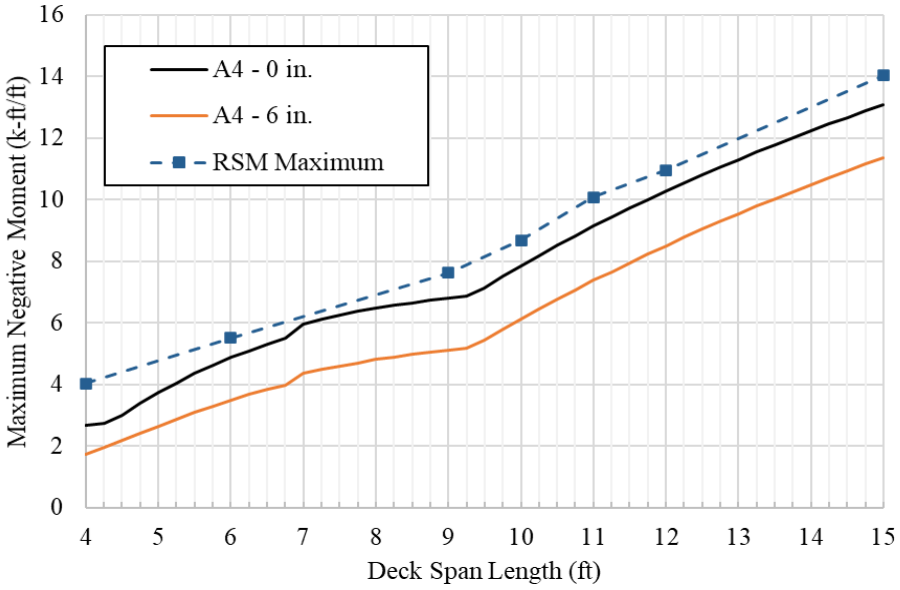

Figure 8.2. Maximum negative moment envelop comparison of RSM models to A4 table.

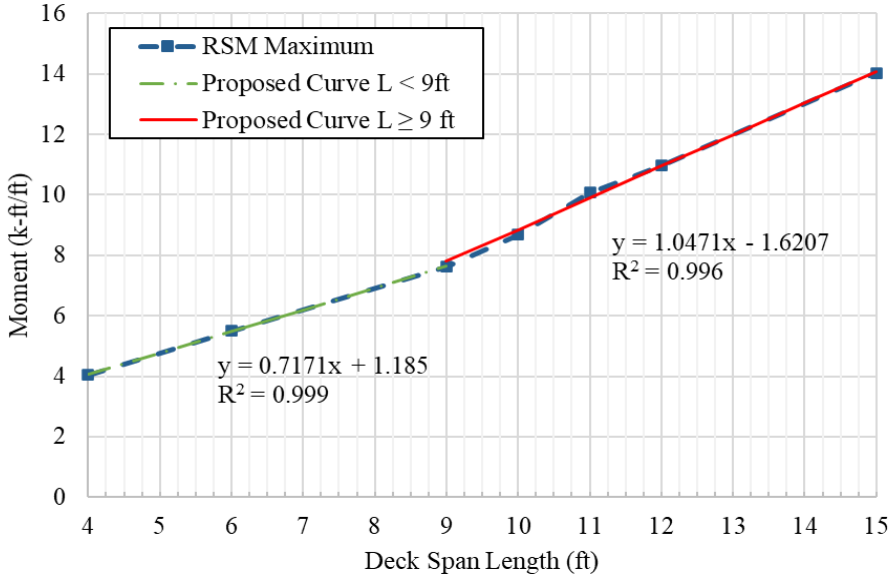

Figure 8.3. Plot of proposed bilinear function for maximum negative moment by deck span.

The proposed curve is meant as an update to the original AASHTO A4 values, so the name CA-A4 was adopted for this equation. The proposed CA-A4 equation for the maximum negative moment can be written as a function of the girder spacing, *S*, with two linear segments, as follows:

$$M_{max} = \begin{cases} 0.7171S + 1.185, \ 4\,ft \le S < 9ft \\ 1.0471S - 1.6207, \ 9ft \le S \le 15\,ft \end{cases} \quad (8.1)$$

where M_{max} has a unit of kip-ft/ft (the per foot indicates a 1 ft wide strip of deck), and *S* is the girder spacing given as the center-to-center distance of the supporting girders in feet. There is a small discontinuity at *S* = 9 ft because the regression analyses were independent of one another. At this discontinuity the second segment has a larger required moment which means it is conservative to make the lower bound of the second segment inclusive. The limitations of this function can be summarized as:

- Only valid for girder spacings from 4 to 15 ft;
- The loading was assumed as the standard 32-kip axle weight evenly distributed between two tires;
- This is only applicable for negative moments in the deck over interior girders, negative moment in edge girders and deck overhangs must be considered separately;
- This function considers the larger live load moment effects from either one or two trucks loading the deck (loading from 3 adjacent trucks produced negligibly different results from two trucks);
- No uniform load was considered;
- This equation only gives the maximum negative value assumed to be at the face of the girder. It does not provide moment drop-off values away from the face of the girder as the original A4 table did; and
- Multiple presence factor (*m*) and dynamic load allowance (*IM*) are included in the moment provided by the equation.

To further illustrate the difference between the proposed CA-A4 function and the original AASHTO A4 values, the negative moments from the AASHTO A4 are tabulated below and compared to the CA-A4 update (**Table 8.2**). The column, R, is the ratio of the CA-A4 values to AASHTO A4 values. It reiterates that for the full domain of deck spans considered, the CA-A4 negative moment demands will increase over the AASHTO-A4 values, shown by values of R >1.0.

8.3.2 Comments on generation of proposed CA-A4

The production run models for this research were designed to provide better estimate than the AASHTO A4 calculations, but decisions were made with a preference for generally overreporting negative moment demands leading to an overall conservative result. This was a guiding principle in setting up these models generally, but there are two specific points about the model development to be highlighted here. First is that the RSM was noted as shifting some of the moment demand to the negative moment region due to the increased stiffness of the support conditions relative to explicitly modeling the full girder depth. The second is that there is some additional stress concentration at the edge of the support plates (which is the location of maximum negative moment) due to the way ATENA handles master/slave surface interfaces. This is all to say that there were multiple small but cumulative simplifications that led to some loss of "realism", but all

tended to make the models more conservative for negative moment demands, which was the more desirable choice from a design perspective.

Table 8.2. Comparison AASHTO A4 negative moment values to proposed CA-A4 function.

Girder Spacing	-Mmax (k-ft/ft)			Girder Spacing	-Mmax (k-ft/ft)		
S (ft)	A4	CA-A4	R	S (ft)	A4	CA-A4	R
4	2.68	4.05	1.51	9.75	7.51	8.59	1.14
4.25	2.73	4.23	1.55	10	7.85	8.85	1.13
4.5	3	4.41	1.47	10.25	8.19	9.11	1.11
4.75	3.38	4.59	1.36	10.5	8.52	9.37	1.10
5	3.74	4.77	1.28	10.75	8.83	9.64	1.09
5.25	4.06	4.95	1.22	11	9.14	9.90	1.08
5.5	4.36	5.13	1.18	11.25	9.44	10.16	1.08
5.75	4.63	5.31	1.15	11.5	9.72	10.42	1.07
6	4.88	5.49	1.12	11.75	10.01	10.68	1.07
6.25	5.1	5.67	1.11	12	10.28	10.94	1.06
6.5	5.31	5.85	1.10	12.25	10.55	11.21	1.06
6.75	5.5	6.03	1.10	12.5	10.81	11.47	1.06
7	5.98	6.20	1.04	12.75	11.06	11.73	1.06
7.25	6.13	6.38	1.04	13	11.31	11.99	1.06
7.5	6.26	6.56	1.05	13.25	11.55	12.25	1.06
7.75	6.38	6.74	1.06	13.5	11.79	12.52	1.06
8	6.48	6.92	1.07	13.75	12.02	12.78	1.06
8.25	6.58	7.10	1.08	14	12.24	13.04	1.07
8.5	6.66	7.28	1.09	14.25	12.46	13.30	1.07
8.75	6.74	7.46	1.11	14.5	12.67	13.56	1.07
9	6.81	7.80	1.15	14.75	12.88	13.82	1.07
9.25	6.87	8.06	1.17	15	13.09	14.09	1.08
9.5	7.15	8.33	1.16				

R is the CA-A4 valued divided by the original AASHTO A4 value.

8.3.3 Maximum positive moments

The positive moment demands were also recorded from each moment envelope for the HL-93 loads. The maximum positive moments for both 2-cell and 4-cell box girders are plotted with the corresponding AASHTO A4 table values in **Figure 8.4**. The RSM results were universally smaller than the existing table values, with the closest RSM value still falling 25% below the AASHTO A4 value. Based on these results and internal team discussion it was decided that we were not comfortable revising down the existing AASHTO A4 table values, especially considering the modeling notes mentioned above regarding shifting moment to the negative region.

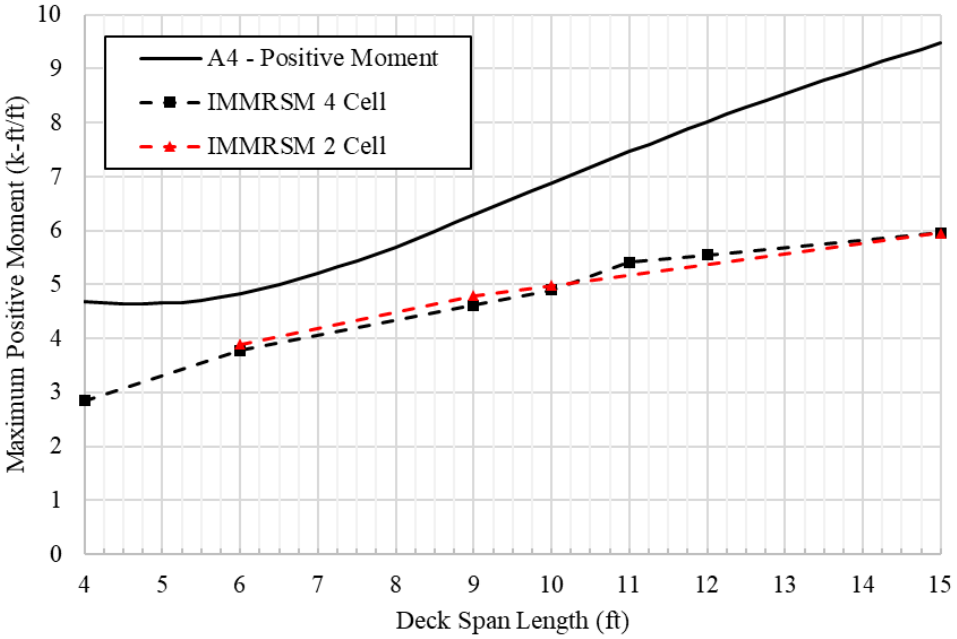

Figure 8.4. Maximum positive moment comparison of RSM models to A4 table.

8.3.4 P-15, SHV and EV3 moment demand comparison to HL-93 case

The scope of work for this project also included running a similar moment demand analysis for the full range of deck configurations using P-15, SHV, and EV3 trucks. To reduce the total volume of models produced, the positions of load from the HL-93 analysis yielding the maximum moments were using as initial positions for the other three vehicle configurations. The load positions were then moved off of that point to confirm that each position still coincided with a local maxima or minima on the moment envelope. From these analyses, it was found that the P-15 and SHV configurations did not produce significantly different moment demands than the HL-93 vehicle. There was a general trend that the heavier gross vehicle weights approached the HL-93 demands (which has the largest single axle weight of the 4 cases considered) for larger girder spacings but never exceeded the HL-93 demands by more than 5%. The P-15 results are compared to the proposed CA-A4 curve in **Figure 8.5** as an example. The EV3 load case was the exception, where for girder spacings above 7 feet, the negative moment demand exceeded the value calculated using the CA-A4 equation, as shown in **Figure 8.6** . Beyond the 7-foot mark, the curves start to diverge, with a maximum difference of 1.84 k-ft/ft for a 15 ft span, which corresponds to a 13% increase over the CA-A4 value.

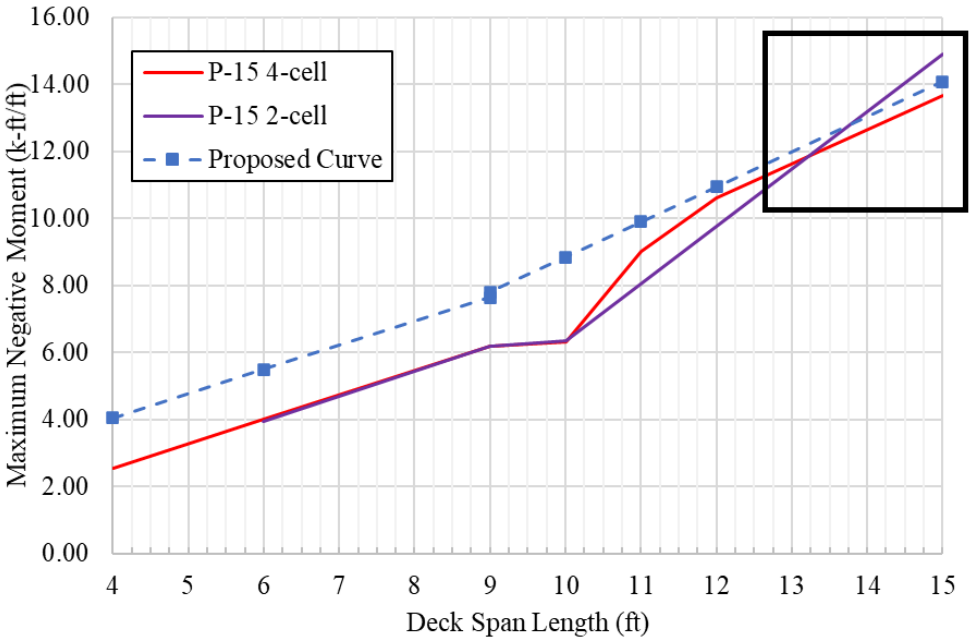

Figure 8.5. Maximum negative moment comparison of proposed CA-A4 and P-15 demands by deck span length

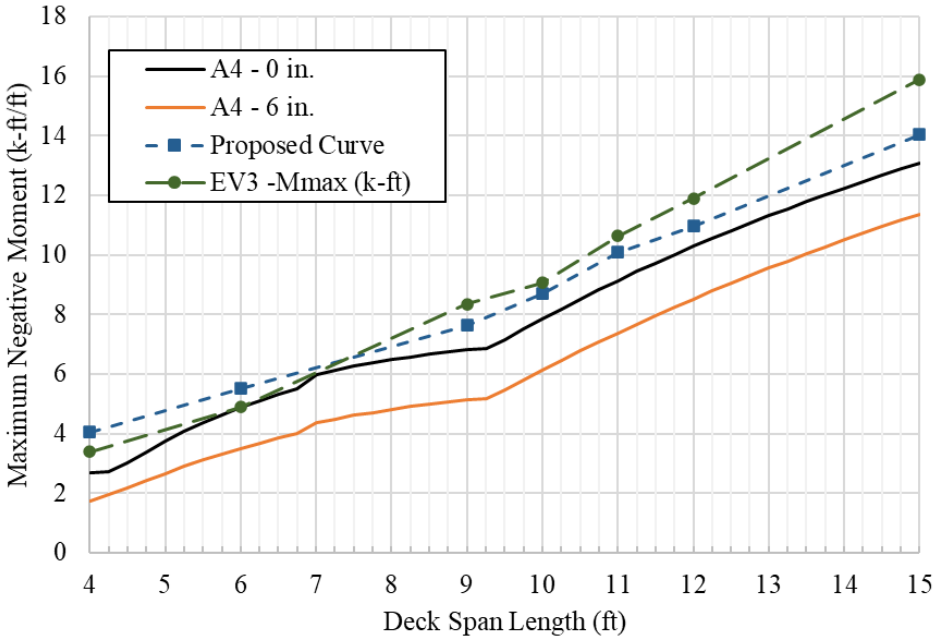

Figure 8.6. Maximum negative moment for AASHTO A4, proposed CA-A4, and EV3 by deck span length

The conclusion of this portion of the analysis is that the proposed CA-A4 negative moments will cover the negative moment demand generated by HL-93, SHV and P-15 vehicles for girder spacings less than 13 ft. Special consideration should be given for EV3 loading and for the other special vehicle types for girder spacings greater than 13 ft.

8.4 Proposed CA-A4 Deck Slab Design Table

The design amendment CA-A4 may be used in determining the deck design moments for different girder arrangements. The following assumptions and limitations were used in developing this table and should be considered for design:

- The deck moments are calculated using envelopes generated from finite element models using effective strip widths of 20 inches for concrete slabs supported on parallel girders;
- Multiple presence factors and dynamic load allowance are included in the tabulated values;
- The negative moments were the maximum moments produced, which occurred at the face of 12" wide girders, but could be taken at the centerline of the girder;
- The moments are applicable for decks supported on at least three girders and having a width not less than 12 ft between centerlines of exterior girders; and
- The moments represent the upper bound for the moments in the interior regions of the slab, and for any specific girder spacing, were taken as the maximum value calculated, assuming a minimum of 3 girders were used in the bridge cross-section. The width of the overhang was varied based on the girder spacing and corresponding standard deck thickness (BDM 9.4, Oct 2021, **Table 8.3**) according to the following constraint: no railing system was used to determine the clear overhang width, which is the distance from the edge of deck to the face of the exterior girder.

Table 8.3. Caltrans girder spacing and deck thickness (BDM 9.4)

Deck Span (ft)	Deck Thickness (in)	Clear Overhang Width (ft)
4	8.0	2
6	8.0	3
9	8.125	3
10	8.5	4
11	8.875	4
12	9.125	4
15	10.375	4

- In the proposed CA-A4 (**Table 8.4**), the negative moments for design do not apply to the deck overhangs and the adjacent regions of the deck, meaning the negative moments can only be used for interior girders. The positive moments were checked starting from the first inflection point extending inward from the centerline of the exterior girder;
- No tandem trailers were considered in this analysis. The maximum moment effects presented are either from a single 32-kip axle or two 32-kip axles in adjacent design lanes with the minimum spacing of 4 ft between the centerlines of the closest tires;
- Consideration was also given to P-15, SHV, and EV3 loads. The P-15 and Special Hauling Vehicles were found to produce similar enough moments to be considered within the acceptable limits for practical design. Specific consideration should be given when designing deck slabs with girder spacings greater than 13 ft for EV3 vehicles, as they can produce larger positive and negative moments than the HL-93 vehicles; and
- The negative moments in the table were generated based on the following equation, which may be used for any girder spacing between a minimum of 4 ft and a maximum of 15 ft.

$$M_{max} = \begin{cases} 0.7171S + 1.185, & 4\,ft \le S < 9ft \\ 1.0471S - 1.6207, & 9ft \le S \le 15\,ft \end{cases} \tag{8.2}$$

Table 8.4. Proposed CA-A4 California Amendment design table for maximum moments per unit width (k-ft/ft)

S		Maximum Positive Moment	Maximum Negative Moment
4'	-0"	4.68	4.05
4'	-3"	4.66	4.23
4'	-6"	4.63	4.41
4'	-9"	4.64	4.59
5'	-0"	4.65	4.77
5'	-3"	4.67	4.95
5'	-6"	4.71	5.13
5'	-9"	4.77	5.31
6'	-0"	4.83	5.49
6'	-3"	4.91	5.67
6'	-6"	5.00	5.85
6'	-9"	5.10	6.03
7'	-0"	5.21	6.20
7'	-3"	5.32	6.38
7'	-6"	5.44	6.56
7'	-9"	5.56	6.74
8'	-0"	5.69	6.92
8'	-3"	5.83	7.10
8'	-6"	5.99	7.28
8'	-9"	6.14	7.46
9'	-0"	6.29	7.80
9'	-3"	6.44	8.06
9'	-6"	6.59	8.33
9'	-9"	6.74	8.59
10'	-0"	6.89	8.85
10'	-3"	7.03	9.11
10'	-6"	7.17	9.37
10'	-9"	7.32	9.64
11'	-0"	7.46	9.90
11'	-3"	7.60	10.16
11'	-6"	7.74	10.42
11'	-9"	7.88	10.68
12'	-0"	8.01	10.94
12'	-3"	8.15	11.21
12'	-6"	8.28	11.47
12'	-9"	8.41	11.73
13'	-0"	8.54	11.99
13'	-3"	8.66	12.25
13'	-6"	8.78	12.52
13'	-9"	8.90	12.78
14'	-0"	9.02	13.04
14'	-3"	9.14	13.30
14'	-6"	9.25	13.56
14'	-9"	9.36	13.82
15'	-0"	9.47	14.09

9 CONCLUSIONS

The prevailing bridge design practices, which differentiate between simple approximation and detailed refinement in deck analysis, appear increasingly inadequate. The reliance on overly simplistic methods raises doubts regarding their effectiveness and cost-efficiency, particularly in light of the complex and varied loading conditions presented by contemporary traffic patterns. The quest for durability and reliability has thus prompted a shift toward more advanced analytical approaches, such as 3D finite element method, which, despite its widespread acceptance in Europe, sees limited application in the US. This discrepancy between the need for detailed analysis and guidance provided by the existing standards reveals a critical gap in the current design paradigm.

The endeavor to accurately model and analyze bridge decks under varied vehicular loads highlights the complexity of this task, necessitating a strategic pivot towards a more manageable modeling approach. The introduction of a Rigid Support Modeling (RSM) strategy, as consented by the Caltrans Technical Advisory Committee (TAC), signifies a pragmatic step forward. This innovative approach aims to streamline the design process, focusing on key factors such as girder spacing and tire pressure, thereby offering a viable alternative that strikes an optimal balance between precision and practicality in bridge deck modeling.

In this report, the workflow of the refined finite element modeling and the rigid support modeling of the small and large box girder prototype bridges is presented in detail, which contains, but not limited to, bridge geometries, definition of material and elements, load and boundary conditions, mesh setting, and mesh study. The verification of the RSM under the comprehensive transverse patch load cases indicates that the RSM is a more efficient, conservative, and practical alternative to the true refined model. The adoption of the RSM can significantly reduce the workload of the original workplan by narrowing down the number of bridge parameters. In addition, different case studies were conducted in this research to investigate the influence on the load demands of bridge decks due to longitudinal position of axle load, spacing between axle loads, girder depth, cross-slope, length of the influence area, and type of truck load. Based on these many case studies, a production run matrix was proposed through deep deliberation and discussion with the TAC team to reach a balance between the practicability of heavy FE modeling and the tangible updates to the existing bridge design guidance.

To evaluate the maximum load demands on bridge decks under multiple truck loading scenarios, a comprehensive investigation was conducted using the HL-93 and P-15 load models, consistent with the provisions of AASHTO Table A4. In total, 529 loading combinations were generated for HL-93 and 57 combinations for P-15. Due to the extensive number of possible scenarios, the study was designed to systematically capture all critical configurations. Accordingly, five representative cases were analyzed for HL-93 and four cases for P-15. The methodology and configuration details for each case are presented in the report, supported by illustrative figures.

In the subsequent production run, axle loads were applied using RSM, assuming a tire pressure of 125 psi and a tire contact width of 10” and various lengths based on axel weight. The study was conducted in two phases. During the first phase, all possible configurations of a single truck placed on the bridge deck were evaluated to determine the maximum values of positive and negative moments as well as positive and negative shear, along with the corresponding deck locations where these peak responses occurred. During the second phase, two trucks were positioned on the bridge deck and translated transversely in accordance with the prescribed loading combinations. This phase aimed to identify the critical response locations for positive and negative

moments as well as positive and negative shear, which are required for the structural design of bridge decks. Based on these results, it is concluded that for smaller girder spacings, the HL-93 loading generally produces the largest moment demands on the bridge decking. This means that for spacings less than approximately 9 ft, consideration for P-15, SHV or EV3 loadings are unlikely to require a larger load demand. However, for spacings larger than 9 ft, the EV3 loading is capable of producing larger moment demands than the HL-93 and will require special consideration in design. If the trend in this study is extrapolated to girder spacings larger than 15 ft, it is likely that all three alternative loading scenarios considered will produce larger moment demands than the HL-93 loading scenario.

At the conclusion of the production run, these trends were compared to the existing AASHTO A4 design table. This comparison showed that the negative moments may be significantly under reported. A proposed amendment to the existing AASHTO A4 table was generated based on the negative moment demands generated in this study. The proposed update is based on a bilinear relationship, where short span demands are largely independent of the number of vehicles present in the load case, and longer spans are governed by two trucks moving in parallel in adjacent lanes. The proposed amendment (CA-A4) was presented as a formula based on span length, allowing for interpolation between the actual data generated by this study. It was also presented as a table in a similar format to the existing A4 table for common girder spacings.

As part of the scope of the project, a comprehensive literature review on fatigue of RC bridge decks has been conducted, focusing on the two-level fatigue performance of bridge deck on material and structure, respectively. Multiple factors that contribute to the fatigue performance of concrete material are summarized from past research, in conjunction with proposed fatigue models of concrete that can be categorized as deterministic, probabilistic, and energy-based ones. Both experimental and analytical efforts on the structural level of RC bridge decks under fatigue loads have been investigated, indicating the typical fatigue failure process and mechanisms as observed from lab testing. Although lacking enough datapoints on fatigue failure of bridge decks, two frameworks are proposed to examine the fatigue life of RC bridge decks for design reference.

9.1 Limitations and Conclusions

9.1.1 Limitations

It should be mentioned that due to the limited budget and tight time frame, the current study has several limitations as summarized below:

- The Rigid Support Modeling (RSM) strategy was adopted for production run instead of the true refined Finite Element (FE) models with simplifications in geometry, structural configuration and boundary conditions. As a result, the calculated bridge deck load demands, although deemed as reasonably accurate, could be deviated from the precise values particularly for negative moments due to the exclusion of frame action;
- The vehicle loads were mostly applied to the bridge deck as one pair of axle patch loads instead of the entire truck with multiple axles, which could lead to slight deviation from the actual structural responses;
- A constant truck tire pressure of 125 psi was used for production run, which may underestimate the load demands of bridge deck particularly that the usage of bigger truck tires with higher tire pressure is growing within the industry;

- The length of influence area or the equivalently deck strip width is crucial in determining the load demands of bridge decks. The current research used a constant 20 in, as associated with the typical punching shear failure location, that might not be appropriate for all bridge configurations;
- Consideration for moment demands in bridge deck overhangs were excluded from the current study and might require special consideration by the designer;
- Not all vehicle types were included in the production run, although the selected HL-93, P-15, SHV and EV3 were believed to yield the governing load demands of bridge decks;
- The results and conclusions of this study are dependent on a specific set of load modifications. All comparisons between the vehicle types presented in this study were made with consideration only for the multiple presence and dynamic load factors. Different conclusions may have been drawn from this study if the "raw" unadjusted model values were used;
- The LRFD load factors were not considered in this study. Note that the LRFD load factors are not the same for all trucks used in this study, which may have also led to different conclusions being drawn. This issue was discussed at the end of the production run;
- Fatigue and environmental impacts such as freeze–thaw cycles, temperature gradient, corrosion and aging were not incorporated into the conducted refined deck analysis. These factors could be critical to bridge deck design;
- Literature review on RC bridge deck fatigue performance only focused on concrete material and structural behavior of bridge decks. Fatigue performance of steel reinforcement and its interaction with concrete were not included; and
- The proposed two frameworks of estimating fatigue life of RC bridge deck, i.e., stress-based method and force-based method, have not been verified by laboratory or on-site testing.

It is crucial to note that the results, discussions, and conclusions presented in this report are all bounded to the abovementioned limitations of the current study; therefore, they may not be generalized without proper justifications and/or further validations through appropriate verification or testing.

9.1.2 Final Remarks

Based on the investigation conducted in this study, several important remarks can be made:

- Updated design values for the negative moment are proposed in CA-A4 table that covers the negative moment demands generated by the HL-93, SHV and P-15 vehicles for girder spacings less than 13 ft. Special consideration is recommended for EV3 vehicle load and for the other special vehicle types for girder spacings greater than 13 ft;
- The analysis demonstrated that the positioning of a single truck had a significant influence on deck moment values. The maximum negative moments were observed at the faces of interior girders, while maximum positive moments occurred between the first and second girders. This variation underscores the critical importance of truck placement in bridge design to ensure structural integrity;
- When overhang sections were excluded from the consideration, the analysis revealed that negative moments consistently developed at the start of these sections. This finding highlights the necessity of incorporating overhang effects into bridge design calculations;

- The cross-slope of 10º has a noticeable influence on the load demands of bridge decks but it is negligible for a typical range of 1.5–2º;
- The shear capacity of RC bridge deck is generally adequate under the vehicle loads based on the current design practice, excluding the influence from fatigue and environmental impact;
- The fatigue process of concrete material is complex, and it can be influenced by normalized stress level, stress reversal, lateral confinement, concrete creep, loading frequency, loading duration, shape of cyclic loading form and loading history, etc.;
- A normalized stress level of $S_{max} > 0.75$ is critical for the fatigue performance of concrete material, and sustained loading with a stress ratio $R > 0.75$ notably reduces fatigue life; and
- Representative RC deck fatigue failure mode is punching shear with fan-shaped or grid-like cracking, as observed from experimental studies.

9.2 Recommendations for Future Research

It is believed that future research investigations are indeed required to address the following aspects:

- The influence due to fatigue and environmental factors require further research efforts to fill the current knowledge gap, because they could significantly affect the longevity and structural performance of RC bridge decks as observed from routine inspections in California;
- Moving vehicle loading applied to RC bridge decks is a dynamic contact process with change in contact area, load pressure, contact time duration, and so forth. Little is known about the influence due to these moving characteristics of vehicles, since the performed refined analysis based on RSMs still falls under the scope of static linear elastic analysis;
- If the dynamic load or multiple presence factors are updated for any of the vehicles used in this study, the conclusions will need to be re-evaluated; and
- Many of the conclusions of this study were in relative comparisons with the FE models. It means these conclusions were mostly independent of flaws in the modeling strategy, as long as it was employed consistently. However, once values become absolute, i.e., the actual moment demands are reported, variations in the models from "reality" would become more important. There are no physical models to back up the presented data, and so there is no metric to evaluate the validity of these absolute values, which could be an area of future research.

10 REFERENCES

AASHTO. (2017). AASHTO LRFD bridge design specifications, customary U.S. units, 8th Edition. Washington, DC: American Association of State Highway and Transportation Officials.

Aas-Jakobsen, K. (1970). Fatigue of concrete beams and columns. Division of Concrete Structures, Norwegian Inst. of Technology, University of Trondheim.

Abughneam, I.S. (2019). Refined analysis of a curved bridge and comparison with spine analysis "an illustrative example". MS Thesis, California State University, Sacramento.

ACI 215R-74 (Revised 1992/Reapproved 1997). Considerations for design of concrete structures subjected to fatigue loading. ACI Committee 215.

ACI Committee. (2019). Building code requirements for structural concrete (ACI 318-19) and commentary. American Concrete Institute.

ACI 343R-95. (1995). Analysis and design of reinforced concrete bridge structures. American Concrete Institute.

Adams, A., Galindez, N., Hopper, T., Murphy, T., Ritchie, P., Storlie, V., & Weisman, J. (2019). Manual for refined analysis in bridge design and evaluation. No. FHWA-HIF-18-046, United States. Federal Highway Administration. Office of Infrastructure.

ATENA. (2020). ATENA program documentation. Prague, Czech Republic: Červenka Consulting.

Bakht, B., & Lam, C. (2000). Behavior of transverse confining systems for steel-free deck slabs. *Journal of Bridge Engineering*, 5(2), 139-147.

Batchelor, B.D., Hewitt, B.E., & Csagoly, P. (1978). An investigation of the fatigue strength of deck slabs of composite steel/concrete bridges. NCHRP Report 664, Transportation Research Record.

Batchelor, B. deV., Hewitt, B.E., Csagoly, P., & Holowka, M. (1978). Investigation of the ultimate strength of deck slabs of composite steel/concrete bridges. Transportation Research Record 664, Bridge Engineering, Vol. 1, Transportation Research Board.

Bode, M., & Marx, S. (2021). Energetic damage analysis regarding the fatigue of concrete. *Structural Concrete*, 22, E851-E859.

Buyukozturk, O., & Tseng, T.M. (1984). Concrete in biaxial cyclic compression. *Journal of Structural Engineering*, 110(3), 461-476.

Caltrans (2008). Memo to Designers 10-20 Attachment 2. Available at: <https://dot.ca.gov/programs/engineering-services/manuals/memo-to-designers>

Caltrans. (2019). Caltrans Bridge Design Practice. California Department of Transportation. 4th Edition.

Caltrans. (2019). California Amendments to the AASHTO LRFD Bridge Design Specifications, 8th Edition.

Caltrans. (2017). Memo to designers 10-20: deck and soffit slab. Sacramento, CA: California Department of Transportation.

Chen, C., Wang, X., & Cheng, L. (2019). Modeling NSM FRP strengthened RC beams under fatigue due to IC-debonding. *International Journal of Fatigue*, 126, 174-187.

Chen, C., & Cheng, L. (2017). Fatigue life-based design of RC beams strengthened with NSM FRP. *Engineering Structures*, 140, 256-266.

Chen, C., & Cheng, L. (2017). Predicting flexural fatigue performance of RC beams strengthened with externally bonded FRP due to FRP debonding. *Journal of Bridge Engineering*, 22(11), 04017082.

Cornelissen, H.A.W., & Reinhardt, H.W. (1984). Uniaxial tensile fatigue failure of concrete under constant-amplitude and programme loading. *Magazine of Concrete Research*, 36(129), 216-226.

Csagoly, P.F., & Lybas, J.M. (1989). Advanced design method for concrete bridge deck slabs. *Concrete International*, 11(5), 53-63.

Cuelho, E., Stephens, J., Smolenski, P., & Johnson, J. (2006). Evaluating concrete bridge deck performance. No. FHWA/MT-06-006/8156-002, Montana. Dept. of Transportation Research Programs.

Cuelho, E., & Stephens, J. (2013). Investigation of methacrylate rehabilitation strategy to extend the service life of concrete bridge decks. No. CA13-1723.

DeJong, S.J., & MacDougall, C. (2006). Fatigue behaviour of MMFX corrosion-resistant reinforcing steel. In Proceedings of the 7th International Conference on Short and Medium Span Bridges, Montreal, Canada.

Drar, A.A.M., & Matsumoto, T. (2016). Fatigue analysis of RC deck slabs reinforced with plain bars based on the bridging stress degradation concept. *Journal of Advanced Concrete Technology*, 14(1), 21-34.

El-Ragaby, A., El-Salakawy, E., & Benmokrane, B. (2007). Fatigue life evaluation of concrete bridge deck slabs reinforced with glass FRP composite bars. *Journal of Composites for Construction*, 11(3), 258-268.

Eurocode, B. S. (2002). EN 1990, 2002. Basis of Structural Design. British Standard Institution.

Fang, I.K., Tsui, C.K. T., Burns, N.H., & Klingner, R.E. (1990). Load capacity of isotropically reinforced, cast-in-place and precast panel bridge decks. *PCI Journal*, 35(4), 104-107.

FIB (2013). Fib model code for concrete structures 2010.

Fu, G., Feng, J., Dekelbab, W., Moses, F., Cohen, H., Mertz, D. & Thompson, P.D. (2003). Effect of truck weight on bridge network costs. NCHRP Report 495, Transportation Research Board, Washington, DC.

Gao, L., & Hsu, C.T.T. (1998). Fatigue of concrete under uniaxial compression cyclic loading. *Materials Journal*, 95(5), 575-581.

Graddy, J.C., Kim, J., Whitt, J.H., Burns, N.H., & Klingner, R.E. (2002). Punching-shear behavior of bridge decks under fatigue loading. *Structural Journal*, 99(3), 257-266.

Hambly, E.C. (1991). Bridge deck behavior. E & FN SPON, Chapman and Hall.

Helgason, T., Hanson, J.M., Somes, N.F., Corley, W.G., & Hognestad, E. (1976). Fatigue strength of high-yield reinforcing bars. NCHRP Report 164, Transportation Research Board.

Hewitt, B.E., & Batchelor, B.D. (1975). Punching shear strength of restrained slabs. *Journal of the Structural Division*, 101(9), 1837-1853.

Hida, S., Ibrahim, F.I.S., Capers, H.A., Bailey, G.L., Friedland, I.M., Kapur, J., Martin Jr, B.T., Mertz, D.R., Perfetti, G.R., Saad, T., & Sivakumar, B. (2010). Assuring bridge safety and serviceability in Europe. No. FHWA-PL-10-014, United States. Federal Highway Administration.

Hilsdorf, H.K., & Kesler, C.E. (1966). Fatigue strength of concrete under varying flexural stresses. In *Journal Proceedings*, 63(10), 1059-1076.

Holmen, J.O. (1982). Fatigue of concrete by constant and variable amplitude loading. *Special Publication*, 75, 71-110.

Holt, J., Garcia, U., Walters, S., Monopolis, C., Zhu, A., Bayrak, O., Powell, L., Halbe, K., Kumar, P., & Chavel, B. (2018). Concrete bridge shear load rating synthesis report. No. FHWA-HIF-18-061, United States. Federal Highway Administration. Office of Infrastructure, 140p.

Homberg, H., & Ropers, W. (1965). Fahrbahnplatten mit verändlicher dicke,1st ed. Berlin, Germany: Springer-Verlag Berlin Heidelberg GmbH.

Hosseini, A., Ghafoori, E., Al-Mahaidi, R., Zhao, X.L., & Motavalli, M. (2019). Strengthening of a 19th century roadway metallic bridge using nonprestressed bonded and prestressed unbonded CFRP plates. *Construction and Building Material*, 209, 240-259.

Hosseini, A., Ghafoori, E., Motavalli, M., Nussbaumer, A., & Zhao, X.L. (2017). Mode I fatigue crack arrest in tensile steel members using prestressed CFRP plates. *Composite Structures*, 178, 119-134.

Hosseini, A., Nussbaumer, A., Motavalli, M., Zhao, X.L., & Ghafoori, E. (2019). Mixed mode I/II fatigue crack arrest in steel members using prestressed CFRP reinforcement. *International Journal of Fatigue*, 127, 345-361.

Hsu, T.T. (1981). Fatigue of plain concrete. In *Journal Proceedings*, 78(4), 292-305.

Isojeh, B., El-Zeghayar, M., & Vecchio, F.J. (2017). Concrete damage under fatigue loading in uniaxial compression. *ACI Materials Journal*, 114(2), 225-235.

Kennedy, G., & Goodchild, C. (2004). Practical yield line design. *Concrete Centre*, Surrey, UK.

Kinnunen, S., & Nylander, H. (1960). Punching of concrete slabs without shear reinforcement. New York: Elander, 112p.

Kolluru, S.V., O'Neil, E.F., Popovics, J.S., & Shah, S.P. (2000). Crack propagation in flexural fatigue of concrete. *Journal of Engineering Mechanics*, 126(9), 891-898.

Lei, D., Zhang, P., He, J., Bai, P., & Zhu, F. (2017). Fatigue life prediction method of concrete based on energy dissipation. *Construction and Building Materials*, 145, 419-425.

Liang, J., Ding, Z., & Li, J. (2017). A probabilistic analyzed method for concrete fatigue life. *Probabilistic Engineering Mechanics*, 49, 13-21.

Lohaus, L., Oneschkow, N., & Wefer, M. (2012). Design model for the fatigue behaviour of normal-strength, high-strength and ultra-high-strength concrete. *Structural Concrete*, 13(3), 182-192.

Maeda, Y., & Matsui, S. (1984). Fatigue of reinforced concrete slabs under trucking wheel load. *Proceedings of JCI*, 6, 221-224.

Maekawa, K., & El-Kashif, K.F. (2004). Cyclic cumulative damaging of reinforced concrete in post-peak regions. *Journal of Advanced Concrete Technology*, 2(2), 257-271.

Maekawa, K., Gebreyouhannes, E., Mishima, T., & An, X. (2006a). Three-dimensional fatigue simulation of RC deck slabs under traveling wheel-type loads. *Journal of Advanced Concrete Technology*, 4(3), 445-457.

Maekawa, K., Okamura, H., & Pimanmas, A. (2003). Non-linear mechanics of reinforced concrete. CRC Press.
Maekawa, K., Toongoenthong, K., Gebreyouhannes, E., & Kishi, T. (2006b). Direct path-integral scheme for fatigue simulation of reinforced concrete in shear. *Journal of Advanced Concrete Technology*, 4(1), 159-177.
Matsui, S. (1991). Prediction of fatigue life of reinforced concrete slabs of highway bridges. *Japan Society for Safety Engineering*, 30(6), 432-440 (in Japanese).
McCall, J.T. (1958, August). Probability of fatigue failure of plain concrete. In *Journal Proceedings*, 55(8), 233-244.
Meadway, J. M. (2008). Evaluation of current deck design practices. MS Thesis, West Virginia University.
Miner, M.A. (1945). Cumulative Damage in Fatigue. *Journal of Applied Mechanics*, 3, 159-164.
Model Code. (2010). Model code for concrete structures. International Federation for Structural Concrete, FIB Bulletin 65.
Mufti, A.A., & Newhook, J.P. (1998). Punching shear strength of restrained concrete bridge deck slabs. *Structural Journal*, 95(4), 375-381.
Murphy, T. (2020). Checking our work: Methods for verifying analyses of structural designs. Aspire, *The Concrete Bridge Magazine*, 56, 8-9.
Murphy, T., Hopper, T., Wasserman, E., Lopez, M., Kulicki, J., Moon, F., Langlois, A.M., & Samtani, N. (2019). Guide specification for service life design of highway bridges. No. NCHRP 12-108, Transportation Research Board.
Nowak, A.S., Szerszen, M.M., & Ferrand, D. (2003). Analytical design procedures and load rating for isotropic bridge decks. No. RC-1430, Michigan Department of Transportation.
Nowak, A.S., Szerszen, M.M., & Kwasniewski, L. (2000). Development of the procedure for efficient evaluation of bridge decks. No. RC-1389A, Michigan Department of Transportation.
O'Brien, E.J., Keogh, D. and O'Connor, A. (2014). Bridge deck analysis. 2nd Edition, CRC Press.
Okada, K., Okamura, H., & Sonoda, K. (1978). Fatigue failure mechanism of reinforced concrete bridge deck slabs. *Transportation Research Record*, 664, 136-144.
Ortega, J.J., Ruiz, G., Rena, C.Y., Afanador-Garcia, N., Tarifa, M., Poveda, E., ... & Evangelista Jr, F. (2018). Number of tests and corresponding error in concrete fatigue. *International Journal of Fatigue*, 116, 210-219.
Palmgren, A.G. (1924). Die Lebensdauer von Kugellagern (Life Length of Roller Bearings or Durability of Ball Bearings). *Zeitschrift des Vereines Deutscher Ingenieure (ZVDI)*, 14, 339-341.
Perdikaris, P.C., & Beim, S. (1988). RC bridge decks under pulsating and moving load. *Journal of Structural Engineering*, 114(3), 591-607.
Perdikaris, P.C., Petrou, M.F., & Wang, A. (1993). Fatigue strength and stiffness of reinforced concrete bridge decks, Final report to ODOT. FHWA/OH-93/016, Department of Civil Engineering, Case Western University, Cleveland, OH.
Petkovic, G., Lenschow, R., Stemland, H., & Rosseland, S. (1990). Fatigue of high-strength concrete. *Special Publication*, 121, 505-526.

Petryna, Y.S., Pfanner, D., Stangenberg, F., & Krätzig, W.B. (2002). Reliability of reinforced concrete structures under fatigue. *Reliability Engineering & System Safety*, 77(3), 253-261.

Pucher, A. (1977). Einflussfelderelastischer Platten/Influence Surfaces of Elastic Plates, 5th ed. Vienna, Austria: SpringerVerlag Wien.

Reinhardt, H. W., & Cornelissen, H.A.W. (1984). Post-peak cyclic behaviour of concrete in uniaxial tensile and alternating tensile and compressive loading. *Cement and Concrete Research*, 14(2), 263-270.

Rüsch, H. (1960). Researches toward a general flexural theory for structural concrete. *Journal of the American Concrete Institute*, 57(1), 1-28.

Saucedo, L., Rena, C.Y., Medeiros, A., Zhang, X., & Ruiz, G. (2013). A probabilistic fatigue model based on the initial distribution to consider frequency effect in plain and fiber reinforced concrete. *International Journal of Fatigue*, 48, 308-318.

Schijve, J. (2001). Fatigue of structures and materials Dordrecht. The Netherlands: Kluwer Academic.

Schijve, J. (2009). Fatigue of structures and materials. Dordrecht: Kluwer Academic.

Schläfli, M., & Brühwiler, E. (1998). Fatigue of existing reinforced concrete bridge deck slabs. *Engineering Structures*, 20(11), 991-998.

Shahrooz, B.M. (2011). Design of concrete structures using high-strength steel reinforcement. NCHRP report 679, Transportation Research Board.

Shakushiro, K., Mitamura, H., Watanabe, T., & Kishi, N. (2011). Experimental study on fatigue durability of RC deck slabs reinforced with round steel bars. *Journal of Structural Engineering*, 57, 1297-1304.

Song, Z., Frühwirt, T., & Konietzky, H. (2018). Characteristics of dissipated energy of concrete subjected to cyclic loading. *Construction and Building Materials*, 168, 47-60.

Sonoda, K., & Horikawa, T. (1982). Fatigue strength of reinforced concrete slabs under moving loads. *Fatigue of Steel and Concrete Structures*, 455-462.

Sparks, Peter R., and J. B. Menzies. (1973). The effect of rate of loading upon the static and fatigue strengths of plain concrete in compression. *Magazine of Concrete Research*, 25(83), 73-80.

Su, E.C., & Hsu, T.T. (1988). Biaxial compression fatigue and the discontinuity of concrete. *Materials Journal*, 85(3), 178-188.

Subramaniam, K.V., & Shah, S.P. (2003). Biaxial tension fatigue response of concrete. *Cement and Concrete Composites*, 25(6), 617-623.

Subramaniam, K.V., Popovics, J.S., & Shah, S.P. (2002). Fatigue fracture of concrete subjected to biaxial stresses in the tensile C-T Region. *Journal of Engineering Mechanics*, 128(6), 668-676.

Sun, W., Mu, R., Luo, X., & Miao, C. (2002). Effect of chloride salt, freeze–thaw cycling and externally applied load on the performance of the concrete. *Cement and Concrete Research*, 32(12), 1859-1864.

Suthiwarapirak, P., & Matsumoto, T. (2006). Fatigue analysis of RC deck slabs and repaired RC deck slabs based on crack bridging degradation concept. *Journal of Structural Engineering*, 132(6), 939-948.

Taliercio, A.L.F., & Gobbi, E. (1996). Experimental investigation on the triaxial fatigue behaviour of plain concrete. *Magazine of Concrete Research*, 48(176), 157-172.

Tauskela, L.M. (2020). Testing a full-scale reinforced concrete bridge deck with GFRP and steel reinforcement using cyclic pulsating and rolling loads. Master's Thesis, Queen's University, 2020.

Tepfers, R. (1982). Fatigue of plain concrete subjected to stress reversals. *Special Publication*, 75, 195-216.

Tepfers, R., & Kutti, T. (1979). Fatigue strength of plain, ordinary, and lightweight concrete. In *Journal Proceedings*, 76(5), 635-652.

Tepfers, R., Görlin, J., & Samuelsson, T. (1973). Concrete subjected to pulsating load and pulsating deformation of different pulse waveform. *Nordisk betong*, 17(4).

Tepfers, R., Hedberg, B., & Szczekocki, G. (1984). Absorption of energy in fatigue loading of plain concrete. *Matériaux et Construction*, 17(1), 59-64.

Torrenti, J.M., Pijaudier-Cabot, G., & Reynouard, J.M. (Eds.). (2013). Mechanical behavior of concrete. John Wiley & Sons.

Vicente, M.A., González, D.C., Mínguez, J., & Martínez, J.A. (2014). Residual modulus of elasticity and maximum compressive strain in HSC and FRHSC after high-stress-level cyclic loading. *Structural Concrete*, 15(2), 210-218.

Yoshitake, I., Kim, Y.J., Yumikura, K., & Hamada, S. (2010). Moving-wheel fatigue for bridge decks strengthened with CFRP strips subject to negative bending. *Journal of Composites for Construction*, 14(6), 784-790.

Youn, S.G., & Chang, S.P. (1998). Behavior of composite bridge decks subjected to static and fatigue loading. *Structural Journal*, 95(3), 249-258.

Zhang, B., Phillips, D.V., & Green, D.R. (1998). Sustained loading effect on the fatigue life of plain concrete. *Magazine of Concrete Research*, 50(3), 263-278.

Zhang, B., Phillips, D.V., & Wu, K. (1996). Effects of loading frequency and stress reversal on fatigue life of plain concrete. *Magazine of Concrete Research*, 48(177), 361-375.

Zokaie, T., Osterkamp, T.A., & Imbsen, R.A. (1991). Distribution of wheel loads on highway bridges. NCHRP Report 12-26, Transportation Research Board, National Research Council, Washington, DC.

11 APPENDICES

11.1 Appendix A: Existing AASHTO A4 deck slab design table (AASHTO 2024)

APPENDIX A4—DECK SLAB DESIGN TABLE

Table A4-1 may be used in determining the design moments for different girder arrangements. The following assumptions and limitations were used in developing this table and should be considered when using the listed values for design:

- The moments are calculated using the equivalent strip method as applied to concrete slabs supported on parallel girders.
- Multiple presence factors and the dynamic load allowance are included in the tabulated values.
- See Article 4.6.2.1.6 for the distance between the center of the girders to the location of the design sections for negative moments in the deck. Interpolation between the listed values may be used for distances other than those listed in Table A4-1.
- The moments are applicable for decks supported on at least three girders and having a width of not less than 14.0 ft between the centerlines of the exterior girders.
- The moments represent the upper bound for the moments in the interior regions of the slab and, for any specific girder spacing, were taken as the maximum value calculated, assuming different number of girders in the bridge cross-section. For each combination of girder spacing and number of girders, the following two cases of overhang width were considered:

  (a) Minimum total overhang width of 21.0 in. measured from the center of the exterior girder, and

  (b) Maximum total overhang width equal to the smaller of 0.625 times the girder spacing and 6.0 ft.

  A railing system width of 21.0 in. was used to determine the clear overhang width. For other widths of railing systems, the difference in the moments in the interior regions of the deck is expected to be within the acceptable limits for practical design.

- The moments do not apply to the deck overhangs and the adjacent regions of the deck that need to be designed taking into account the provisions of Article A13.4.1.
- It was found that the effect of two 25^k axles of the tandem, placed at 4.0 ft from each other, produced maximum effects under each of the tires approximately equal to the effect of the 32^k truck axle. The tandem produces a larger total moment, but this moment is spread over a larger width. It was concluded that repeating calculations with a different strip width for the tandem would not result in a significant difference.

Table A4-1—Maximum Live Load Moments per Unit Width, kip-ft/ft

S	Positive Moment	Negative Moment						
		Distance from CL of Girder to Design Section for Negative Moment						
		0.0 in.	3 in.	6 in.	9 in.	12 in.	18 in.	24 in.
4'–0"	4.68	2.68	2.07	1.74	1.60	1.50	1.34	1.25
4'–3"	4.66	2.73	2.25	1.95	1.74	1.57	1.33	1.20
4'–6"	4.63	3.00	2.58	2.19	1.90	1.65	1.32	1.18
4'–9"	4.64	3.38	2.90	2.43	2.07	1.74	1.29	1.20
5'–0"	4.65	3.74	3.20	2.66	2.24	1.83	1.26	1.12
5'–3"	4.67	4.06	3.47	2.89	2.41	1.95	1.28	0.98
5'–6"	4.71	4.36	3.73	3.11	2.58	2.07	1.30	0.99
5'–9"	4.77	4.63	3.97	3.31	2.73	2.19	1.32	1.02
6'–0"	4.83	4.88	4.19	3.50	2.88	2.31	1.39	1.07
6'–3"	4.91	5.10	4.39	3.68	3.02	2.42	1.45	1.13
6'–6"	5.00	5.31	4.57	3.84	3.15	2.53	1.50	1.20
6'–9"	5.10	5.50	4.74	3.99	3.27	2.64	1.58	1.28
7'–0"	5.21	5.98	5.17	4.36	3.56	2.84	1.63	1.37
7'–3"	5.32	6.13	5.31	4.49	3.68	2.96	1.65	1.51
7'–6"	5.44	6.26	5.43	4.61	3.78	3.15	1.88	1.72
7'–9"	5.56	6.38	5.54	4.71	3.88	3.30	2.21	1.94
8'–0"	5.69	6.48	5.65	4.81	3.98	3.43	2.49	2.16
8'–3"	5.83	6.58	5.74	4.90	4.06	3.53	2.74	2.37
8'–6"	5.99	6.66	5.82	4.98	4.14	3.61	2.96	2.58
8'–9"	6.14	6.74	5.90	5.06	4.22	3.67	3.15	2.79
9'–0"	6.29	6.81	5.97	5.13	4.28	3.71	3.31	3.00
9'–3"	6.44	6.87	6.03	5.19	4.40	3.82	3.47	3.20
9'–6"	6.59	7.15	6.31	5.46	4.66	4.04	3.68	3.39
9'–9"	6.74	7.51	6.65	5.80	4.94	4.21	3.89	3.58
10'–0"	6.89	7.85	6.99	6.13	5.26	4.41	4.09	3.77
10'–3"	7.03	8.19	7.32	6.45	5.58	4.71	4.29	3.96
10'–6"	7.17	8.52	7.64	6.77	5.89	5.02	4.48	4.15
10'–9"	7.32	8.83	7.95	7.08	6.20	5.32	4.68	4.34
11'–0"	7.46	9.14	8.26	7.38	6.50	5.62	4.86	4.52
11'–3"	7.60	9.44	8.55	7.67	6.79	5.91	5.04	4.70
11'–6"	7.74	9.72	8.84	7.96	7.07	6.19	5.22	4.87
11'–9"	7.88	10.01	9.12	8.24	7.36	6.47	5.40	5.05
12'–0"	8.01	10.28	9.40	8.51	7.63	6.74	5.56	5.21
12'–3"	8.15	10.55	9.67	8.78	7.90	7.02	5.75	5.38
12'–6"	8.28	10.81	9.93	9.04	8.16	7.28	5.97	5.54
12'–9"	8.41	11.06	10.18	9.30	8.42	7.54	6.18	5.70
13'–0"	8.54	11.31	10.43	9.55	8.67	7.79	6.38	5.86
13'–3"	8.66	11.55	10.67	9.80	8.92	8.04	6.59	6.01
13'–6"	8.78	11.79	10.91	10.03	9.16	8.28	6.79	6.16
13'–9"	8.90	12.02	11.14	10.27	9.40	8.52	6.99	6.30
14'–0"	9.02	12.24	11.37	10.50	9.63	8.76	7.18	6.45
14'–3"	9.14	12.46	11.59	10.72	9.85	8.99	7.38	6.58
14'–6"	9.25	12.67	11.81	10.94	10.08	9.21	7.57	6.72
14'–9"	9.36	12.88	12.02	11.16	10.30	9.44	7.76	6.86
15'–0"	9.47	13.09	12.23	11.37	10.51	9.65	7.94	7.02

11.2 Appendix B: Case Study for Recommended Force-Based Framework to Calculate Required Concrete Deck Thickness Subjected to Cyclic Loading

Limited by the scope of the current research, only the force-based framework as introduced in Chapter 4.5.2 was adopted for the tryout case study to calculate the required thickness of RC bridge deck subjected to cyclic loading. To further ease the calculation process, some assumptions were also made in the following:

- Only the standard HL-93 truck with a 32 kip axle load was considered (P = 16 kip), with an ADTT of 5000 per lane, ignoring the effect of other vehicle types;
- The passage of each HL-93 truck was equal to 2.5 fatigue cycles;
- Load and resistance factors were not considered;
- An impact factor of 33% was used per AASHTO;
- The tire pressure was assumed to be 133 psi;
- A target service life of 75 years, equal to a fatigue life N_f of 342 million cycles, was considered for the RC bridge deck; and
- Dry condition was assumed to implement the fatigue model of Matsui *(*C = 1.52).

This tryout case study aimed to explore the difference in estimated fatigue life of RC bridge decks using different model combinations, hence, the assumptions made above might not be realistic. For example, the HL-93 with 32 kip axle is not the only type of truck on the road, the influence of other trucks with different tire patch load also need to be considered for design purpose. In that case, the PM rule as introduced in Chapter 4.3.2 is a promising method to incorporate the effect of other types of vehicles. Of course, a case-by-case investigation is always beneficial to determine the statistical variation on axle loads at the target traffic location.

In the tryout case study, two static models were explored to estimate the local punching shear carrying capacity P_s of the bridge deck, including (a) the fatigue punching shear model of Matsui (1991), referred to as S1; and (b) the general punching shear model (Graddy et al. 2002), referred to as S2. The introduction of these two static models was presented in Chapter 4.4.2. Two fatigue life models were explored to estimate the required thickness of RC bridge deck targeting the service life of 75 years, including (a) the model of Matsui (1991), referred to as F1; (b) the model of El-Ragaby et al. (2007), referred to as F2. The introduction of these two fatigue models was also presented in Chapter 4.4.2. These two static models were explored because of their simplicity for design, also they were both based on the punching shear theory. Additionally, the using of Matsui's static model was consistent with the fatigue life model as proposed by Matsui. However, the static and fatigue models explored in the combination S2F2 were not derived or calibrated from the same set of test database, and they were proposed by different independent researchers. In other words, the combination S2F2 had never been verified by lab or field test and it was selected only to serve as comparison cases to quantify the difference in predicted fatigue life using different models.

The predicted fatigue life of RC bridge deck is summarized in **Table 11.1**. The design details of RC bridge deck, e.g., deck thickness, size of reinforcement, spacing of rebars, etc., referred to the MTD 10-20 (Caltrans 2008), and were used as model input to estimate the fatigue life. The bottom and top clear cover was assumed as 1 in and 2 in, respectively. The compressive strength of concrete was assumed as 3250 psi, and the grade 60 rebar with an elastic modulus of 29000 ksi was adopted for this tryout case study. To obtain the target 342 million cycles (75 years), a minimum deck thickness of 7.5 in is required for case S1F1 and 4.875 in for case S2F2. It should be noted that the latter case was calculated based on a tire print size of 12×10 in and did not require

the steel reinforcement detail, hence, calculations are not presented for simplicity. However, California requires a minimum deck thickness of 7 in, as a result, the latter case can reach a much longer fatigue life with a 7 in deck thickness and it is far beyond the 342 million cycles threshold, as illustrated in **Figure 11.1**. The large variation in the predicted fatigue life is primarily caused by the selection of the static model to estimate the punching shear capacity of the RC deck slab. For example, P_s of case *S2* is at least 70% higher than that of case S1, as shown in **Table 11.1**.

This tryout case study indicates the importance of using an appropriate static model to accurately estimate the punching shear capacity of the RC deck slab. Moreover, a large database from experiments is necessary to examine the reliability of different models as introduced in this review, but the corresponding workload is heavy and beyond the scope of the current research.

Table 11.1 Results of predicted fatigue life using different models

Girder Spacing (ft)	Deck thickness (in)	Rebar size	Rebar spacing (in)	P_s (S1[a]) (kip)	P_s (S2[b]) (kip)	N_f (S1F1[c]) (million cycles)	N_f (S2F2[d]) (million cycles)
4	7	#5	12.00	62.54	114.93	89.93	78780.95
4.25	7	#5	12.00	62.54	114.93	89.93	78780.95
4.5	7	#5	12.00	62.54	114.93	89.93	78780.95
4.75	7	#5	12.00	62.54	114.93	89.93	78780.95
5	7	#5	12.00	62.54	114.93	89.93	78780.95
5.25	7	#5	12.00	62.54	114.93	89.93	78780.95
5.5	7	#5	12.00	62.54	114.93	89.93	78780.95
5.75	7	#5	11.00	64.83	114.93	142.36	78780.95
6	7.125	#5	11.00	65.62	117.79	167.69	99561.84
6.25	7.125	#5	11.00	65.62	117.79	167.69	99561.84
6.5	7.25	#5	11.00	66.41	120.69	197.11	125143.94
6.75	7.375	#5	11.00	67.19	123.61	231.22	156485.21
7	7.5	#5	10.00	70.77	126.56	451.91	194705.88
7.25	7.5	#5	10.00	70.77	126.56	451.91	194705.88
7.5	7.625	#5	10.00	71.58	129.54	528.05	241111.28
7.75	7.75	#5	10.00	72.40	132.55	615.87	297217.32
8	7.75	#5	10.00	72.40	132.55	615.87	297217.32
8.25	7.875	#5	10.00	73.22	135.58	716.98	364778.90
8.5	8	#5	10.00	74.04	138.65	833.20	445821.44
8.75	8.125	#5	10.00	74.86	141.74	966.56	542675.83
9	8.125	#5	10.00	74.86	141.74	966.56	542675.83
9.25	8.25	#5	10.00	75.68	144.86	1119.36	658017.25
9.5	8.375	#5	10.00	76.50	148.01	1294.15	794908.03
9.75	8.375	#5	10.00	76.50	148.01	1294.15	794908.03
10	8.5	#6	12.00	84.87	151.19	4891.14	956845.03
10.25	8.625	#6	11.00	89.12	154.39	9197.06	1147812.00
10.5	8.625	#6	11.00	89.12	154.39	9197.06	1147812.00
10.75	8.75	#6	11.00	90.06	157.63	10590.65	1372337.27
11	8.875	#6	11.00	91.00	160.89	12176.61	1635557.37
11.25	8.875	#6	11.00	91.00	160.89	12176.61	1635557.37

11.5	9	#6	11.00	91.94	164.19	13978.95	1943287.04
11.75	9.125	#6	11.00	92.88	167.51	16024.39	2302096.29
12	9.125	#6	10.00	96.93	167.51	27634.21	2302096.29
12.25	9.25	#6	10.00	97.91	170.86	31631.96	2719395.21
12.5	9.375	#6	10.00	98.89	174.23	36156.84	3203527.14
12.75	9.5	#6	10.00	99.87	177.64	41271.75	3763871.05
13	9.5	#6	10.00	99.87	177.64	41271.75	3763871.05
13.25	9.625	#6	10.00	100.85	181.07	47046.33	4410954.10
13.5	9.75	#6	10.00	101.83	184.54	53557.58	5156575.20
13.75	9.75	#6	10.00	101.83	184.54	53557.58	5156575.20
14	9.875	#6	10.00	102.81	188.03	60890.59	6013940.75
14.25	10	#6	10.00	103.79	191.55	69139.26	6997813.70
14.5	10.125	#6	10.00	104.77	194.49	78407.11	7921749.54
14.75	10.25	#6	10.00	105.75	197.45	88808.19	8951646.89
15	10.375	#6	10.00	106.73	200.41	100467.98	10097949.76

Note: [a]punching shear model proposed by Matsui (1991); [b]general punching shear model (Graddy et al. 2002); [c]static and fatigue model of Matsui (1991); and [d]general punching shear model (Graddy et al. 2002) and fatigue model of El-Ragaby et al. (2007). Combination S2F2 had never been verified by lab or field test and it was selected only to serve as a comparison case to quantify the difference in predicted fatigue life using different models.

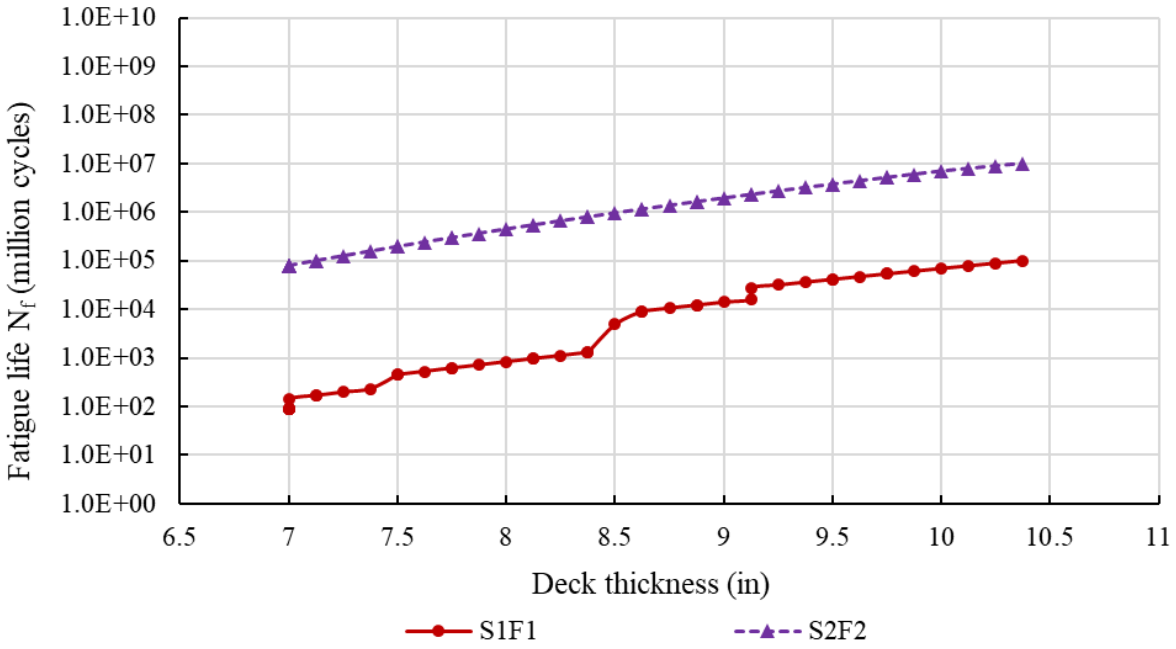

Figure 11.1. Comparison of predicted fatigue life using different models

11.3 Appendix C: Results for One HL-93 Truck for Production Run using RSM

6 (ft) Girder Spacing with Four Cells

In modeling a 6 ft girder spacing deck slab, at first, the truck is positioned at the end of the deck, then it is moved transversely as 10% of the girder spacing (6×12×0.1 = 7.2 inches). In this way, a total of 16 combinations is created for each girder spacing until one of the patch loads (truck tires) crosses the centerline of the bridge.

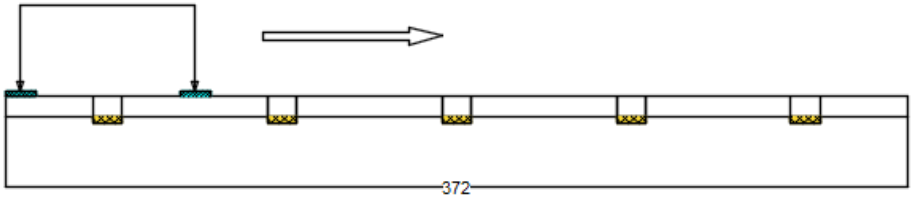

Figure 11.2. The placement of HL-93 load on the deck slab with 6 ft girder spacing (first combination)

Table 11.2 The total number of combinations created for 6 ft girder spacing with a one truck

No	Type of Deck	Distance from the face of the tire to the EOD (inches)
1	6 ft	0
2		7.2
3		14.4
4		21.6
5		28.8
6		36
7		43.2
8		50.4
9		57.6
10		64.8
11		72
12		79.2
13		86.4
14		93.6
15		100.8
16		108

Moment and shear diagrams for a 6 ft girder spacing are provided for each scenario, and corresponding moment, shear, and related envelopes are presented in **Figure 11.3 Figure 11.6**, respectively.

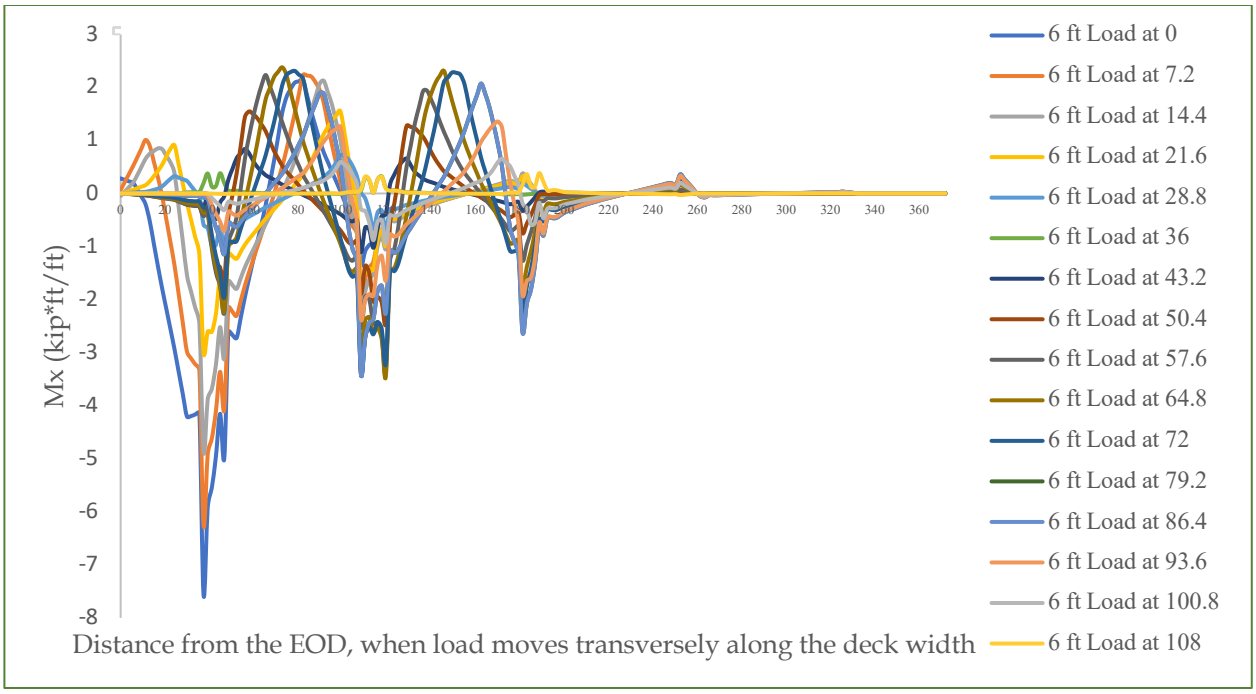

Figure 11.3. Moment profile for deck slab with 6 ft girder spacing and single truck

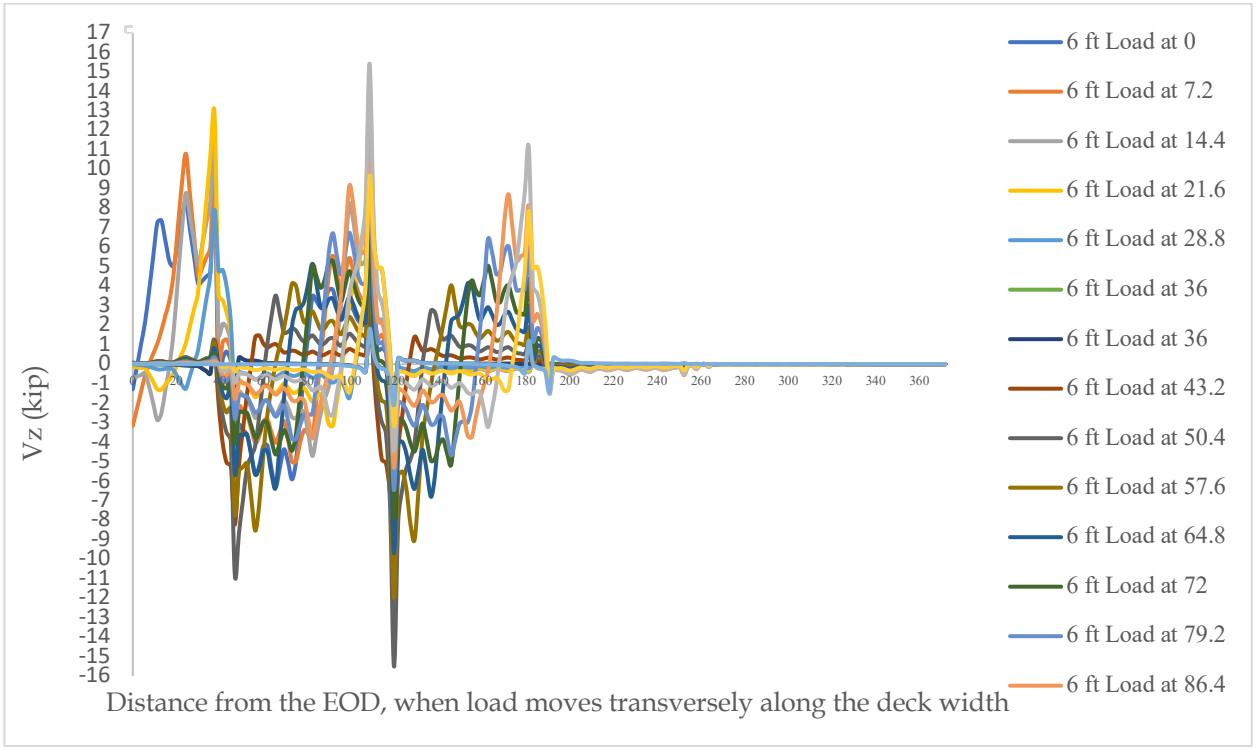

Figure 11.4. Shear profile for deck slab with 6 ft girder spacing and single truck

Figure 11.5. Moment envelope for deck slab with 6 ft girder spacing and single truck

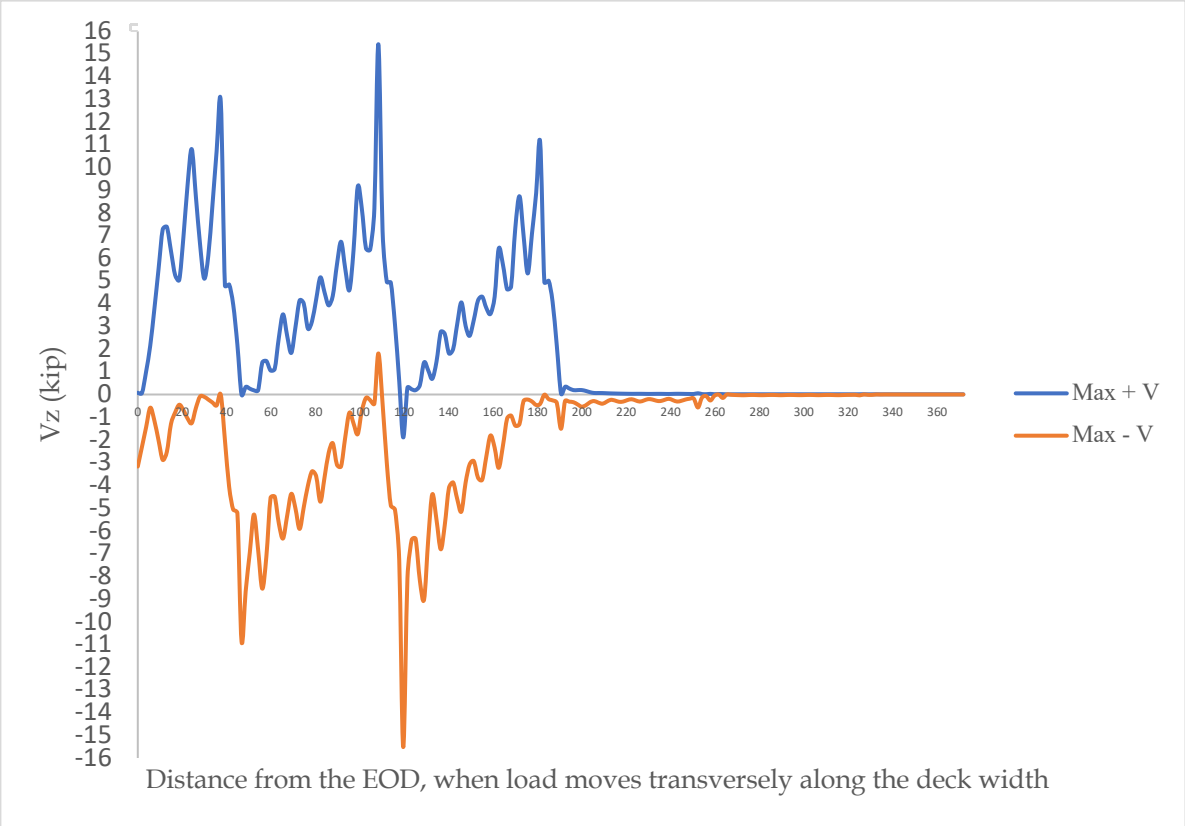

Figure 11.6. Shear envelope for deck slab with 6 ft girder spacing and single truck

When the moment results were compared, it was discovered that the maximum positive moment for a 6 ft. girder spacing deck slab occurred when the load patch was located at 64.8 inches away from the end of the slab, with a value of approximately 2.29 kip-ft/ft, and the maximum negative moment occurred when the truck patch load was located at the end of the slab, with a value of approximately -7.57 kip-ft/ft.

When the shear results were compared, it was discovered that the maximum positive shear for a 6 ft. girder spacing deck slab occurred when the load patch was located at 93.6 inches away from the end of the slab, with a value of approximately 15.42 kip, and the maximum negative shear occurred when the truck patch load was located 50.4 inches away from the end of the slab, with a value of approximately -15.53 kip.

9 (ft) Girder Spacing with Four Cells

In modeling a 9 ft. girder spacing deck slab, at first, the truck is positioned at the end of the deck, then it is moved transversely as 10 percent of the deck (9×12×0.1 = 10.8 inches). In this way, a total of 18 combinations are created until one of the patch loads (truck tires) crosses the centerline of the bridge.

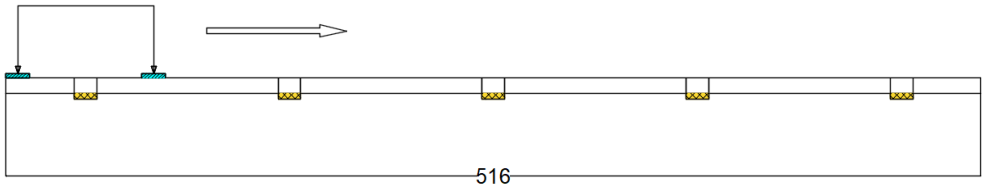

Figure 11.7. The placement of HL-93 load on the deck slab with 9 ft girder spacing (first combination)

Table 11.3. The total number of combinations created for 9 ft girder spacing with a one truck

No	Type of the deck	Distance from the face of the tire to the EOD (inches)
1	9 ft	0
2		10.8
3		21.6
4		32.4
5		43.2
6		54
7		64.8
8		75.6
9		86.4
10		97.2
11		108
12		118.8
13		129.6
14		140.4
15		151.2
16		162
17		172.8
18		183.6

Moment and shear Figures for a 9 ft girder spacing are provided for each scenario, and corresponding moment, shear and related envelopes are presented in below.

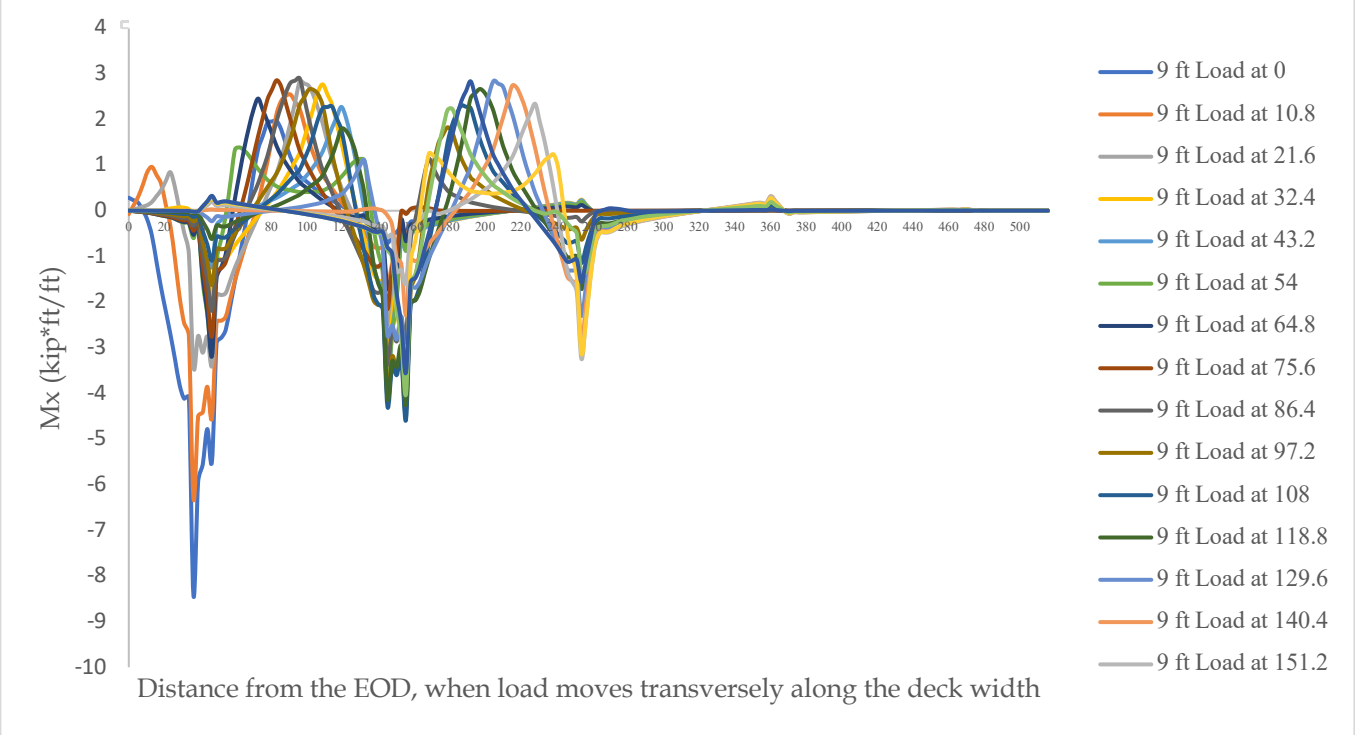

Figure 11.8. Moment profile for deck slab with 9 ft girder spacing and single truck

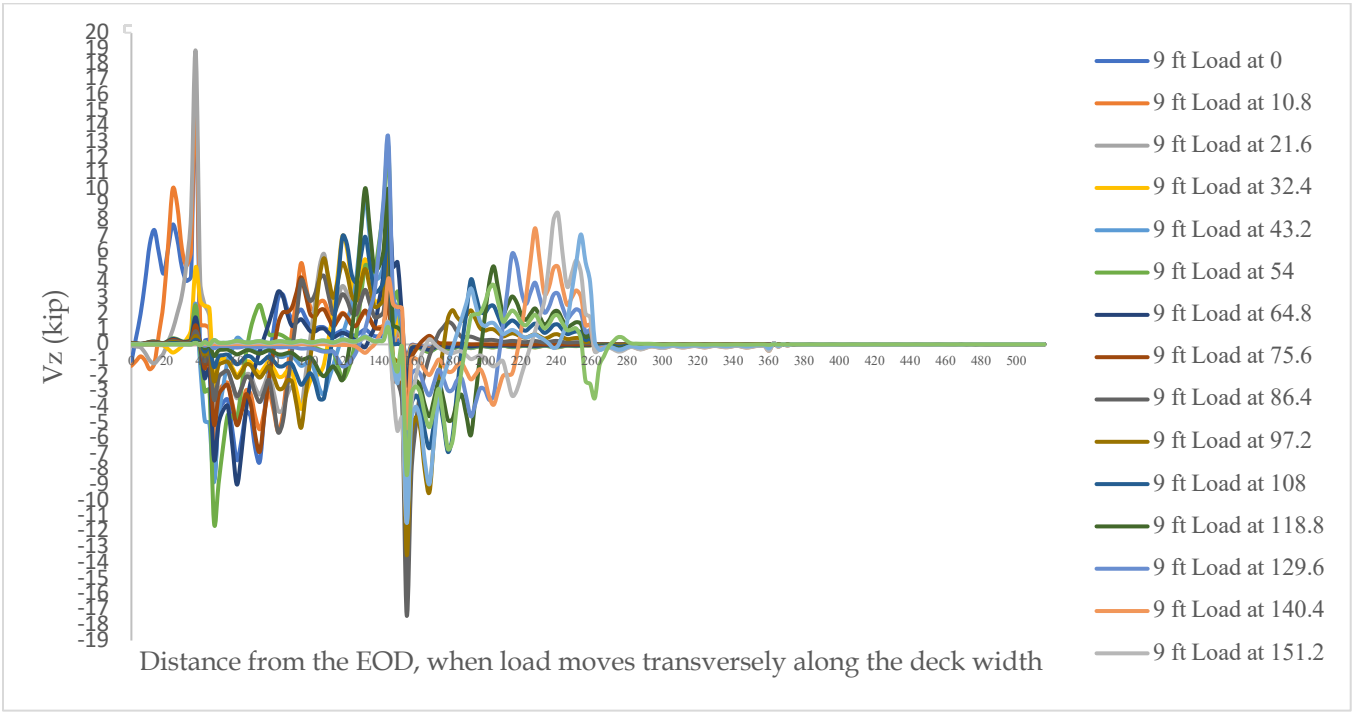

Figure 11.9. Shear profile for deck slab with 9 ft girder spacing and single truck

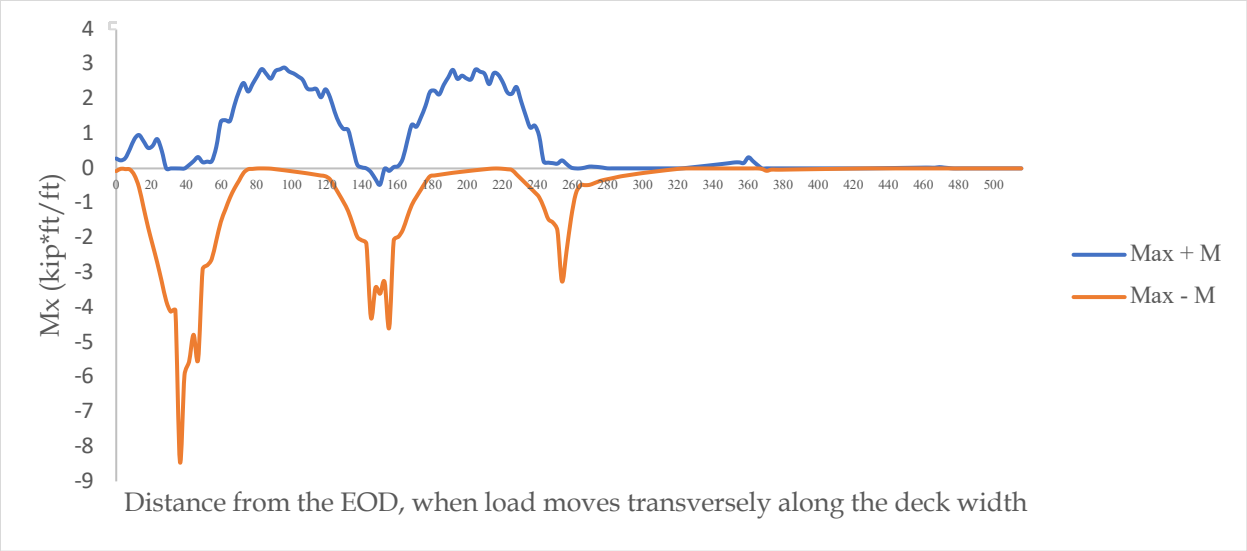

Figure 11.10. Moment envelope for deck slab with 9 ft girder spacing and single truck

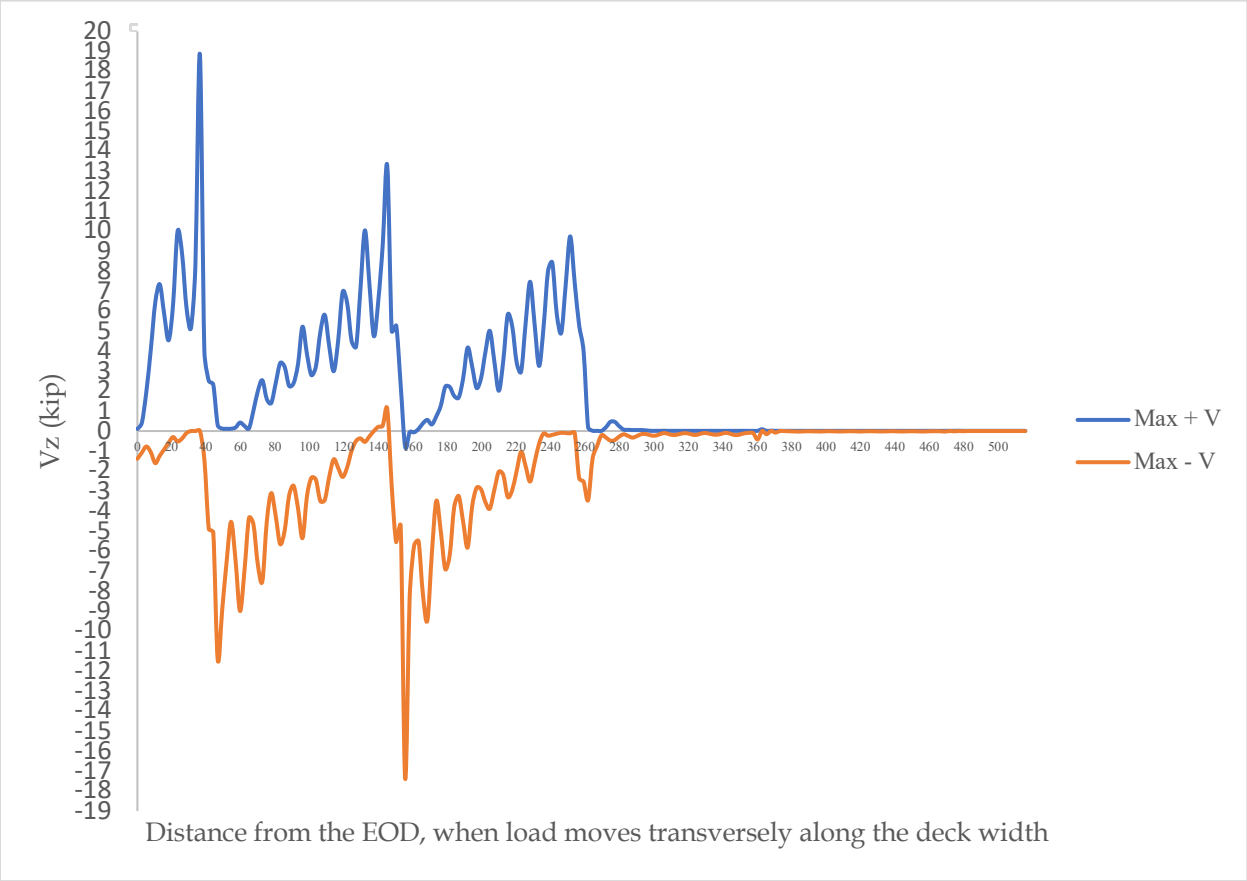

Figure 11.11. Shear envelope for deck slab with 9 ft girder spacing and single truck

When the moment results were compared, it was discovered that the maximum positive moment for a 9 ft. girder spacing deck slab occurred when the load patch was located at 86.4 inches away from the end of the slab, with a value of approximately 3 kip-ft/ft, and the maximum negative

moment occurred when the truck patch load was located at the end of the slab, with a value of approximately -8.44 kip-ft/ft.

When the shear results were compared, it was discovered that the maximum positive shear for a 9 ft. girder spacing deck slab occurred when the load patch was located at 21.6 inches away from the end of the slab, with a value of approximately 18.83 kip, and the maximum negative shear occurred when the truck patch load was located 86.4 inches away from the end of the slab, with a value of approximately -17.38 kip.

12 (ft) Girder Spacing with Four Cells

In modeling a 12 ft. girder spacing deck slab, at first, the truck is positioned at the end of the deck, then it is moved transversely as 10 percent of the deck (12×12×0.1 = 14.4 inches). In this way, a total of 19 combinations are created until one of the patch loads (truck tires) crosses the centerline of the bridge.

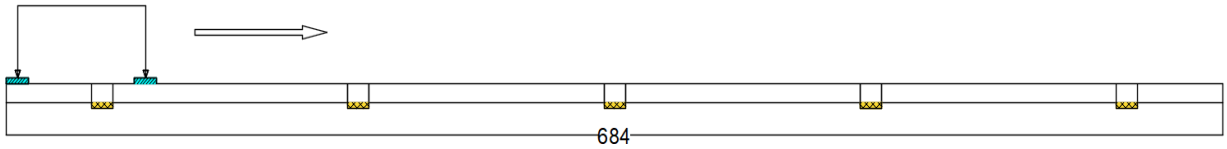

Figure 11.12. The placement of HL-93 load on the deck slab with 12 ft girder spacing (first combination)

Table 11.4. The total number of combinations created for 12 ft girder spacing with a one truck

No	Type of the deck	Distance from the face of the tire to the EOD (inches)
0	12 ft	0
1		14.4
2		28.8
3		43.2
4		57.6
5		72
6		86.4
7		100.8
8		115.2
9		129.6
10		144
11		158.4
12		172.8
13		187.2
14		201.6
15		216
16		230.4
17		244.8
18		259.2
19		273.6

Moment and shear Figures for a 12 ft girder spacing are provided for each scenario, and corresponding moment, shear and related envelopes are presented in the figures below.

Figure 11.13. Moment profile for deck slab with 12 ft girder spacing and single truck

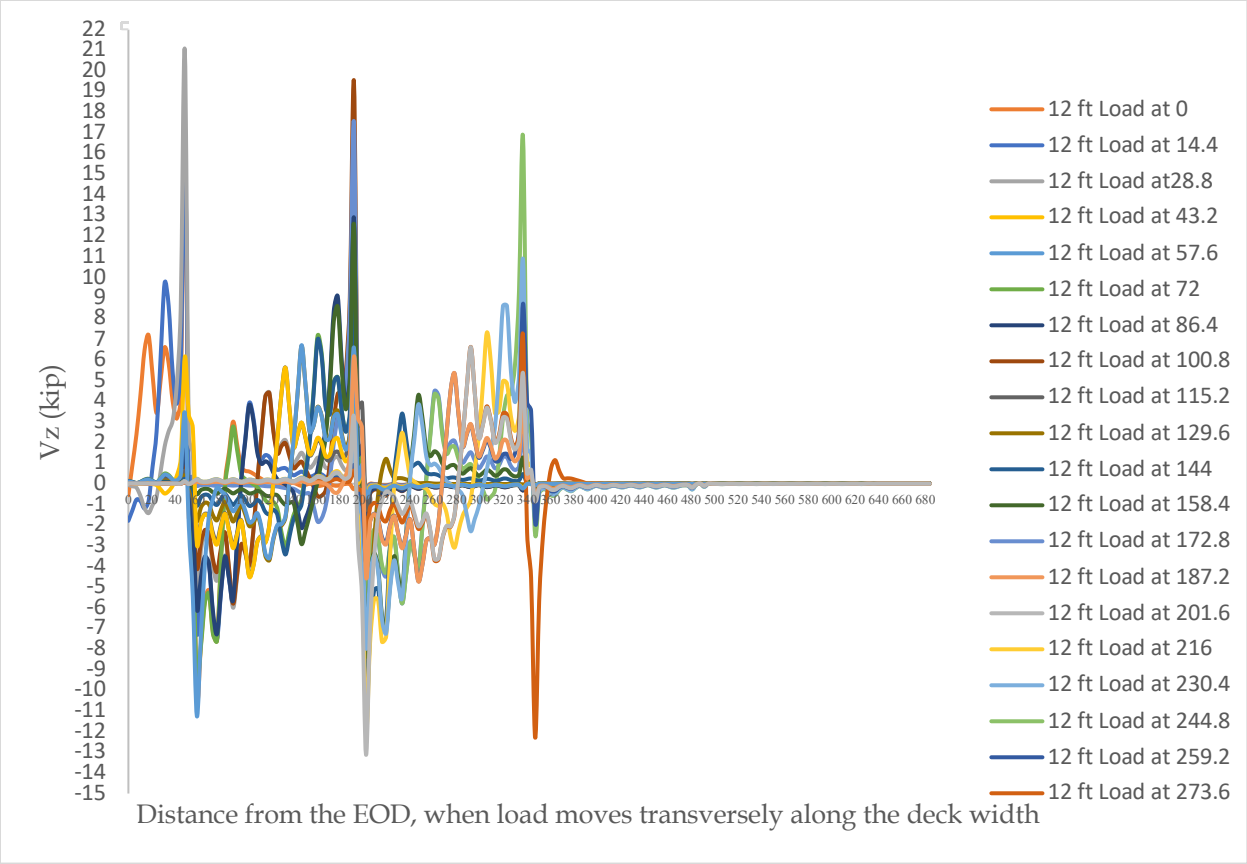

Figure 11.14. Shear profile for deck slab with 12 ft girder spacing and single truck

Figure 11.15. Moment envelope for deck slab with 12 ft girder spacing and single truck

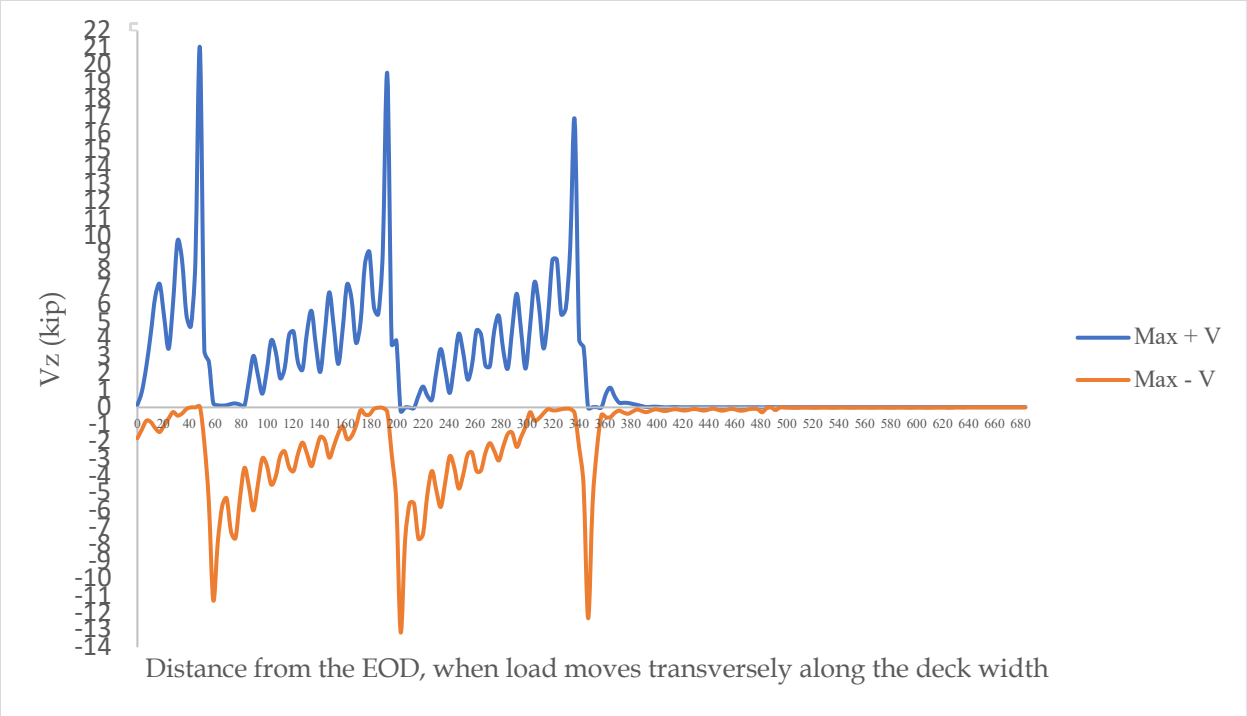

Figure 11.16. Shear envelope for deck slab with 12 ft girder spacing and single truck

When the moment results were compared, it was discovered that the maximum positive moment for a 12 ft. girder spacing deck slab occurred when the load patch was located at 115.2 inches away from the end of the slab, with a value of approximately 3.47 kip-ft/ft, and the maximum negative moment occurred when the truck patch load was located at 14.4 inches away from the end of the slab, with a value of approximately -7.63 kip-ft/ft.

When the shear results were compared, it was discovered that the maximum positive shear for a 12 ft. girder spacing deck slab occurred when the load patch was located at 28.8 inches away from the end of the slab, with a value of approximately 21 kip, and the maximum negative shear occurred when the truck patch load was located 201.6 inches away from the end of the slab, with a value of approximately -13.13 kip.

15 (ft) Girder Spacing with Four Cells

In modeling a 15 ft. girder spacing deck slab, at first, the truck is positioned at the end of the deck, then it is moved transversely as 10 percent of the deck (15×12×0.1 = 18 inches). In this way, a total of 19 combinations are created until one of the patch loads (truck tires) crosses the centerline of the bridge.

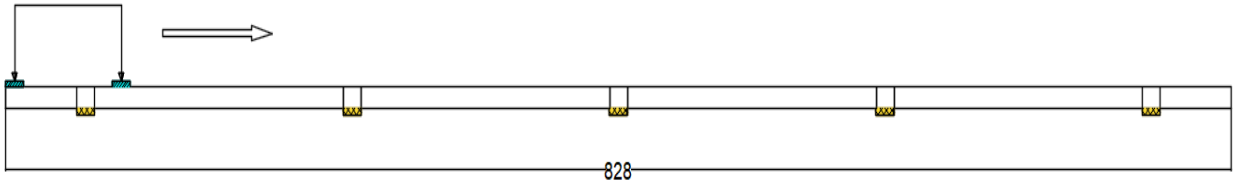

Figure 11.17. The placement of HL-93 load on the deck slab with 15 ft girder spacing (first combination)

Table 11.5 The total number of combinations created for 15 ft girder spacing with a one truck

No	Type of the deck	Distance from the face of the tire to the EOD (inches)
0	15 ft	0
1		18
2		36
3		54
4		72
5		90
6		108
7		126
8		144
9		162
10		180
11		198
12		216
13		234
14		252
15		270
16		288
17		306
18		324
19		342

Moment and shear diagrams for a 15 ft girder spacing are provided for each scenario, and corresponding moment, shear and related envelopes are presented in the figures below.

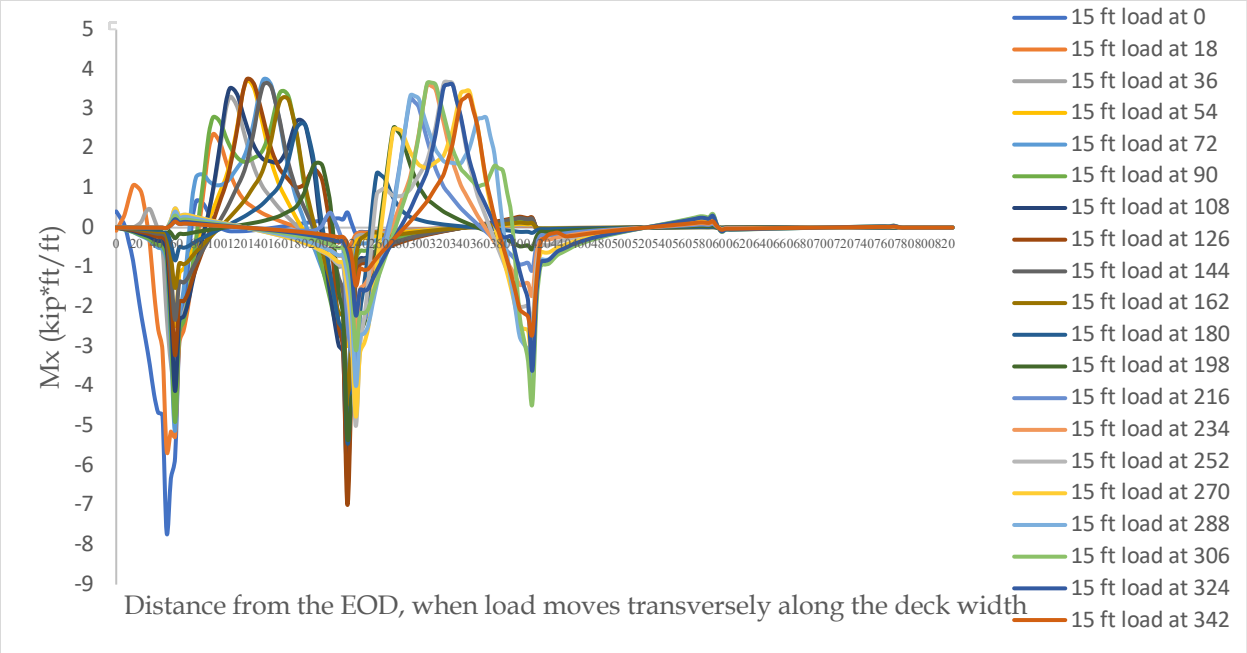

Figure 11.18. Moment profile for deck slab with 15 ft girder spacing and single truck

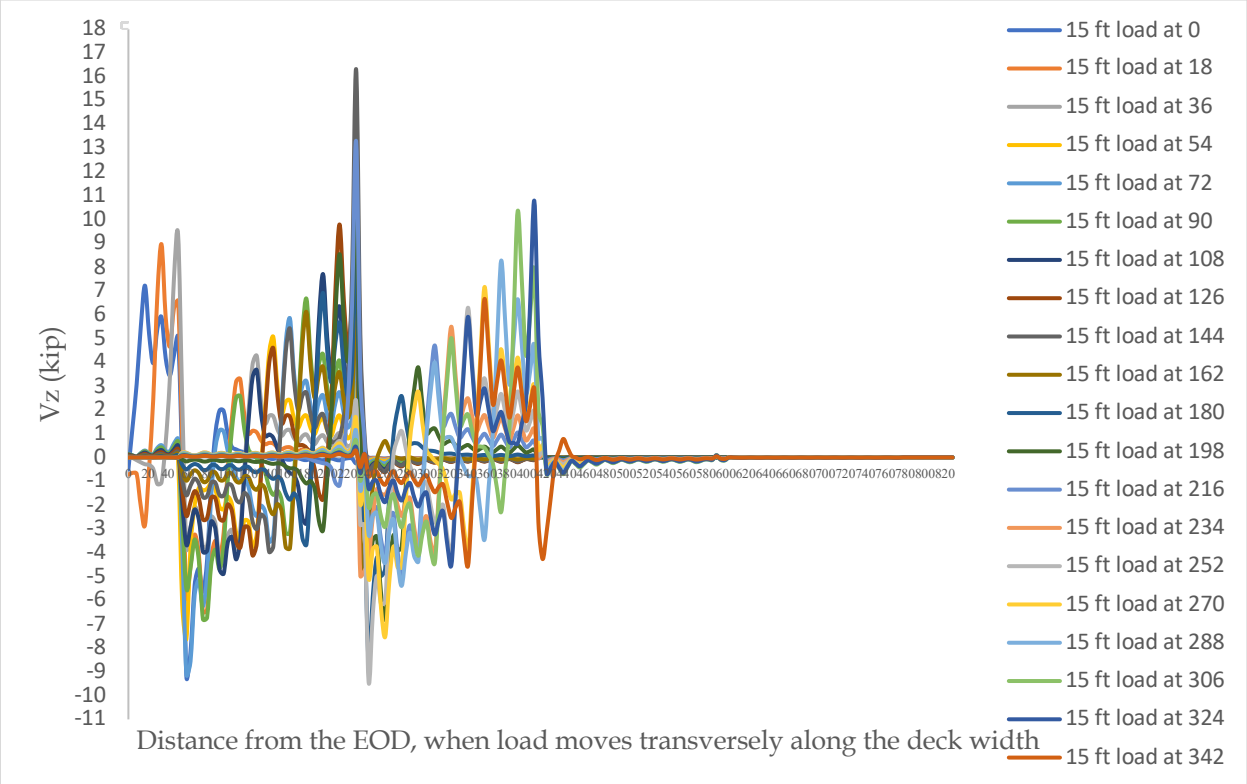

Figure 11.19. Shear profile for deck slab with 15 ft girder spacing and single truck

Figure 11.20. Moment envelope for deck slab with 15 ft girder spacing and single truck

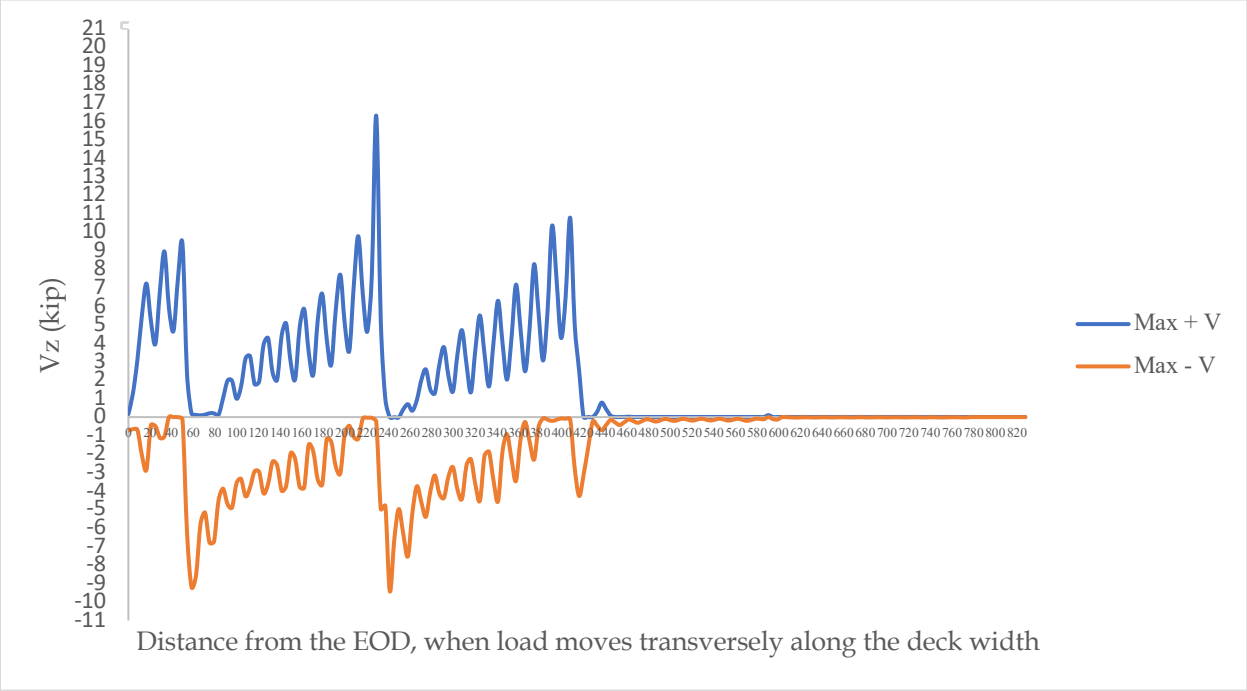

Figure 11.21. Shear envelope for deck slab with 15 ft girder spacing and single truck

When the moment results were compared, it was discovered that the maximum positive moment for a 15 ft. girder spacing deck slab occurred when the load patch was located at 126 inches away from the end of the slab, with a value of approximately 3.73 kip-ft/ft, and the maximum negative moment occurred when the truck patch load was located at the end of the slab, with a value of approximately -7.70 kip-ft/ft.

When the shear results were compared, it was discovered that the maximum positive shear for a 15 ft. girder spacing deck slab occurred when the load patch was located at 144inches away from the end of the slab, with a value of approximately 16.3 kip, and the maximum negative shear

occurred when the truck patch load was located 252 inches away from the end of the slab, with a value of approximately -9.42 kip.

9 (ft) Girder Spacing with Two Cells

In modeling a 9 ft. girder spacing deck slab with two cells, at first, the truck is positioned at the end of the deck, then it is moved transversely as 10 percent of the deck (9×12×0.1 = 10.8 inches). In this way, a total of 8 combinations are created until one of the patch loads (truck tires) crosses the centerline of the bridge.

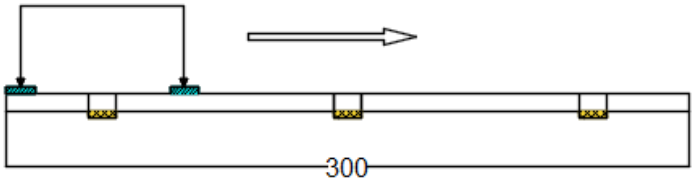

Figure 11.22. The placement of HL-93 load on the deck slab with 9 ft girder spacing (with two cells) (first combination).

Table 11.6 The total number of combinations created for 9 ft girder spacing with a one truck (with two cells)

No	Type of the deck	Distance from the face of the tire to the EOD (inches)
1	9 ft with two cells	0
2		10.8
3		21.6
4		32.4
5		43.2
6		54
7		64.8
8		75.6

Moment and shear Figures for a 9 ft girder spacing with two cells are provided for each scenario, and corresponding moment, shear and related envelopes are presented in the figures below.

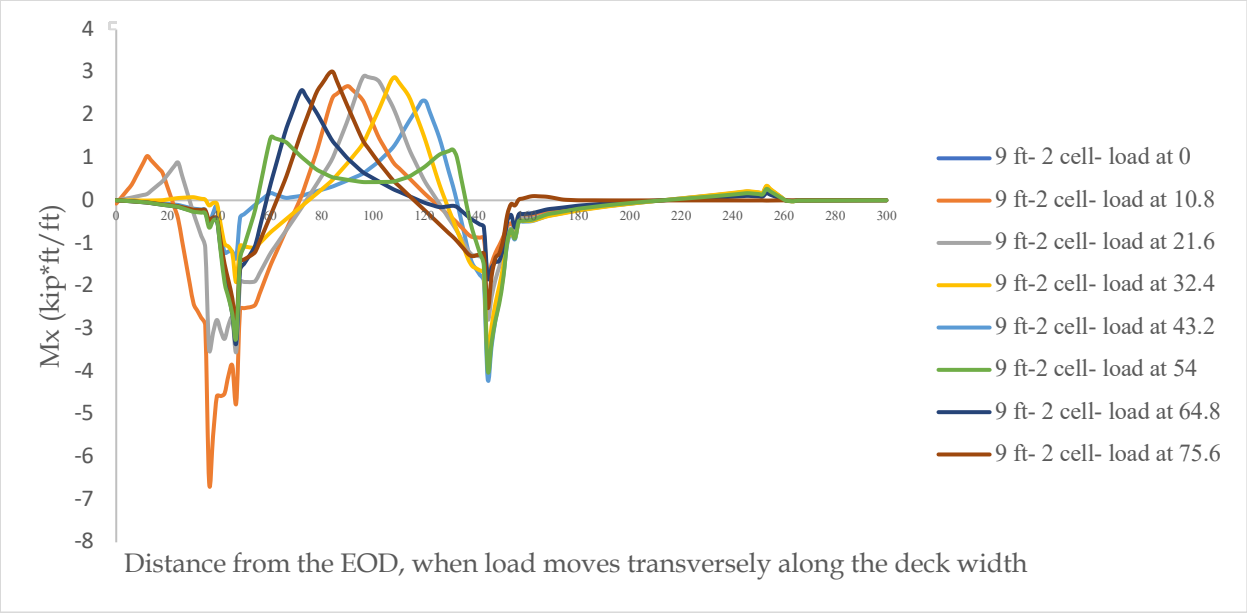

Figure 11.23. Moment profile for deck slab with 9 ft girder spacing and single truck (with two cells)

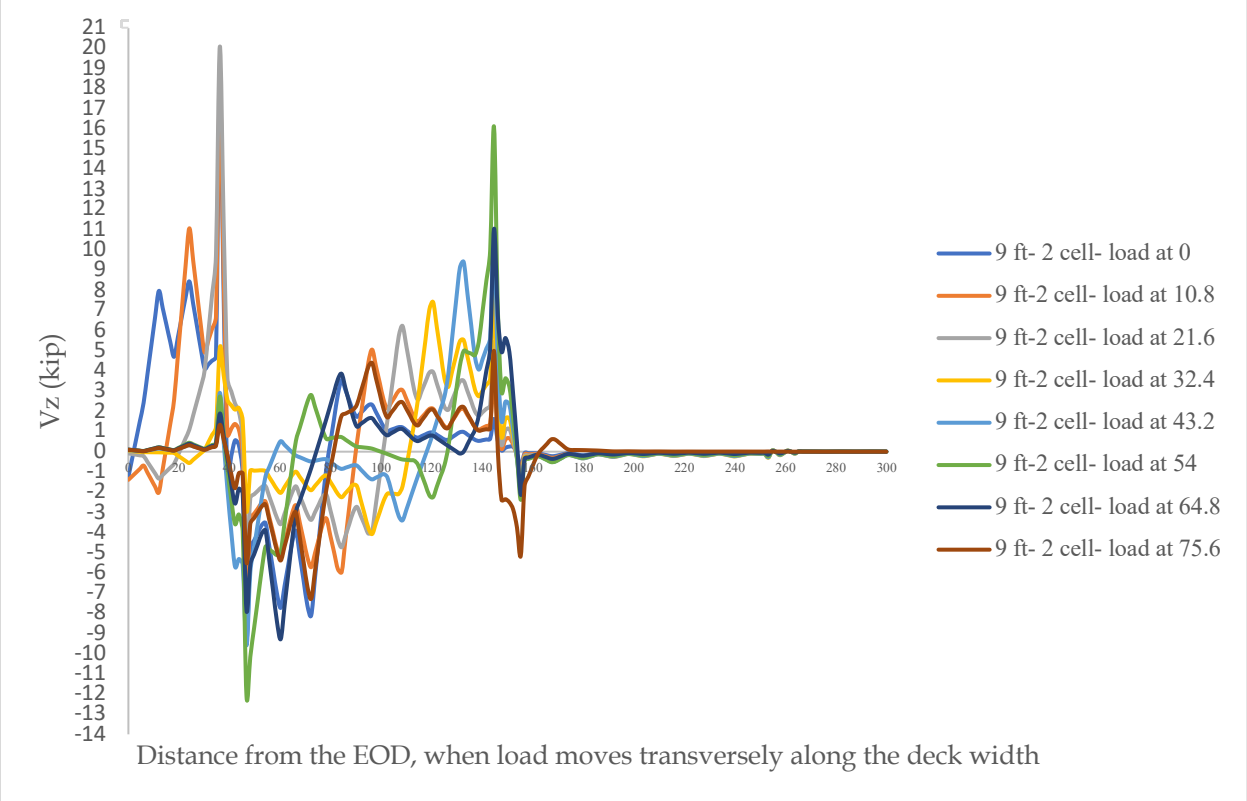

Figure 11.24. Shear profile for deck slab with 9 ft girder spacing and single truck (with two cells)

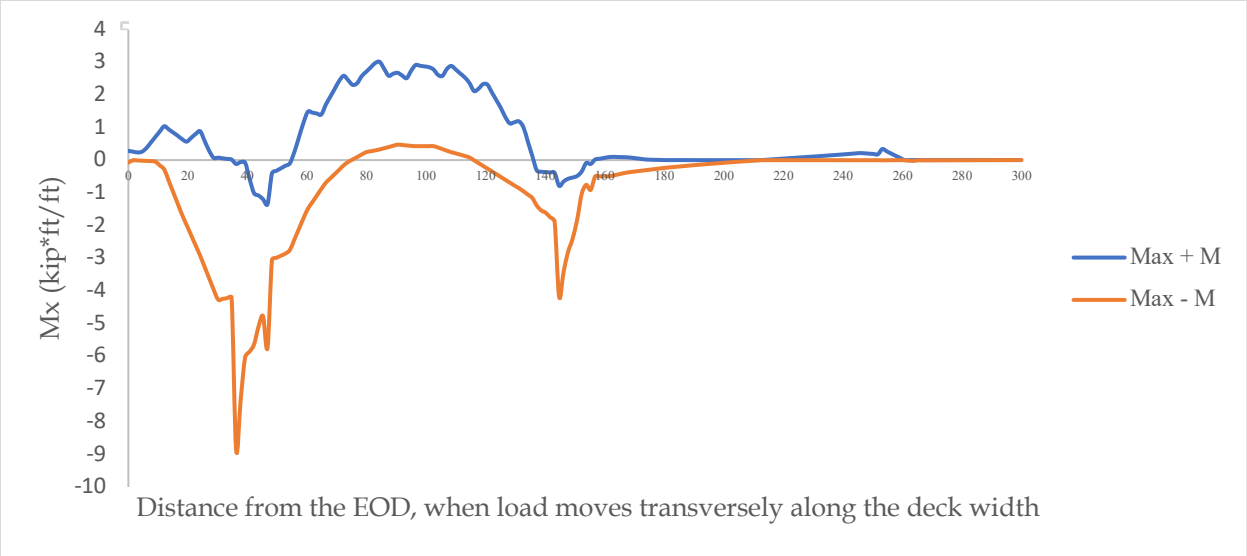

Figure 11.25. Moment envelope for deck slab with 9 ft girder spacing and single truck (with two cells)

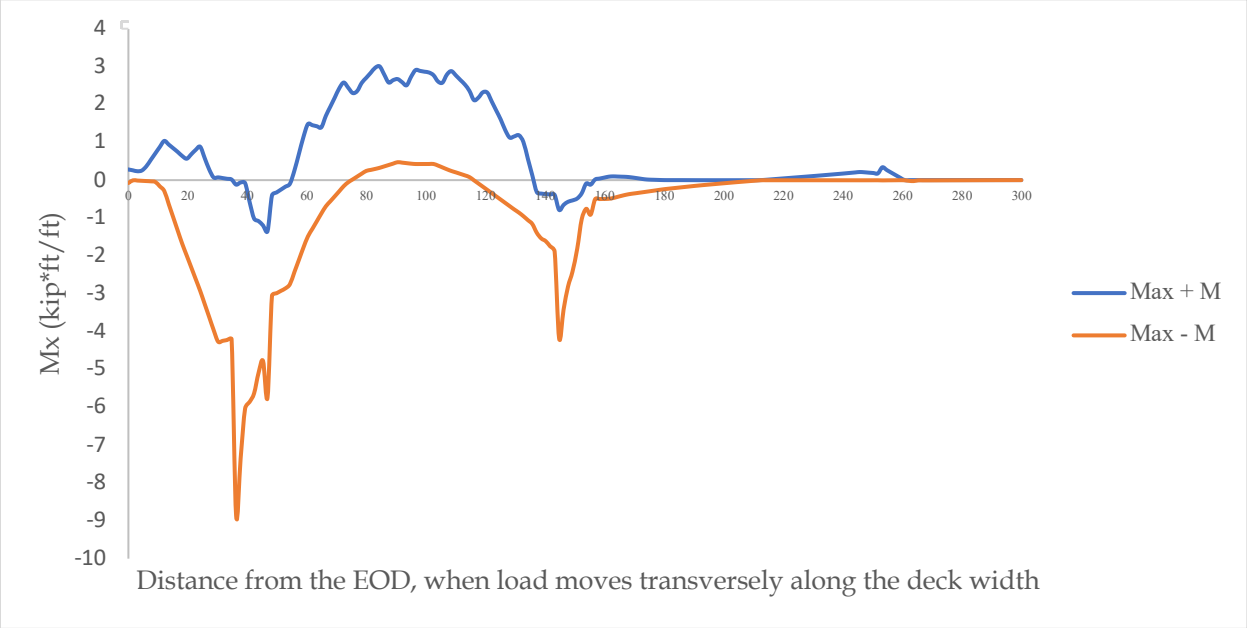

Figure 11.26. Shear envelope for deck slab with 9 ft girder spacing and single truck (with two cells)

15 (ft) Girder Spacing with Two Cells

In modeling a 15 ft. deck slab with two cells, at first, the truck is positioned at the end of the deck, then it is moved transversely as 10 percent of the deck (15×12×0.1 = 18 inches). In this way, a total of 10 combinations are created until one of the patch loads (truck tires) crosses the centerline of the bridge.

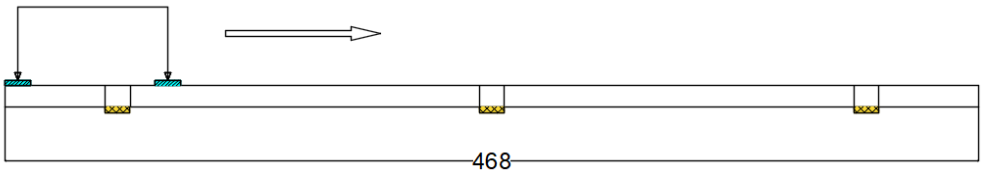

Figure 11.27. The placement of HL-93 load on the deck slab with 15 ft girder spacing (with two cells) (first combination)

Table 11.7 The total number of combinations created for 15 ft girder spacing with a one truck (with two cells)

No	Type of the deck	Distance from the face of the tire to the EOD (inches)
1	15 ft with two cells	0
2		18
3		36
4		54
5		72
6		90
7		108
8		126
9		144
10		162

Moment and shear Figures for a 15 ft girder spacing with two cells are provided for each scenario, and corresponding moment, shear and related envelopes are presented in the figures below.

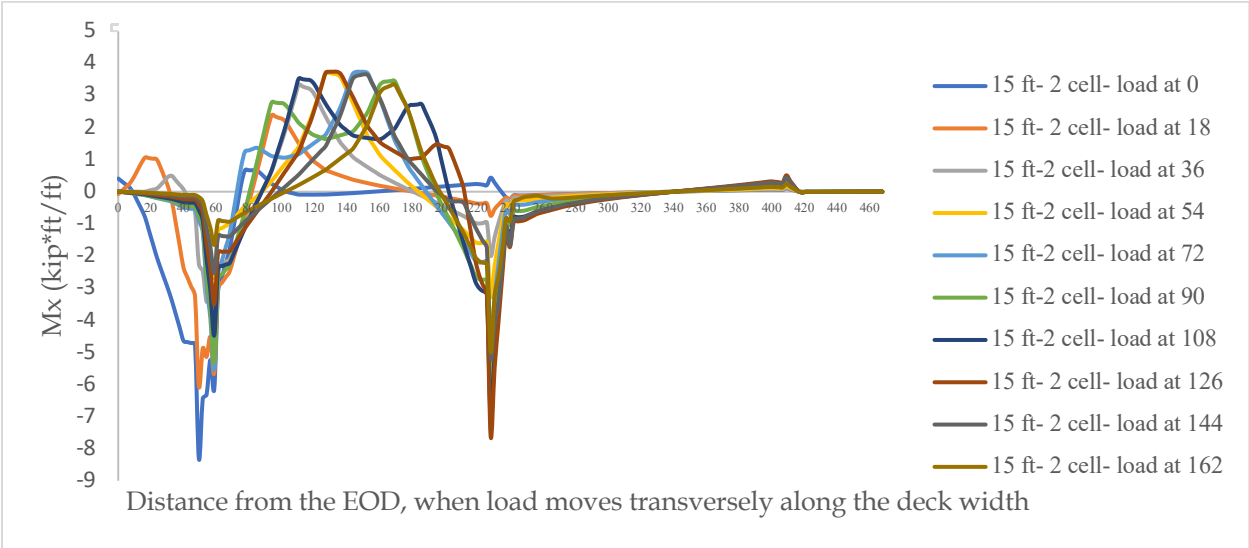

Figure 11.28. Moment profile for deck slab with 15 ft girder spacing and single truck (with two cells)

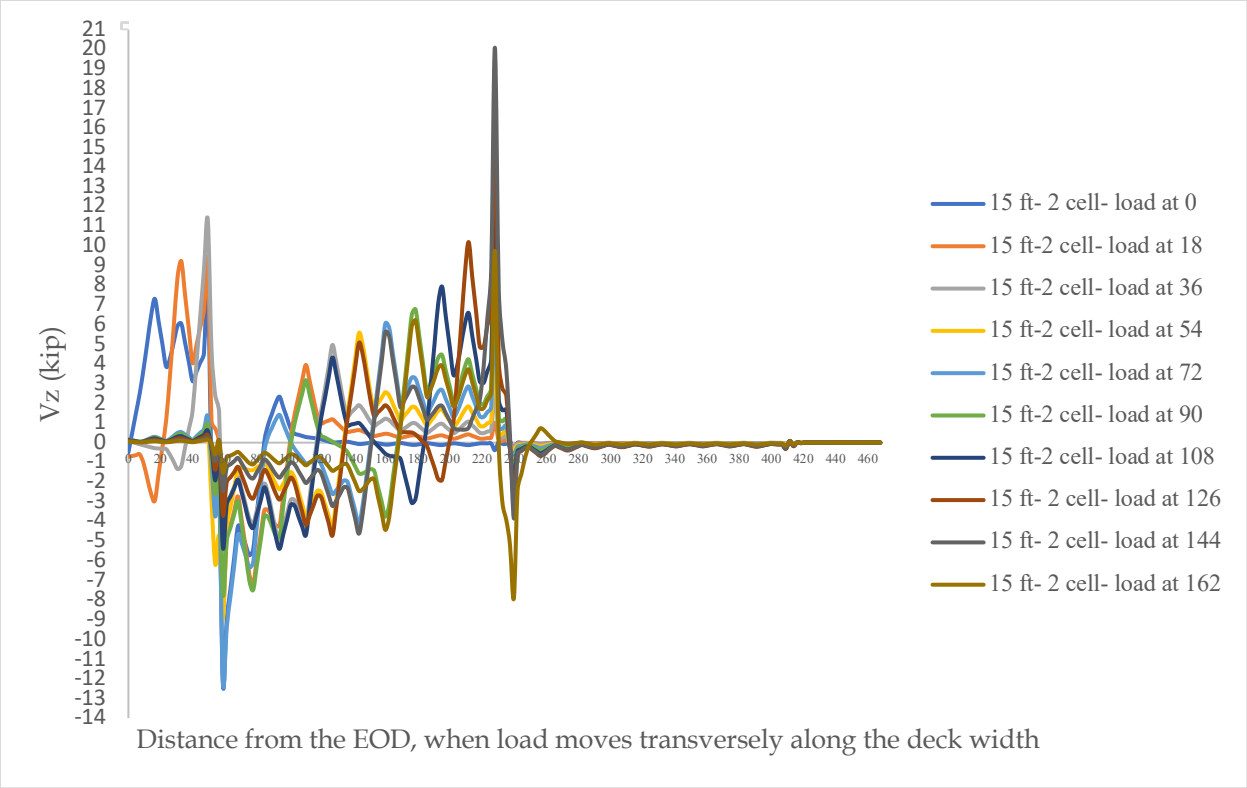

Figure 11.29. Shear profile for deck slab with 15 ft girder spacing and single truck (with two cells)

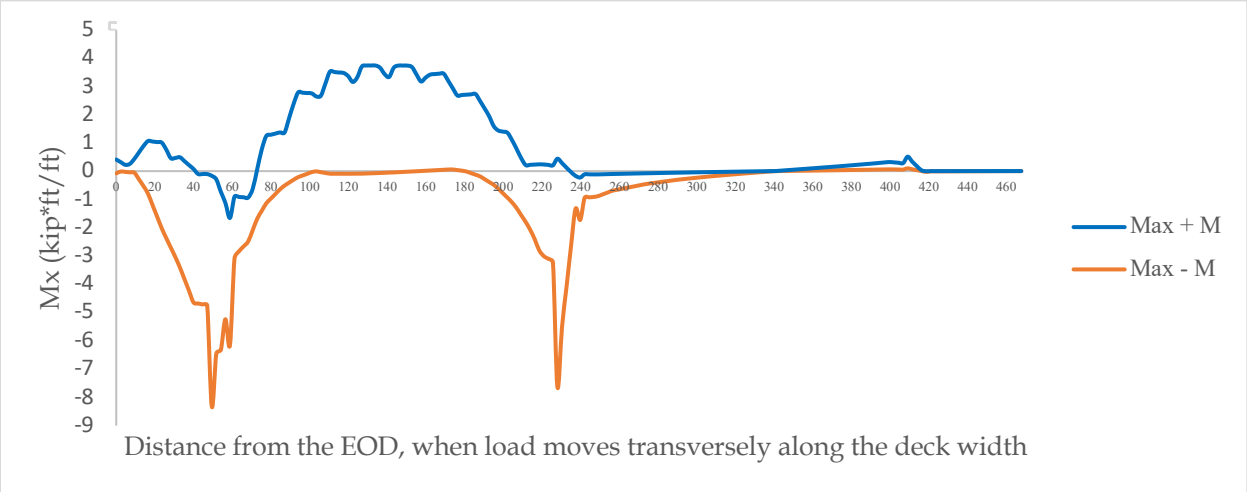

Figure 11.30. Moment envelope for deck slab with 15 ft girder spacing and single truck (with two cells)

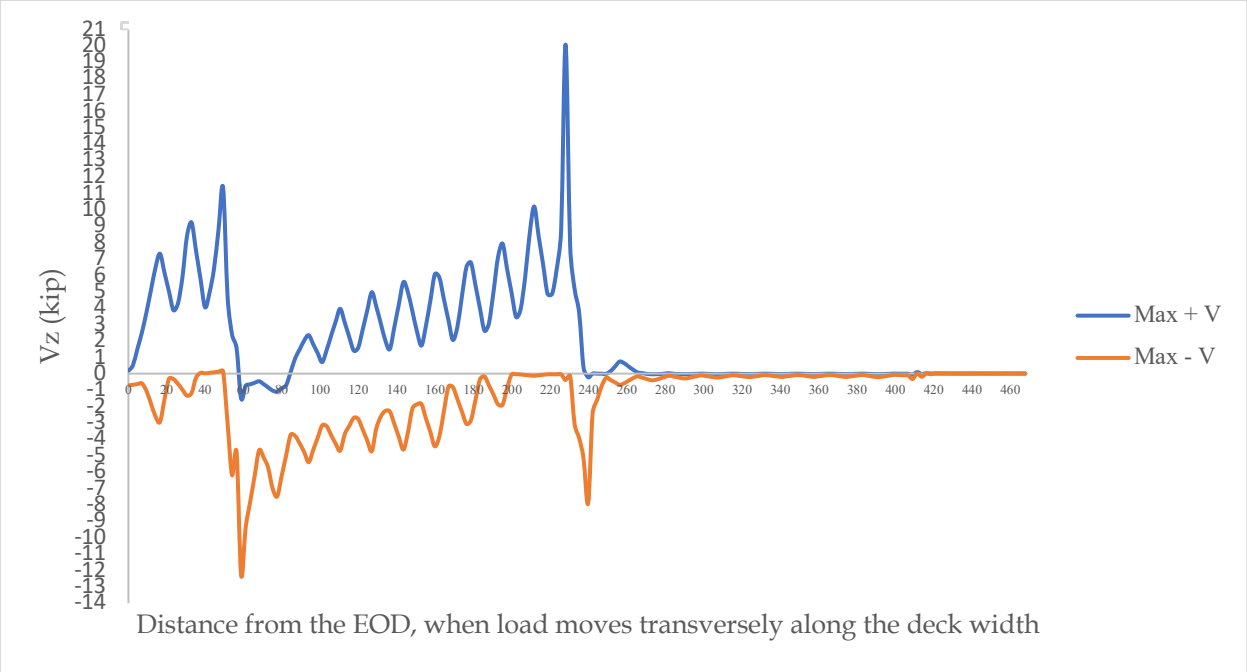

Figure 11.31. Shear envelope for deck slab with 15 ft girder spacing and single truck (with two cells)